

DOCTORAL THESIS

Contributions to the Modelling and Control of Fin-Actuated Autonomous Underwater Vehicles

Mohamed Walid Remmas

TALLINN UNIVERSITY OF TECHNOLOGY
DOCTORAL THESIS
71/2023

Contributions to the Modelling and Control of Fin-Actuated Autonomous Underwater Vehicles

MOHAMED WALID REMMAS



TALLINN UNIVERSITY OF TECHNOLOGY
School of Information Technologies
Department of Computer Systems

The dissertation was accepted for the defence of the degree of Doctor of Philosophy (Computer and Systems Engineering) on 30 November 2023

Supervisors: Pr. Maarja Kruusmaa,
Department of Computer Systems, School of Information Technologies
Tallinn University of Technology
Tallinn, Estonia

Pr. François Pierrot,
CNRS, LIRMM
University of Montpellier
Montpellier, France

Co-supervisor: Dr. Ahmed Chemori,
CNRS, LIRMM
University of Montpellier
Montpellier, France

Opponents: Pr. Luc Jaulin,
Lab-STICC, Robex
ENSTA-Bretagne
Brest, France

Pr. Tor Arne Johansen,
Department of Engineering Cybernetics
Norwegian University of Science and Technology
Trondheim, Norway

Defence of the thesis: 18 December 2023, Tallinn

Declaration:

Hereby I declare that this doctoral thesis, my original investigation and achievement, submitted for the doctoral degree at Tallinn University of Technology, has not been submitted for any academic degree elsewhere.

Mohamed Walid Remmas

signature

Copyright: Mohamed Walid Remmas, 2023
ISSN 2585-6898 (publication)
ISBN 978-9916-80-094-2 (publication)
ISSN 2585-6901 (PDF)
ISBN 978-9916-80-095-9 (PDF)

TALLINNA TEHNIKAÜLIKOOL
DOKTORITÖÖ
71/2023

Uimedega autonoomsete allveesõidukite modelleerimis- ja juhtimisloogika edendamine

MOHAMED WALID REMMAS



Contents

List of Publications	7
Author's Contributions to the Publications	8
1 Introduction	9
1.1 Problem formulation and related work	9
1.1.1 Human-AUV interaction	9
1.1.2 Complex dynamics of fin-actuated AUVs	10
1.1.3 Motion control challenges	11
1.1.4 Fault tolerance	12
1.2 Contributions of the thesis	13
1.2.1 Contribution 1: Data-fusion based diver tracking	13
1.2.2 Contribution 2: Inverse modelling of fin dynamics	13
1.2.3 Contribution 3: Control allocation for 6-DOF control of fin-Actuated AUVs	14
1.2.4 Contribution 4: Fault-tolerant control for fin-actuated AUVs	14
1.3 Thesis outline	14
2 Hardware and Modelling	15
2.1 Experimental platform U-CAT	15
2.2 Kinematics modelling	15
2.2.1 Coordinates system	15
2.2.2 Kinematic Model:	17
2.3 Dynamics Modelling	17
2.3.1 Weight and Buoyancy:	18
2.3.2 Hydrodynamic Damping:	18
2.3.3 Coriolis and Centrifugal Inertia Forces:	18
2.3.4 Fins-Generated wrenches:	18
2.3.5 External Disturbances:	19
2.4 Fin dynamics modelling	19
2.5 Control allocation	20
3 Data-fusion Based Diver Tracking	22
3.1 Overview and motivation	22
3.2 Proposed tracking algorithm	22
3.2.1 Visual detection using DNN	23
3.2.2 Acoustic Detection	23
3.2.3 Data-fusion scheme	24
3.2.4 Control scheme	24
3.3 Experimental results and discussion	24
3.3.1 Experimental scenarios	25
3.3.2 Visual tracking	25
3.3.3 Acoustic tracking	26
3.3.4 Data-fusion based tracking	26
3.4 Conclusions	28
4 Inverse modelling of fin dynamics	30
4.1 Overview and motivation	30

4.2	Proposed thrust to amplitude model	30
4.2.1	Empirical model	30
4.2.2	The proposed fin model: A nonlinear analytical model	31
4.3	Experimental Results and Discussion.....	33
4.3.1	Experimental scenario 1: Control in nominal case	34
4.3.2	Experimental scenario 2: Robustness test towards buoyancy change	34
4.3.3	Experimental scenario 3: External disturbances rejection	34
4.4	Conclusions	36
5	Control allocation for 6-DOF control of fin-Actuated AUVs	37
5.1	Overview and motivation	37
5.2	Solving the control allocation problem.....	38
5.2.1	Direct solution	38
5.2.2	Optimization-based solution.....	39
5.2.3	Proposed analytic solution	40
5.3	Method assessment.....	41
5.3.1	Simulation setup	41
5.3.2	Experimental setup.....	41
5.4	Results and discussions	42
5.4.1	Simulation results	42
5.4.2	Experimental Results	44
5.5	Conclusions	48
6	Fault-tolerant control for fin-actuated AUVs	49
6.1	Overview and Motivation	49
6.2	Proposed FTC scheme.....	49
6.3	Experimental results and discussions	52
6.4	Conclusions.....	55
7	Conclusions and future work.....	57
	References.....	59
	Acknowledgments.....	68
	Abstract.....	69
	Kokkuvõte	70
	Appendix 1: Publication I	71
	Appendix 2: Publication II	87
	Appendix 3: Publication III	99
	Appendix 4: Publication IV	110
	Curriculum Vitae	132
	Elulookirjeldus.....	135

List of Publications

The present Ph.D. thesis is based on the following publications that are referred to in the text by Roman numbers.

- I Walid Remmas, Ahmed Chemori, and Maarja Kruusmaa. Diver tracking in open waters: A low-cost approach based on visual and acoustic sensor fusion. *Journal of Field Robotics*, 38(3):494–508, 2021
- II Walid Remmas, Ahmed Chemori, and Maarja Kruusmaa. Inverse-model intelligent control of fin-actuated underwater robots based on drag force propulsion. *Ocean Engineering*, 239:109883, 2021
- III Walid Remmas, Ahmed Chemori, and Maarja Kruusmaa. Fault-tolerant control allocation for a bio-inspired underactuated auv in the presence of actuator failures: Design and experiments. *Ocean Engineering*, 15(20):54–66, 2023

Submissions under review

- IV Walid Remmas, Christian Meurer, Ahmed Chemori, and Maarja Kruusmaa. Control Allocation for 6-DOF Control of a Highly Manoeuvrable Under-actuated Bio-inspired AUV. *Submitted to IEEE Transactions on Robotics*, 2023

Other Related Publications

This work is also published/presented in adjacent fields but does not form a main part of this thesis.

1. Walid Remmas, Roza Gkliva, and Asko Ristolainen. Dynamic modelling of a screw actuator for improved locomotion control on various terrains. In *EGU General Assembly Conference Abstracts*, pages EGU22–5726, 2022

Author's Contributions to the Publications

- I In [Publication I] I was the main author; defined the research problem, designed the data-fusion based diver tracking scheme, implemented the proposed solution on the robot's hardware, planned and carried out the experiments, analysed the results, and wrote the manuscript.
- II In [Publication II], I was the main author, defined the research problem, derived the inverse fin model, implemented the proposed solution on the robot's hardware, planned and carried out the experiments, analysed the results and validated the model experimentally, and wrote the manuscript.
- III In [Publication III] I was the main author, defined the research problem, designed the FTC scheme, implemented the proposed solution on the robot's hardware, planned and carried out the experiments, analysed the results, and wrote the manuscript.
- IV In [Publication IV] I was co-first author, I participated in all of the following items: defining the research problem, coding the robot's simulation software, proposing the control allocation solution for 6DOF control, implementations on the robot's hardware, planning and carrying-out out the experiments, analysing the results, and writing the manuscript.

1 Introduction

Importance of fin-actuated AUVs:

The vastness of the underwater domain, with its intricate terrains and unpredictable dynamics, has always posed challenges for exploration and research. While effective in many scenarios, traditional propeller-driven Autonomous Underwater Vehicles (AUVs) often fall short when navigating complex environments such as coral reefs, shipwrecks, or underwater caves. The limitations of these conventional AUVs have led to a growing interest in alternative propulsion mechanisms, particularly those inspired by nature [6, 7].

Inspired by these biological principles, Fin-actuated AUVs have emerged as a promising alternative to traditional AUVs [8, 9]. Through millions of years of evolution, marine animals have developed efficient locomotion mechanisms that allow them to navigate diverse underwater terrains with remarkable agility. Observing these creatures, it becomes evident that their fins play a pivotal role in their movement. While aerial creatures like birds and insects use flapping motions to generate thrust and lift, certain aquatic species predominantly employ fin flapping to produce thrust. This has spurred a surge of interest in the design and control of fin-actuated robotic systems [10, 11, 12, 13].

Biomimetic fins offer several advantages, unlike propellers, which can be environmentally harmful and less efficient in intricate environments. Firstly, they provide better locomotion efficiency, allowing the AUV to cover longer distances with the same energy expenditure [14]. Secondly, fin-actuated AUVs are environmentally benign, reducing the risk of damaging delicate underwater ecosystems or harming marine life. This is particularly crucial in areas like coral reefs, which are biodiversity hotspots and highly susceptible to external disturbances.

However, the transition from propeller-driven to fin-actuated AUVs is not straightforward. The dynamics of fin propulsion are inherently different and more complex. Understanding these dynamics is crucial for designing efficient fin-actuated AUVs. Moreover, the control mechanisms for these AUVs need to account for the unique challenges posed by fin propulsion, such as ensuring stability while navigating with oscillating fins.

1.1 Problem formulation and related work

Inspired by marine life, Fin-actuated AUVs have risen as a potential answer to this call. Their bio-mimetic design and agile manoeuvrability uniquely suit them for various underwater tasks. Yet, their deployment is not without challenges:

1.1.1 Human-AUV interaction

The potential of underwater human-robot collaboration has garnered significant attention in recent research [15, 16, 17]. While underwater robots offer promising capabilities, their autonomy is hindered due to communication and localisation challenges inherent to underwater conditions. Conversely, human divers face constraints such as limited payload capacity, restricted diving durations, and the risks associated with confined spaces. This has led to the exploration of AUVs as potential aids for divers, assisting in tasks like payload transport, data collection, and area inspection.

A pivotal aspect of this collaboration is the ability to detect and track divers accurately. Achieving precise diver following using compact underwater vehicles can pave the way for the development of companion robots, beneficial for applications like underwater archaeology and off-shore structure inspections [16].

While target detection and tracking are well-established for terrestrial applications [18, 19, 20, 21, 22], the underwater environment presents unique challenges. Factors such as

electromagnetic wave propagation limitations and the distinct optical properties of water, including absorption, diffusion, and turbidity, complicate the use of conventional vision-based tracking methods [23].

Despite these challenges, substantial research has been conducted using vision-based and acoustic-based methods. Although limited by detection range and feature extraction challenges, vision-based techniques are effective in certain conditions, such as when operating in clear or shallow waters. Various features, including colour and shape, have been explored for underwater object detection [24, 25, 26, 27, 28]. However, each method has limitations, often requiring optimal visibility and proximity to the target. The challenge of ensuring the target remains within the camera’s field of view further complicates these techniques.

Recent advancements in GPU computing power have facilitated the adoption of deep neural networks (DNN) for image processing [29]. State-of-the-art algorithms for terrestrial object detection now leverage DNN architectures [30, 31, 32, 33]. This approach is being adapted for underwater target tracking with digital cameras and sonar imagery [34, 35, 36, 37, 38, 39]. These DNN models, especially the downscaled versions, offer the potential for rapid and reliable target detection even on vehicles with constrained computational resources.

However, all vision-based techniques, whether relying on digital cameras or acoustic imaging, face a common limitation: the diver needs to remain within the sensor’s field of view. This restricts diver mobility and poses challenges if external disturbances cause the diver to exit the camera’s view. Addressing this issue remains a gap in current research.

In underwater settings, acoustic methods are often more viable. They can be employed in various capacities, from sonar imaging to precise beacon localisation. Acoustic signals also present challenges, influenced by reflections, low frequencies, and environmental disturbances. The quality of these signals can vary based on the underwater environment, with factors like water depth, surface movement, and ambient noise playing crucial roles [40, 41].

Combining acoustic perception with machine vision techniques offers a comprehensive solution [42]. The fusion of these modalities overcomes their limitations, presenting a more robust approach to diver tracking [43].

1.1.2 Complex dynamics of fin-actuated AUVs

Designing efficient fin-actuated AUVs necessitates a nuanced understanding of hydrodynamics, further complicated by the flexible nature of oscillating fins and the intricate fluid-structure interactions they entail. Fin-actuated underwater vehicles typically modulate their motion by altering various locomotion primitives of the fins, such as frequency, amplitude, and phase shift. More advanced designs also consider parameters like angle of attack, stiffness, and surface area [44]. Over the years, control mechanisms for Median Paired Fin (MPF) actuated robots have evolved, incorporating techniques from PID control [45] to adaptive control [46], RISE control [47], fuzzy logic control [1], and bio-inspired Central Pattern Generator (CPG) control [48, 49]. However, the efficacy of these control mechanisms is often constrained by the availability of a reliable and invertible model that can relate the controller output to the fin’s oscillating parameters.

In this context, numerous studies have been undertaken to model the thrust generated by flapping foils. For instance, the work in [50] related average thrust to mass flow rate but was limited to specific mass flow rate ranges—another approach [51] focused on lift force to simulate robot dynamics. While computational fluid dynamics have been employed for precise modelling [52, 53, 54], their real-time implementation on resource-

constrained robots remains a challenge. Authors in [55] presented a low-order set of ordinary differential equations focused on open-loop control, offering a step in this direction but leaving room for further exploration and refinement.

The need for an invertible model becomes evident when considering the limitations of existing methods. An invertible model would allow for a more direct and efficient translation of control outputs to fin oscillation parameters, enhancing the AUV's navigational capabilities.

1.1.3 Motion control challenges

Unlike traditional AUVs, which are typically designed to be either fully actuated or over-actuated, fin-actuated vehicles offer a unique advantage; they can utilise the fins not only for thrust generation but also for thrust vectoring, allowing for motion control in multiple DOF with fewer actuators. However, this advantage comes with complex challenges due to the need for precise control of both thrust magnitude and direction using the limited number of fin actuators. Effectively managing these challenges requires the development of specialised control allocation methods tailored to the unique characteristics of fin-actuated vehicles.

While several studies have addressed the control allocation problem for motion control in AUVs [56], these investigations have predominantly focused on propeller-based actuation systems. These studies have proposed various methodologies, such as direct control allocation [57, 58], daisy chaining [59, 60], and real-time optimisation using constrained linear or quadratic programming [61, 62, 63, 64]. Recent advancements in AUV designs with tiltable thrusters have also explored control allocation techniques to manage actuation redundancy [65, 66]. For instance, research has demonstrated the efficacy of pseudo-inverse control allocation methods with predefined tilting angles for stable hovering performance in propeller-based AUVs [65]. Decomposing the nonlinear force input term of tilting thrusters into horizontal and vertical directions and using pseudo-inverse and null-space solutions has proven effective in minimising thrust force [66]. However, it is essential to acknowledge that control allocation methods developed for propeller-based actuation systems may not directly apply to fin-actuated vehicles. Unlike fixed thrusters, fins require rotation to change the thrust direction, leading to delays and disturbances in control response. While tiltable thrusters need a similar amount of rotation, they do not create the same amount of disturbances due to the difference in geometry compared to fins, which create a significant amount of drag when rotated. Additionally, tiltable thrusters can theoretically produce thrust throughout the rotation, while thrust generation is halted during rotation for fin-based actuation. These characteristics of fin actuation necessitate the development of tailored control allocation approaches that account for the specific characteristics of fin-actuated vehicles. It is thus hypothesised that a minimisation of necessary fin rotations and an intelligent choice of the number of actuators contributing to each DOF are crucial for successful trajectory tracking.

Beyond control allocation, regarding motion control, the control of turtle-like fin-driven vehicles has mainly been manual or without feedback. A considerable focus has been on open-loop gait generation, with several works emphasising the use of CPGs for this purpose [67, 68, 69, 70, 71].

In the realm of feedback-based control, Geder et al. explored a model-free control framework specifically for heading or depth control [54]. Licht et al. [72] delved into attitude control tailored for various turning manoeuvres. Siegenthaler et al. [73] employed a model-free angular rate controller to stabilize forward swimming. However, these solutions predominantly addressed a single Degree of Freedom (DOF) at a time, often relying

on more straightforward model-free control frameworks that may not guarantee robustness or provable stability.

Chemori et al. [47] took a step further by investigating depth control for the U-CAT AUV. By comparing a model-free RISE controller to a standard PID control, they demonstrated the superior performance of the RISE controller, especially in scenarios with external disturbances. Yet, this approach still focused on a single DOF.

The challenges of path following and trajectory tracking, essential for monitoring tasks, remain relatively understudied for the AUV types under consideration. Some works, such as [50] and [74], have delved into modelling and model-based control of the Aqua AUV for trajectory tracking control, but again, these studies often address only a single DOF at a time. Giguere et al. [75] presented a multi-DOF control approach for the Aqua AUV, employing PID and PI controllers. Their method, while effective, required the tuning of 45 control parameters.

Salumäe et al. [76] proposed a more comprehensive framework for the U-CAT AUV, enabling simultaneous motion in multiple DOFs. Their model-based approach, termed inverse dynamics, utilized feedback linearization with acceleration feedforward. This controller outperformed standard PID controllers, especially in the presence of external disturbances. However, complexities arising from motion coupling were addressed by prioritizing specific DOFs, meaning that not all trajectories were followed simultaneously.

Fin-based actuation's inherent agility and versatility have not been fully leveraged in existing solutions. Smallwood and Whitcomb [77] highlighted the potential advantages of adaptive model-based control approaches over fixed model-based controllers. While adaptive model-based control for 6-DOF tracking has been extensively studied for standard propeller-driven AUVs [78, 79, 80], the common orientation representations for such frameworks, which often rely on Euler angles, contain singularities. This has led to the exploration of quaternion-based controllers, which offer a singularity-free representation of 3D orientation [81, 82]. However, achieving global asymptotic stabilization with continuous-time state feedback remains a challenge [83].

In this context, Basso et al. [84] introduced a hybrid adaptive control approach, which was experimentally validated using a BlueROV2. This work adapted their framework to test two control tasks for an under-actuated fin-actuated AUV with only four actuators. The challenges posed by fin actuation, such as the need for precise control of thrust magnitude and direction with limited actuators, necessitate innovative control allocation methods tailored to fin-actuated vehicles.

1.1.4 Fault tolerance

Given the hostile nature of underwater environments, AUVs are vulnerable to various faults, from external disturbances to system malfunctions. Ensuring the fault tolerance of these systems is not just a technical requirement but a safety imperative. The pursuit of robust fault-tolerant control (FTC) strategies for thruster-based underwater robots has been a focal point of research endeavours in recent times [85, 86]. This domain encompasses a spectrum of techniques addressing the triad of FTC components: (i) Fault Detection: This phase is concerned with identifying operational anomalies that hinder the robot's optimal functionality. (ii) Fault Isolation: Post detection, this step zeroes in on the root cause and specific location of the detected fault. (iii) Fault Accommodation: The final component ensures the robot can fulfil its designated tasks despite detected faults. Readers are directed to seminal works such as [85, 87, 86] and the encompassed references for a comprehensive understanding of fault detection and isolation.

Fault accommodation strategies in the literature predominantly bifurcate into active

and passive FTC paradigms.

Active FTC: This approach, exemplified by methodologies like control reconfiguration [88, 89] and control allocation [90, 91, 92], is characterized by its proactive stance. It mandates continuous system surveillance to detect potential faults preemptively, deploying corrective actions to either avert or minimise the ramifications of hardware malfunctions.

Passive FTC: Contrasting with its active counterpart, passive FTC, as illustrated in studies like [93, 94], capitalises on the built-in redundancy and resilience of the system's design. This inherent robustness enables the system to withstand and operate through faults without necessitating active oversight or interventions.

While a significant portion of the research, as mentioned above, is tailored to thruster-actuated AUVs, there's a burgeoning interest in fin-actuated AUVs [8, 9]. This inclination stems from their enhanced locomotion efficacy [14] and superior manoeuvring capabilities [95]. However, the literature landscape reveals a conspicuous gap in FTC strategies designed explicitly for fin-actuated AUVs. To the best of the authors' knowledge, the solitary contribution in this niche is [96], where a passive FTC mechanism was introduced. This mechanism leveraged a CPG-based controller to rectify the directional orientation of a bio-inspired robot equipped with a multi-joint tail design.

1.2 Contributions of the thesis

To address the multifaceted challenges within underwater robotics, this thesis is driven by a set of clear and ambitious objectives. These objectives are designed to push the boundaries of what is currently achievable in the field, leveraging insights from marine life and the latest advancements in robotics. The primary objectives of this thesis are outlined below:

1.2.1 Contribution 1: Data-fusion based diver tracking

The first objective of this thesis is to design and implement an advanced diver tracking solution tailored explicitly for fin-actuated AUVs. These AUVs offer the advantage of safe fin actuation, making them ideal for operations near divers. The proposed solution is engineered to function robustly in challenging underwater conditions, such as limited visibility and dynamic marine settings. The proposed solution aims for superior tracking accuracy by combining visual and acoustic data from low-cost sensors. This integrated approach not only enhances the robustness of the tracking but also contributes to the safety and efficiency of underwater operations [Publication I].

1.2.2 Contribution 2: Inverse modelling of fin dynamics

The second objective addresses the challenges associated with the dynamic modelling of fin-actuated AUVs. Unlike traditional propeller-driven AUVs, fin-actuated vehicles exhibit complex fluid-structure interactions due to their oscillating fins. The aim is to develop an invertible nonlinear analytical model that captures the relationship between oscillation amplitude, frequency, and the required thrust force. This model is empirically validated and computationally efficient, making it suitable for real-time implementation on resource-constrained underwater vehicles. This model serves as a critical foundation for developing more advanced and efficient control strategies by providing a direct mapping between controller outputs and fin oscillation parameters. It offers a significant step forward in understanding fin-actuated AUVs' unique propulsion mechanisms and navigational capabilities [Publication II].

1.2.3 Contribution 3: Control allocation for 6-DOF control of fin-Actuated AUVs

Achieving precise control in all six degrees of freedom (6-DOF) with only four actuators is a formidable challenge, yet it is a central objective of this thesis. Building upon the dynamic model developed in Objective 2, this objective seeks to pioneer a novel 6-DOF control method explicitly tailored for fin-actuated AUVs. This innovative control method will enable these vehicles to navigate intricate underwater paths with remarkable precision, significantly advancing the capabilities of underwater robotics [Publication IV].

1.2.4 Contribution 4: Fault-tolerant control for fin-actuated AUVs

In the unpredictable and often hostile underwater environment, fault tolerance is paramount. The fourth objective of this thesis is to establish a robust fault-tolerant framework for fin-actuated AUVs. This framework ensures these vehicles' continued operation and safety, even in system faults, external disturbances, and challenging underwater conditions. By addressing fault tolerance, this objective contributes to the reliability and resilience of aquatic robotic systems, mitigating potential risks and losses [Publication III].

1.3 Thesis outline

Chapter 2 initiates with an introduction to the U-CAT platform, covering body kinematics, dynamics, and fin modelling. An established control allocation model concludes the chapter. **Chapter 3**, on **Data-fusion Based Diver Tracking**, provides an overview and motivation for diver tracking. A data-fusion-based tracking algorithm is introduced, concluded with experimental results and discussions related to the proposed data-fusion-based tracking system. **Chapter 4**, titled **Inverse modeling of fin dynamics**, starts with an overview and motivation for a thrust-to-amplitude model. An empirical and a nonlinear analytical model are described, followed by experimental validation. **Chapter 5**, on **Control allocation for 6-DOF control of fin-Actuated AUVs**, starts with an overview and motivation for solving the control allocation problem. The chapter then explores various solutions. Method assessment is carried out through simulation and experimental setups, and the chapter concludes with results and discussions that assess the proposed solutions. **Chapter 6**, on **Fault-tolerant control for fin-actuated AUVs**, offers an overview and motivation for AUV resilience. A Fault-Tolerant Control scheme is proposed and validated through experiments. Finally, **Chapter 7** serves as the conclusion, summarising findings and suggesting future research.

2 Hardware and Modelling

This section presents the foundational concepts necessary for understanding the dynamics and control of the underwater vehicle, U-CAT. It initiates with a description of the experimental platform, followed by discussions on body dynamics and fin dynamics modelling. Finally, control allocation is also presented, determining how control inputs are translated into vehicle actions.

2.1 Experimental platform U-CAT

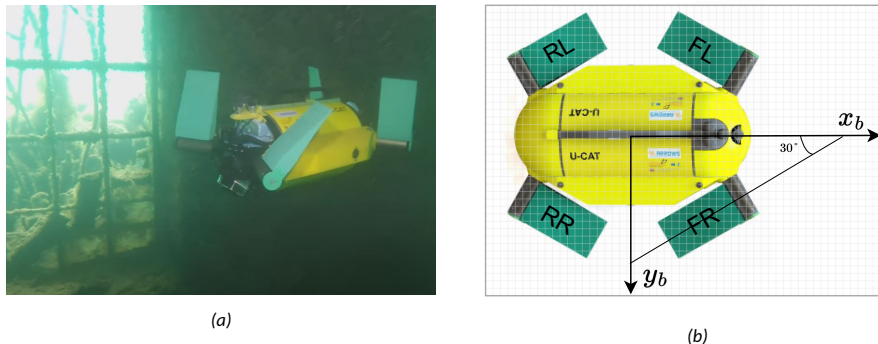


Figure 1: a) View of U-CAT robot during an inspection mission in a submerged structure. b) Illustration of U-CAT's fins configuration. The robot's front right, rear right, rear left, and front left fins are denoted by FR, RR, RL, and FL, respectively. In equations, these fins are indexed as 1, 2, 3, and 4, corresponding to FR, RR, RL, and FL. ([Publication II] ©2021 Elsevier Ltd).

U-CAT, as shown in Figure 1a, is a bio-inspired AUV, conceived during the European Union's 7th Framework ARROWS project [97]. Unlike similar underwater robots, U-CAT's unique four-finned design is driven purely by the specific needs and environmental challenges of shipwreck exploration. Its primary function is to capture detailed video footage of underwater sites. To cater to the specific demands of archaeological shipwreck inspections [98], a design of a 4-flipper structure to manage its 6-DOFs was created. The orientation of the four motors powering the fins is depicted in Figure 1b, enabling the robot's omnidirectional movement. The fins are outward-facing to maximize forward thrust, while side-to-side control is reserved for meticulous movements in tight areas. Additionally, U-CAT's weight distribution ensures its natural stability, with its centre of mass positioned just below its buoyancy centre. Comprehensive technical details about U-CAT are in Table 1.

2.2 Kinematics modelling

This section focuses on the modelling of underwater vehicles. The modelling objective is to find a mathematical representation that captures the real system's behaviour, which can later be used for simulation purposes or control law synthesis.

2.2.1 Coordinates system

Various representations exist for marine vehicles. This section introduces the most common representation, as defined in 1950 by the SNAME (Society of Naval Architects and Marine Engineers) and detailed in [99]. This representation necessitates the definition of

two frames:

- **Fixed Frame:** This frame, attached to the Earth, has its origin O and the orientation of the axes x , y and z following the North East Down (NED) convention will be used, where O_x points north, O_y points east, and O_z is oriented downwards perpendicular to the Earth's surface. The origin O is positioned on the surface at a fixed point within the robot's operational zone. This frame will be denoted as R_n , with index 'n' denoting NED.
- **Mobile Frame:** This frame, attached to the vehicle, is denoted as R_b (with index 'b' indicating Body fixed frame). The centre O is located at the vehicle's centre of gravity. The axes O_x , O_y , and O_z are aligned with the vehicle's primary symmetry axes. The O_x axis (longitudinal) points towards the vehicle's front, the O_y axis (transversal) points to starboard, and the O_z axis (normal) points downwards.

The state vector representing the vehicle's position and orientation in the earth frame R_n is denoted as $\eta = [x, y, z, \phi, \theta, \psi]^T$. The coordinates (x, y, z) , measured in meters, represent the position of the frame R_b centre within the frame R_n . The angles ϕ , θ , and ψ , in radians, describe the orientation of the frame R_b relative to the frame R_n . These angles are respectively termed roll, pitch, and yaw.

The transformation from frame R_n to frame R_b can be expressed in matrix form. The associated rotation matrix is R_n^b . Conversely, to go from frame R_b to frame R_n , the rotation matrix R_b^n is used. These matrices are related by:

$$R_n^b = (R_b^n)^{-1} = (R_b^n)^T \quad (1)$$

The vector $v = [u, v, w, p, q, r]^T$ aggregates linear and angular velocities in the frame R_b associated with the vehicle.

The velocities u , v , and w , in m/s , correspond to the velocities along the vehicle's axes O_x , O_y , and O_z . They are respectively termed surge (longitudinal speed), sway (transversal speed), and heave. The rotational p , q , and r , in rad/s , are the roll, pitch, and yaw velocities of the vehicle.

Table 1: Main technical specifications of the U-CAT robot

Technical specification	Specification / Description
Onboard camera	PointGrey Chameleon 2
Hydrophones	Aquarian Audio H1c
Motors	Maxon EC-max
Attitude sensor	MPU-6050 IMU
Depth sensor	GEMS 22CS Series Pressure Sensor
Batteries	4x HP Compaq NX8200 8cell batteries
Maximal speed (surge)	0.25 m/s
Maximal depth	100m
Autonomy	~6 hours
Mass	19 Kg
Dimensions	560mm × 329mm × 258mm
Fins' material	Zhermack Elite Double 22

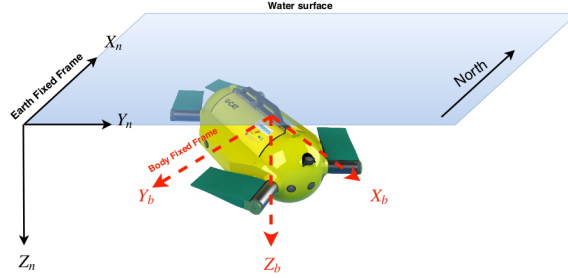


Figure 2: Illustration of the Earth Fixed Frame R_n (North East Down convention) and the robot's Body Fixed Frame R_b . ([Publication 1] ©2020 Wiley Periodicals LLC)

2.2.2 Kinematic Model:

The derivative $\dot{\eta}$ of the state vector η in frame R_n can be computed from the velocities v in frame R_b using the relation:

$$\dot{\eta} = J(\eta)v \quad (2)$$

Where $J(\eta)$ is a transformation matrix defined as:

$$\dot{\eta} = \begin{bmatrix} R_b^n & O_{3 \times 3} \\ O_{3 \times 3} & \Theta \end{bmatrix} \quad (3)$$

R_b^n is the previously described rotation matrix, used to calculate the linear velocities $\dot{x}, \dot{y}, \dot{z}$ in the frame R_n based on the linear velocities u, v, w in the mobile frame R_b .

Θ is the transformation matrix used to compute the derivatives $\dot{\phi}, \dot{\theta}, \dot{\psi}$ of the nautical angles from the angular rotation velocities p, q, r .

These matrices depend on the vehicle's orientation and are expressed as:

$$R_b^n = \begin{bmatrix} c\psi c\theta & -s\psi c\theta + c\psi s\theta s\phi & s\psi s\theta + c\psi s\theta c\phi \\ s\psi c\theta & c\psi c\theta + s\psi s\theta s\phi & -c\psi s\theta + s\psi s\theta c\phi \\ -s\theta & c\theta s\phi & c\theta c\phi \end{bmatrix} \quad (4)$$

and

$$\Theta = \begin{bmatrix} 1 & s\phi t\theta & c\phi t\theta \\ 0 & c\phi & -s\phi \\ 0 & \frac{s\phi}{c\theta} & \frac{c\phi}{c\theta} \end{bmatrix} \quad (5)$$

Where $\phi, \theta,$ and ψ are the previously defined nautical angles, and $c. = \cos(.), s. = \sin(.),$ and $t. = \tan(.).$

2.3 Dynamics Modelling

In general, the NED frame is considered a Galilean frame even though it's fixed to the Earth's surface. This is because the forces on the vehicle due to Earth's rotation are negligible compared to hydrodynamic forces [100]. Below are the different forces acting on the vehicle:

2.3.1 Weight and Buoyancy:

Gravitational force (weight) and hydrostatic force (buoyancy) play crucial roles in an underwater vehicle's stability. Vehicles are typically balanced such that weight is nearly equivalent or marginally less than buoyancy for energy-efficient submersion and spontaneous surfacing during malfunctions.

Let B represent the magnitude of the buoyancy force (in N) on the vehicle, and W be the magnitude of the vehicle's weight (in N). If the vehicle's centre of gravity is positioned at (x_g, y_g, z_g) and the centre of volume at (x_b, y_b, z_b) in the frame R_b tied to the vehicle, the hydrostatic forces and moments vector, F_G , is expressed in R_b as:

$$f_G = G(\eta) = \begin{bmatrix} -(W - B)s\theta \\ (W - B)c\theta s\phi \\ (W - B)c\theta c\phi \\ (y_g W - y_b B)c\theta c\phi - (z_g W - z_b B)c\theta s\phi \\ -(x_g W - x_b B)c\theta c\phi - (z_g W - z_b B)s\theta \\ (x_g W - x_b B)c\theta s\phi + (y_g W - y_b B)s\theta \end{bmatrix} \quad (6)$$

2.3.2 Hydrodynamic Damping:

The combined damping forces, F_D , are represented as [99]:

$$F_D = -D(v)v = -(D_l + D_n(v))v \quad (7)$$

Where $D_l \in \mathbb{R}^{6 \times 6}$ is the linear damping matrix, $D_n(v) \in \mathbb{R}^{6 \times 6}$ is the non-linear damping matrix, and $v = [u, v, w, p, q, r]^T$ is the vector of translational and rotational velocities in the vehicle's frame.

Often, $D(v)$ is approximated as diagonal such as:

$$D_l = \begin{bmatrix} D_u & \dots & 0 \\ \vdots & \ddots & \vdots \\ 0 & \dots & D_r \end{bmatrix} \quad (8)$$

$$D_n = \begin{bmatrix} D_{nu}|u| & \dots & 0 \\ \vdots & \ddots & \vdots \\ 0 & \dots & D_{nr}|r| \end{bmatrix} \quad (9)$$

2.3.3 Coriolis and Centrifugal Inertia Forces:

In applying fundamental dynamic principles, accounting for inertia forces is vital. Thus, the combined effect, F_C , of these forces is expressed by the matrix product: $F_C = -C_{RB}(v)v$. Parameters of the matrix C_{RB} are typically estimated using strip theory [101] or hydrodynamic simulations.

2.3.4 Fins-Generated wrenches:

Thrust and torque produced by the U-CAT robot's fins depend on several factors, like the angle of attack, oscillation frequency, and amplitude. The resultant force is denoted τ :

$$\tau = [\tau_x, \tau_y, \tau_z, \tau_\phi, \tau_\theta, \tau_\psi]^T \quad (10)$$

A more detailed derivation of τ based on fins actuation parameters is described in 2.4

2.3.5 External Disturbances:

Significant disturbances on the U-CAT robot, denoted as w , include marine currents and the umbilical when teleoperated. Though their modelling is challenging, there are many studies in this area. Chapter 4 in the reference [99] elaborates further.

After describing all forces acting on the vehicle, the vehicle's dynamic model is:

$$\begin{aligned}\dot{\eta} &= J(v)v \\ \dot{v} &= M^{-1}(-G(\eta) - C(v)v - D(v)v + \tau + w)\end{aligned}\quad (11)$$

Where $\dot{v} = [\dot{u}, \dot{v}, \dot{w}, \dot{p}, \dot{q}, \dot{r}]^T$ is the vehicle's acceleration vector, $M \in \mathbb{R}^{6 \times 6}$ is the vehicle's inertia matrix, given by:

$$M = \begin{bmatrix} m & 0 & 0 & 0 & mz_g & -my_g \\ 0 & m & 0 & -mz_g & 0 & mx_g \\ 0 & 0 & m & my_g & -mx_g & 0 \\ 0 & -mz_g & my_g & I_x & -I_{xy} & -I_{xz} \\ mz_g & 0 & -mx_g & -I_{yx} & I_y & -I_{yz} \\ -my_g & mx_g & 0 & -I_{zx} & -I_{zy} & I_z \end{bmatrix} + M_{am} \quad (12)$$

where m the mass of the robot, $[x_g, y_g, z_g]$ denote the coordinates of the centre of gravity in R_b , and the matrix M_{am} is a matrix summarizing parameters describing the hydrodynamic effect of added mass [99].

2.4 Fin dynamics modelling

The dynamic model utilized to describe the fins of the U-CAT AUV is based on the rigid paddle model, as documented in [102]. This model's validity has been previously established and confirmed in research conducted by Georgiades et al. [12], where it was employed to simulate the underwater hexapod robot AQUA [103].

The fins of the U-CAT are assumed to generate horizontal (f_x) and vertical (f_z) forces relative to the fin's resting frame, as illustrated in Figure 3. The model relies on the following mathematical expressions:

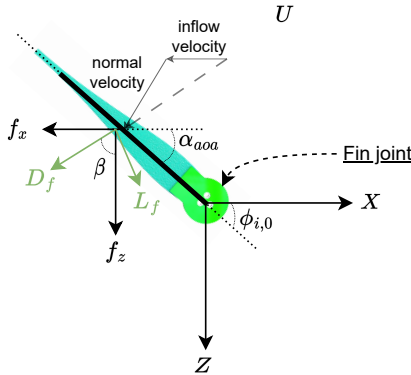


Figure 3: Visualization of forces on i^{th} fin based on the simple lift and drag model (model and figure adopted from [12]).

$$\begin{aligned} f_x &= D_f \sin(\beta) + L_f \cos(\beta) \\ f_z &= -L_f \sin(\beta) + D_f \cos(\beta) \end{aligned} \quad (13)$$

Here, β denotes the direction of the flow impinging on the fin, and D_f and L_f represent the lift and drag forces, respectively. These forces are defined as:

$$\begin{aligned} L_f &= 0.5\rho U_f^2 S_f C_{Lmax} \sin(2\alpha_{aoa}) \\ D_f &= 0.5\rho U_f^2 S_f C_{Dmax} (1 - \cos(2\alpha_{aoa})) \end{aligned} \quad (14)$$

In these equations, α_{aoa} signifies the angle of attack, while U_f corresponds to the velocity of the flow impacting the fin. Additionally, S_f corresponds to the surface area of the fin. Lastly, C_{Lmax} and C_{Dmax} represent the maximum lift and drag coefficients of the paddle, respectively.

For a more comprehensive discussion on the modelling of fin forces, interested readers are encouraged to refer to Georgiades et al.'s work [12].

2.5 Control allocation

To produce the wrenches required to control the 6-DOF body motions, U-CAT's actuation follows an oscillatory movement described by:

$$\varphi_i^{osc}(t) = A_i^{osc} \sin(\omega_i^{osc} t + \varphi_{off,i}^{osc}) + \phi_{0,i} \quad (15)$$

with the oscillation amplitude A_i^{osc} , the oscillation rate ω_i^{osc} , the phase offset $\varphi_{off,i}^{osc}$ and the zero direction of the oscillation $\phi_{0,i}$.

This will result in wrenches in body frame that can be modelled as:

$$\tau(\varphi^{osc}) = \sum_{i=0}^n [Ad_{T_{i,b}}] R(\phi_{0,i}) \mathbf{f}_i^{th}(\varphi^{osc}) \quad (16)$$

with n being the total number of fins. $R(\phi_{0,i})$ is the two-dimensional rotation matrix for fin i which maps the thrust produced along $\phi_{0,i}$ to horizontal and vertical forces in the rest frame of the fin.

$$R(\phi_{0,i}) = \begin{bmatrix} c\phi_{0,i} & 0 & s\phi_{0,i} & \\ 0 & 1 & 0 & 0_{3 \times 3} \\ -s\phi_{0,i} & 0 & c\phi_{0,i} & \\ & 0_{3 \times 3} & & 0_{3 \times 3} \end{bmatrix} \quad (17)$$

Furthermore, $[Ad_{T_{i,b}}]$ is the adjoint representation of the homogeneous transformation matrix $T_{f,b}$ that is used to map wrenches produced in the static fin frame to the robot's body frame:

$$[Ad_{T_{i,b}}] = \begin{bmatrix} R(\Phi_i^{fin}) & 0_{3 \times 3} \\ [p_i^{fin}]_{\times} R(\Phi_i^{fin}) & R(\Phi_i^{fin}) \end{bmatrix} \quad (18)$$

with $p_i^{fin} = [x_i^{fin}, y_i^{fin}, z_i^{fin}]$ being the fin coordinates relative to the centre of the vehicle and with $R(\Phi_i)$ being the rotation matrix mapping from fin to body frame based on the orientation vector of the fin rest frame $\Phi_i^{fin} = [\phi_i^{fin}, \theta_i^{fin}, \psi_i^{fin}]^T$:

$$R(\Phi) = \begin{bmatrix} c\psi c\theta & -s\psi c\phi + c\psi s\theta s\phi & s\psi s\phi + c\psi c\phi s\theta \\ s\psi c\theta & c\psi c\phi + s\phi s\theta s\psi & -c\psi s\phi + s\theta s\psi c\phi \\ -s\theta & c\theta s\phi & c\theta c\phi \end{bmatrix} \quad (19)$$

To simplify the modelling, the instantaneous thrust f^{th} produced by each fin can be averaged over one oscillation period T_{osc} [104]:

$$\overline{f^{th}} = \frac{1}{T_{osc}} \int_0^{T_{osc}} f^{th}(\varphi^{osc}, \tau^{int}) d\tau^{int} \quad (20)$$

with τ^{int} being the integration time variable. Now by using (18) and defining $\psi^{fin} = |\psi_1^{fin}|$, $x^{fin} = x_1^{fin}$ and $y^{fin} = y_1^{fin}$ we can define the resulting wrenches τ in the body frame as a system of six algebraic equations with the fins' zero directions $\phi_{0,1-4}$ and thrusts $\overline{f^{th}}_{1-4}$ as independent variables written in matrix form $\tau = BX$:

$$\tau = \begin{bmatrix} \tau_x \\ c\psi_f \\ \tau_y \\ s\psi_f \\ \tau_z \\ \tau_\Phi \\ y_f \\ x_f \\ \tau_\Psi \\ M_a \end{bmatrix} = \begin{bmatrix} 1 & -1 & -1 & 1 & 0 & 0 & 0 & 0 \\ -1 & -1 & 1 & 1 & 0 & 0 & 0 & 0 \\ 0 & 0 & 0 & 0 & 1 & 1 & 1 & 1 \\ 0 & 0 & 0 & 0 & 1 & 1 & -1 & -1 \\ 0 & 0 & 0 & 0 & -1 & 1 & 1 & -1 \\ -1 & 1 & -1 & 1 & 0 & 0 & 0 & 0 \end{bmatrix} \begin{bmatrix} c\phi_{0,1} \overline{f^{th}}_1 \\ c\phi_{0,2} \overline{f^{th}}_2 \\ c\phi_{0,3} \overline{f^{th}}_3 \\ c\phi_{0,4} \overline{f^{th}}_4 \\ s\phi_{0,1} \overline{f^{th}}_1 \\ s\phi_{0,2} \overline{f^{th}}_2 \\ s\phi_{0,3} \overline{f^{th}}_3 \\ s\phi_{0,4} \overline{f^{th}}_4 \end{bmatrix} \quad (21)$$

with $M_a = x^{fin} c\psi^{fin} - y^{fin} s\psi^{fin}$.

3 Data-fusion Based Diver Tracking

3.1 Overview and motivation

This chapter delves into the intricate challenge of robustly tracking divers in dynamic underwater environments using the U-CAT autonomous underwater vehicle. The motivation for this investigation stems from the inherent complementarity of acoustic and vision-based object detection methods. By fusing visual and acoustic signals, we aim to circumvent the limitations of each sensing modality, offering a more comprehensive and accurate tracking solution, especially in challenging open water conditions.

The work presented herein, building upon the foundational studies in [43], seeks to harness the strengths of both visual and acoustic signals captured using cost-effective sensors. The diver is visually detected through a digital camera employing a streamlined embedded DNN. In contrast, acoustically, the diver's relative orientation is ascertained by tracking a pinger they carry using an array of economical hydrophones. This fusion enhances the system's robustness and ensures successful tracking irrespective of the diver's position within the camera's field of view.

When juxtaposed with existing methodologies, the distinct advantage of this approach lies in its heightened resilience and accuracy in diver tracking. This is achieved without escalating costs, as the proposed solution leverages relatively low-cost sensors. The culmination of this research is implementing the proposed diver tracking scheme on the underwater robot U-CAT, with its efficacy being rigorously tested in an open water environment.

3.2 Proposed tracking algorithm

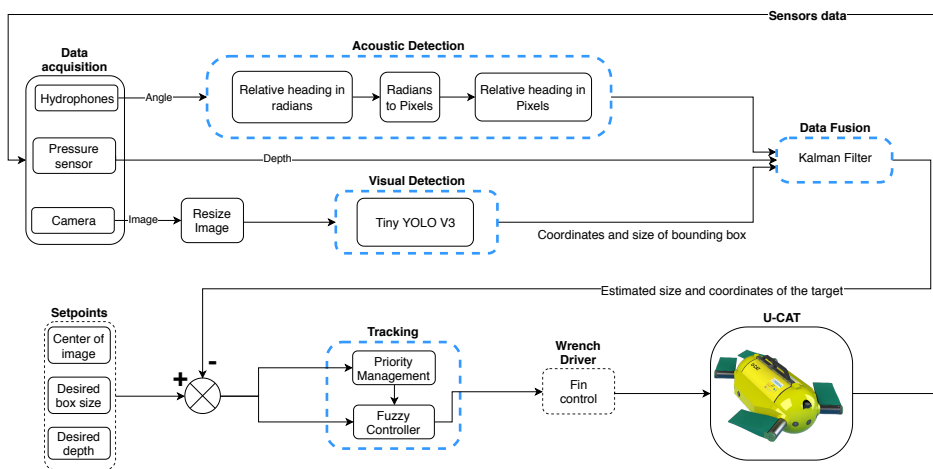


Figure 4: Block diagram of the proposed tracking control scheme: Dashed-blue blocks are elaborated in [Publication 1]. The entire tracking scheme runs online on U-CAT's embedded computer using ROS. ([Publication 1] ©2020 Wiley Periodicals LLC).

The tracking algorithm proposed in this work leverages both visual and acoustic signals to track divers robustly in underwater environments. This section presents a holistic view of the proposed solution, emphasising the synergy between its constituent blocks.

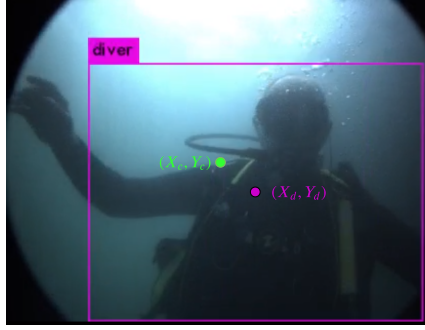


Figure 5: Visual detection: The goal is to centre the detected box at the centre of the image. ([Publication I] ©2020 Wiley Periodicals LLC).

3.2.1 Visual detection using DNN

The down-scaled DNN model, tiny-YOLOv3 [30], is employed for visual detection. This model was chosen because it provides fast (approximately 20 fps) and reliable detection, even on resource-constrained systems like the U-CAT's Jetson TX2 embedded computer. The implementation was facilitated using the Robot Operating System (ROS).

The visual detection concept aims to centre the detected object within the image. The errors E_C and E_W between the centres and widths of the two boxes are computed as:

$$E_C = \begin{bmatrix} X_c \\ Y_c \end{bmatrix} - \begin{bmatrix} X_m \\ Y_m \end{bmatrix} \quad (22)$$

$$E_W = W_c - W_m \quad (23)$$

This approach facilitates three DOF tracking control. The difference between the two boxes' centres E_C defines the desired depth and heading orientation of the robot, while the difference in their widths E_W determines the desired distance between the robot and the target.

3.2.2 Acoustic Detection

The acoustic detection employs a *Sonotronics EMT-01-3* Pinger operating at 9.6kHz as a beacon. This beacon emits a short burst signal every second. The received signal by each hydrophone is amplified and filtered. The phase shift for each hydrophone is then used to compute the relative yaw angle to the robot, denoted by Ψ_p .

The yaw angle of the pinger with respect to the robot is represented by quaternions Q_Ψ and Q_{Ψ_p} . The shortest angle between these two quaternions is given by ΔQ , which is then converted back to the desired yaw angle φ . This yaw angle error is further converted to pixel coordinates error, denoted E_P , using the function $\Phi(\varphi, a)$ such that:

$$\Phi(x, a) = \begin{cases} 0 & , \text{if } x < a \\ ImageWidth & , \text{if } x > -a \\ \frac{ImageWidth}{2} \left(\frac{-x}{a} + 1 \right) & , \text{otherwise } , (a \neq 0) \end{cases} \quad (24)$$

The function Φ remaps the measured pinger orientation into an image's X-coordinate pixel based on a user-defined angle a .

3.2.3 Data-fusion scheme

The data-fusion scheme employed is based on the Kalman filter [105]. The state and measurement vectors are defined as:

$$X_t = [x_t, y_t, w_t, z_t]^T \quad (25)$$

$$Y_t = [X_m, Y_m, W_m, Z_m, X_p]^T \quad (26)$$

Here, X_t is the state vector at time t , with x_t and y_t representing the estimated pixel coordinates of the target. w_t is the estimated width of a bounding box containing the target, while z_t denotes the estimated depth of the robot. Y_t is the measurement vector, where (X_m, Y_m) and W_m represent the position coordinates and width of the detected bounding box by the camera. Z_m is the measured depth of the robot using the onboard pressure sensor, and X_p is the image coordinates of the detected heading measured by the hydrophones array.

The estimated state vector X_t is then used to compute the tracking errors:

$$E_x = X_c - x_t \quad (27)$$

$$E_y = Y_c - y_t \quad (28)$$

$$E_w = W_c - w_t \quad (29)$$

$$E_z = Z_{desired} - z_t \quad (30)$$

3.2.4 Control scheme

In our efforts to ensure the diver remains centred within the camera's field of view, a three degrees of freedom (3-DOF) control scheme, encompassing surge, heave, and yaw, was employed. The foundation of this control strategy is a fuzzy logic Mamdani controller [106]. This controller ingests the tracking errors and their variations as inputs, subsequently producing a force vector $\tau \in \mathbb{R}^{3 \times 1}$ as its output, where $\tau = [\tau_x, \tau_z, \tau_\psi]$.

The output generated by the controller is then transformed into fin oscillation zero-directions and amplitudes through the wrench driver, leveraging the empirical control allocation method delineated in [76]. However, due to the inherent high coupling in U-CAT's actuation across its various DOFs, a straightforward control allocation doesn't yield a perfect decoupling. To address this, a priority management strategy was introduced in [45]. This strategy was further expanded to the 3-DOF control in our work, where Gaussian membership functions were utilized to modulate the control of each DOF based on the specific control objective. Given U-CAT's inherent stability in roll and pitch, these DOFs were not considered in the current control scheme.

For a more in-depth exploration of each component, readers are referred to the annexed paper [Publication I].

3.3 Experimental results and discussion

To validate the proposed control scheme, a series of experiments were conducted near a small harbour in Banyuls-Sur-Mer, France (42° 28' 52.0"N, 3° 08' 10.0"E). These experiments spanned four distinct scenarios, each designed to underscore the importance of sensor complementarity in diver tracking and to demonstrate the efficacy of the proposed tracking control scheme. This section provides an overview of the experimental setup for each scenario, followed by a detailed presentation and discussion of the results obtained.



Figure 6: Underwater images from U-CAT's camera in open water conditions (a) Frame example where visual detection is unsuccessful due to poor visibility conditions. (b) Frame example where the diver is successfully detected when close enough. ([Publication 1] ©2020 Wiley Periodicals LLC).

3.3.1 Experimental scenarios

1. **Visual tracking (Scenario 1):** U-CAT relied solely on visual guidance to track the diver. The primary objective was to gauge the robustness of the proposed vision detection and tracking algorithm under real-world operating conditions.
2. **Acoustic tracking (Scenario 2):** In this scenario, U-CAT was tasked with tracking the diver using only acoustic sensing. This test aimed to evaluate the performance of acoustic sensing, which utilised an array of three hydrophones and a pinger for diver tracking.
3. **Data-fusion based static tracking (Scenario 3):** This scenario tested the proposed data-fusion tracking scheme's capability to track a stationary target. The robot autonomously detected and tracked a pinger attached to a coloured waterproof light source, initially positioned outside its camera's field of view. A simple colour segmentation detector was employed for visual detection. This scenario was repeated thrice, with U-CAT starting from different initial positions relative to the target.
4. **Data-fusion based dynamic tracking (Scenario 4):** This scenario assessed the efficiency of the proposed diver tracking algorithm. A diver, equipped with a pinger, was instructed to move freely in open water at a depth of two meters. This depth was chosen to facilitate reliable top-view monitoring of both the diver and the AUV using a static camera. The scenario was replicated three times, with the diver starting from different initial positions relative to the robot.

3.3.2 Visual tracking

As depicted in Figure 7, the AUV successfully tracked and centred the detected target within the image frame. However, after approximately 8 seconds, the diver exited the camera's field of view. Consequently, the robot continued tracking based on the last detected position but failed to relocate the target. Field experiments often present challenges such as turbid waters and poor visibility due to light scattering and absorption. Such conditions can lead to visual detection failures, as Figure 6 illustrates. This underscores the need for an auxiliary sensor to complement visual tracking, ensuring consistent diver detection even when visual cues are compromised.

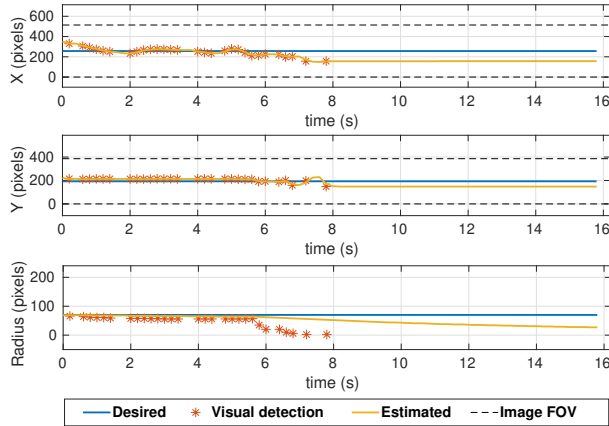


Figure 7: **Visual tracking (Scenario 1)**: experimental results describing visual detection and estimation using the camera to track the diver. ([Publication 1] ©2020 Wiley Periodicals LLC).

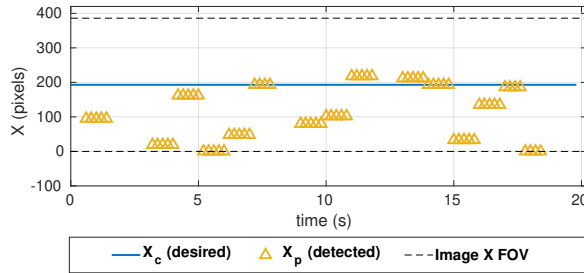


Figure 8: **Acoustic tracking (Scenario 2)**: experimental results for tracking the diver based on acoustic signals only. ([Publication 1] ©2020 Wiley Periodicals LLC).

3.3.3 Acoustic tracking

In this scenario, the diver, equipped with a pinger, began a few meters away from the robot and remained stationary throughout the experiment. Given the absence of distance feedback using the acoustic method, U-CAT continued its movement even after reaching the diver's vicinity. Figure 8 reveals that the remapped detected relative heading was predominantly on the image's left side. This behaviour can be attributed to the robot's continuous circling around the diver upon reaching him. The figure also highlights the noisy nature of the acoustic data, likely due to reflections, emphasising the necessity of a complementary visual sensor for efficient diver tracking.

3.3.4 Data-fusion based tracking

Two distinct scenarios, static and dynamic tracking, were explored to assess the performance of the proposed control tracking scheme. Scenario 3 focused on tracking a static object initially outside the camera's FOV, while Scenario 4 evaluated the solution's efficacy in dynamically tracking a diver.

Table 2: Scenario 3: RMSE between the camera's centre and desired width, and the object pixels location and its width. ([Publication I] ©2020 Wiley Periodicals LLC).

RMSE (in pixels)	Test 1 Facing the target	Test 2 right to the target	Test 3 left to the target
RMSE X	42	67	72
RMSE Y	17	20	21
RMSE Width	12	15	8

Static tracking (Scenario 3)

For this experiment, a target was positioned approximately 6 meters away from U-CAT. The robot advanced towards the target, exhibiting slight oscillations to the left and right due to acoustic detection reflections. After nearly 40 seconds, the robot aligned itself to face the target. Figure 10 demonstrates that the robot subsequently centred the target within the camera's frame using visual feedback. Given that both the target and the AUV operated at the same depth, the target was almost already centred on the Y-axis. Any minor vertical deviations from the camera's centre were corrected using visual feedback. Notably, the proposed tracking scheme successfully detected and tracked a static target initially outside the camera's FOV. Figure 10 further indicates that the desired width of the target within the camera's frame was maintained, ensuring a consistent relative distance to the target. This underscores the robustness of combining both visual and acoustic measurements for object tracking.

For results pertaining to scenarios where the robot began to the right and left of the target, readers are referred to [Publication I].

To quantify the performance of the proposed approach, Table 2 presents the error between the target's camera location and the camera's centre for the three scenarios. The results indicate that once the target was visually identified, it was predominantly kept at the camera frame's centre. This highlights the robustness and repeatability of the proposed method, enabling the detection and tracking of an object initially distant from the robot, a feat unachievable with vision-only methods. The results also demonstrate the robot's capability for station-keeping when tracking a static object.

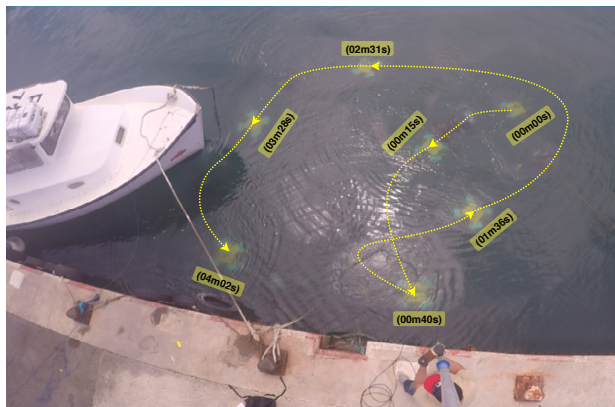


Figure 9: U-CAT illustrative diver tracking trajectory: description at different times. ([Publication I] ©2020 Wiley Periodicals LLC).

Dynamic tracking (Scenario 4)

In this scenario, the proposed control approach was tested for actively tracking a diver. The diver, equipped with a pinger, moved freely in a 2D trajectory at a constant depth. Given U-CAT's relatively slow swimming velocity, the diver was instructed to move at a slow pace.

As illustrated in Figure 11 the proposed solution enabled tracking of the moving diver for over 8 minutes. The target exited the camera's field of view multiple times, but its location was consistently recovered. The synergy of the proposed approach facilitated rapid orientation towards the diver, ensuring he remained centred in the camera's image.

As shown in Figure 9, U-CAT accurately tracked the target throughout the experiment. The results underscore the robustness of the proposed approach, validated across various scenarios, with the AUV operating in open waters under poor visibility conditions and subject to acoustic reflections and noise.

Table 3 presents the tracking performance in terms of the error between the desired and feedback position of the diver within the camera's frame. The more significant errors are along the image's X-axis, given the diver's primary horizontal movement. Both errors in the Y-axis and width are minimal, considering the diver maintained a constant depth and moved relatively slowly. This indicates that the diver was primarily centred on the camera, even after exiting its FOV multiple times.

The results also highlight that the proposed controller facilitates 3D tracking motion, despite the high coupling in U-CAT's actuators. However, it's worth noting that the proposed tracking algorithm is limited to 3DOF tracking.

Table 3: Scenario 4: RMSE between the camera's centre and desired width, and the object pixels location and its width. ([Publication 1] ©2020 Wiley Periodicals LLC).

RMSE (in Pixels)	Test1	Test 2	Test 3
	Diver initially close from the robot	Diver initially away from the robot	Shorter experiment
RMSE X	119	124	106
RMSE Y	37	28	33
RMSE W	24	19	31

3.4 Conclusions

The primary objective of this chapter was to design and implement a cost-effective data-fusion based diver tracking control scheme. Recognizing U-CAT's unique actuation characteristics and hardware capabilities, a data-fusion technique was introduced that synergistically combined acoustic and visual signals. This innovative approach was rigorously tested in open-water field experiments, yielding promising results that underscored the efficacy and robustness of the proposed control algorithm. This dual-sensor approach ensures that the system remains resilient, and capable of recovering the diver's location even when visual detection encounters challenges.

In summary, the contributions of the work described in this chapter include:

- The development and implementation of a cost-effective data-fusion based diver tracking control scheme tailored for the U-CAT underwater robot.
- The integration of acoustic and visual signals to ensure robust diver tracking, even in challenging visibility conditions.

- Comprehensive open water field experiments that validated the effectiveness and robustness of the proposed control algorithm.
- Demonstrating the capability of the system to locate, detect, and consistently track a target, even when positioned at a considerable distance from the robot.

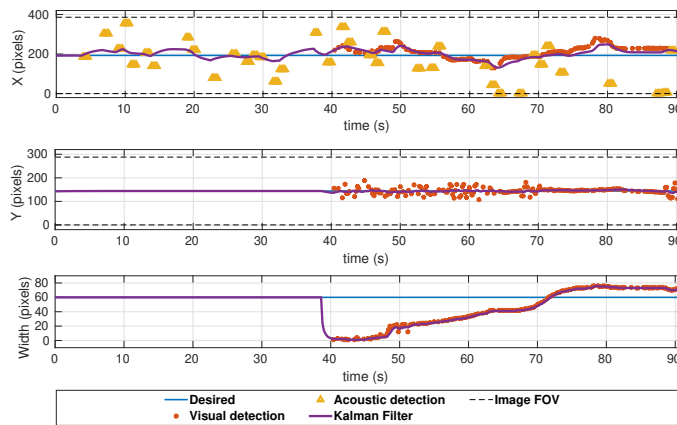


Figure 10: Data-fusion based static tracking (Scenario 3): experimental results describing static target tracking based on the proposed data-fusion scheme where the AUV started facing the target. ([Publication 1] ©2020 Wiley Periodicals LLC).

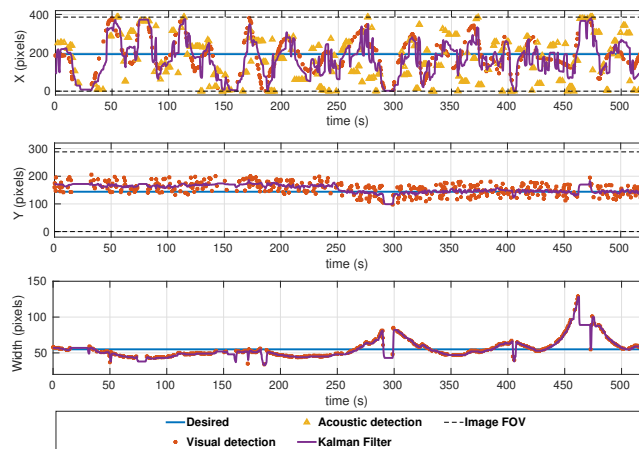


Figure 11: Data-fusion based dynamic tracking (Scenario 4): Diver starting close to the robot. ([Publication 1] ©2020 Wiley Periodicals LLC).

4 Inverse modelling of fin dynamics

4.1 Overview and motivation

Controlling fin-actuated vehicles is challenging due to the nonlinear relationship between fin oscillation and the thrust it produces. To control these vehicles with precision, a thorough understanding of this relationship is essential, along with the development of models that can both predict and adjust the thrust based on how the fins oscillate.

The U-CAT robot's actuation fins function similarly to caudal or tail fins. The oscillation of a tail fin can produce thrust by pushing water backwards, creating a propulsive flow [107]. When considering the control of robots like the U-CAT, the need for a model that describes how changes in fin actuation relate to the force of the thrust produced becomes evident. With this challenge in mind, this chapter introduces a new approach. An analytical model based on drag-force generation is presented and refined using experimental data. This model effectively describes the relationship between how a fin oscillates and the thrust it generates. Building upon this model, an inverse model has been developed. The derived model allows the adjustment of oscillation amplitude and frequency to achieve the desired thrust. It serves as a critical component in controlling fin-actuated vehicles, with its effectiveness demonstrated using the U-CAT as an example.

But the focus isn't solely on theory. Practical application is equally important. The developed models have been tested in real-world conditions using the U-CAT robot. The results highlight the potential of the proposed model in enhancing the control of fin-actuated underwater robots, paving the way for more complex underwater missions in the future.

4.2 Proposed thrust to amplitude model

Controlling fin-actuated vehicles like U-CAT involves understanding the relationship between the generated thrust and the oscillation of the fins. As detailed in (15), the generated thrust can be characterized by three primary parameters: i) the amplitude of oscillations, ii) the frequency of oscillations, and iii) the zero-direction angle. This section delves into how the required thrust force is converted into fins oscillating magnitude for U-CAT, given a constant oscillating frequency. Two models are discussed: a simple empirical model used in prior research and a more advanced nonlinear analytical model.

4.2.1 Empirical model

As used in [47], the initial fin model aimed to establish a relationship between the generated thrust force and the oscillating amplitude, with the latter chosen as the control input for U-CAT's hydrodynamic model. This relationship was identified experimentally using U-CAT's test bed, resulting in a second-order polynomial function between $\overline{f^{th}}$ and A_i^{osc} . Figure 12 illustrates the evolution of the generated mean fin thrust for various actuation parameters. For an oscillating frequency of 1.1 Hz, a relationship between the required thrust force and the oscillating amplitude was derived based on polynomial interpolation [76]:

$$A_i^{osc} = -0.01170\overline{f^{th}}^2 + 0.4363\overline{f^{th}} + 0.2480 \quad (31)$$

where θ represents the oscillating amplitude, and F denotes the thrust force generated by the robot's four fins.

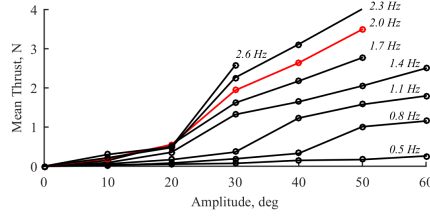


Figure 12: Evolution of the generated mean fin thrust for different actuation parameters (oscillation amplitude ranging from 0 to 60° and oscillation frequency ranging from 0.5 Hz to 2.6 Hz). ([Publication II] ©2021 Elsevier Ltd).

4.2.2 The proposed fin model: A nonlinear analytical model

A more comprehensive model was developed to enhance the fin model's fidelity. The oscillating motion of a fin requires a rotational force that can overcome both inertia and drag. In [108], a force balance expression was proposed for fin paddling as a simple linear motion. To estimate the required force for fin rotation, a rotational force balance was considered, leading to a torque balance between the angular momenta of the oscillating motion of a tail fin and the drag [109]:

$$I \frac{d\omega}{dt} = r_c (F_f - D_f) \quad (32)$$

$$D_f = \frac{1}{2} C_{d_{rot}} \rho (r_c \omega)^2 S_f = \frac{C_{d_{rot}}}{2} \rho V r_c \omega \quad (33)$$

where I denotes the inertia moment of the rotating fin, ω represents the angular velocity of the fin, F_f is the force for rotating the fin, r_c is the distance between the rotation axis and the centre of gravity of the fin, and D_f is the drag acting on the fin. $C_{d_{rot}}$ stands for the rotational drag coefficient, and S_f is the projection area of the fin. Equation (33) can be reformulated to include the momentum of the transported fluid whose volume is V . This implies that the fin converts the momentum of fluids to drag.

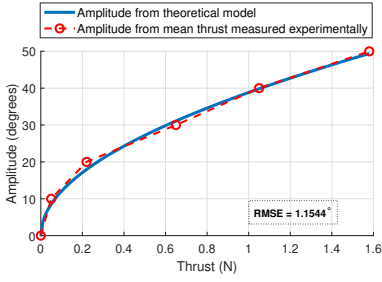
The angular component parallel to the swimming direction of the rotational force is used as thrust F . It can be expressed by:

$$F = F_f \sin|\theta| = \left(\frac{C_{d_{rot}} \rho V r_c \omega}{2} + \frac{I}{r_c} \frac{d\omega}{dt} \right) \sin|\theta| \quad (34)$$

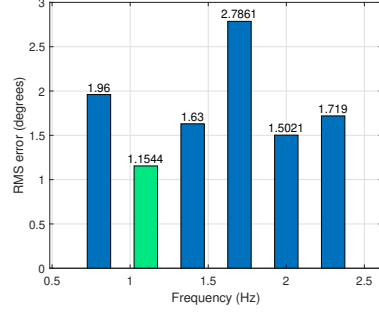
where θ is the angle of the fin, the angle between the fin cord line and the thrust direction. Equation (34) characterizes the instantaneous thrust generated by a rotating fin.

To find the relationship between the oscillation amplitude and the generated thrust, it's understood that a fin obtains thrust through a reaction of motion of the surrounding fluid induced by its rotation. The rotating fin translates the force of fin rotation into a thrust. In drag-based thrust generation, the thrust is related to drag based on a momentum transfer theory [110]. The theoretical thrust generated by a rotating fin was estimated by momentum theory:

$$\bar{F} = \int \left(\frac{C_{d_{rot}} \rho V r_c \omega}{2} + \frac{I}{r_c} \frac{d\omega}{dt} \right) \sin|\theta| d\theta \quad (35)$$



(a)



(b)

Figure 13: (a): Validation of the proposed theoretical model for fin amplitude allocation, with experimental data for a constant frequency $f = 1.1\text{Hz}$. (b): Evolution of the RMS error between the proposed theoretical model and the experimental data for different frequencies (in green $f = 1.1\text{Hz}$, is the robot's fins' constant oscillating frequency used within our control scheme.) ([Publication II] ©2021 Elsevier Ltd).

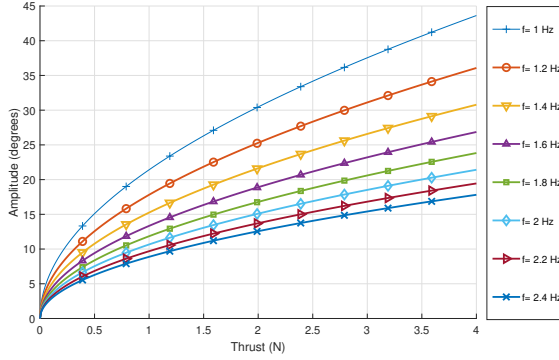


Figure 14: Estimated single fin needed oscillating amplitude versus the required thrust for different oscillating frequencies. ([Publication II] ©2021 Elsevier Ltd).

where \bar{F} stands for time-averaged theoretical thrust during one cycle. This can be further simplified to:

$$\bar{F} = 2 \int_0^{\theta_{max}} (C_{d_{rot}} \rho V r_c \omega) \sin(\theta) d\theta \quad (36)$$

From equation (36), the thrust can be deduced:

$$\bar{F} = -2(C_{d_{rot}} \rho V r_c \omega) (\cos(\theta_{max}) - 1) \quad (37)$$

Inverting equation (37) gives the expression of the control input (i.e. the oscillating amplitude) in terms of the required thrust force:

$$\theta_{max} = \arccos \left(\frac{-\bar{F}}{2C_{d_{rot}} \rho V r_c \omega} + 1 \right) \quad (38)$$

Given that $V = S_f \omega r_c$, equation (38) can be expressed in terms of the required thrust

\bar{F} and the oscillating frequency f as:

$$\theta_{max} = \arccos \left(\frac{-\bar{F}}{8C_d \rho S_f (r_c \pi f)^2} + 1 \right) \quad (39)$$

Table 4: Summary of the fin's parametric values of the theoretical model.

ρ (kg/m ³)	S_f (m ²)	R_c (m)
997	0.02	0.1

In equation (39), all constants are known (as summarised in Table 4), and the coefficient C_d was identified based on the experimental fins' thrust data [111]. A minimal RMS error between the experimental assessment of the fins and the proposed analytical model is obtained for $C_d = 0.23$. Figure 13a depicts the evolution of the oscillating amplitude versus the horizontal thrust. The proposed inverse solution matches the experimental data, with an RMS error of 1.154°. Moreover, the proposed analytical inverse model is valid for various frequencies, as illustrated in Figure 13b, where the RMS error between the proposed model and the gathered experimental data is less than 3° for all the studied frequencies.

4.3 Experimental Results and Discussion

2-DOF (depth and yaw) trajectory tracking was considered to validate the proposed model. By integrating the proposed inverse model with a fuzzy logic controller and an empirically described control allocation, the controller output was converted to fins zero direction and fins thrust. Details about the fuzzy logic controller and the control allocation can be found in [Publication II]. Subsequently, the proposed model was used to determine the fins amplitudes.

Various experimental scenarios were executed to assess the control scheme's effectiveness. These scenarios include:

- **Scenario 1 (Nominal case):** the robot operates without any external disturbances or uncertainties. The aim was to validate the proposed fin model. This scenario was repeated five times, each with a different oscillating frequency: (0.8Hz, 1.1Hz, 1.4Hz, 1.7Hz, 2.0Hz).
- **Scenario 2 (Robustness test):** A buoyancy foam was attached to the robot, increasing its buoyancy. This setup was designed to test how the control law would respond to such an unexpected change. The oscillating frequency for this test was kept constant at 1.1Hz.
- **Scenario 3 (External disturbances rejection):** In this setup, the robot faced an external disturbing force, primarily affecting its yaw angle. The oscillating frequency for this test was also set at 1.1Hz.

It's important to highlight that once tuned for the nominal case, the controller parameters remained unchanged across all scenarios. In Scenario 2, the primary variable was the robot's buoyancy B . For Scenario 3, the external disturbance was introduced in a manner that predominantly influenced the vehicle's yaw angle.

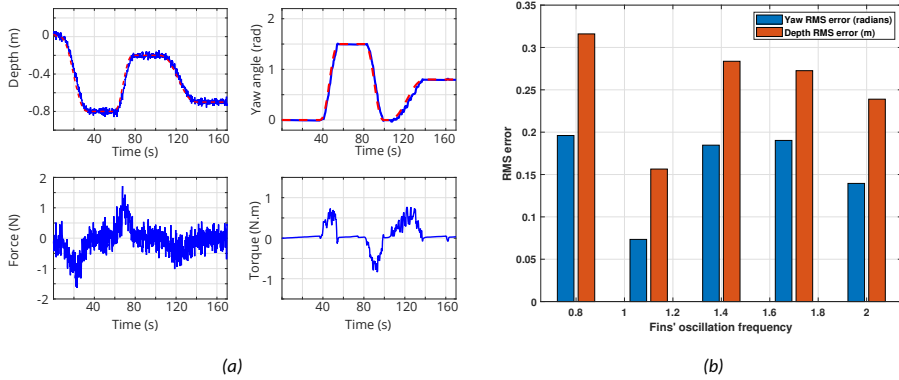


Figure 15: (a) Obtained experimental results using the proposed fin model and a fuzzy-logic controller in the nominal case (at an oscillating fin frequency of $1.1Hz$). (b) RMS tracking errors for the nominal case using different fins oscillating frequencies. ([Publication II] ©2021 Elsevier Ltd).

4.3.1 Experimental scenario 1: Control in nominal case

The RMS errors for depth and yaw tracking are presented in Figure 15b. As can be observed from Figure 15b, the proposed fin model yields satisfactory results across all tested oscillating frequencies, spanning from $0.8Hz$ to $2Hz$. The optimal performance was achieved with the fin's oscillating frequency set to $1.1Hz$, recording RMS errors of $0.15m$ for depth and 4.01° for yaw tracking. Using an oscillating frequency of $1.1Hz$, the tracking results are illustrated in Figure 15a. Figure 15a shows that the proposed control scheme performs well under nominal conditions. The robot adeptly tracks the desired trajectories, even when both degrees of freedom are simultaneously in flux. The associated control signal for depth exhibits high-frequency variations, leading to minor adjustments in fin direction, yet the control performance remains unaffected. In this scenario, both control signals stay within the permissible range of the robot's actuators.

4.3.2 Experimental scenario 2: Robustness test towards buoyancy change

For this test, a buoyancy foam of volume $300cm^3$ was affixed to the robot's top centre, increasing its buoyancy. In this configuration, the robot ascends to the water's surface when the fins remain inactive, indicating a loss of the robot's neutral buoyancy. The results from this scenario are displayed in Figure 16. Despite the augmented buoyancy, the robot successfully tracks the desired trajectories for depth and yaw. Minor oscillations in yaw tracking are evident, attributed to the robot's continuous fin adjustments to counterbalance the heightened buoyancy. The RMS errors for this test are $0.29m$ for depth and 10.42° for yaw tracking. Even with the added buoyancy, the robot maintains a commendable tracking accuracy.

4.3.3 Experimental scenario 3: External disturbances rejection

During this test, the robot encountered an external disturbance. A stick was employed to perturb the robot twice, reorienting it at arbitrary angles. An initial, milder disturbance was applied as the robot dived, followed by a more pronounced disturbance once the robot achieved a stable depth. The outcomes are showcased in Figure 17, with the disturbance timings highlighted in the top right plot of Figure 17. After the first disturbance, the robot realigned to the desired yaw angle, even while diving (with vertically positioned

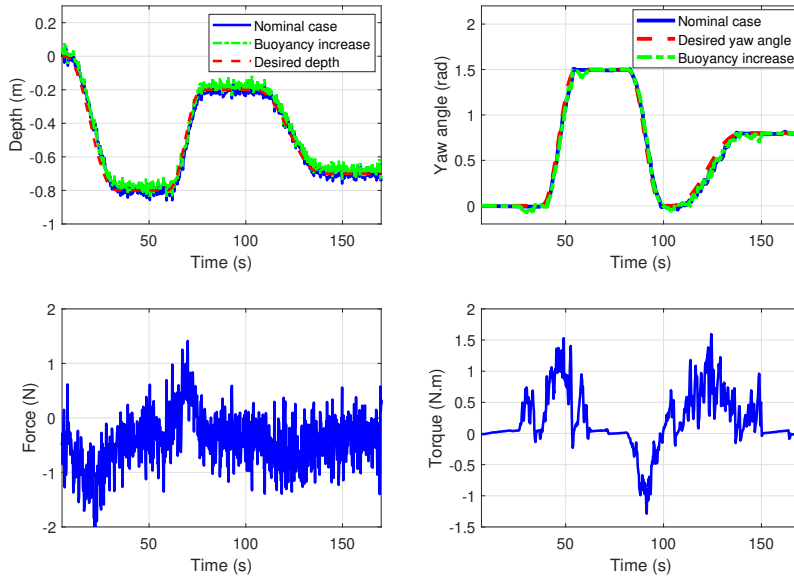


Figure 16: Experimental results obtained with the proposed fuzzy-logic controller under increased buoyancy conditions. The top plots illustrate the trajectory tracking time series and the bottom plots show the controller output for depth and yaw, respectively. ([Publication II] ©2021 Elsevier Ltd).

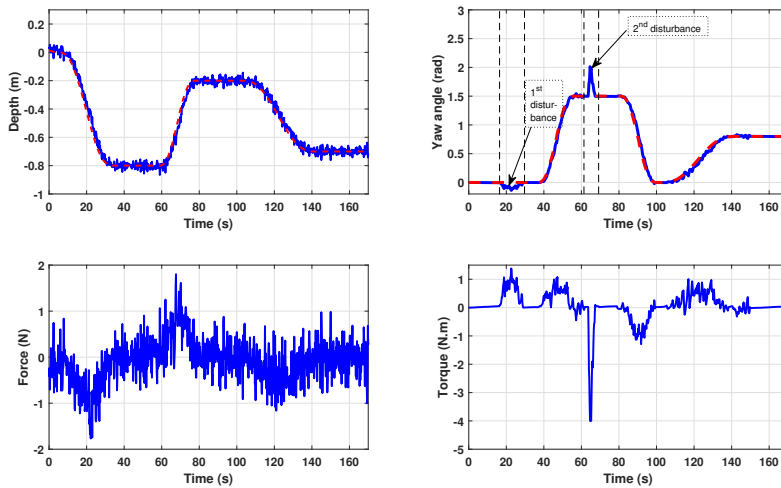


Figure 17: experimental results using the proposed fuzzy-logic control in an external disturbances rejection scenario. Top plots focus on the trajectory tracking time series, while bottom plots reveal the controller output for depth and yaw, respectively. ([Publication II] ©2021 Elsevier Ltd).

fins). The robot exhibited a swifter recovery following the second, more intense disturbance. It was attributed to its fins' horizontal orientation during non-diving phases, generating a more substantial torque force from all four fins. The RMS errors for this test stand at $0.17m$ for depth and 14.64° for yaw tracking.

4.4 Conclusions

The challenge of dynamic modelling and control of fin-actuated underwater vehicles is complex, and this chapter aims to address it comprehensively. A significant focus was placed on deriving a dynamic model that aptly represents the robot's fins. The introduced model offers a nonlinear analytical relationship that links the amplitude and frequency of oscillations to the thrust force required for controlling fin-actuated vehicles. Experimental validation was a vital component of this work, and the proposed model was rigorously tested against thrust generated across various operating frequencies. The outcomes were promising, underscoring the model's applicability across different oscillating frequencies.

Moreover, the practical implementation of the proposed model and its inverse on a fin-actuated AUV was a testament to its real-world relevance. The experiments showcased the potential of amplitude modulation, with a set constant frequency, as a viable control mechanism for a fin-actuated AUV. The results indicated the model's efficacy and robustness across diverse oscillating frequencies.

Specifically, the contributions of this chapter include:

- The introduction of a nonlinear analytical model that captures the relationship between oscillation amplitude and frequency and the required thrust force for fin-actuated vehicles.
- Experimental validation of the proposed model across various oscillating frequencies, confirming its accuracy and relevance.
- Demonstrating the real-world applicability of the model and its inverse on a fin-actuated AUV, highlighting the potential of amplitude modulation as a control mechanism.

5 Control allocation for 6-DOF control of fin-Actuated AUVs

5.1 Overview and motivation

Fin-actuated AUVs, such as the U-CAT, have the unique capability of using fins for thrust generation and vectoring. This feature enhances manoeuvrability while reducing the number of actuators required for full 6-DOF control. However, the dual-purpose nature of these fins introduces complex control challenges distinct from those faced by propeller-based systems.

Traditional control allocation methods designed for propeller-based actuation are not directly applicable to fin-actuated vehicles. Fins require rotation to change the thrust direction, introducing delays and disturbances in control response. Unlike tiltable thrusters, which can produce thrust throughout rotation, fins halt thrust generation during rotation. These characteristics necessitate tailored control allocation methods that account for the specific dynamics of fin-actuated vehicles.

In previous sections, control allocation was primarily based on empirical models, limiting the robot's control capabilities to 3-DOF. This section introduces an analytic control allocation method designed explicitly for fin-actuated AUVs to address these challenges. The method integrates a state-of-the-art adaptive hybrid feedback controller to enable an AUV with only four actuators to achieve accurate 6-DOF trajectory tracking.

The proposed method has been rigorously assessed through extensive Monte Carlo simulations and validated by real-world pool experiments. These assessments focus on evaluating the proposed control allocation method's performance, energy efficiency, and computational speed in full 6-DOF trajectory tracking.

In summary, this section aims to contribute a novel control framework that balances performance, energy efficiency, and computational speed, thereby advancing the field of 6-DOF tracking for under-actuated underwater robots.

To enable 6-DOF control for the U-CAT, the control allocation problem $\tau = BX$ must be addressed, as formulated in Equation 40 and detailed in Section 2.5.

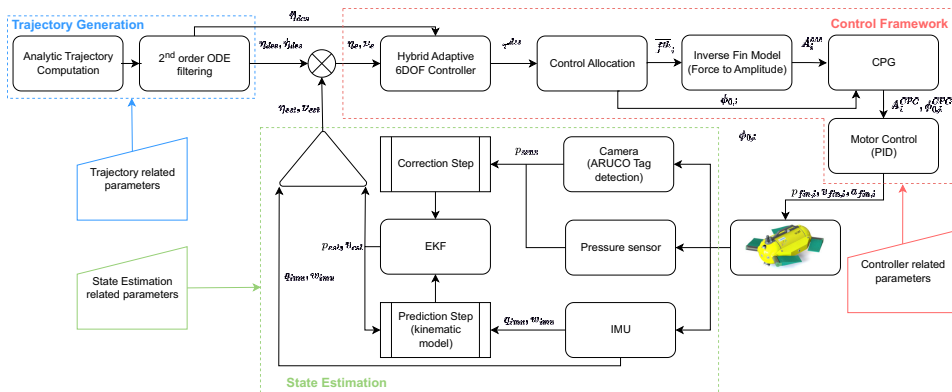


Figure 18: Proposed autonomy architecture consisting of: 1) trajectory generation module in blue, 2) control module including hybrid adaptive 6-DOF controller and control allocation in red, 3) state estimation module with sensors and EKF in green.

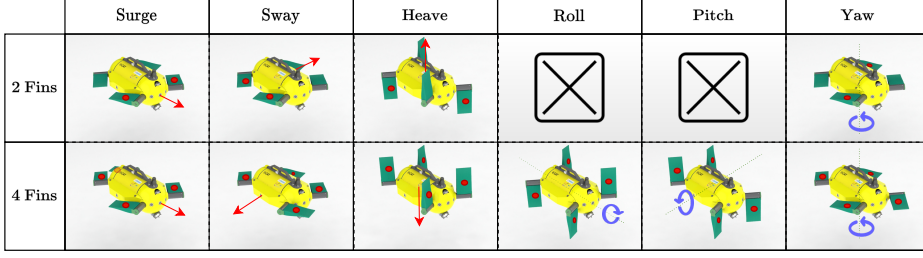


Figure 19: Illustration of the different fin configurations for controlling the U-CAT robot in each degree of freedom, using two or four fins. The fins responsible for actuation in each configuration are marked with a red dot.

5.2 Solving the control allocation problem

$$\tau = \begin{bmatrix} \tau_x \\ c\psi_f \\ \tau_y \\ s\psi_f \\ \tau_z \\ \tau_\Phi \\ y_f \\ \tau_\Theta \\ x_f \\ \tau_\Psi \\ M_a \end{bmatrix} = \begin{bmatrix} 1 & -1 & -1 & 1 & 0 & 0 & 0 & 0 \\ -1 & -1 & 1 & 1 & 0 & 0 & 0 & 0 \\ 0 & 0 & 0 & 0 & 1 & 1 & 1 & 1 \\ 0 & 0 & 0 & 0 & 1 & 1 & -1 & -1 \\ 0 & 0 & 0 & 0 & -1 & 1 & 1 & -1 \\ -1 & 1 & -1 & 1 & 0 & 0 & 0 & 0 \end{bmatrix} \begin{bmatrix} c\phi_{0,1} \overline{f^{th}}_1 \\ c\phi_{0,2} \overline{f^{th}}_2 \\ c\phi_{0,3} \overline{f^{th}}_3 \\ c\phi_{0,4} \overline{f^{th}}_4 \\ s\phi_{0,1} \overline{f^{th}}_1 \\ s\phi_{0,2} \overline{f^{th}}_2 \\ s\phi_{0,3} \overline{f^{th}}_3 \\ s\phi_{0,4} \overline{f^{th}}_4 \end{bmatrix} \quad (40)$$

Several methods exist to solve the problem mentioned above. A naive pseudo-inverse approach offers a straightforward but suboptimal allocation strategy. Alternatively, optimization-based techniques, such as quadratic programming [61], aim for an optimal distribution of control efforts. However, this work introduces a novel control allocation method that focuses on minimising fin rotations. The hypothesis behind this approach is that reduced fin rotations should result in fewer delays and minimal disturbances in the control response.

5.2.1 Direct solution

The matrix B is full-rank, allowing for a non-unique solution via the Moore-Penrose inverse, expressed as $X = B^T (BB^T)^{-1} \tau$. Given the symmetric configuration of the fins, denoted $i = 1, \dots, 4$, the solution can be formulated as follows, where the forces and orientations of the fins remain coupled:

$$c\phi_{0,i} \overline{f^{th}}_i = \frac{1}{4} \left(\frac{\tau_x}{c\psi_i} + \frac{\tau_y}{s\psi_i} + \frac{\text{sign}(\psi_i) \tau_\Psi}{M_a} \right), \quad (41)$$

$$s\phi_{0,i} \overline{f^{th}}_i = \frac{1}{4} \left(\tau_z + \frac{\tau_\Phi}{y_i} - \frac{\tau_\Theta}{x_i} \right). \quad (42)$$

To simplify, the sums of wrenches in Equations (41) and (42) are defined in terms of horizontal f_i^{hor} and vertical f_i^{ver} contributions:

$$f_i^{hor} = \frac{\tau_x}{c\psi_i} + \frac{\tau_y}{s\psi_i} + \frac{\text{sign}(\psi_i) \tau_\Psi}{M_a}, \quad (43)$$

$$f_i^{ver} = \tau_z + \frac{\tau_\Phi}{y_i} - \frac{\tau_\Theta}{x_i}. \quad (44)$$

By dividing Equation (42) by Equation (41), the zero direction $\phi_{0,i}$ for each fin is deduced:

$$\phi_{0,i} = \arctan 2 \left(f_i^{ver}, f_i^{hor} \right). \quad (45)$$

The required thrust forces for each fin are then calculated by squaring and summing Equations (41) and (42):

$$\overline{f^th}_i = \frac{1}{4} \sqrt{(f_i^{hor})^2 + (f_i^{ver})^2}. \quad (46)$$

It should be noted that in this control allocation method, termed CA_{inv} , all four fins are actuated irrespective of the controller's output τ^{des} . This can result in undesirable fin rotations, causing significant disturbances when changing the fin's orientation.

5.2.2 Optimization-based solution

An alternative to the direct solution for the control allocation problem is to employ optimization techniques that can be executed near real-time. The constraints in Equation (40) are modified to relax the trigonometric functions, leading to the following optimization problem:

$$\min_{\overline{f^th}} J = \overline{f^th}^T \overline{f^th} \quad (47)$$

Subject to:

$$\begin{aligned} \tau_x &= c\psi_f \left(\Gamma_1^{opt} \overline{f^th}_1 - \Gamma_2^{opt} \overline{f^th}_2 - \Gamma_3^{opt} \overline{f^th}_3 + \Gamma_4^{opt} \overline{f^th}_4 \right) \\ \tau_y &= s\psi_f \left(-\Gamma_1^{opt} \overline{f^th}_1 - \Gamma_2^{opt} \overline{f^th}_2 + \Gamma_3^{opt} \overline{f^th}_3 + \Gamma_4^{opt} \overline{f^th}_4 \right) \\ \tau_z &= \Lambda_1^{opt} \overline{f^th}_1 + \Lambda_2^{opt} \overline{f^th}_2 + \Lambda_3^{opt} \overline{f^th}_3 + \Lambda_4^{opt} \overline{f^th}_4 \\ \tau_\Phi &= y_f \left(\Lambda_1^{opt} \overline{f^th}_1 + \Lambda_2^{opt} \overline{f^th}_2 - \Lambda_3^{opt} \overline{f^th}_3 - \Lambda_4^{opt} \overline{f^th}_4 \right) \\ \tau_\Theta &= x_f \left(-\Lambda_1^{opt} \overline{f^th}_1 + \Lambda_2^{opt} \overline{f^th}_2 + \Lambda_3^{opt} \overline{f^th}_3 - \Lambda_4^{opt} \overline{f^th}_4 \right) \\ \tau_\Psi &= M_a \left(-\Gamma_1^{opt} \overline{f^th}_1 + \Gamma_2^{opt} \overline{f^th}_2 - \Gamma_3^{opt} \overline{f^th}_3 + \Gamma_4^{opt} \overline{f^th}_4 \right) \\ 1 &= \Gamma_i^{opt} + \Lambda_i^{opt} \quad i = 1 \dots 4 \\ -1 &\leq \Gamma_i^{opt} \leq 1 \quad i = 1 \dots 4 \\ -1 &\leq \Lambda_i^{opt} \leq 1 \quad i = 1 \dots 4 \\ 0 &\leq \overline{f^th}_i \leq F_{max} \quad i = 1 \dots 4 \end{aligned} \quad (48)$$

The cost function aims to minimize the exerted force. Notably, the optimization does not include a term for minimizing zero-direction change, as it led to non-convergence issues.

Sequential Quadratic Programming (SQP) [112] is used to solve the optimization problem to find $[\overline{f}^{th}, \Gamma^{opt}, \Lambda^{opt}]$ during runtime, with initial conditions for all parameters set to zero. The zero-directions ϕ_0 are then calculated using:

$$\phi_{0,i} = \text{atan2}(\Lambda_i^{opt}, \Gamma_i^{opt}) \quad i = 1 \dots 4 \quad (49)$$

This optimization-based approach has its limitations. It does not explicitly aim to minimize zero-direction change, which may not guarantee an optimal solution for this specific criterion. Additionally, the iterative nature of the optimization algorithm demands more computational resources, posing a challenge for real-time execution within hardware constraints.

For the remainder of this paper, this optimization-based control allocation method is denoted as CA_{opt} .

5.2.3 Proposed analytic solution

Addressing the shortcomings of CA_{inv} and CA_{opt} , a new analytic method is introduced. This method aims to solve the control allocation problem while minimizing the change in zero-direction.

Given U-CAT's symmetrical fin configuration, it becomes evident that for specific degrees of freedom—surge, sway, heave, and yaw—only two fins might be sufficient to generate the necessary thrust vector, as depicted in Fig. 19.

The control allocation equations (45) and (46) are adapted to account for the desired number n_d of fins used for each degree of freedom. This adaptation employs Heaviside unit step functions $H(\cdot)$ [113, p. 61].

$$f_i^{hor}(\tau, n_d) = \frac{h_H(\tau_x, c\psi_i, n_d)}{c\psi_i} + \frac{h_H(\tau_y, s\psi_i, n_d)}{s\psi_i} + \frac{h_H(\tau_\Psi, \psi_i, n_d)}{M_a} \quad (50)$$

$$f_i^{ver}(\tau, n_d) = h_H(\tau_z, -\psi_i, n_d) + \frac{\tau_\Phi}{y_i} - \frac{\tau_\Theta}{x_i} \quad (51)$$

$$h_H(\tau, s, n_d) = \begin{cases} 2 H(\text{sign}(s)\tau) \tau & n_d = 2 \\ \tau & n_d = 4 \end{cases} \quad (52)$$

$$\phi_{0,i} = \arctan\left(\frac{f_i^{ver}(\tau, n_d)}{f_i^{hor}(\tau, n_d)}\right) \quad (53)$$

$$\overline{f}^{th}_i = \frac{1}{4} \sqrt{f_i^{hor}(\tau, n_d)^2 + f_i^{ver}(\tau, n_d)^2} \quad (54)$$

Moreover, the symmetry of the fins is used to further minimize the change in zero-direction. When controlling forces and torques in the vertical plane, the fins are oriented at angles of $\pm \frac{\pi}{2}$ according to equation (53). To counteract the non-linearity in the arctan function, opposing horizontal forces are introduced that naturally cancel each other out, as shown in Fig. 20.

$$\overline{f}^{th}_i = \frac{1}{4} \sqrt{(f_{comp} + f_i^{hor}(\tau, n_d))^2 + f_i^{hor}(\tau, n_d)^2} \quad (55)$$

$$f_{comp} = \alpha_{comp} \sum_j (1 - f_j^{norm}) |f_j^{norm}| \quad (56)$$

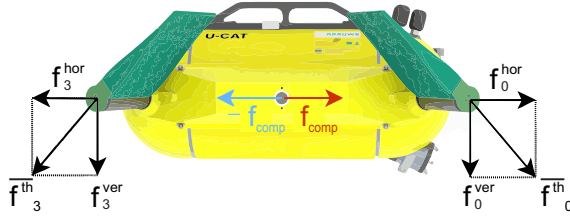


Figure 20: Illustration of the horizontal force compensation principle to minimize the fins' zero-direction change when controlling vertical forces.

with $j = z, \Theta, \Psi$ and $f_j^{norm} = \frac{|\tau_j|}{f_j^{th_{max}}}$, it's worth noting that the compensation term is omitted in two specific scenarios: when $f_j^{norm} = 0$ and when $f_j^{norm} = 1$. The scalar α_{comp} serves to balance the impact of the introduced term f_c , aiming to reduce zero-direction change while potentially increasing oscillation amplitudes. This control allocation method is henceforth referred to as CA_{prop} .

5.3 Method assessment

The primary objective of this work is to assess the performance of the proposed control allocation method in comparison to two existing methods: the pseudo-inverse and optimization-based solutions. However, it's important to note that these control allocation methods are integrated into a broader autonomy framework for the U-CAT AUV. This framework, as illustrated in Figure 18, includes a trajectory generator, a hybrid adaptive controller derived from the work of [84], an inverse fin model—elaborated upon Section 2.4, a Central Pattern Generator (CPG) algorithm, and a state estimator based on an Extended Kalman Filter (EKF) as presented in [114].

For those interested in a comprehensive understanding of how each of these components synergizes to achieve precise 6-DOF control, a detailed description is available in [Publication IV].

5.3.1 Simulation setup

The simulation framework is crafted in Python for rapid deployment. It is based on Fossen's vectorial dynamics model [115] and incorporates the lift and drag model described in Section 2.4 for simulating fin forces. Monte Carlo Simulations are executed with 500 iterations for each of the three control allocation methods: CA_{inv} , CA_{opt} , and CA_{prop} .

Two distinct trajectory scenarios are considered: full 6-DOF trajectory tracking (6T) and 3-DOF trajectory tracking (surge, heave, yaw) with roll and pitch stabilization (3T2S). Within these scenarios, two types of trajectories are randomly selected: Ellipse and Lissajous. To emulate real-world sensor noise, white Gaussian noise is added to the sensor readings in the simulation.

Inspired by the work of Manhaes et al [116], a comprehensive set of evaluation metrics is employed to rigorously assess the performance of the control allocation methods under study. These metrics are detailed further in [Publication IV]

5.3.2 Experimental setup

Validation experiments are conducted in a swimming pool to corroborate the simulation findings. The experimental setup illustrated in Figure 21 includes a fabric grid with ArUco markers to provide position measurements. Two control allocation methods are subjected

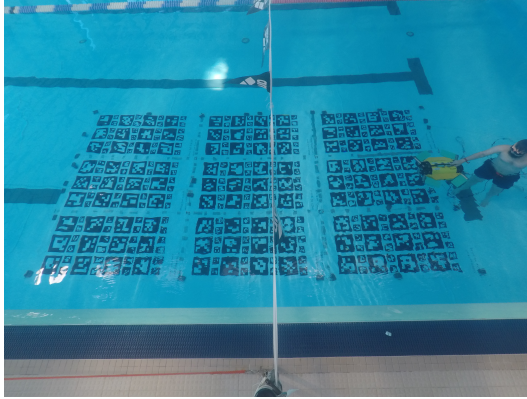


Figure 21: Experimental setup at Keila swimming pool (Estonia).

to testing: the proposed analytic method (CA_{prop}) and the optimization-based method (CA_{opt}). The naive control allocation method (CA_{inv}) was excluded from these experimental trials due to its demonstrated ineffectiveness for fin-actuated robots, as evidenced by the simulation results that will be presented in section 5.4.1.

For each of the two control allocation methods, five trials are conducted for each of the two trajectory types (Ellipse and Lissajous), making a total of 10 trials for each method. The 6T scenario was not considered in these experiments due to the potential loss of ArUco marker-based position feedback when controlling roll and pitch. Additionally, the distribution of centre of mass and centre of buoyancy created a passively stabilizing system which would have disturbed the controller and potentially exceeded the available control authority. Due to the inherent limitations of the experimental setup, not all simulation metrics are directly transferrable. Nonetheless, RMSE tracking errors are recorded, along with root mean square metrics for demanded forces/torques. Computation times for the control allocation are also recorded.

5.4 Results and discussions

This section provides a detailed analysis of the results from the simulations and experiments.

5.4.1 Simulation results

Control allocation comparative results

First, simulation tests were conducted to assess the performance of the control allocation methods under study. A desired 6-DOF wrench vector was set to switch its sign every 5 seconds. The mean body forces produced by the fins for each control allocation method are shown in Fig. 22.

Fig. 22 reveals that CA_{prop} closely follows the desired wrenches without any overshoot, a result of its design to minimize zero-direction change. However, a minor delay in response is observed for heave, roll, and pitch. Table 5 shows that CA_{prop} outperforms the other methods in terms of both linear MAE_{lin} and angular MAE_{ang} allocation errors.

CA_{opt} , on the other hand, responds quickly but experiences significant overshoot. This is primarily due to abrupt changes in the fins' zero-direction angles, which lead to higher MAE_{lin} and MAE_{ang} values compared to CA_{prop} .

CA_{inv} proves to be ineffective for fin-actuated control. All fins contribute to all DOF,

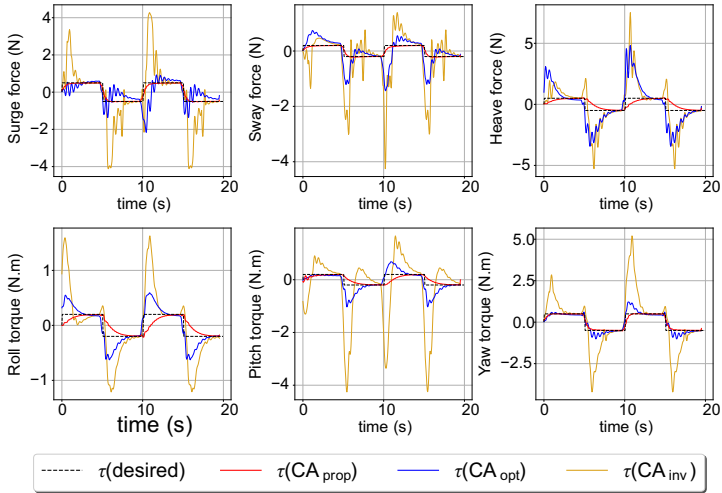


Figure 22: Comparison of the studied control allocation approaches for tracking a desired control input.

disregarding zero-direction change, leading to substantial overshoots in body forces as seen in Fig. 22.

The data clearly indicate the superior performance of CA_{prop} in minimizing force allocation errors. This is attributed to its analytical design focus on minimizing zero-direction change. While CA_{opt} does not explicitly consider zero-direction change in its optimization function, it tends to stay close to the initial fin conditions, offering better performance than CA_{inv} .

Table 5: Comparison of control allocation methods (CA_{prop} , CA_{opt} , and CA_{inv}) in terms of mean allocation errors for linear (MAE_{lin}) and angular (MAE_{ang}) DOF.

	CA_{prop}	CA_{opt}	CA_{inv}
MAE_{lin} [N]	0.293	1.369	2.451
MAE_{ang} [Nm]	0.206	0.467	2.613

Trajectory tracking simulation - 6T Scenario

Table 6 provides a comprehensive summary of the simulation results for the 6T scenario. Across most evaluation metrics, the proposed CA_{prop} method surpasses CA_{inv} and CA_{opt} . Specifically, CA_{prop} registers the lowest RMSE values for both linear and angular degrees of freedom, indicating superior tracking performance. The contrast in performance is particularly stark when comparing CA_{prop} to CA_{inv} , with the latter showing substantial deviations in tracking—up to 1.15 m and 103 deg.

The inadequacy of CA_{inv} stems from its inability to minimize disturbances during fin rotations, a problem addressed in CA_{prop} through selective fin usage and force compensation. Although CA_{opt} does not explicitly minimize fin rotations, it appears to do so implicitly, resulting in better performance than CA_{inv} but still falling short of CA_{prop} .

In terms of energy efficiency, as measured by MAW, MAE_{lin} , and MAE_{ang} , CA_{prop} also outperforms the other methods. Notably, CA_{inv} demands actuator forces well beyond the

maximum wrench magnitude of 12.5 N, indicating an unsustainable operational requirement.

Regarding computational efficiency, CA_{inv} leads due to its simpler computational structure. However, CA_{prop} offers a significant advantage over CA_{opt} , requiring approximately 40 times less computation time. This efficiency is crucial for systems with limited computational resources and high update rates, where CA_{opt} could become a bottleneck.

In summary, the results affirm the capability of CA_{prop} and CA_{opt} to enable precise and efficient 6-DOF trajectory tracking with a limited actuator set, when paired with a state-of-the-art hybrid adaptive controller.

Table 6: Summary statistics represented by median (IQR), of defined evaluation metrics for Monte Carlo simulation framework with 500 trials in the 6T scenario. Results are presented for 3 different control allocation scenarios: CA_{prop} , CA_{opt} , CA_{inv} .

Summary Statistic	CA_{prop}	CA_{opt}	CA_{inv}
$RMSE_{lin}$ [m]	0.04 (0.02)	0.05 (0.01)	1.15 (0.3)
$RMSE_{ang}$ [rad]	0.06 (0.003)	0.07 (0.008)	1.83 (0.18)
MEM_{lin} [m]	0.15 (0.01)	0.15 (0.01)	2.4 (0.72)
MEM_{ang} [rad]	0.53 (0.04)	0.55 (0.06)	4.42 (0.48)
MAW [N]	1.34 (0.28)	1.69 (0.17)	6.93 (1.02)
MW [N]	4.19 (0.22)	4.34 (0.28)	38.68 (6.52)
MCT [ms]	0.08 (0.002)	3.3 (0.19)	0.07 (0.002)
MAE_{lin} [N]	0.48 (0.04)	0.71 (0.03)	5.0 (0.34)
MAE_{ang} [Nm]	0.32 (0.03)	0.42 (0.03)	1.37 (0.11)

Trajectory Tracking Simulation - 3T2S Scenario

Table 7 summarizes the simulation outcomes for the 3T2S scenario. Consistent with the 6T scenario, CA_{prop} and CA_{opt} demonstrate robust performance, whereas CA_{inv} falls short on multiple fronts. Specifically, CA_{inv} registers high RMSE values and inefficient median actuation efforts, with maximum demanded wrenches surpassing the 12.5 N limit.

For CA_{prop} and CA_{opt} , the metrics remain largely unchanged between the 6T and 3T2S scenarios. This consistency suggests effective sway compensation in the trajectory generation, affirming the framework's potential for precise 3D trajectory tracking with roll and pitch stabilization in non-holonomic vehicles equipped with only four actuators.

In summary, the simulation results for both 6T and 3T2S scenarios reinforce the efficacy of the proposed CA_{prop} method. It offers a balanced solution that excels in tracking performance, actuator efficiency, and computational demands, making it a viable control allocation strategy for fin-actuated underwater robots in various operational scenarios.

5.4.2 Experimental Results

Fig. 23a presents the ellipse trajectory tracking results from a single trial. Both CA_{prop} and CA_{opt} deliver satisfactory tracking performance across all controlled degrees of freedom (DOF). The line-of-sight implementation also enables tracking of the non-directly commanded sway component. Passive stability in roll and pitch DOF keeps their tracking errors near zero, albeit with minor oscillations due to the oscillatory actuation.

Fig. 23b displays a whisker plot summarizing five runs in the ellipse trajectory tracking scenario. The data suggests that CA_{opt} slightly surpasses CA_{prop} in tracking accuracy.

Table 7: Summary statistics, represented by median (IQR), of defined evaluation metrics for Monte Carlo simulation framework with 500 trials in the 3T2S scenario. Results are presented for 3 different control allocation scenarios: CA_{prop} , CA_{opt} , CA_{inv} .

Summary Statistic	CA_{prop}	CA_{opt}	CA_{inv}
$RMSE_{lin}$ [m]	0.04 (0.02)	0.05 (0.02)	2.1 (1.21)
$RMSE_{ang}$ [rad]	0.06 (0.02)	0.09 (0.05)	1.74 (0.12)
MEM_{lin} [m]	0.13 (0.03)	0.15 (0.05)	4.17 (2.14)
MEM_{ang} [rad]	0.34 (0.49)	0.7 (0.67)	3.22 (0.07)
MAW [N]	1.27 (0.24)	1.6 (0.15)	4.87 (2.07)
MW [N]	4.09 (0.12)	3.86 (0.34)	34.35 (6.87)
MCT [ms]	0.08 (0.009)	3.8 (0.55)	0.07 (0.002)
MAE_{lin} [N]	0.42 (0.02)	0.63 (0.06)	4.66 (1.12)
MAE_{ang} [Nm]	0.34 (0.03)	0.47 (0.04)	1.37 (0.15)

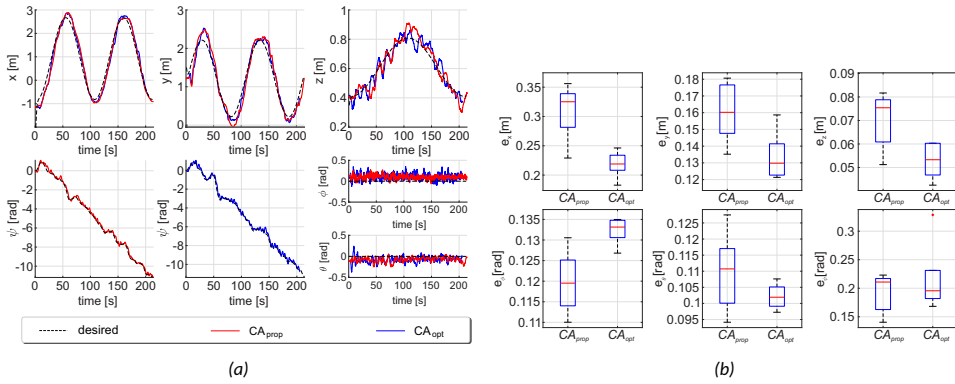


Figure 23: (a) Experimental tracking results for the 3D ellipsoidal trajectory: In the dotted black line is the desired trajectory. In the red line is the performed trajectory using the proposed solution CA_{prop} . In the blue line is the performed trajectory using the optimal solution CA_{opt} . (b) Box-plot of tracking errors for the 3D ellipse trajectory.

Specifically, the median error in surge tracking for CA_{prop} stands at 33 cm, compared to 22 cm for CA_{opt} . This discrepancy arises from the controller gains, set to prevent the robot from overtaking the desired trajectory x_d and thereby avoiding a full turn.

Fig. 24a shows results from a single Lissajous trajectory tracking trial. Similar to the ellipse scenario, both control allocation methods perform well. The passive stability in roll and pitch DOF remains effective, keeping their tracking errors close to zero.

Fig. 24b offers a box plot of five runs in the Lissajous scenario. Here, CA_{prop} records a median error of 41 cm in surge tracking, while CA_{opt} registers 25 cm. The controller gains are again the contributing factor, set to prevent the robot from surpassing the desired trajectory.

It's worth noting that tracking errors in the experiments are significantly higher than in simulations. This discrepancy is attributed to several factors. First, the simulations do not account for low-level motor control imperfections or time lags in fin actuation. Second, the fin model used in simulations, denoted by (14), does not capture complex fluid-body

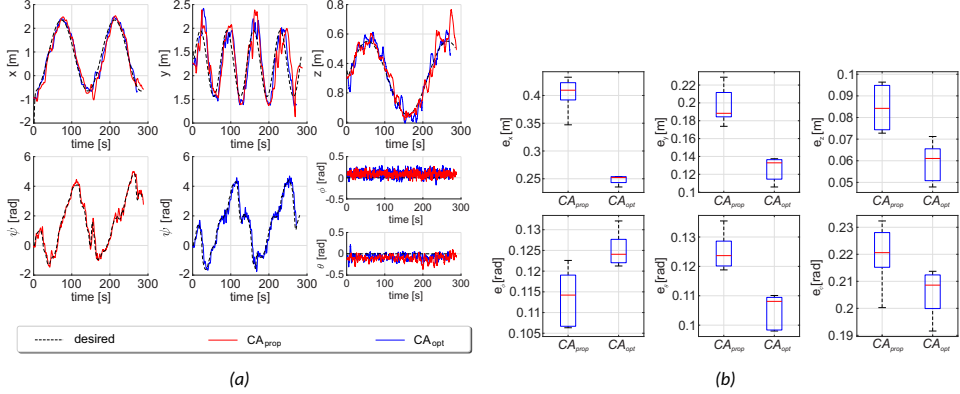


Figure 24: (a) Experimental tracking results for the 3D Lissajous trajectory: In the dotted black line is the desired trajectory. In the red line is the performed trajectory using the proposed solution CA_{prop} . In the blue line is the performed trajectory using the optimal solution CA_{opt} . (b) Box-plot of tracking errors for the 3D Lissajous trajectory.

Table 8: Computation times for CA_{prop} and CA_{opt} methods

Trajectory type	CA_{prop}		CA_{opt}	
	Ellipse	Lissajous	Ellipse	Lissajous
Mean time (ms)	0.0068	0.0067	22.2779	21.0504
Max time (ms)	0.3199	0.1588	3931.6030	1812.4072

interactions. Third, environmental disturbances, such as pool activities during the experiments, introduce additional variables not present in the simulations. These factors also potentially explain why CA_{opt} outperforms CA_{prop} in the experimental setting, contrary to simulation results.

In terms of tracking performance, our maximal RMSEs stand at 8.5 cm for depth and 11° for yaw. When compared to previous works, such as 2.22 cm in depth set point stabilization and 2.91° in yaw tracking [45], our performance appears less accurate. However, these studies often focused on fewer DOFs, making our work more comprehensive in scope. This suggests that the current work significantly advances the state-of-the-art for fin-driven, turtle-like AUVs by expanding the tracked DOF while maintaining comparable accuracy.

Comparing our results to the hybrid adaptive controller from Basso et al. [84] is also instructive. While they did not report numerical metrics, the figures suggest our tracking performance is in a similar range. Notably, we achieve this with half the number of actuators and on a functionally non-holonomic system. Additionally, our starting values for adaptive parameters are approximations, unlike in [84] where they are derived from an identified dynamics model. This underscores the robustness and applicability of our approach, even when compared to more specialized systems.

Fig. 25 presents a box plot of the root mean square (RMS) of the generated controller outputs (τ^{des}) for both CA_{prop} and CA_{opt} . The data indicates that CA_{prop} requires slightly higher forces in linear directions and lower torque for yaw. This is attributed to the force compensation term f_{comp} (56), which minimizes changes in zero-direction angle but necessitates higher forces. This highlights a trade-off between minimizing disturbances and actuator energy efficiency, a consideration that will be application-specific.

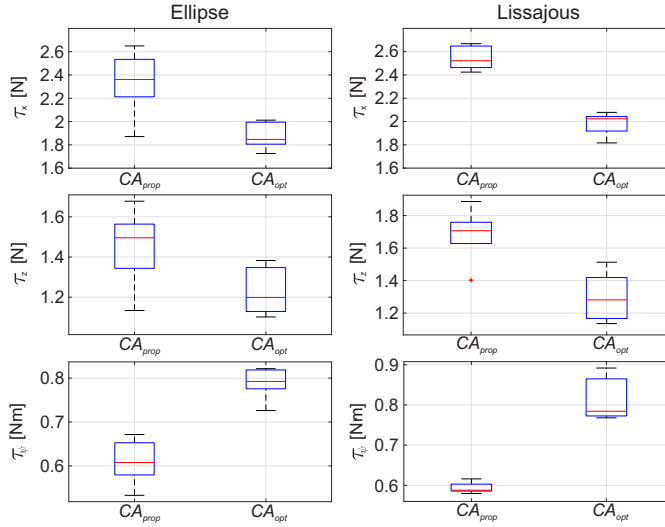


Figure 25: Box-plot of root mean square forces and torques. Left: During ellipse trajectory. Right: During Lissajous trajectory.

Table 8 compares the computation times for CA_{prop} and CA_{opt} on the Jetson TX2 embedded computer. The mean times for CA_{prop} are around 0.0068 ms and 0.0067 ms for ellipse and Lissajous trajectories, respectively. The maximum times are well below 1 ms. In contrast, CA_{opt} requires mean times of 22 ms and 21 ms and maximum times reaching up to 3931 ms and 1812 ms for the two trajectories. The computational burden is notably higher on the embedded system compared to a laptop, emphasizing the efficiency of CA_{prop} .

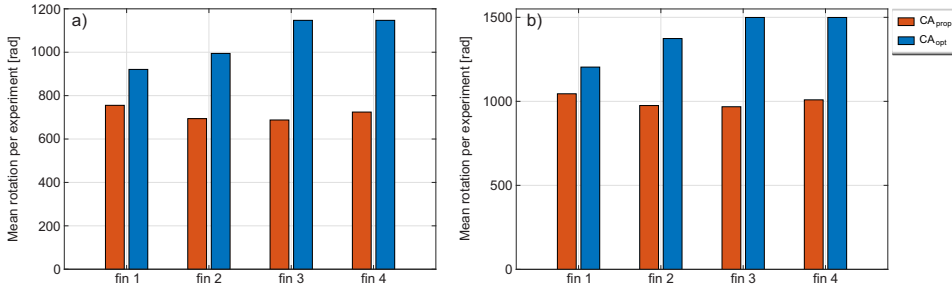


Figure 26: Mean accumulated rotation of U-CAT's four fins per experiment for a) the ellipse trajectory and b) the Lissajous trajectory.

Fig. 26 a) and b) show the mean accumulated fin rotations for both trajectories. The data indicates that CA_{prop} requires less actuation effort, enhancing energy efficiency.

There are limitations to the current work. Roll and pitch stabilization were not tested due to the U-CAT's inherent passive stability in these DOFs. While simulations accounted for these factors, the mechanical reconfiguration needed to test them was beyond the scope of this study. Additionally, the maximum tested velocities were around 0.2 m/s, which may be insufficient in strong currents. This limitation is due to both the experimental setup and the current fin design, but we see these as engineering challenges rather than fundamental issues.

Despite these limitations, the results offer a thorough evaluation of the proposed methods. The data confirms the effectiveness of CA_{prop} in tracking complex 3D trajectories with minimal error, efficient actuation, and reduced computational time.

5.5 Conclusions

This chapter presents a comprehensive investigation into the challenges and solutions associated with 6-DOF tracking control for under- and fin-actuated AUVs. The focal point of this work is the development and validation of an innovative analytic control allocation method, CA_{prop} , specifically tailored for fin-actuated AUVs. This method was designed to address the unique challenges posed by fin-based actuation, offering a balance between computational efficiency and actuator energy usage.

The proposed control allocation method was rigorously tested in both simulation and real-world environments. In simulation, the method demonstrated superior performance in terms of tracking accuracy and actuator efficiency when compared to other existing methods. Real-world experiments in a semi-controlled environment further corroborated these findings. The method was tested using complex 3D trajectories. The results consistently indicated that CA_{prop} is both robust and efficient, making it a promising solution for fully autonomous 6-DOF navigation in fin-actuated AUVs. The key contributions of this work are:

- Rigorous development and validation of a novel analytic control allocation method, CA_{prop} , optimized for fin-actuated AUVs.
- Comprehensive testing of the proposed method in both simulated and real-world settings, confirming its robustness, efficiency, and suitability for 6-DOF tracking in fin-actuated AUVs.
- A detailed comparative analysis against existing control allocation methods, highlighting the advantages of CA_{prop} in terms of tracking accuracy, actuator efficiency, and computational demands.
- First-ever demonstration of 6-DOF control in an under-actuated AUV, establishing a new benchmark in the field.

6 Fault-tolerant control for fin-actuated AUVs

6.1 Overview and Motivation

The need for fault-tolerant control in underwater robotics is not just academic; it's essential for real-world missions. Underwater conditions are harsh and unpredictable, making actuator failures likely. For a fin-actuated AUV like U-CAT, a single fin failure can seriously affect the vehicle's ability to navigate and complete tasks. Developing a reliable fault-tolerant control scheme for fin-actuated AUVs is not just an engineering problem; it's a requirement for successful missions.

This chapter focuses on an active fault-tolerant control scheme for a four-fin-actuated AUV. The key feature is a control allocation switching mechanism that can adaptively redistribute control forces among the fins if a failure occurs. The scheme uses the column elimination method [117, 118], adapted to handle the specific challenges of fin-based actuation, which is nonlinear and highly coupled.

Two different control strategies are used to test the proposed fault-tolerant control method: PID and Sliding Mode control. These tests aim to provide a thorough evaluation under different conditions.

By addressing the need for more research on fault-tolerant control for fin-actuated AUVs, this work aims to contribute to the field significantly. The goal is to improve the reliability and resilience of these specialised underwater vehicles.

6.2 Proposed FTC scheme

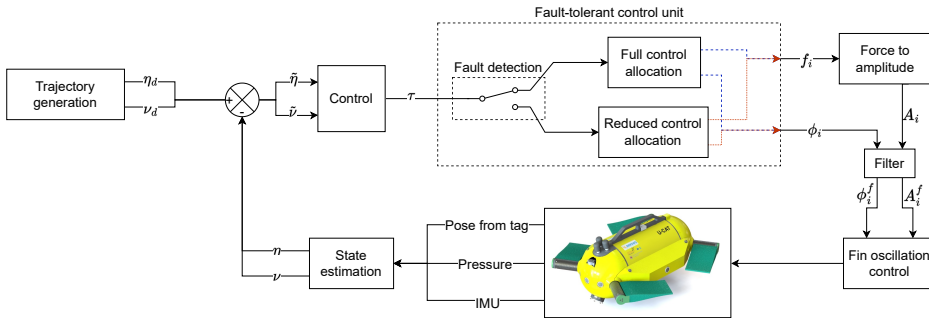


Figure 27: Block Diagram illustration of the proposed fault-tolerant control strategy. ([Publication III] ©2023 Elsevier Ltd).

A recapitulation of the control allocation in the nominal case is warranted before delving into the fault-tolerant control scheme, as illustrated in Fig. ???. In a scenario where all fins are fully functional, the equation system in (40) can be compactly expressed as $B[H_c, V_c]^T = \tau_n$. This is mathematically represented as:

$$\begin{bmatrix} C_h^1 & C_h^2 & C_h^3 & C_h^4 & C_v^1 & C_v^2 & C_v^3 & C_v^4 \\ 1 & -1 & -1 & 1 & 0 & 0 & 0 & 0 \\ -1 & -1 & 1 & 1 & 0 & 0 & 0 & 0 \\ 0 & 0 & 0 & 0 & 1 & 1 & 1 & 1 \\ 0 & 0 & 0 & 0 & 1 & 1 & -1 & -1 \\ 0 & 0 & 0 & 0 & -1 & 1 & 1 & -1 \\ -1 & 1 & -1 & 1 & 0 & 0 & 0 & 0 \end{bmatrix} \begin{bmatrix} H_c \\ V_c \end{bmatrix} = \tau_n \quad (57)$$

The system in (57) is virtually over-actuated, given the infinite number of possible fin configurations. A straightforward approach involves using the Moore-Penrose inverse [119], such that $[H_c, V_c]^T = B^\dagger \tau_n$. The Moore-Penrose inverse $B^\dagger = B^T (BB^T)^{-1}$ is given by:

$$B^\dagger = \frac{1}{4} \begin{bmatrix} 1 & -1 & 0 & 0 & 0 & -1 \\ -1 & -1 & 0 & 0 & 0 & 1 \\ -1 & 1 & 0 & 0 & 0 & -1 \\ 1 & 1 & 0 & 0 & 0 & 1 \\ 0 & 0 & 1 & 1 & -1 & 0 \\ 0 & 0 & 1 & 1 & 1 & 0 \\ 0 & 0 & 1 & -1 & 1 & 0 \\ 0 & 0 & 1 & -1 & -1 & 0 \end{bmatrix} \quad (58)$$

This leads to a solution where the fins' forces and orientations remain coupled. The equations are as follows:

$$c\phi_{i,0} \overline{f^{th}}_i = \frac{1}{4} \left(E_{i,1} \frac{\tau_x}{c\psi_f} + E_{i,2} \frac{\tau_y}{s\psi_f} + E_{i,6} \frac{\tau_\Psi}{M_\Psi} \right) \quad (59)$$

$$s\phi_{i,0} \overline{f^{th}}_i = \frac{1}{4} \left(E_{i,3} \tau_z + E_{i,4} \frac{\tau_\Phi}{M_\Phi} + E_{i,5} \frac{\tau_\Theta}{M_\Theta} \right) \quad (60)$$

Where $E_{i,j}$ denotes the element located at row i and column j of the matrix B^\dagger . By dividing equation (59) by equation (60), the zero-direction angles $\phi_{i,0}$ can be deduced:

$$\phi_{i,0} = \text{atan} \left(\frac{E_{i,3} \tau_z + E_{i,4} \frac{\tau_\Phi}{M_\Phi} + E_{i,5} \frac{\tau_\Theta}{M_\Theta}}{E_{i,1} \frac{\tau_x}{c\psi_f} + E_{i,2} \frac{\tau_y}{s\psi_f} + E_{i,6} \frac{\tau_\Psi}{M_\Psi}} \right) \quad (61)$$

The forces $\overline{f^{th}}_i$ are then derived by summing and squaring equations (59) and (60):

$$\overline{f^{th}}_i = \frac{1}{4} \sqrt{\left(E_{i,1} \frac{\tau_x}{c\psi_f} + E_{i,2} \frac{\tau_y}{s\psi_f} + E_{i,6} \frac{\tau_\Psi}{M_\Psi} \right)^2 + \left(E_{i,3} \tau_z + E_{i,4} \frac{\tau_\Phi}{M_\Phi} + E_{i,5} \frac{\tau_\Theta}{M_\Theta} \right)^2} \quad (62)$$

The solution derived above for controlling the fins' orientations and thrust forces, as discussed in Section 5.2.1, lacks optimization for accurately tracking time-varying trajectories. Specifically, all four fins must be actuated regardless of the control input τ . This could, for example, result in a 180-degree rotation of all fins when the surge component changes its sign. Taking advantage of the symmetrical configuration of U-CAT fins offers a solution. For forces and torques produced in the horizontal plane of the body-fixed frame, such as surge, sway, and yaw, only two fins are necessary for movement in one direction. The control allocation can thus be reformulated as follows:

$$\phi_{i,0} = \text{atan} \left(\frac{E_{i,3} \tau_z + E_{i,4} \frac{\tau_\Phi}{M_\Phi} + E_{i,5} \frac{\tau_\Theta}{M_\Theta}}{2 \left(E_{i,1} \frac{H(\tau_x) \tau_x}{c\psi_f} + E_{i,2} \frac{H(-\tau_y) \tau_y}{s\psi_f} + E_{i,6} \frac{H(-\tau_\Psi) \tau_\Psi}{M_\Psi} \right)} \right) \quad (63)$$

$$\overline{f^{th}}_i = \frac{1}{4} \sqrt{2 \left(E_{i,1} \frac{H(\tau_x) \tau_x}{c \psi_f} + E_{i,2} \frac{H(-\tau_y) \tau_y}{s \psi_f} + E_{i,6} \frac{H(-\tau_\psi) \tau_\psi}{M_\psi} \right)^2 + \left(E_{i,3} \tau_z + E_{i,4} \frac{\tau_\Phi}{M_\Phi} + E_{i,5} \frac{\tau_\Theta}{M_\Theta} \right)^2} \quad (64)$$

This study focuses solely on fin failure as a fault condition, assuming that such a fault can be both identified and isolated. Additionally, it's assumed that only one actuator failure occurs at a time. For the remainder of this section, a "faulty" fin refers to a completely nonfunctional fin.

Upon the occurrence of an actuation failure, the elimination of column method adapts the control allocation system. Specifically, the matrix B from equation (21) is reduced by two columns, contingent on which fin is identified as faulty (see Fig. 1b for illustration). The columns to be eliminated are as follows:

- C_h^1 and C_v^1 , if the fin FR is faulty
- C_h^2 and C_v^2 , if the fin RR is faulty
- C_h^3 and C_v^3 , if the fin RL is faulty
- C_h^4 and C_v^4 , if the fin FL is faulty

After identifying and eliminating the appropriate columns, the reduced matrix, denoted as $A_r \in \mathbb{R}^{6 \times 6}$, becomes a full-rank square matrix. In a faulty fin scenario, this implies that A_r is invertible, and a unique fin configuration exists that solves the control allocation problem. The inverse of this matrix, A_r^{-1} , can be generalized for all the faulty cases listed above:

$$B_r^{-1} = \begin{bmatrix} H_1^1 & H_1^2 & 0 & 0 & 0 & V_1^1 \\ H_2^1 & H_2^2 & 0 & 0 & 0 & V_2^1 \\ H_3^1 & H_3^2 & 0 & 0 & 0 & V_3^1 \\ 0 & 0 & H_4^1 & V_4^1 & V_4^2 & 0 \\ 0 & 0 & H_5^1 & V_5^1 & V_5^2 & 0 \\ 0 & 0 & H_6^1 & V_6^1 & V_6^2 & 0 \end{bmatrix} \quad (65)$$

The values of B_r^{-1} for all faulty fin scenarios are summarized in [Publication III].

Following the same solving procedure detailed in equations (59) to (62), both the required forces and zero-direction angles for the three healthy fins can be deduced:

$$\overline{f^{th}}_i \cos(\phi_{i,0}) = H_i^1 \frac{\tau_x}{c \psi_f} + H_i^2 \frac{\tau_y}{s \psi_f} + V_i^1 \frac{\tau_\psi}{M_\psi} = \Gamma_i^h \quad (i = 1 \dots 3) \quad (66)$$

$$\overline{f^{th}}_i \sin(\phi_{i,0}) = H_{i+3}^1 \tau_z + V_{i+3}^1 \frac{\tau_\Phi}{M_\Phi} + V_{i+3}^2 \frac{\tau_\Theta}{M_\Theta} = \Gamma_i^v \quad (i = 1 \dots 3) \quad (67)$$

The required zero-direction angles and forces are then derived and expressed as:

$$\overline{f^{th}}_i = \sqrt{\Gamma_i^{h2} + \Gamma_i^{v2}} \quad (i = 1 \dots 3) \quad (68)$$

$$\phi_{i,0} = \tan^{-1} \left(\frac{\Gamma_i^v}{\Gamma_i^h} \right) \quad (i = 1 \dots 3) \quad (69)$$

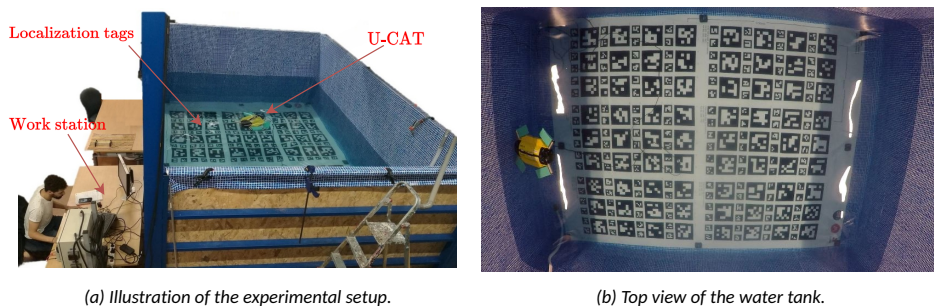


Figure 28: The experimental setup used for real-time experiments at LIRMM laboratory (Montpellier, France). ([Publication III] ©2023 Elsevier Ltd).

The computed forces $\overline{f_i^{th}}$ are transformed into fin oscillation amplitudes A_i^{osc} using the proposed inverse model in [Publication II].

The resulting fin oscillating amplitudes and zero-direction angles are allocated to the respective fins in an ascending order of i :

- RR, RL, and FL, when the FR fin is faulty.
- FR, RL, and FL, when the RR fin is faulty.
- FR, RR, and FL, when the RL fin is faulty.
- FR, RR, and RL, when the FL fin is faulty.

6.3 Experimental results and discussions

A series of validation experiments were performed in a laboratory pool with a depth of $1.30m$ (c.f. Fig. 28a). The setup includes a large grid of dimensions $3m \times 4m$ (cf. Fig 28b). The onboard camera captures images at a frequency of $10Hz$. Detected markers serve as the basis for actual position measurements in the Earth fixed frame R_n .

Given the shallow depth of the pool, constraints were placed on the range of motion for certain degrees of freedom. This limitation also impacts vision-based odometry, as marker detection becomes unreliable at greater depths. Consequently, a planar elliptical trajectory was selected as the reference trajectory for tracking.

It's crucial to underline that the FTC scheme doesn't operate in isolation but is part of a more comprehensive autonomy framework for the U-CAT AUV. As depicted in Figure 27, this framework encompasses a trajectory generator and two alternative controllers for comparative evaluation against the FTC controller: PID and Sliding Mode. Once the zero-direction angles and forces are ascertained via the FTC controller, these forces undergo conversion into oscillation amplitudes, courtesy of the model delineated in Section 4. To guarantee smooth transitions, a 2nd-order filter is employed for both the zero-direction angles and the oscillation amplitudes.

For readers keen on a more in-depth grasp of how these elements coalesce to facilitate precise control, additional insights are provided in [Publication III].

To assess the fault-tolerant control (FTC) scheme in conjunction with PID and SM controllers, a series of experimental scenarios were designed. These scenarios aim to evaluate the tracking performance of the proposed control allocation method under varying fin conditions. The scenarios are as follows:

- Scenario 1 (Nominal): In this case, all fins are operational, serving as the baseline for performance evaluation.
- Scenario 2 (RR): Here, the rear right fin is rendered nonfunctional, introducing a fault into the system.
- Scenario 3 (RL): In this scenario, the rear left fin is considered faulty.
- Scenario 4 (FL): The front left fin is assumed to be nonfunctional.
- Scenario 5 (FR): Lastly, the front right fin is considered to be out of operation.

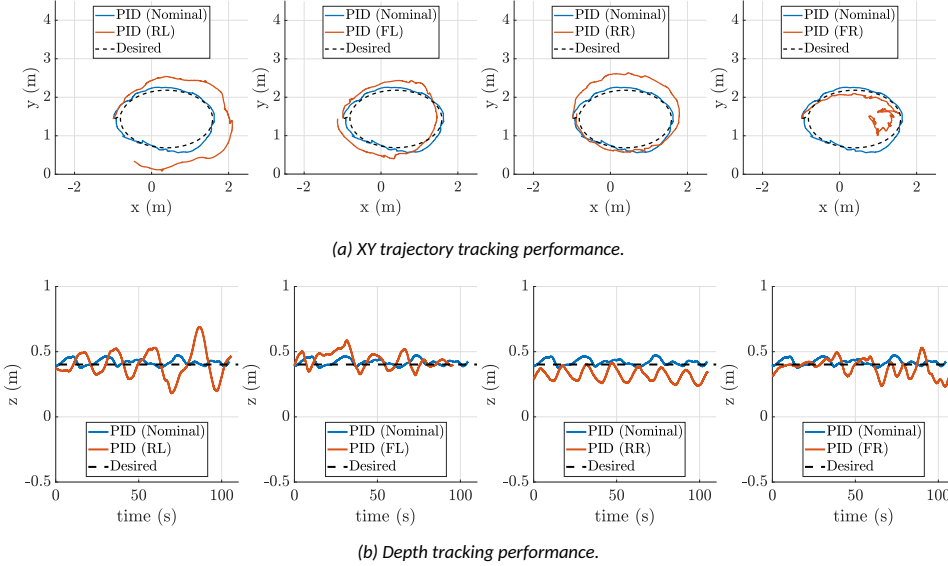


Figure 29: Trajectory tracking results across the different experimental scenarios using the PID controller. ([Publication III] ©2023 Elsevier Ltd).

In the first scenario, where all fins are operational, tracking of the desired trajectory is achieved with both PID and SM controllers, as evidenced by Figures 29 and 30. Notable is the increased oscillation in the zero-direction angle of the rear right fin when utilizing the PID controller, a phenomenon that primarily affects depth adjustments (Figure 31). In contrast, the PID SM controller exhibits reduced oscillations in the same parameter, leading to an improvement in tracking performance in terms of root mean square errors (RMS), as depicted in Figure 33.

For the second scenario, involving a faulty rear right fin, a decline in tracking performance is observed with the PID controller (Figure 29). This decline manifests as an offset in depth tracking accompanied by oscillations, attributable to the robot's positive buoyancy and the fins' limitations in generating adequate heave force without a configuration switch (Figure 31). On the other hand, the SM controller maintains relatively better tracking performance under the same faulty conditions, as shown in Figure 30. While depth tracking is somewhat compromised, the overall trajectory tracking remains within acceptable limits. A smoother profile for fin zero-directions is also observed (Figure 32).

In the third scenario, featuring a faulty rear left fin, a notable decline in tracking performance across all degrees of freedom is observed with the PID controller, as shown in

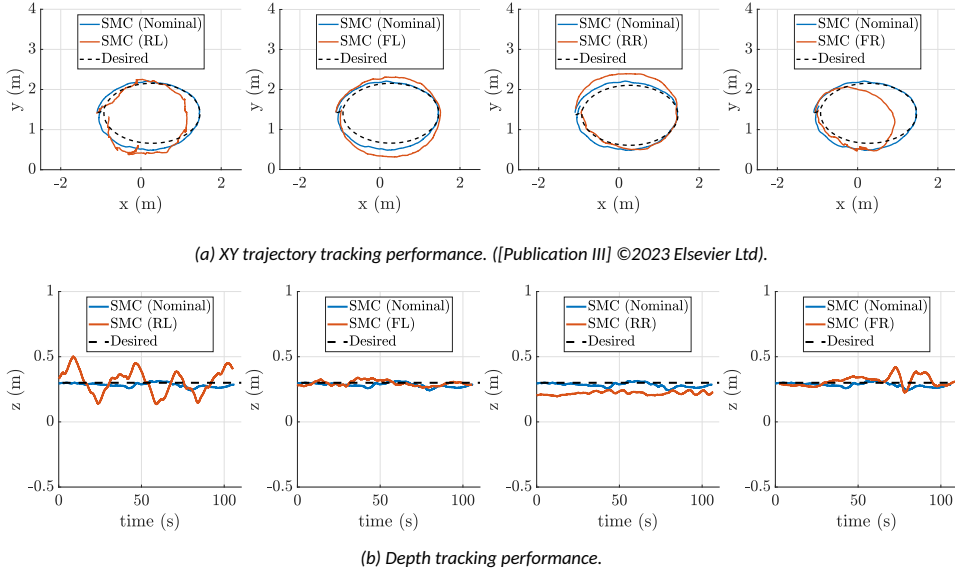


Figure 30: Trajectory tracking results across the different experimental scenarios using the SMC controller. ([Publication III] ©2023 Elsevier Ltd).

Figure 29. Given the rear left fin’s crucial role in heading adjustments for a clockwise trajectory, the PID controller compensates by generating control inputs that induce oscillatory behaviour in the fins’ zero-directions. Contrarily, the SM controller maintains superior tracking performance, as evidenced in Figures 30 and 33.

For the fourth scenario, which involves a faulty front left fin, a slight degradation in tracking performance relative to the nominal case is noted with the PID controller (Figure 29). As the front left fin is chiefly responsible for generating surge force, its loss predominantly affects the tracking of x , as indicated in Figure 33. Moreover, Figure 31 reveals that the rear right fin alters its orientation to π to compensate for the surge force and heading yaw adjustments. In contrast, the SM controller maintains commendable depth control and overall trajectory tracking (Figure 30). The zero-directions generated are notably smoother, contributing to improved performance, as depicted in Figure 32.

In the fifth scenario, characterized by a faulty front right fin, tracking the reference trajectory proves challenging for the PID controller, as evidenced in Figure 29. Given the front right fin’s dual role in surge force generation and heading adjustment for a clockwise trajectory, the remaining fins find it difficult to adequately compensate for the PID inputs. This is further illustrated in Figure 31, where the front left fin’s zero-direction undergoes frequent sign changes after the first 50 seconds, coinciding with a hard turn. Conversely, the SM controller manages to improve tracking performance across all degrees of freedom, as shown in Figure 30. While the front-right fin’s significance in tracking this specific trajectory is evident, the SM controller navigates the challenge more effectively than the PID controller.

In summary, the SM controller, when integrated with the proposed FTC scheme, yields satisfactory tracking performance even when fin failures occur. The outcomes validate the robot’s capability to adhere to the reference trajectory using only the three remaining, highly-coupled fins, eliminating the need for controller gain adjustments.

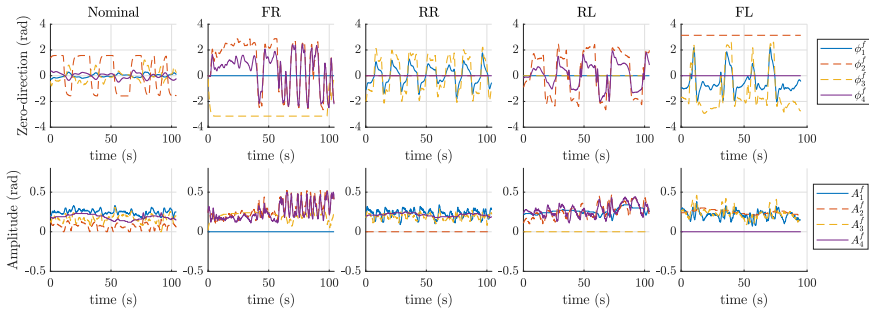


Figure 31: Time-series of the generated zero-direction angles and amplitudes for the different experimental scenarios using the PID controller. ([Publication III] ©2023 Elsevier Ltd).

Furthermore, the results attest to the efficacy of the proposed FTC scheme in managing actuation failures, even under the most challenging conditions for tracking the studied reference trajectory. This holds particular relevance for symmetrical robots with symmetrical designs, as the worst-case scenarios can be inferred based on the nature of the reference trajectory. Such insights are valuable for the development of high-level controllers that can adapt the reference trajectory to avoid worst-case scenarios.

6.4 Conclusions

This chapter addresses the complex issue of fault-tolerant control in a fin-actuated AUV, a system characterized by high coupling between actuators. An active fault-tolerant control scheme has been developed, featuring a control allocation switching mechanism. This mechanism effectively allocates control forces to operational fins in the event of a fault. Experimental validation was conducted through trajectory tracking tasks, employing two distinct control laws: PID and Sliding Mode Control. The findings suggest that the integration of a robust controller, such as Sliding Mode Control, with the proposed fault-tolerant control scheme, yields improved performance in handling faults, compared to using PID control alone. While the primary focus of this study is on the fault-tolerant control allocation strategy, it is acknowledged that real-world applications may involve specific distur-

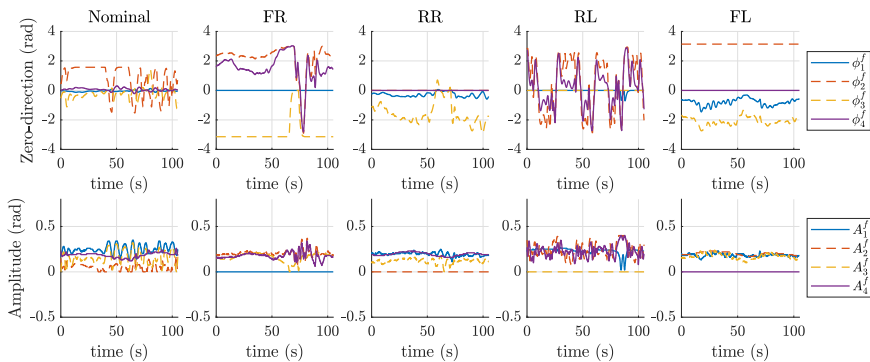


Figure 32: Time-series of the generated zero-direction angles and amplitudes for the different experimental scenarios using the SM controller. ([Publication III] ©2023 Elsevier Ltd).

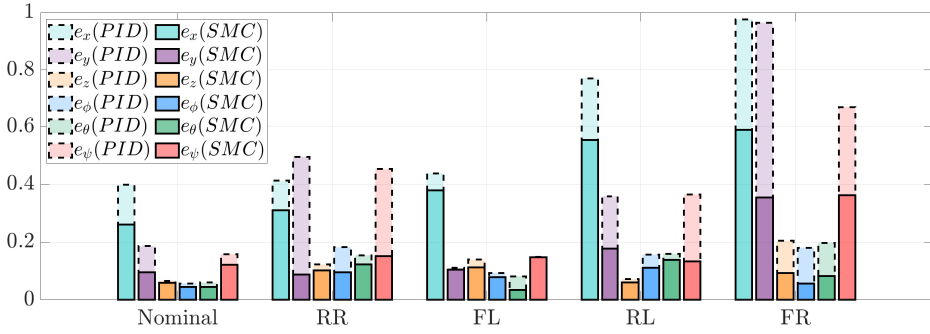


Figure 33: Bar plot of the RMS errors for trajectory tracking of all the studied scenarios. The errors for the position and orientation, expressed in meters and radians, respectively, are reported for a single trial for each case. ([Publication III] ©2023 Elsevier Ltd).

bances, such as sea currents. Although the current experimental setup does not explicitly account for such external disturbances, the analysis offers valuable insights into the scheme’s performance and robustness under actuator failure conditions.

The main contributions of this work are as follows:

- Development of an active fault-tolerant control scheme with a control allocation switching mechanism for a fin-actuated AUV with highly coupled actuators.
- Experimental validation of the proposed scheme through trajectory tracking tasks in a controlled environment.
- Comparative analysis of the scheme’s performance when using two different control laws: PID and Sliding Mode Control.
- Provision of insights into the scheme’s robustness and performance under actuator failure conditions.

7 Conclusions and future work

The primary aim of this thesis was to explore the complexities and offer solutions within the scopes of control, navigation, and fault tolerance for fin-actuated AUVs. The work is documented across Publications I to IV, corresponding to Sections 3 through 6 of this thesis.

Publication I and Section 3 addressed the challenge of diver tracking in underwater environments. A data-fusion-based control scheme was developed, integrating acoustic and visual signals. The work presented in this thesis offers a distinct advantage over existing methods [34, 35]. Specifically, the proposed data-fusion-based control scheme demonstrates increased robustness in tracking divers, irrespective of their presence in the camera's field of view (FOV). This is a notable improvement over the solutions presented in [43, 36], which rely on more expensive sensor setups. The proposed scheme underwent rigorous validation through open-water field experiments, providing evidence of its robustness and resilience.

In Publication II and Section 4, the nonlinear analytical model introduced in this thesis fills a gap in the existing literature. While previous studies [74] have proposed valid functions only within specific mass flow rate ranges, the model presented here is more universally applicable. Additionally, unlike the computational fluid dynamics approaches used in [53, 120], the proposed model is computationally efficient enough to run in real-time on robots with limited computing capabilities.

Publication IV and Section 5 presented a pioneering analytic control allocation method for fin-actuated AUVs. Most existing studies [56, 65, 66] have focused on propeller-based actuation systems and often involve over-actuated AUVs. In contrast, the proposed method is the first to fully control an under-actuated AUV in 6-DOF, marking a significant advancement in the field. The method underwent comprehensive testing in both simulated and real-world environments. The results indicated that the proposed solution balances computational efficiency and actuator energy usage for 6-DOF tracking in fin-actuated AUVs.

Publication III and Section 6 focused on the critical issue of fault tolerance in fin-actuated AUVs. An active fault-tolerant control scheme, among the first for fin-actuated AUVs, was developed, featuring a control allocation switching mechanism. While some work has been done on fault-tolerant control for bio-inspired robots [96], the study has been limited to heading control. The fault-tolerant control scheme proposed in this thesis manages control in 4DOFs, making it a more comprehensive solution.

While each chapter has its unique focus and contributions, they form a cohesive body of work that advances the understanding of fin-actuated AUVs. Although the experiments did not account for specific external disturbances like sea currents, the findings offer valuable insights into the performance and robustness of the proposed methods.

In summary, the thesis contributes to the existing literature by providing tested and validated methods for controlling and navigating fin-actuated AUVs. These contributions lay the groundwork for future research to develop more robust, efficient, and fault-tolerant underwater vehicles.

The research journey embarked upon in this thesis has illuminated several promising avenues for future exploration, particularly in the field of fin-actuated AUVs. One of the most compelling directions for future work lies in adaptive diver tracking. The data-fusion-based diver tracking scheme developed in this thesis has shown significant promise in enhancing the U-CAT AUV's capabilities. However, the system could benefit from incorporating adaptive algorithms that dynamically adjust the weighting between acoustic and visual signals based on real-time environmental conditions. Such an adaptive system could offer a more robust and reliable tracking mechanism, especially in challenging underwater

conditions where visibility is limited or acoustic signals are distorted.

Another intriguing area for future investigation is the concept of dynamic stiffness adjustment in the fins of the AUV. The nonlinear analytical model developed in this research provides a solid foundation for understanding the relationship between oscillation amplitude and frequency and the required thrust force. Extending this model to include dynamic stiffness adjustment mechanisms would allow the AUV to adapt its fin characteristics to varying underwater conditions in real-time. This could lead to significant improvements in the AUV's performance and energy efficiency, addressing one of the current limitations in fin-actuated AUV design.

The proposed control allocation method developed in this thesis has proven effective for 6-DOF tracking in fin-actuated AUVs. However, there's still room for further research in this context. One intriguing direction for future work is reconsidering the adopted method of minimising fin rotation. The research has shown that lateral fin forces are often more predominant than the generated thrust forces. This observation suggests that these lateral forces could be harnessed to enhance the AUV's manoeuvrability rather than being treated as a limitation to be minimised. Incorporating these lateral forces into the control allocation model could offer a more comprehensive understanding of the AUV's dynamics and provide new opportunities for control. This approach could lead to developing control schemes that take full advantage of the AUV's unique actuation capabilities, enabling exceptional manoeuvrability and adaptability in complex underwater environments. Such an advancement could be particularly beneficial in scenarios that require agile navigation and rapid decision-making.

References

- [1] Walid Remmas, Ahmed Chemori, and Maarja Kruusmaa. Diver tracking in open waters: A low-cost approach based on visual and acoustic sensor fusion. *Journal of Field Robotics*, 38(3):494–508, 2021.
- [2] Walid Remmas, Ahmed Chemori, and Maarja Kruusmaa. Inverse-model intelligent control of fin-actuated underwater robots based on drag force propulsion. *Ocean Engineering*, 239:109883, 2021.
- [3] Walid Remmas, Ahmed Chemori, and Maarja Kruusmaa. Fault-tolerant control allocation for a bio-inspired underactuated auv in the presence of actuator failures: Design and experiments. *Ocean Engineering*, 15(20):54–66, 2023.
- [4] Walid Remmas, Christian Meurer, Ahmed Chemori, and Maarja Kruusmaa. Control Allocation for 6-DOF Control of a Highly Manoeuvrable Under-actuated Bio-inspired AUV. *Submitted to IEEE Transactions on Robotics*, 2023.
- [5] Walid Remmas, Roza Gkliva, and Asko Ristolainen. Dynamic modelling of a screw actuator for improved locomotion control on various terrains. In *EGU General Assembly Conference Abstracts*, pages EGU22–5726, 2022.
- [6] Michael S Triantafyllou, Alexandra H Techet, and Franz S Hover. Review of experimental work in biomimetic foils. *IEEE Journal of Oceanic Engineering*, 29(3):585–594, 2004.
- [7] Naga Praveen Babu Mannam, Md MahbubAlam, and P Krishnankutty. Review of biomimetic flexible flapping foil propulsion systems on different planetary bodies. *Results in Engineering*, page 100183, 2020.
- [8] AM Aminur RB, B Hemakumar, and MPR Prasad. Robotic fish locomotion & propulsion in marine environment: A survey. In *2018 2nd International Conference on Power, Energy and Environment: Towards Smart Technology (ICEPE)*, pages 1–6. IEEE, 2018.
- [9] David Scaradozzi, Giacomo Palmieri, Daniele Costa, and Antonio Pinelli. Bcf swimming locomotion for autonomous underwater robots: a review and a novel solution to improve control and efficiency. *Ocean Engineering*, 130:437–453, 2017.
- [10] Kristi A Morgansen, Benjamin I Triplett, and Daniel J Klein. Geometric methods for modeling and control of free-swimming fin-actuated underwater vehicles. *IEEE Transactions on Robotics*, 23(6):1184–1199, 2007.
- [11] Li Wen, Tianmiao Wang, Guanhao Wu, Jianhong Liang, and Chaolei Wang. Novel method for the modeling and control investigation of efficient swimming for robotic fish. *IEEE Transactions on Industrial Electronics*, 59(8):3176–3188, 2011.
- [12] Christina Georgiades, Meyer Nahon, and Martin Buehler. Simulation of an underwater hexapod robot. *Ocean Engineering*, 36(1):39–47, 2009.
- [13] Stephen Licht, Franz Hover, and Michael S Triantafyllou. Design of a flapping foil underwater vehicle. In *Proceedings of the 2004 International Symposium on Underwater Technology (IEEE Cat. No. 04EX869)*, pages 311–316. IEEE, 2004.

- [14] Junzhi Yu and Long Wang. Parameter optimization of simplified propulsive model for biomimetic robot fish. In *Proceedings of the 2005 IEEE International Conference on Robotics and Automation*, pages 3306–3311. IEEE, 2005.
- [15] Md Jahidul Islam, Marc Ho, and Junaed Sattar. Understanding human motion and gestures for underwater human-robot collaboration. *Journal of Field Robotics*, 36(5):851–873, 2019.
- [16] N. Mišković, M. Bibuli, A. Birk, M. Caccia, M. Egi, K. Grammer, A. Marroni, J. Neasham, A. Pascoal, A. Vasilijević, and Z. Vukić. Overview of the fp7 project “caddy — cognitive autonomous diving buddy”. In *OCEANS 2015 - Genova*, pages 1–5, 2015.
- [17] Arturo Gomez Chavez, Andrea Ranieri, Davide Chiarella, Enrica Zereik, Anja Babić, and Andreas Birk. Caddy underwater stereo-vision dataset for human-robot interaction (hri) in the context of diver activities. *Journal of Marine Science and Engineering*, 7(1):16, 2019.
- [18] P. Ren, W. Fang, and S. Djahel. A novel yolo-based real-time people counting approach. In *2017 International Smart Cities Conference (ISC2)*, pages 1–2, 2017.
- [19] K. Kakinuma, M. Hashimoto, and K. Takahashi. Outdoor pedestrian tracking by multiple mobile robots based on slam and gps fusion. In *2012 IEEE/SICE International Symposium on System Integration (SII)*, pages 422–427, 2012.
- [20] K. K. Lekkala and V. K. Mittal. Simultaneous aerial vehicle localization and human tracking. In *2016 IEEE Region 10 Conference (TENCON)*, pages 379–383, 2016.
- [21] M. Yagimli and H. S. Varol. A gps-based system design for the recognition and tracking of moving targets. In *2009 4th International Conference on Recent Advances in Space Technologies*, pages 6–12, 2009.
- [22] J. Zou and Y. Tseng. Visual track system applied in quadrotor aerial robot. In *2012 Third International Conference on Digital Manufacturing Automation*, pages 1025–1028, 2012.
- [23] S. Q. Duntley. Light in the sea*. *J. Opt. Soc. Am.*, 53(2):214–233, 1963.
- [24] Son-Cheol Yu, T. Ura, T. Fujii, and H. Kondo. Navigation of autonomous underwater vehicles based on artificial underwater landmarks. In *MTS/IEEE Oceans 2001. An Ocean Odyssey. Conference Proceedings (IEEE Cat. No.01CH37295)*, volume 1, pages 409–416 vol.1, 2001.
- [25] G. Dudek, M. Jenkin, C. Prahacs, A. Hogue, J. Sattar, P. Giguere, A. German, Hui Liu, S. Saunderson, A. Ripsman, S. Simhon, L. . Torres, E. Milios, P. Zhang, and I. Rekletis. A visually guided swimming robot. In *2005 IEEE/RSJ International Conference on Intelligent Robots and Systems*, pages 3604–3609, 2005.
- [26] K. M. Han and H. T. Choi. Shape context based object recognition and tracking in structured underwater environment. In *2011 IEEE International Geoscience and Remote Sensing Symposium*, pages 617–620, 2011.

- [27] Pan-Mook Lee, Bong-Hwan Jeon, and Sea-Moon Kim. Visual servoing for underwater docking of an autonomous underwater vehicle with one camera. In *Oceans 2003. Celebrating the Past ... Teaming Toward the Future (IEEE Cat. No.03CH37492)*, volume 2, pages 677–682 Vol.2, 2003.
- [28] D. Kim, D. Lee, H. Myung, and H. Choi. Object detection and tracking for autonomous underwater robots using weighted template matching. In *2012 Oceans - Yeosu*, pages 1–5, 2012.
- [29] Y. LeCun, Y. Bengio, and G. Hinton. Deep learning. In *Nature*, volume 521.7553, pages 436–444, 2015.
- [30] Joseph Redmon and Ali Farhadi. Yolov3: An incremental improvement. *arXiv*, 2018.
- [31] Yanghao Li, Yuntao Chen, Naiyan Wang, and Zhaoxiang Zhang. Scale-aware trident networks for object detection. *arXiv preprint arXiv:1901.01892*, 2019.
- [32] Yue Cao, Jiarui Xu, Stephen Lin, Fangyun Wei, and Han Hu. Gcnet: Non-local networks meet squeeze-excitation networks and beyond. *arXiv preprint arXiv:1904.11492*, 2019.
- [33] Kaiwen Duan, Song Bai, Lingxi Xie, Honggang Qi, Qingming Huang, and Qi Tian. Centernet: Keypoint triplets for object detection. In *Proceedings of the IEEE International Conference on Computer Vision*, pages 6569–6578, 2019.
- [34] M. J. Islam, M. Fulton, and J. Sattar. Toward a generic diver-following algorithm: Balancing robustness and efficiency in deep visual detection. *IEEE Robotics and Automation Letters*, 4(1):113–120, Jan 2019.
- [35] F. Shkurti, W. Chang, P. Henderson, M. J. Islam, J. C. G. Higuera, J. Li, T. Manderson, A. Xu, G. Dudek, and J. Sattar. Underwater multi-robot convoying using visual tracking by detection. In *2017 IEEE/RSJ International Conference on Intelligent Robots and Systems (IROS)*, pages 4189–4196, Sep. 2017.
- [36] P. O. Cardozo, M. Machado dos Santos, P. Lilles, and S. Silva. Forward looking sonar scene matching using deep learning. In *2017 16th IEEE International Conference on Machine Learning and Applications (ICMLA)*, pages 574–579, 2017.
- [37] S. Kamal, S. K. Mohammed, P. R. S. Pillai, and M. H. Supriya. Deep learning architectures for underwater target recognition. In *2013 Ocean Electronics (SYMPOL)*, pages 48–54, 2013.
- [38] S. Lee. Deep learning of submerged body images from 2d sonar sensor based on convolutional neural network. In *2017 IEEE Underwater Technology (UT)*, pages 1–3, 2017.
- [39] Y. Song, Y. Zhu, G. Li, C. Feng, B. He, and T. Yan. Side scan sonar segmentation using deep convolutional neural network. In *OCEANS 2017 - Anchorage*, pages 1–4, 2017.
- [40] James Preisig. Acoustic propagation considerations for underwater acoustic communications network development. *ACM SIGMOBILE Mobile Computing and Communications Review*, 11(4):2–10, 2007.
- [41] Finn B Jensen, William A Kuperman, Michael B Porter, and Henrik Schmidt. *Computational ocean acoustics*. Springer Science & Business Media, 2011.

- [42] Arturo Gomez Chavez, Christian A Mueller, Andreas Birk, Anja Babic, and Nikola Miskovic. Stereo-vision based diver pose estimation using lstm recurrent neural networks for auv navigation guidance. In *OCEANS 2017-Aberdeen*, pages 1–7. IEEE, 2017.
- [43] Filip Mandić, Ivor Rendulić, Nikola Mišković, and Đula Nađ. Underwater object tracking using sonar and usbl measurements. *Journal of Sensors*, 2016, 2016.
- [44] S. C. Licht. *Biomimetic oscillating foil propulsion to enhance underwater vehicle agility and maneuverability*. DTIC Document, 2008.
- [45] Taavi Salumäe, Ahmed Chemori, and Maarja Kruusmaa. Motion control architecture of a 4-fin u-cat auv using dof prioritization. In *2016 IEEE/RSJ International Conference on Intelligent Robots and Systems (IROS)*, pages 1321–1327. IEEE, 2016.
- [46] N. Plamondon and M. Nahon. Adaptive controller for a biomimetic underwater vehicle. *Journal of Unmanned Vehicle Systems*, 1:1–13, 2013.
- [47] Ahmed Chemori, Keijo Kuusmik, T Salumäe, and Maarja Kruusmaa. Depth control of the biomimetic u-cat turtle-like auv with experiments in real operating conditions. In *2016 IEEE International Conference on Robotics and Automation (ICRA)*, pages 4750–4755. IEEE, 2016.
- [48] G. Yao and et al. Development of a turtle-like underwater vehicle using central pattern generator. In *IEEE International Conference on Robotics and Biomimetics (ROBIO)*, pages 44–49, Shenzhen, China, 2013.
- [49] Cafer Bal, Gonca Ozmen Koca, Deniz Korkmaz, Zuhtu Hakan Akpolat, and Mustafa Ay. Cpg-based autonomous swimming control for multi-tasks of a biomimetic robotic fish. *Ocean Engineering*, 189:106334, 2019.
- [50] N Plamondon and M Nahon. A trajectory tracking controller for an underwater hexapod vehicle. *Bioinspiration & biomimetics*, 4(3):036005, 2009.
- [51] Philippe Giguere, Chris Prahacs, and Gregory Dudek. Characterization and modeling of rotational responses for an oscillating foil underwater robot. In *2006 IEEE/RSJ International Conference on Intelligent Robots and Systems*, pages 3000–3005. IEEE, 2006.
- [52] Subramanian Ramasamy and Sahjendra N Singh. Biology-inspired robust dive plane control of non-linear auv using pectoral-like fins. *Applied Bionics and Biomechanics*, 7(2):153–168, 2010.
- [53] Sahjendra N Singh, Aditya Simha, and Rajat Mittal. Biorobotic auv maneuvering by pectoral fins: inverse control design based on cfd parameterization. *IEEE Journal of Oceanic Engineering*, 29(3):777–785, 2004.
- [54] Jason D Geder, Ravi Ramamurti, Marius Pruessner, and John Palmisano. Maneuvering performance of a four-fin bio-inspired uuv. In *2013 OCEANS-San Diego*, pages 1–7. IEEE, 2013.
- [55] Karen A Harper, Matthew D Berkemeier, and Sheryl Grace. Modeling the dynamics of spring-driven oscillating-foil propulsion. *IEEE Journal of Oceanic Engineering*, 23(3):285–296, 1998.

- [56] Tor A Johansen and Thor I Fossen. Control allocation—a survey. *Automatica*, 49(5):1087–1103, 2013.
- [57] Wayne C Durham. Constrained control allocation. *Journal of Guidance, control, and Dynamics*, 16(4):717–725, 1993.
- [58] Michael W Oppenheimer, David B Doman, and Michael A Bolender. Control allocation for over-actuated systems. In *2006 14th Mediterranean Conference on Control and Automation*, pages 1–6. IEEE, 2006.
- [59] Richard J Adams, James M Buffington, Andrew G Sparks, and Siva S Banda. *Robust multivariable flight control*. Springer Science & Business Media, 2012.
- [60] James M Buffington and Dale F Enns. Lyapunov stability analysis of daisy chain control allocation. *Journal of Guidance, Control, and Dynamics*, 19(6):1226–1230, 1996.
- [61] Marc Bodson. Evaluation of optimization methods for control allocation. *Journal of Guidance, Control, and Dynamics*, 25(4):703–711, 2002.
- [62] Joseph A Paradiso. Adaptable method of managing jets and aerosurfaces for aerospace vehicle control. *Journal of Guidance, Control, and Dynamics*, 14(1):44–50, 1991.
- [63] Ola Harkegard. Efficient active set algorithms for solving constrained least squares problems in aircraft control allocation. In *Proceedings of the 41st IEEE Conference on Decision and Control, 2002.*, volume 2, pages 1295–1300. IEEE, 2002.
- [64] John AM Petersen and Marc Bodson. Constrained quadratic programming techniques for control allocation. *IEEE Transactions on Control Systems Technology*, 14(1):91–98, 2005.
- [65] Sangrok Jin, Jihoon Kim, Jongwon Kim, and TaeWon Seo. Six-degree-of-freedom hovering control of an underwater robotic platform with four tilting thrusters via selective switching control. *IEEE/ASME Transactions on mechatronics*, 20(5):2370–2378, 2015.
- [66] Jeongae Bak, Yecheol Moon, Jongwon Kim, Santhakumar Mohan, TaeWon Seo, and Sangrok Jin. Hovering control of an underwater robot with tilting thrusters using the decomposition and compensation method based on a redundant actuation model. *Robotics and Autonomous Systems*, 150:103995, 2022.
- [67] Akihisa Konno, Takuro Furuya, Akisato Mizuno, Kazuhisa Hishinuma, Koichi Hirata, and Masakuni Kawada. Development of turtle-like submergence vehicle. In *Proceedings of the 7th international symposium on marine engineering*, 2005.
- [68] Kin-Huat Low, Chunlin Zhou, TW Ong, and Junzhi Yu. Modular design and initial gait study of an amphibian robotic turtle. In *2007 IEEE International Conference on Robotics and Biomimetics (ROBIO)*, pages 535–540. IEEE, 2007.
- [69] Wei Zhao, Yonghui Hu, Long Wang, and Yingmin Jia. Development of a flipper propelled turtle-like underwater robot and its cpq-based control algorithm. In *2008 47th IEEE Conference on Decision and Control*, pages 5226–5231. IEEE, 2008.

- [70] Guocai Yao, Jianhong Liang, Tianmiao Wang, Xingbang Yang, Qi Shen, Yucheng Zhang, Hailiang Wu, and Weicheng Tian. Development of a turtle-like underwater vehicle using central pattern generator. In *2013 IEEE International Conference on Robotics and Biomimetics (ROBIO)*, pages 44–49. IEEE, 2013.
- [71] Caiwang Wang, Guangming Xie, Xinyan Yin, Liang Li, and Long Wang. Cpg-based locomotion control of a quadruped amphibious robot. In *2012 IEEE/ASME International Conference on Advanced Intelligent Mechatronics (AIM)*, pages 1–6. IEEE, 2012.
- [72] Stephen C Licht. Biomimetic oscillating foil propulsion to enhance underwater vehicle agility and maneuverability. Technical report, WOODS HOLE OCEANOGRAPHIC INSTITUTION MA, 2008.
- [73] Cédric Siegenthaler, Cédric Pradalier, Fabian Günther, Gregory Hitz, and Roland Siegwart. System integration and fin trajectory design for a robotic sea-turtle. In *2013 IEEE/RSJ International Conference on Intelligent Robots and Systems*, pages 3790–3795. IEEE, 2013.
- [74] Nicolas Plamondon. *Modeling and control of a biomimetic underwater vehicle*. PhD thesis, McGill University, 2010.
- [75] Philippe Giguere, Yogesh Girdhar, and Gregory Dudek. Wide-speed autopilot system for a swimming hexapod robot. In *2013 International Conference on Computer and Robot Vision*, pages 9–15. IEEE, 2013.
- [76] T. Salumäe, A. Chemori, and M. Kruusmaa. Motion control of a hovering biomimetic four-fin underwater robot. *IEEE Journal of Oceanic Engineering*, 44(1):54–71, 2019.
- [77] David A Smallwood and Louis L Whitcomb. The effect of model accuracy and thruster saturation on tracking performance of model based controllers for underwater robotic vehicles: experimental results. In *Proceedings 2002 IEEE International Conference on Robotics and Automation (Cat. No. 02CH37292)*, volume 2, pages 1081–1087. IEEE, 2002.
- [78] Thor I Fossen and Svein I Sagatun. Adaptive control of nonlinear systems: A case study of underwater robotic systems. *Journal of Robotic Systems*, 8(3):393–412, 1991.
- [79] Gianluca Antonelli, F Caccavle, Stefano Chiaverini, and Giuseppe Fusco. A novel adaptive control law for autonomous underwater vehicles. In *Proceedings 2001 ICRA. IEEE International Conference on Robotics and Automation (Cat. No. 01CH37164)*, volume 1, pages 447–452. IEEE, 2001.
- [80] Karl D von Ellenrieder. Stable backstepping control of marine vehicles with actuator rate limits and saturation. *IFAC-PapersOnLine*, 51(29):262–267, 2018.
- [81] Emil Fresk and George Nikolakopoulos. Full quaternion based attitude control for a quadrotor. In *2013 European control conference (ECC)*, pages 3864–3869. IEEE, 2013.
- [82] Silvain Louis, Lionel Lapierre, Yadpiroon Onmek, Karen Godary Dejean, Thomas Claverie, and Sebastien Villéger. Quaternion based control for robotic observation of marine diversity. In *OCEANS 2017-Aberdeen*, pages 1–7. IEEE, 2017.

- [83] Sanjay P Bhat and Dennis S Bernstein. A topological obstruction to continuous global stabilization of rotational motion and the unwinding phenomenon. *Systems & control letters*, 39(1):63–70, 2000.
- [84] Erlend Andreas Basso, Henrik M Schmidt-Didlaukies, Kristin Y Pettersen, and Asgeir Johan Sorensen. Global asymptotic tracking for marine vehicles using adaptive hybrid feedback. *IEEE Transactions on Automatic Control*, 2022.
- [85] Gianluca Antonelli. A survey of fault detection/tolerance strategies for auvs and rovs. In *Fault diagnosis and fault tolerance for mechatronic systems: Recent advances*, pages 109–127. Springer, 2003.
- [86] Fuqiang Liu, Hao Tang, Yi Qin, Chaoqun Duan, Jun Luo, and Huayan Pu. Review on fault diagnosis of unmanned underwater vehicles. *Ocean Engineering*, 243:110290, 2022.
- [87] Ihab Samy, Ian Postlethwaite, and Da-Wei Gu. Survey and application of sensor fault detection and isolation schemes. *Control Engineering Practice*, 19(7):658–674, 2011.
- [88] Lingli Ni. *Fault-tolerant control of unmanned underwater vehicles*. PhD thesis, Virginia Polytechnic Institute and State University, 2001.
- [89] Nilanjan Sarkar, Tarun Kanti Podder, and Gianluca Antonelli. Fault-accommodating thruster force allocation of an auv considering thruster redundancy and saturation. *IEEE Transactions on Robotics and Automation*, 18(2):223–233, 2002.
- [90] Edin Omerdic and Geoff Roberts. Thruster fault diagnosis and accommodation for open-frame underwater vehicles. *Control engineering practice*, 12(12):1575–1598, 2004.
- [91] Halim Alwi and Christopher Edwards. Fault tolerant control using sliding modes with on-line control allocation. *Automatica*, 44(7):1859–1866, 2008.
- [92] A Baldini, L Ciabattini, R Felicetti, F Ferracuti, A Monteriù, A Fasano, and A Freddi. Active fault tolerant control of remotely operated vehicles via control effort redistribution. In *International Design Engineering Technical Conferences and Computers and Information in Engineering Conference*, volume 58233, page V009T07A002. American Society of Mechanical Engineers, 2017.
- [93] Xiaofeng Liu, Mingjun Zhang, Xing Liu, and Wende Zhao. Finite-time extended state observe based fault tolerant control for autonomous underwater vehicle with unknown thruster fault. *Journal of Marine Science and Engineering*, 10(11):1624, 2022.
- [94] Yujia Wang, Philip A Wilson, Xing Liu, et al. Adaptive neural network-based backstepping fault tolerant control for underwater vehicles with thruster fault. *Ocean Engineering*, 110:15–24, 2015.
- [95] Gabriel D Weymouth. Biologically inspired force enhancement for maritime propulsion and maneuvering. *arXiv preprint arXiv:1609.06559*, 2016.
- [96] Yueqi Yang, Jian Wang, Zhengxing Wu, and Junzhi Yu. Fault-tolerant control of a cpg-governed robotic fish. *Engineering*, 4(6):861–868, 2018.

- [97] Benedetto Allotta, Riccardo Costanzi, Alessandro Ridolfi, Ovidio Salvetti, Marco Reggiannini, Maarja Kruusmaa, Taavi Salumae, David Mike Lane, Gordon Frost, Nikolaos Tsiogkas, et al. The arrows project: robotic technologies for underwater archaeology. In *IOP conference series: materials science and engineering*, volume 364, page 012088. IOP Publishing, 2018.
- [98] Taavi Salumäe, Rasmus Raag, Jaan Rebane, Andres Ernits, Gert Toming, Mart Ratas, and Maarja Kruusmaa. Design principle of a biomimetic underwater robot u-cat. In *2014 Oceans-St. John's*, pages 1–5. IEEE, 2014.
- [99] Thor I Fossen. Marine control systems—guidance, navigation, and control of ships, rigs and underwater vehicles. *Marine Cybernetics, Trondheim, Norway, Org. Number NO 985 195 005 MVA*, www.marinecybernetics.com, ISBN: 82 92356 00 2, 2002.
- [100] V. Creuze. Robots marins et sous-marins perception, modélisation, commande. *Techniques de l'ingénieur Applications en robotique*, 2014.
- [101] Michael S Triantafyllou. Strip theory of ship motions in the presence of a current. *Journal of Ship Research*, 24(01):40–44, 1980.
- [102] Anthony J Healey, SM Rock, Steven Cody, D Miles, and JP Brown. Toward an improved understanding of thruster dynamics for underwater vehicles. *IEEE Journal of oceanic Engineering*, 20(4):354–361, 1995.
- [103] Christina Georgiades, Andrew German, Andrew Hogue, Hui Liu, Chris Prahacs, Arlene Ripsman, Robert Sim, L-A Torres, Pifu Zhang, Martin Buehler, et al. Aqua: an aquatic walking robot. In *2004 IEEE/RSJ International Conference on Intelligent Robots and Systems (IROS)(IEEE Cat. No. 04CH37566)*, volume 4, pages 3525–3531. IEEE, 2004.
- [104] Ziyu Ren, Tianmiao Wang, and Li Wen. Hydrodynamic function of a robotic fish caudal fin: effect of kinematics and flow speed. In *2015 IEEE/RSJ International Conference on Intelligent Robots and Systems (IROS)*, pages 3882–3887. IEEE, 2015.
- [105] R. E. Kalman. A new approach to linear filtering and prediction problems. *Journal of Basic Engineering*, 82(1):35, 1960.
- [106] E. H. Mamdani and N. Baaklini. Prescriptive method for deriving control policy in a fuzzy-logic controller. *Electronics Letters*, 11(25):625–626, 1975.
- [107] M. Sfakiotakis, DM. Lane, and JBC. Davies. Review of fish swimming modes for aquatic locomotion. *IEEE Journal of Oceanic Engineering*, 24(2):237–252, 1999.
- [108] A. Azuma. Swimming by Fanning. *American Institute of Aeronautics and Astronautics.*, pages 313–386, 2006.
- [109] K Kikuchi, Y Uehara, Y Kubota, and O Mochizuki. Morphological considerations of fish fin shape on thrust generation. *Journal of Applied Fluid Mechanics*, vol. 7(No. 4):625–632, 2014.
- [110] H. Schlichting. Boundary-layer theory. *New York: McGraw-Hill*, 1979.

- [111] Roza Gkliva, Michael Sfakiotakis, and Maarja Kruusmaa. Development and experimental assessment of a flexible robot fin. In *2018 IEEE International Conference on Soft Robotics (RoboSoft)*, pages 208–213. IEEE, 2018.
- [112] Paul T Boggs and Jon W Tolle. Sequential quadratic programming. *Acta numerica*, 4:1–51, 1995.
- [113] R. Bracewell. *The Fourier Transform and its Applications, 3rd ed.* New York: McGraw-Hill, 2000.
- [114] Narcís Palomeras, Sharad Nagappa, David Ribas, Nuno Gracias, and Marc Carreras. Vision-based localization and mapping system for auv intervention. In *2013 MTS/IEEE OCEANS-Bergen*, pages 1–7. IEEE, 2013.
- [115] Thor I Fossen. *Handbook of marine craft hydrodynamics and motion control.* John Wiley & Sons, 2011.
- [116] Musa Morena Marcusso Manhaes, Sebastian A Scherer, Luiz Ricardo Douat, Martin Voss, and Thomas Rauschenbach. Use of simulation-based performance metrics on the evaluation of dynamic positioning controllers. In *OCEANS 2017-Aberdeen*, pages 1–8. IEEE, 2017.
- [117] Keith C Yang, Junku Yuh, and Song K Choi. Experimental study of fault-tolerant system design for underwater robots. In *Proceedings. 1998 IEEE International Conference on Robotics and Automation (Cat. No. 98CH36146)*, volume 2, pages 1051–1056. IEEE, 1998.
- [118] Jagadeesh Kadiyam, Anjali Parashar, Santhakumar Mohan, and Devendra Deshmukh. Actuator fault-tolerant control study of an underwater robot with four rotatable thrusters. *Ocean Engineering*, 197:106929, 2020.
- [119] Roger Penrose. A generalized inverse for matrices. In *Mathematical proceedings of the Cambridge philosophical society*, volume 51, pages 406–413. Cambridge University Press, 1955.
- [120] J. D. Geder and et al. Maneuvering performance of a four-fin bio-inspired uuv. In *Oceans-San Diego*, pages 1–7, 2013.

Acknowledgments

As I reflect on my PhD journey, I feel immense gratitude towards all the incredible individuals who have been a part of this experience. I want to thank Dr. Ahmed Chemori and Prof. Maarja Kruusmaa for their exceptional mentorship and for welcoming me into their respective research labs. I genuinely appreciate your support in enabling me to conduct my research independently and autonomously, and I am grateful for your trust and confidence in me. Thank you also for providing such an encouraging research environment, full of learning opportunities. I would also like to thank everyone at the Centre for Biorobotics, whose skills, talent, and eagerness to share knowledge created an environment rich in learning and collaboration. The friendship and teamwork in the lab have been invaluable.

A special thank you goes to Christian and Roza. You have been more than colleagues; you've been mentors and dear friends. The times we've spent together, from teaching to hiking and exploring Estonia, have been some of the most memorable moments of my time at our lab.

I want to express my deepest gratitude to my parents, Mustapha and Kheira, whose unwavering love and support have been my foundation, guiding me through challenges and inspiring me to persevere, you have been my constant source of strength and motivation. To Madjda, my life partner, thank you for your love, understanding, and support, which have been my sanctuary. You've brought joy, balance, and deep fulfilment to my life. Your presence has been a guiding light through this journey. To my siblings, Wassim and Nawel, thank you for always being there for me and believing in me, your support means everything to me.

To Anis, Calix, Hafid, Dr Hakim, Hicham, Lacen, Mhammed, Oussama, Raouf, Yacine, and Zinou, even though we are kilometres apart, your friendship has meant so much to me, and I hold the memories we've shared close to my heart. To Anees, Ikram, Ines, and Karl, thank you for welcoming me into your circle and making Estonia a place of warmth and friendship. Finally, to my teammates at Rumori Calcio, the football field has been a place of friendship, fun, and relaxation. Playing alongside you has been an integral part of my life in Estonia, offering a sense of community and unforgettable experiences.

This thesis was made possible with financial support from:

- the European Union's Research and Innovation programme Horizon 2020 project ROBOMINERS (grant agreement 820971).
- the Estonian Centre of Excellence in ICT Research project EXCITE (TAR16013).
- the IUT institutional research funding of the Estonian Ministry of Education and Research "Bio-inspired underwater robots" (IUT33-9).
- the ROBOTURTLE KIM Sea & Coast Research project.
- the Archimedes Foundation (Sihtasutus Archimedes) with the Dora+ short-term mobility scholarship programme.

Abstract

Traditional propeller-driven AUVs have been instrumental for underwater applications, but their limitations in agility are becoming increasingly evident. This thesis rigorously investigates the capabilities of fin-actuated AUVs, which draw inspiration from the locomotion principles of marine life.

The thesis begins by addressing a critical challenge in underwater operations: the robust and accurate tracking of divers. Existing methodologies often need better visibility conditions and can be expensive. A diver tracking system that capitalises on fin-actuated AUVs' agility and safety advantages is introduced to overcome these limitations. By synergistically integrating visual and acoustic data from low-cost sensors, the system achieves enhanced tracking accuracy, making it both cost-effective and safe for operations involving divers.

Transitioning from diver tracking, the thesis addresses a gap in the current literature concerning the locomotion dynamics of fin-actuated AUVs. Specifically, models that relate fin actuation parameters to generated thrust that can be easily inverted for control purposes are lacking. A nonlinear dynamic model is proposed to capture the relationship between fin thrust and its oscillation parameters. Empirically validated, this model serves as the foundation for developing an inverse model, offering a novel approach to vehicle control.

Control precision is a critical aspect of AUV operations. Traditional AUVs face challenges in achieving 6-DOF (Degrees of Freedom) control, particularly when constrained by a limited number of actuators. A novel 6-DOF control method tailored for fin-actuated AUVs is presented. This method enables intricate underwater motions, achieving 6-DOF control with only four actuators, a significant advancement in the field.

The necessity for fault-tolerant control in underwater robotics extends beyond academic interest; it is critical for real-world missions. Given the harsh and unpredictable underwater conditions, actuator failures are not uncommon. A single fin failure can severely impede the vehicle's operational capabilities for fin-actuated AUVs. The thesis introduces an active fault-tolerant control scheme designed explicitly for fin-actuated AUVs. The scheme features a control allocation switching mechanism that adaptively redistributes control forces among the fins in the event of a failure.

In conclusion, the thesis offers a comprehensive study on fin-actuated AUVs, covering perception, modelling, and control aspects. Each contribution addresses a specific challenge and lays the groundwork for future advancements in underwater robotics. The experimentally validated results underscore the potential utility of fin-actuated AUVs in complex underwater exploration and operations.

Kokkuvõte

Traditsioonilised propelleritega autonoomsed veealused sõidukid (AVS) on olnud veealuste rakenduste jaoks tähtsad, kuid nende liikuvuse puudujäägid muutuvad üha ilmsemaks. Käesolevas väitekirjas uuritakse põhjalikult uimetäituritega AVSi võimeid, mis on ammutanud inspiratsiooni mereelustiku liikumisviisidest.

Käesolev doktoritöös võetakse esmalt vaatluse alla veealustes operatsioonides kriitilise tähtsusega väljakutse: sukeldujate robustne ja täpne jälgimine. Olemasolevate meetodite puudujääkideks on otsene sõltuvus nähtavusest ning nende kallidus. Nende piirangute ületamiseks tutvustatakse antud töös sukeldujate jälgimissüsteemi, mis kasutab ära uimedega AVS eeliseid liikuvuse ja ohutuse osas. Odavate visuaalsete ja akustiliste sensorite andmete sünergilise integreerimisega loodi süsteem, mis oli suurema jälgimistäpsusega ning muutis selle sukeldujatega seotud operatsioonide jaoks nii kulutasuvamaks kui ka ohutumaks.

Sukeldujate jälgimise järel adresseeritakse käesolevas töös lünka kirjanduses, mis käsitleb uimedega AVSide liikumisviisi dünaamikat. Täpsemalt, puuduvad mudelid, mis seoks omavahel uime käitamise parameetreid tekitatud tõukejõuga ning mida saab juhtimise eesmärgil hõlpsasti inverteerida. Antud töös luuakse mittelineaarne dünaamiline mudel, mis seob omavahel uime tõukejõud ja selle vonkeparameetri. Empiirilisel valideeritud mudel on aluseks pöördmudeli väljatöötamisel, mis pakub uutset lähenemist antud töös käsitletud allveesõidukite juhtimisel.

Juhtimise täpsus on AVSide opereerimisel kriitiline aspekt. Traditsiooniliste AVSide puhul on 6-vabadusastmeline juhtimise saavutamine keeruline, eriti piiratud arvu aktuaatorite korral. Antud töös pakutakse uudne 6-vabadusastmeline juhtimismeetod, mis on kohandatud uimedega AVSide jaoks. Antud meetod võimaldab saavutada keerukaid veealuseid liikumisi, saavutades 6-vabadusastmeline juhtimise vaid nelja aktuaatoriga, mis on märkimisväärne edasimineku antud valdkonnas.

Vajadus tõrkekindla juhtimise järele veealuses robotikas ulatub akadeemilisest huvist kaugemale; see on kriitilise tähtsusega ka reaalsetes rakendustes. Võttes arvesse karmid ja ettearvamatud veealused tingimused, ei ole aktuaatorite tõrked sugugi haruldased. Ühe täituri rike võib tõsiselt häirida uimedega AVS opereerimisvõimet. Käesolevas töös tutvustatakse aktiivset tõrkekindlat juhtimisskeemi, mis on loodud spetsiaalselt uimedega AVSide jaoks. Antud juhtimisskeem sisaldab juhtimissüsteemi ümberlülitamise mehhanisme, mis jaotab vea korral täitursüsteemi tõukejõud uimedele adaptiivselt ümber.

Kokkuvõtteks, pakub käesolev väitekirj põhjaliku uurimuse uimedega AVSide kohta, käsitledes seejuures tajumise, modelleerimise ja juhtimise aspekte. Iga antud töö osa adresseerib konkreetset probleemi ja paneb aluse tulevastele arendustele veealuse robotika valdkonnas. Eksperimentaalselt valideeritud tulemused rõhutavad uimedega autonoomsete allvee robotite rakenduseeliseid keerukates veealustes uuringutes ja rakendustes.

Appendix 1: Publication I

Publication I:

Walid Remmas, Ahmed Chemori, and Maarja Kruusmaa. Diver tracking in open waters: A low-cost approach based on visual and acoustic sensor fusion. *Journal of Field Robotics*, 38(3):494–508, 2021

Diver tracking in open waters: A low-cost approach based on visual and acoustic sensor fusion

Walid Remmas^{1,2}  | Ahmed Chemori² | Maarja Kruusmaa¹

¹Department of Computer Systems, Tallinn University of Technology, Tallinn, Estonia

²Laboratoire d'Informatique, de Robotique et de Micro-électronique de Montpellier, University of Montpellier, CNRS, Montpellier, France

Correspondence

Walid Remmas, Department of Computer Systems, Tallinn University of Technology, Ehitajate tee 5, 12616 Tallinn, Estonia.
Email: walid.remmas@taltech.ee

Funding information

Estonian Research Competency Council, Grant/Award Number: IUT-339

Abstract

The design of a robust perception method is a substantial component towards achieving underwater human–robot collaboration. However, in complex environments such as the oceans, perception is still a challenging issue. Data-fusion of different sensing modalities can improve perception in dynamic and unstructured ocean environments. This study addresses the control of a highly maneuverable autonomous underwater vehicle for diver tracking based on visual and acoustic signals data fusion measured by low-cost sensors. The underwater vehicle U-CAT tracks a diver using a 3-degree-of-freedom fuzzy logic Mamdani controller. The proposed tracking approach was validated through open water real-time experiments. Combining acoustic and visual signals for underwater target tracking provides several advantages compared to previously done related research. The obtained results suggest that the proposed solution ensures effective detection and tracking in poor visibility operating conditions.

KEYWORDS

collaborative robotics, computer vision, data-fusion, diver tracking, underwater robotics

1 | INTRODUCTION

Research on collaborative robots (Colgate et al., 1996), has brought humans and robots to share the same workspace. Combining the high accuracy and speed of robots with the expertise of humans, cobots are used to reduce high-risk and/or laborious work requiring human intervention, thus, reducing work-related accidents. Collaborative robots are used in various applications, such as in industry (Hentout et al., 2019) for manufacturing and assembling, in robotics for rehabilitation (Aggogeri et al., 2019) nursing (Robinson et al., 2014), and in space exploration (Bernard et al., 2018).

Underwater human–robot collaboration is another potential application in this field of research (GomezChavez et al., 2019; Islam et al., 2019; Mišković et al., 2015). On one side, the autonomy of underwater robots is still limited, due to the fact that most of the communication and localization technology developed for on-land applications is impractical under water. On the other side, humans have relatively limited payload capacity, limited diving time, and cannot risk to go in confined spaces. Therefore, autonomous

underwater vehicles (AUVs) could be used in underwater missions to help divers, carrying extra payload, collecting data and samples, taking footage of the inspected area, performing photogrammetry, and so on.

A substantial component to achieve underwater human–robot collaboration, is to detect and track a diver. Accurately tracking a diver using small underwater vehicles would be a big step into developing underwater companion robots that can be used for underwater archaeology and off-shore structures inspection (Mišković et al., 2015; cf. Figure 1).

The research of target detection and tracking is quite mature in land applications (Kakinuma et al., 2012; Lekkala & Mittal, 2016; Ren et al., 2017; Yagimli & Varol, 2009; Zou & Tseng, 2012); however, it is still a challenging topic in underwater environments. The poor propagation of electromagnetic waves under water restricts high-bandwidth communication, which makes most of the communication and localization technology developed for on-land applications impractical in sea. Furthermore, the particular optical properties of light propagation in water (absorption and diffusion phenomena, presence

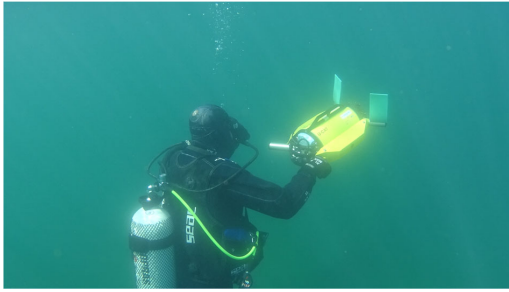


FIGURE 1 Picture of the U-CAT robot with a diver during lake inspection [Color figure can be viewed at wileyonlinelibrary.com]

of sediments, high turbidity, etc.) limits the use of vision based methods for underwater target tracking (Duntley, 1963).

A lot of research has been done in this context, using either vision-based, and/or acoustic-based methods. In spite of the limited detection range and the difficulty of feature extraction using digital cameras, there are situations where the visibility conditions are good, for example, when the object is close, or when the AUV operates in calm or shallow waters. A wide variety of vision-based research has been conducted, and different features can be used to detect an object. The color as a feature was used by Yu et al. (2001), and later by Dudek et al. (2005) to visually guide an amphibious legged underwater robot. This technique is robust against scale and rotational variations, and partial occlusions, however, the phenomenon of color absorption in water limits the use of this technique to only clear water and close-range applications.

Shape as a feature for underwater object detection was used in Han and Choi (2011) and Lee et al. (2003). However, this technique is only robust when the target has an a priori known, and invariant shape. A study comparing other methods such as Template Matching, Weighted Template Matching, and Mean-Shift based techniques were conducted in Kim et al. (2012). Yet, template matching techniques require good visibility to extract relevant features from the image. Many other techniques exist, for instance, optical flow can be used for underwater pipeline tracking (Cheng & Jiang, 2012), however, optical flow techniques are not well-suited for diver tracking applications, as using this method leads to the detection of all moving objects in a scene. Background subtraction techniques can also be used for detecting a moving object (Prabowo et al., 2017); nevertheless, this technique works better when having a static camera. Sattar and Dudek (2007, 2009) proposed an algorithm based on the periodic motion of a diver's flippers. However, this method requires good visibility, and close distance to the flippers. Buelow and Birk (2011) proposed an algorithm based on the Fourier Mellin Invariant to detect moving objects, such as divers, on a moving scene. Chavez et al. (2015) proposed a variation of the Nearest Class-Mean Forests to detect and track divers visually. DeMarco et al. (2013) showed the potential of sonar imagery in detecting divers based on computer vision segmentation techniques to detect moving objects in

the sonar image, and processing the identified blobs using cluster classification.

Recently, enabled by the increase of computing power of GPUs' parallel architectures, neural network modeling is widely used in image processing (LeCun et al., 2015). Therefore, state of the art algorithms for on-land object detection and classification are based on deep neural networks (DNN) architectures (Cao et al., 2019; Duan et al., 2019; Li et al., 2019; Redmon & Farhadi, 2018). Many researchers are now using DNN techniques either with digital cameras for underwater target tracking (Islam et al., 2019; Shkurti et al., 2017) and multitarget tracking (de Langis & Sattar, 2020; Xia & Sattar, 2019), or with sonar imagery (Cardozo et al., 2017; Kamal et al., 2013; Lee, 2017; Song et al., 2017). Depending on the data-set on which this method is trained on, it can be robust against partial occlusions, rotations, and scale-variations. Furthermore, down-scaled DNN models have been recently proposed in the literature (Howard et al., 2017; Redmon & Farhadi, 2018). Such models can be implemented on vehicles with limited computing capabilities, for fast and reliable target (or multitarget) detection. In spite of the work and research developed for underwater target tracking, vision-based techniques still require good visibility, being in a close range to the target, and having the target inside the camera's FOV.

All the vision techniques based either on digital camera or acoustic imaging mentioned above suffer from the same issue; the diver needs to be within the sensor's field of view (FOV). This limits the diver's mobility and cognitive load as the diver has to always stay in the camera's FOV. Moreover, during underwater missions, underwater vehicles can be subject to external perturbations which might cause losing the diver from the camera's FOV. Recovering from such a scenario has so far not been addressed.

To address this issue, we have investigated a solution which combines visual and acoustic signals for diver detection. Acoustic signals enable a wider range for underwater target detection. This solution allows to detect and track divers that can be far from the robot, or outside its camera's FOV, allowing the diver to move freely without being constrained to stay within a limited distance to the robot, and allows to recover from eventual cases where the robot loses the diver from its camera's FOV. This robust solution is also low-cost compared to previous studies, where a multimodal diver detection scheme was used (Chavez et al., 2017; Mandić et al., 2016).

In underwater environments, the acoustic modality is generally more suitable, and can be used in various ways, such as sonar imaging, or accurately localizing a beacon. Many techniques and applications using sonar imagery have been developed in the literature. A sonar-based real-time underwater object detection using the AdaBoost method was proposed by Kim and Yu (2017) which uses Haar-like Viola and Jones (2001) features. Zhao et al. (2009) presented a method to detect spherical shaped objects using sonar images. Petillot et al. (2002) proposed a robust pipeline detection and tracking technique using side-scan sonars and a multibeam echosounder. However, devices for sonar imaging are quite expensive, and cannot be implemented on small size AUV's. Acoustic signals can also be used for self-localization (Costanzi et al., 2017) or to localize

an acoustic pinger using an array of hydrophones (Choi et al., 2017; Kasetkasem et al., 2017). Still, the drawback of using acoustic sensors is influenced by several factors, such as reflections, low operating frequencies, aquatic life disturbance, and their efficiency is highly affected when placed near the robot's mechanisms. Furthermore, the physics of sound propagation differ from one underwater environment to another. Indeed, depending on the type of the environment where the robot is operating, several factors may impact the quality and accuracy of acoustics signals. In shallow waters, reflections on the sea bottom and on the sea surface occur more often than in deep waters. Moreover, the movement of the sea surface also affects the signal and the reflections' delays. The ambient noise, such as breaking waves, rain, bubbles, and biological sources also affects the quality of the acoustic communication (Jensen et al., 2011; Preisig, 2007). All these factors need to be taken into account, and an appropriate acoustic filter needs to be used depending on the type of the underwater environment.

Acoustic perception can be augmented with machine vision techniques (Chavez et al., 2017). This study is motivated by the complementarity of acoustic and vision based object detection methods, as illustrated in Figure 2. The fusion of visual and acoustic signals removes their respective limitations, and provides advantages for diver following compared to aforementioned approaches (Mandić et al., 2016). In this context, the goal of this study is to track a diver (or any other dynamic target) by fusing acoustic and visual signals acquired from low-cost sensors, to have a more robust, more accurate and more complete detection in open water conditions, while taking into account the underwater robot hardware capabilities. The advantage of the presented work, compared to what has already been done in the aforementioned studies, is an increased robustness towards diver tracking, where the tracking is successful, whether the diver is on the camera's FOV or not. Moreover, the proposed solution involves the use of relatively low-cost sensors, where the diver is detected visually by a digital camera using a down-scaled embedded DNN, and acoustically, by tracking a pinger carried by the diver using an array of

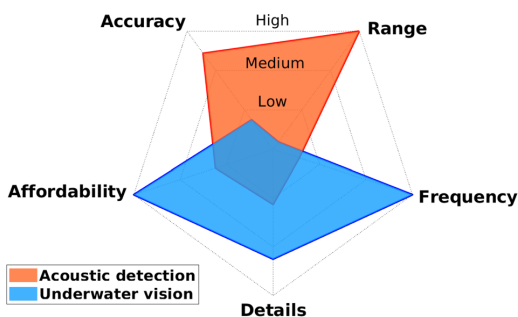


FIGURE 2 Comparison of two methods of underwater perception: Acoustic detection is more accurate and works in a wider range, while underwater vision is more affordable, has a higher sampling frequency and higher resolution [Color figure can be viewed at wileyonlinelibrary.com]

low-cost hydrophones. The proposed diver tracking scheme is implemented on the omnidirectional underwater robot U-CAT (Salumäe et al., 2016), and validated in an open water environment.

2 | U-CAT BIO-MIMETIC AUV

Inspired by the swimming abilities of marine animals, U-CAT (Chemori et al., 2016; Salumäe et al., 2016) is an autonomous underwater vehicle (AUV) actuated by four oscillating fins. It was developed, as part of the ARROWS European project, at the Center for Biorobotics (Tallinn University of Technology) in Estonia.

U-CAT is a low-cost, resource constrained robot, that has a small size allowing it to manoeuvre in confined environments (Preston et al., 2018). Its design is user-friendly, and its weight does not exceed 19 kg, which allows for quick and easy deployment. U-CAT can operate in depths up to 100 m, and has a battery life of at least 6 h (Figure 3).

Using its four flexible fins, the robot can easily move and manoeuvre in six degrees of freedom (6 DOF). U-CAT is equipped with an MPU-9150 inertial measurement unit (IMU), and low-cost perception sensors, such as an array of three *Aquarian Audio H1c* hydrophones for establishing the heading relative to an acoustic beacon, and a *PointGrey Chameleon2* camera running at 15 frames per second.

3 | PROPOSED TRACKING CONTROL SCHEME

This section describes the proposed control scheme for diver detection and tracking using visual and acoustic signals (as illustrated in Figure 4). The visual detection of the diver is described in Section 3.1.

The down-scaled DNN model *tiny-YOLOv3* (Redmon & Farhadi, 2018) is used for detecting the diver visually using the on-board digital camera. This approach is chosen because it enables fast (≈ 20 fps) and reliable detection on resource constrained computers. The algorithm is implemented on U-CAT's Jetson TX2 embedded computer using robot operating system (Bjelonic, 2018). The chosen DNN structure is a trainable model that achieves state-of-the-art performances for object detection on resource-constrained embedded systems. The data-set for the training of the model was a collection of diver images from previous experiments with U-CAT in different environments (lakes, oceans). A total of 3000 diver selected images were manually annotated using YOLO-annotation-tool.

The annotated images were then augmented to 8000 images by performing scale and rotation variations. Another no-diver 2000 images (also collected by U-CAT's camera in previous experiments) were added to the data set. The performance of the model is evaluated and summarized in Table 1 based on mean average precision (mAP) and intersection over union (IoU) scores.

Table 1 shows the evaluation of the detection accuracy. Indeed, the performance of this scaled-down DNN model is low compared to other methods containing more hidden neural layers

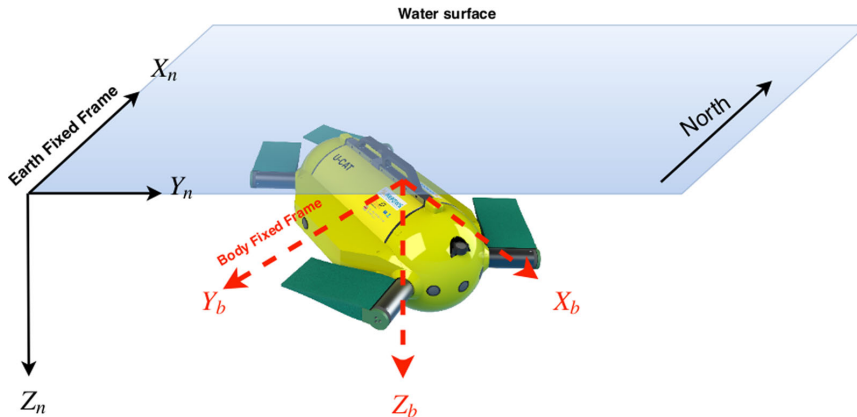


FIGURE 3 Illustration of the earth fixed frame R_n (north east down convention) and the robot's body fixed frame R_b

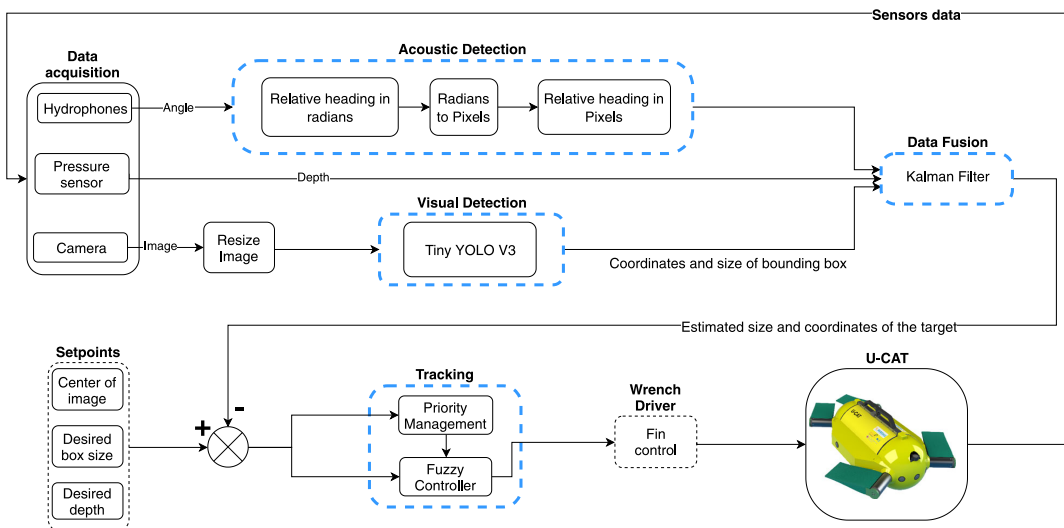


FIGURE 4 Block diagram of the proposed tracking control scheme: Dashed-blue blocks are described in Section 3. The proposed tracking scheme is implemented on U-CAT using robot operating system, and all of the steps in this figure run online on U-CAT's embedded computer [Color figure can be viewed at wileyonlinelibrary.com]

(Islam et al., 2019). The used DNN model was not compared to relative works in the literature due to the lack of a data-base that includes diver images in different water types and different visibility conditions. However, experimental results show that combining visual measurements

using the implemented DNN model with acoustic measurements is enough to achieve an efficient and accurate diver tracking.

Figure 5 shows an illustration of the vision detection result. The object of interest is wrapped inside a pink bounding box. Its center's pixel coordinates are denoted (X_m, Y_m) and its width W_m . As the goal is to track the object, the objective here is to fit the detected object inside a virtual bounding box located at the center of the image whose coordinates are (X_c, Y_c) , and its width is W_c .

The acoustic detection approach is described in Section 3.2. A quaternion based scheme using a low-cost array of hydrophones to detect the acoustic pinger is presented. Later on we describe the data-fusion scheme which is based on a model-free Kalman Filter (Kalman, 1960),

TABLE 1 Tiny-YOLOv3 performance

mAP (%)	54.26
IoU (%)	58.41
Frames per second	20

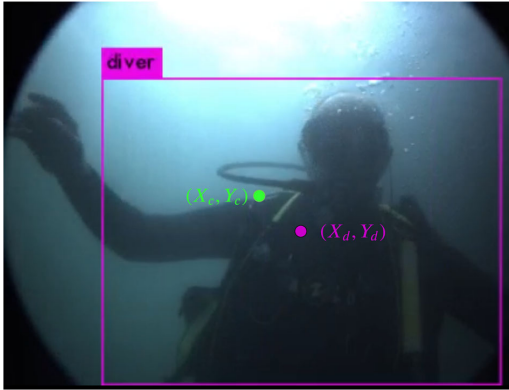


FIGURE 5 Visual detection: The goal is to center the detected box at the center of the image [Color figure can be viewed at wileyonlinelibrary.com]

since we do not have a mathematical model in disposal that captures the diver's free motion. Moreover, this data-fusion approach is chosen for its implementation simplicity, and its low computational cost.

Lastly, an adaptive fuzzy logic Mamdani controller for the 3-DOF (surge, depth, and yaw) control of U-CAT is described. This approach is selected based on a previous study in which various control laws (PID, nonlinear PID, sliding mode, adaptive state feedback, and fuzzy control) were tested and compared on U-CAT (Remmas, 2017). The obtained results showed that the fuzzy logic controller gives the best trajectory tracking results for heave and yaw control. The results are justified by the inaccuracies in U-CAT's dynamic model that limits the use of model-based control schemes, and the fact that fuzzy "expertise" based controller that gives the best results.

3.1 | Visual detection

The errors E_C and E_W between the two boxes centers and widths are given by:

$$E_C = \begin{bmatrix} X_c \\ Y_c \end{bmatrix} - \begin{bmatrix} X_m \\ Y_m \end{bmatrix}, \quad (1)$$

$$E_W = W_c - W_m, \quad (2)$$

This concept allows a 3-DOF tracking control, such that the difference between the two boxes' centers E_C defines the desired depth and heading orientation of the robot, and the difference between the two boxes' widths E_W defines the desired distance between the robot and the target. The virtual box's width W_c is customizable and allows to define how close the robot should be to the object. In all our experiments, this parameter is chosen as $W_c = 60$. This value is selected so that the AUV keeps the diver within the camera's FOV without necessarily going too close to him.

3.2 | Acoustic detection

A Sonotronics EMT-01-3 Pinger operating at 9.6 kHz is used as a beacon. It transmits a short burst signal every second. The received signal by each hydrophone is amplified and filtered. The phase shift for each hydrophone is then used to compute the relative yaw angle to the robot. The relative yaw angle between the pinger and the robot in the Earth Fixed Frame R_n (cf. Figure 3) is denoted by Ψ_p .

Considering only the yaw angle of the pinger with respect to the robot, let Q_Ψ be the quaternion representation of Ψ (yaw angle of robot in R_n) measured by the on-board IMU, and Q_{Ψ_p} the quaternion representation of Ψ_p such that:

$$Q_\Psi = \left[\cos\left(\frac{\Psi}{2}\right) \ 0 \ 0 \ \sin\left(\frac{\Psi}{2}\right) \right]^T, \quad (3)$$

$$Q_{\Psi_p} = \left[\cos\left(\frac{\Psi_p}{2}\right) \ 0 \ 0 \ \sin\left(\frac{\Psi_p}{2}\right) \right]^T. \quad (4)$$

The shortest angle between these two quaternions is given by:

$$\Delta Q = [q_0, q_1, q_2, q_3]^T = Q_{\Psi_p} \otimes Q_\Psi^{-1}, \quad (5)$$

where \otimes denotes the quaternion multiplication, and Q^{-1} is the quaternion inverse of Q .

The quaternion angle error ΔQ is converted back to the desired yaw angle φ , that is:

$$\varphi = a \tan 2(2q_0q_3, 1 - 2q_3^2). \quad (6)$$

Since the heading orientation to the pinger will be fused with camera measurements, the heading angle error is converted to pixel coordinates error noted $E_p = \Phi(\varphi, a)$ such that:

$$\Phi(x, a) = \begin{cases} 0, & \text{if } x < a, \\ \text{Imagewidth}, & \text{if } x > -a. \\ \frac{\text{Imagewidth}}{2} \left(\frac{-x}{a} + 1 \right), & \text{otherwise } (a \neq 0). \end{cases} \quad (7)$$

The function Φ remaps the measured pinger orientation into an image's X -coordinate pixel as illustrated in Figure 6. In our study, we consider $a = \pi/3$.

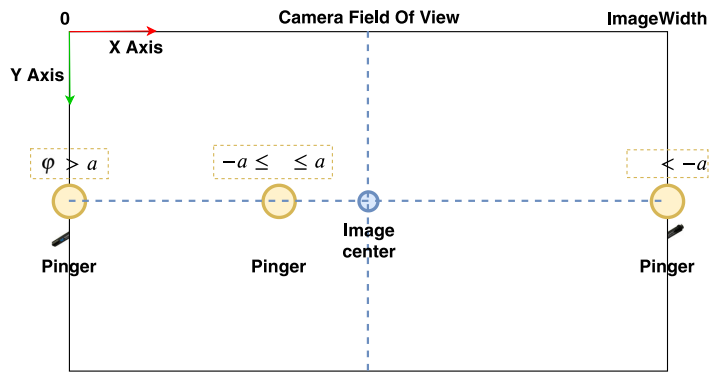
3.3 | Proposed data-fusion control-scheme

One of the most popular data-fusion and estimation techniques is the Kalman filter. It was originally proposed by Kalman (1960) and has been widely studied and applied since then. The used state and measurement vectors are defined as follows:

$$X_t = [x_t, y_t, w_t, z_t]^T, \quad (8)$$

$$Y_t = [X_m, Y_m, W_m, Z_m, X_p]^T, \quad (9)$$

FIGURE 6 Acoustic detection: Conversion scheme from yaw angle error in radians to error in pixel coordinates in the camera frame [Color figure can be viewed at wileyonlinelibrary.com]



where X_t is the state vector at time t . The variables x_t and y_t represent the estimated pixel coordinates of the target and w_t is the estimated width of a bounding box containing the target. The variable z_t represents the estimated depth of the robot. Y_t is the measurement vector. The variables (X_m, Y_m) and W_m represent the position coordinates and width of the detected bounding box by the camera, Z_m is the measured depth of the robot using the on-board pressure sensor, and X_p is the image coordinates of the detected heading measured by the hydrophones array.

The estimated state vector $X_t = [x_t, y_t, w_t, z_t]^T$ is used to compute tracking errors as follows:

$$E_x = X_c - x_t, \tag{10}$$

$$E_y = Y_c - y_t, \tag{11}$$

$$E_w = W_c - w_t, \tag{12}$$

$$E_z = Z_{desired} - z_t, \tag{13}$$

E_x is the horizontal error between the center of the frame and the estimated bounding box's center, E_y is the vertical error between the center of the frame and the estimated bounding box's center. E_w is the error between the virtual box's width and the estimated one, and E_z is the error between a desired depth and the estimated depth of the robot.

3.4 | Fuzzy logic controller

Based on the tracking errors defined in (10)–(13), a fuzzy logic Mamdani controller (Mamdani & Baaklini, 1975) was designed to control the robot, for the aim of tracking the diver as shown in Figure 7. In this study, the controller's inputs are the tracking errors and their variations, and the output is the force vector $\tau \in \mathbb{R}^{3 \times 1}$ to be applied to the robot, with $\tau = [\tau_x, \tau_y, \tau_\psi]$.

The inputs are fuzzified using trapezoidal membership functions (Figure 7). Such membership functions may lead to a steady state

error which depends on the choice of a_1 and a_2 . Furthermore, this type of membership functions prevents oscillations around the target (since perfectly fitting the detected bounding box at the center of the image is rather challenging).

The rule base for our controller is defined in Table 2, where E_i and \dot{E}_i ($i = \{x, y, w, z\}$) are the tracking error vector and its first-time derivative:

The output is computed using the center of gravity defuzzification method, based on the membership function of Figure 8, and the forces are converted to fin oscillation directions and amplitudes by the wrench driver (Salumäe et al., 2019).

3.5 | Priority management

The priority management was proposed in Salumäe et al. (2016) as a solution to compensate for the high coupling in the actuation of the different DOFs of U-CAT. The proposed technique is based on Gaussian membership functions used to moderate the control of each DOF depending on the control objective.

To prioritize the DOFs, the universe of discourse for the defuzzification process is modified through the multiplication of the constants c_i by the priority weights ρ_x, ρ_y , and ρ_ψ (cf. Figure 8).

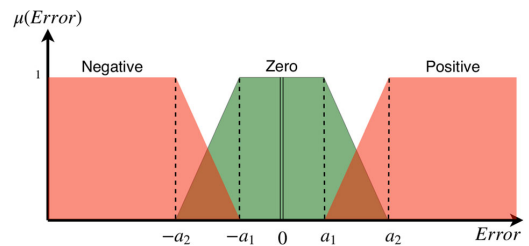


FIGURE 7 Fuzzification membership functions: a_1 and a_2 are positive constants defining the universe of discourse for each degree of freedom [Color figure can be viewed at wileyonlinelibrary.com]

TABLE 2 Fuzzy controller rule base

$E_i \setminus \dot{E}_i$	Negative	Zero	Positive
Negative	Negative	Negative	Zero
Zero	Negative	Zero	Positive
Positive	Zero	Positive	Positive

The priority is given to yaw control, then to depth control and finally to surge control as follows:

$$p_x = e^{-\frac{E_x^2 + E_y^2}{2\sigma^2}}, \quad (14)$$

$$p_y = e^{-\frac{E_x^2}{2\sigma^2}}, \quad (15)$$

$$p_\psi = 1 - e^{-\frac{E_z^2}{2\sigma^2}}, \quad (16)$$

where σ^2 is the variance of the Gaussian functions.

Since U-CAT is relatively stable in roll and pitch, the control of those DOFs was not taken into consideration at this stage.

4 | EXPERIMENTAL RESULTS IN OPEN WATERS

To validate the proposed control scheme, various experiments were conducted out near a small harbour in Banyuls-Sur-Mer, France (42° 28' 52.0"N, 3° 08' 10.0"E). Four experimental scenarios were tested to show the need of sensors' complementary for diver tracking, and to highlight the efficiency of the proposed tracking control scheme. In this section, a description of the experimental setup for the different scenarios will be presented, followed by a presentation and discussion of the obtained results.

- *Visual tracking (Scenario 1)*: In this scenario, U-CAT is only visually guided to track the diver. The goal of this test was to assess the robustness of the proposed vision detection and tracking algorithm in field operating conditions.

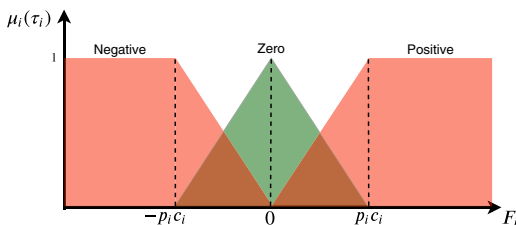


FIGURE 8 Defuzzification membership functions: c_i is the maximum achievable force or torque along i axis. p_i are weights for the control priority management (more details are given in Section 3.5). The defuzzification process is done by using the center of gravity method [Color figure can be viewed at wileyonlinelibrary.com]

- *Acoustic tracking (Scenario 2)*: In this test, U-CAT has to track the diver using acoustic sensing only. This experiment was carried out to evaluate the acoustic sensing based on an array of three hydrophones and a pinger for diver tracking.
- *Data-fusion-based static tracking (Scenario 3)*: In this test, the proposed data-fusion tracking scheme was tested for tracking a static target. The robot had to autonomously detect and track a pinger fixed to a colored waterproof source of light that was initially positioned far from the robot and out of its camera's FOV. A simple color segmentation detector was used to visually detect the colored source of light in this case. The same scenario was conducted three times where U-CAT started in different initial conditions; either facing the target, placed to its left, or its right.
- *Data-fusion based dynamic tracking (Scenario 4)*: In this last scenario, the proposed diver tracking algorithm's efficiency was evaluated. A diver carrying the pinger was asked to move freely in open water at a known depth. The diver's depth was chosen to be 2 m to ensure more reliable top view monitoring of the diver and the AUV from a static camera. This scenario was conducted three times, where the diver started at different initial locations, either close and within the robot's camera's FOV, or away and out of the embedded camera's FOV.

4.1 | Visual tracking (Scenario 1)

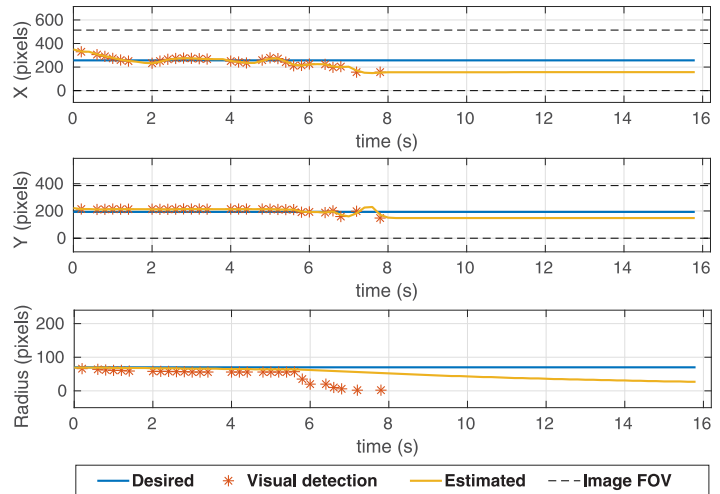
Initially, the diver was in U-CAT's camera's FOV so that he can be detected from the beginning of the experiment. The diver then moved freely at a constant depth. The obtained results are shown in Figure 9.

Figure 9 shows that the AUV was tracking and centering the detected target on the image. After 8 s of tracking, the diver left the camera's FOV. The robot was tracking the last detected value; however, it failed to find the target. Furthermore, in field experiments, where the water is often turbid, and the visibility conditions are poor due to light scattering and absorption, visual detection often fails (as illustrated in Figure 10), which causes the tracking to fail. This shows the motivation behind using another sensor to complement the vision, and ensure detecting the diver when this last one's detection fails.

4.2 | Acoustic tracking (Scenario 2)

For this scenario, the pinger was carried by the diver who was initially a few meters away from the robot. The diver was asked to stay at a stationary spot for this experiment. As there is no distance feedback to the diver using this acoustic method, U-CAT will move continuously even when reaching the diver. Figure 11 shows that the remapped detected relative heading was mostly on the left side of the image. This is because the robot kept swimming around the diver after reaching him. Figure 11 shows also noisy acoustic data due to reflections. This shows clearly the need of a complementary visual sensor to track the diver efficiently.

FIGURE 9 Visual tracking (Scenario 1): Experimental results describing visual detection and estimation using the camera to track the diver [Color figure can be viewed at wileyonlinelibrary.com]



4.3 | Data-fusion-based tracking

As discussed previously, two different scenarios were conducted, namely static and dynamic tracking. The objective of Scenario 3 is to evaluate the performance of the proposed control tracking scheme for the case of tracking a static object that was initially placed out of the camera's FOV. The goal of Scenario 4 is to assess the performance of the proposed solution for dynamic diver tracking.

4.3.1 | Static tracking (Scenario 3)

In this experiment, a target was mounted next to the pinger approximately 6 m away from U-CAT (as illustrated in Figure 12).

The robot moves towards the target, slightly oscillates left and right due to reflections in acoustic detection, and is facing the target after nearly 40 s. Figure 13 shows that the target was then centered on the camera's image based on the visual feedback. Since both the target and the AUV were operating at the same depth, the target was almost already centered in Y axis, and the slight vertical error to the camera's center is corrected based on visual feedback. It is worth to note that the proposed tracking scheme can successfully detect and track a static target that is initially out of the on-board camera's FOV. Figure 13 also shows that the desired width of the target within the camera's frame is retained, which translates into a maintained relative distance to the target. This clearly shows that combining both visual and acoustic measurements allows a more robust tracking of the object.

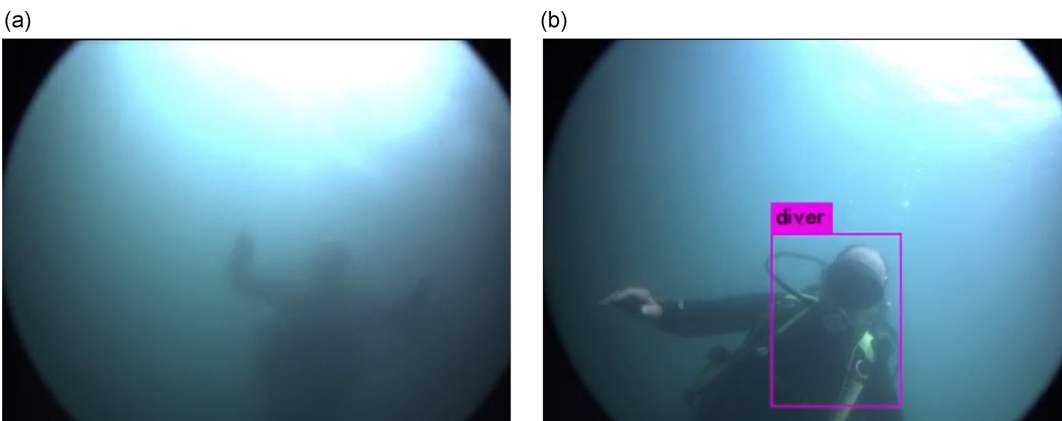


FIGURE 10 Underwater images from U-CAT's camera in open water conditions. (a) Frame example where visual detection is not successful due to poor visibility conditions. (b) Frame example where the diver is successfully detected when close enough [Color figure can be viewed at wileyonlinelibrary.com]

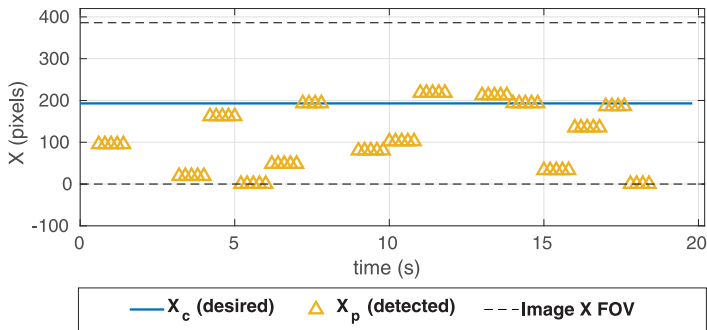


FIGURE 11 Acoustic tracking (Scenario 2): Experimental results for tracking the diver based on acoustic signals only. FOV, field of view [Color figure can be viewed at wileyonlinelibrary.com]

Figures 14 and 15 show the obtained results when starting respectively, placed to the right, and to the left of the target. In the experiment illustrated by Figure 14, The robot relies on acoustics at the first 40–50 s when the target is out of the camera's visibility reach. When the target is detected visually, the target estimated location within the camera's frame is improved, which allows the robot to reduce oscillations around the target, and center it in the camera's frame. In the last experiment for this scenario, where the robot started to the left of the target, it took longer (107 s) to detect the target visually. This is mainly due to acoustic reflections, and motors noise since the robot was operating at a harbour where motorised vehicle were passing by. Nevertheless, the target was

reached successfully, and after the object was detected visually, the robot managed to keep it in its camera's frame center.

As there is no ground truth to evaluate for the acoustic detections, we present the Table 3 that shows the error between the target's camera location, and the camera's center, for the three case scenarios. The results show that once the target was retrieved visually, it was mainly kept at the center of the camera's frame.

This clearly shows the robustness of the proposed method, but also its repeatability. This allows to detect and track an object initially far away from the robot, where no other method based on vision only could succeed. The results also show that the robot manages to do station keeping when tracking a static object.

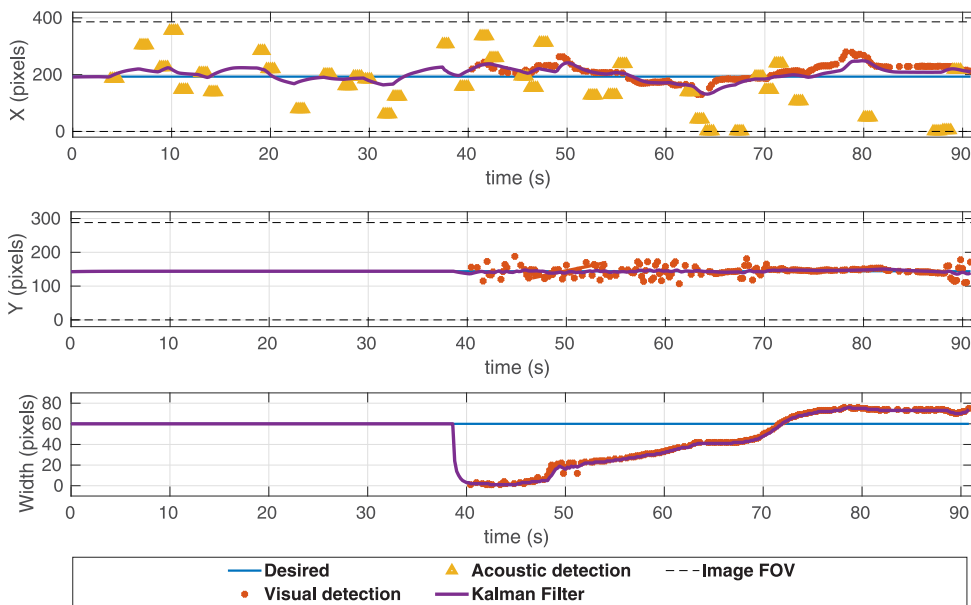


FIGURE 12 U-CAT illustrative trajectory when homing towards a static target using the proposed data-fusion scheme: At time T1, the autonomous underwater vehicle was heading towards the target based on acoustic detection. At time T2, U-CAT has found the target by combining both visual and acoustic sensors' data [Color figure can be viewed at wileyonlinelibrary.com]

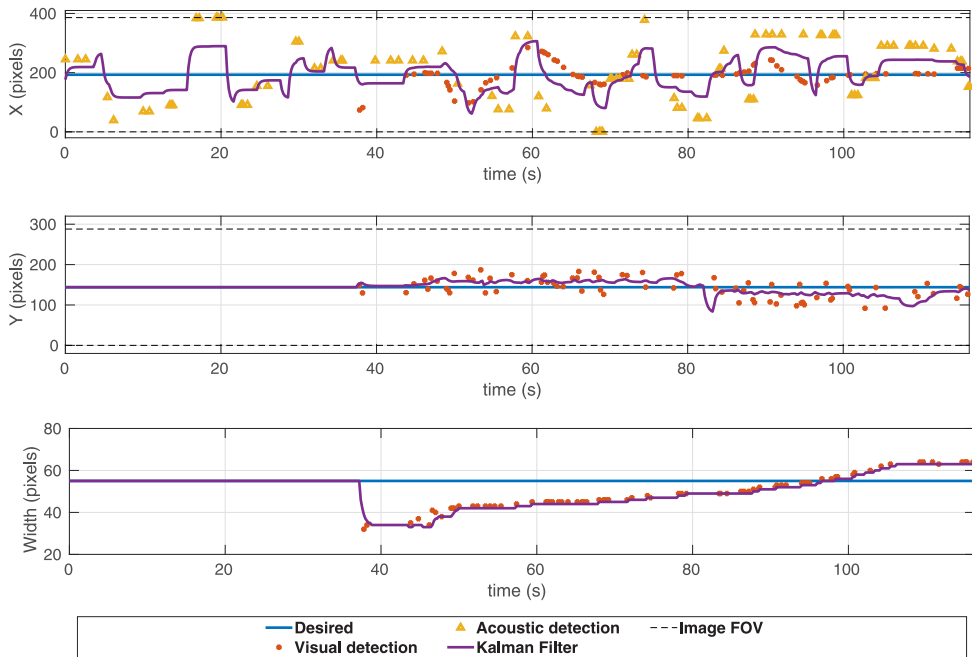


FIGURE 13 Data fusion based static tracking (Scenario 3): Experimental results describing static target tracking based on the proposed data-fusion scheme where the autonomous underwater vehicle started facing the target. FOV, field of view [Color figure can be viewed at wileyonlinelibrary.com]

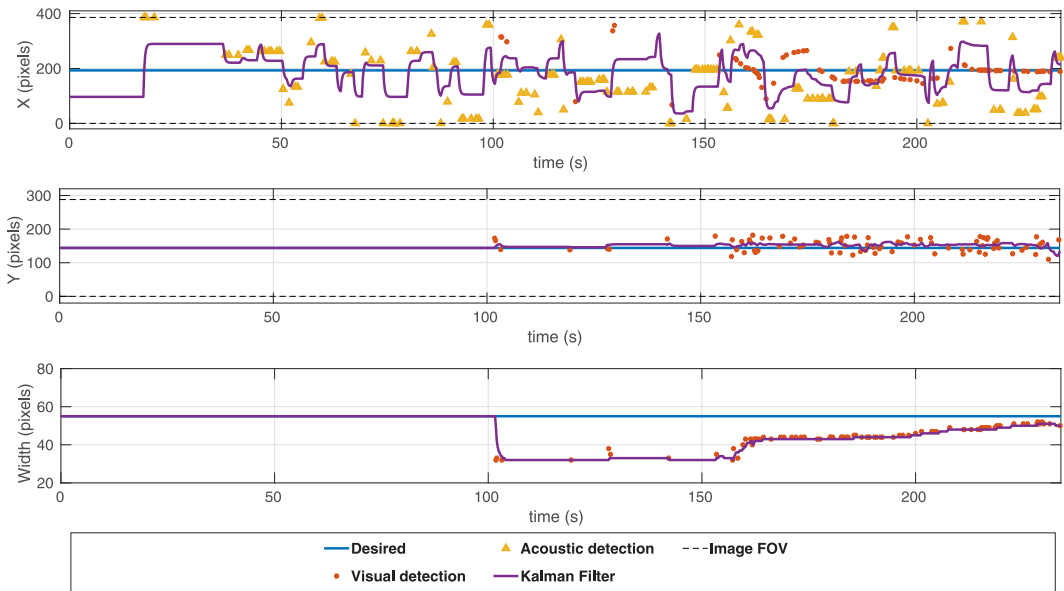


FIGURE 14 Data fusion-based static tracking (Scenario 3): Experimental results describing static target tracking based on the proposed data-fusion scheme where the autonomous underwater vehicle started to the right of the target. FOV, field of view [Color figure can be viewed at wileyonlinelibrary.com]

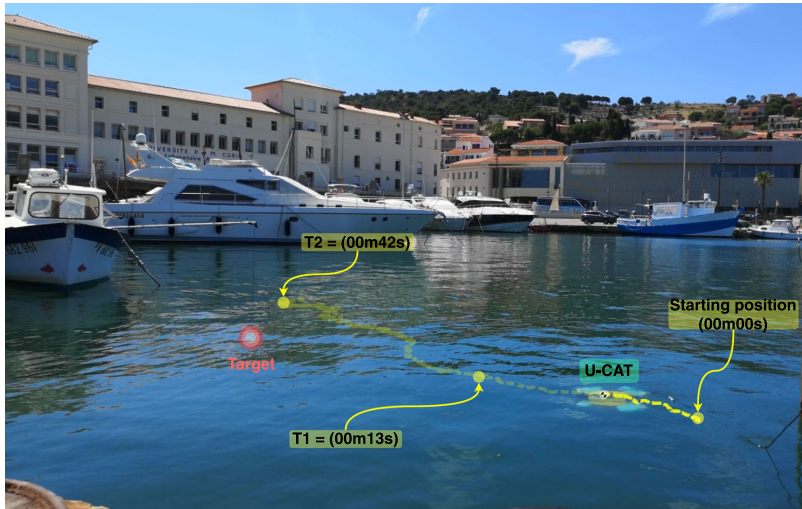


FIGURE 15 Data fusion-based static tracking (Scenario 3): Experimental results describing static target tracking based on the proposed data-fusion scheme where the autonomous underwater vehicle started to the left of the target. FOV, field of view [Color figure can be viewed at wileyonlinelibrary.com]

4.3.2 | Dynamic tracking (Scenario 4)

In this last scenario, we tested the proposed control approach to actively track a diver. The diver was carrying the pinger and moving freely in a two-dimensional trajectory at a constant depth. As the robot can only swim at relatively slow velocity, the diver was asked to also move slowly.

When the diver starts within the camera's FOV, the robot has a better estimate of its location based on both visual and acoustic detections, as shown in Figure 16. When the diver starts out of the camera's FOV, as shown in Figure 17, it takes longer at the beginning to accurately detect and track the diver. But in both cases, the proposed solution allowed to track the moving diver for more than 8 min. The target left the camera's FOV several times, nevertheless, its location could always be recovered. The complementarity of the proposed approach allows to quickly head towards the diver, and keep him centered in the camera's image.

A shorter experiment was conducted for better data-clarity, and for illustrating the trajectory of both the robot and the diver

graphically. As illustrated in Figure 18, U-CAT was accurately tracking the target throughout this experiment. Figure 19 shows clearly how the diver left the camera's FOV several times. The proposed tracking control approach allows to recover the diver location within the camera's FOV, and allows to center it within the camera's frame, and within a desired bounding box width. The presented results show the robustness of the proposed approach, where experimental results were validated throughout different scenarios, and where the AUV was operating in open-waters at poor visibility conditions, and subject to acoustic reflections and noise.

Table 4 shows the tracking performance in terms of error between desired and the fed-back position of the diver within the camera's frame. The higher errors are along the image X axis, since the diver was moving mainly horizontally. Both errors in Y and width are low considering the diver was keeping his depth constant, and moving relatively slowly. This shows that the diver was mainly centered in the camera, despite leaving its FOV numerous times.

The results also illustrate that the proposed controller allows to achieve a three-dimensional tracking motion, in spite of the high coupling in U-CAT actuators.

TABLE 3 Scenario 3: RMSE between the camera's center and desired width, and the object pixels location and its width

RMSE (in pixels)	Test 1 facing the target	Test 2 right to the target	Test 3 left to the target
RMSE X	42	67	72
RMSE Y	17	20	21
RMSE Width	12	15	8

Abbreviation: RMSE, root mean square error.

5 | CONCLUSION AND FUTURE WORKS

The aim of this study was to design and develop a low-cost data-fusion-based diver tracking control scheme and to implement it on a highly manoeuvrable underwater robot U-CAT. Taking into account U-CAT's actuation characteristics and hardware capabilities, a data-fusion based technique combining acoustic and visual signals was proposed. The proposed control strategy was validated through

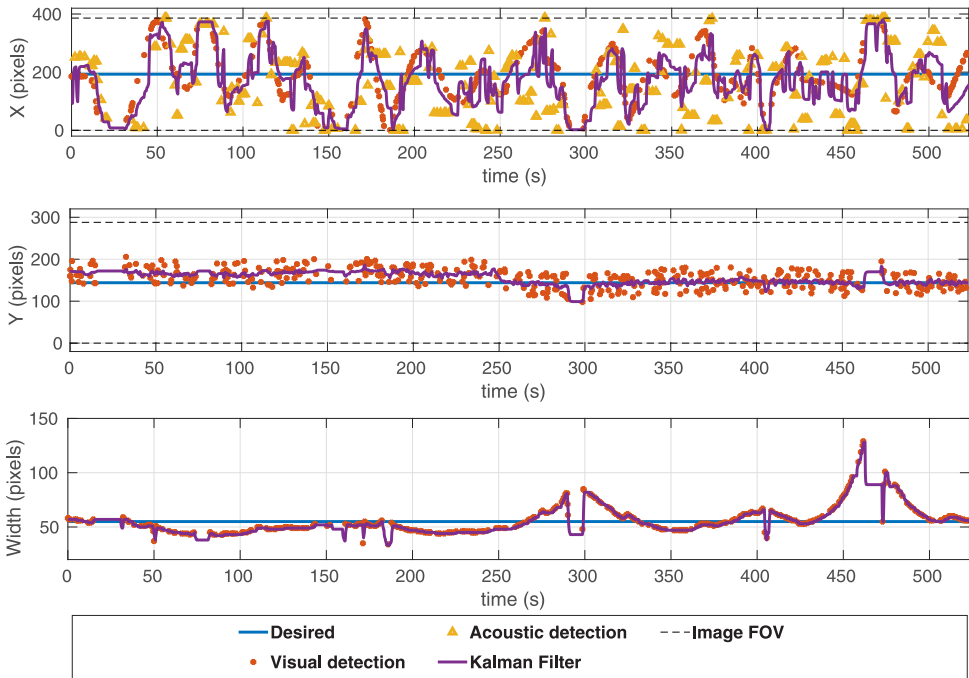


FIGURE 16 Data-fusion based dynamic tracking (Scenario 4): Diver starting close to the robot. FOV, field of view [Color figure can be viewed at wileyonlinelibrary.com]

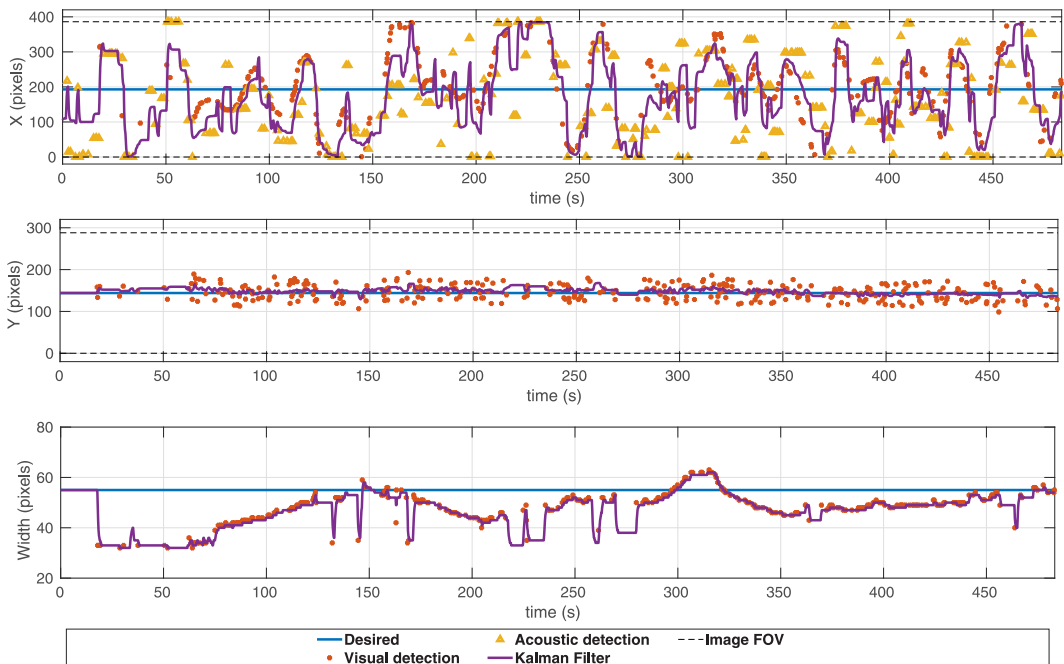


FIGURE 17 Data-fusion based dynamic tracking (Scenario 4): Diver starting away from the robot. FOV, field of view [Color figure can be viewed at wileyonlinelibrary.com]

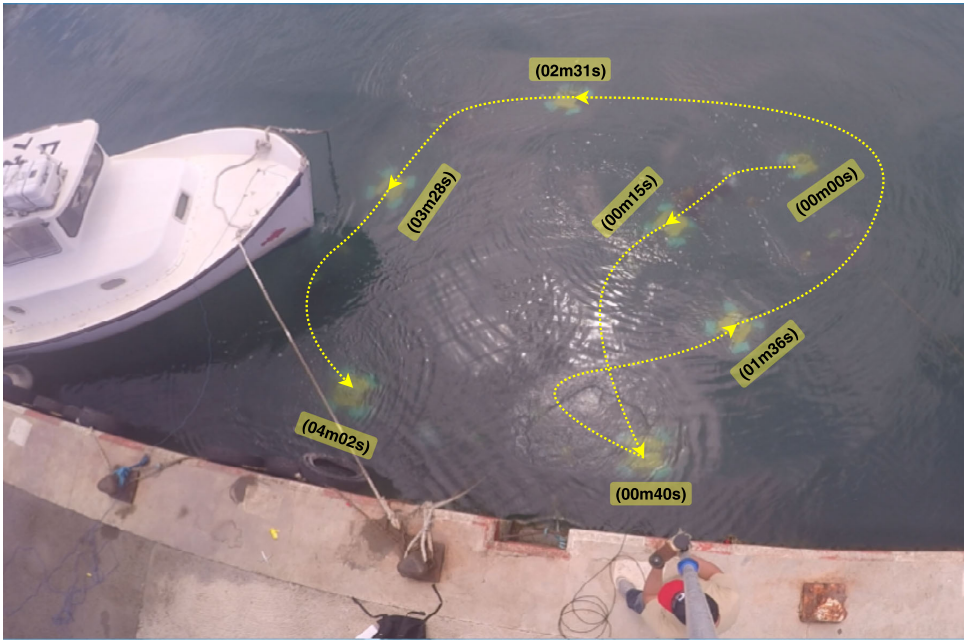


FIGURE 18 U-CAT illustrative diver tracking trajectory: Description at different times [Color figure can be viewed at wileyonlinelibrary.com]

open water field experiments. Promising results were obtained, demonstrating the effectiveness and performance of the proposed data-fusion-based control algorithm. The proposed solution demonstrates also that the target can be found, detected, and tracked,

even if it is initially far away from a robot operating in poor visibility conditions.

Combining acoustic and visual signals for underwater detection and tracking shows a robust performance in harsh field conditions,

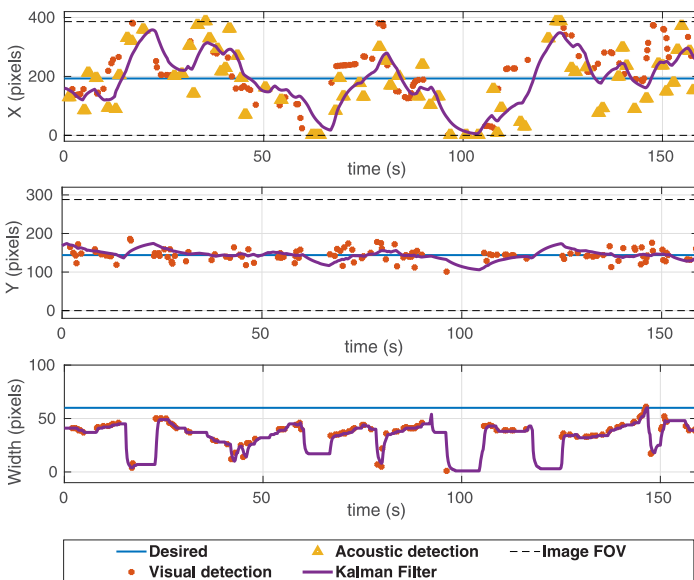


FIGURE 19 Data-fusion based dynamic tracking (Scenario 4): This shorter experiment is presented for plot clarity. FOV, field of view [Color figure can be viewed at wileyonlinelibrary.com]

TABLE 4 Scenario 4: RMSE between the camera's center and desired width, and the object pixels location and its width

RMSE (in pixels)	Test 1 diver initially close from the robot	Test 2 diver initially away from the robot	Test 3 shorter experiment
RMSE X	119	124	106
RMSE Y	37	28	33
RMSE W	24	19	31

Abbreviation: RMSE, root mean square error.

and the ability to recover the diver's location when visual detection fails.

Further work will be carried out in future, which will include testing at larger trial areas, and improving of the acoustic detection accuracy, considering 3-DOF orientation detection with the hydrophones instead of heading orientation only, which will allow a diver tracking at any depth. The visual detection part will also be improved with the advancement of real-time object detection algorithms. Another interesting idea would be the implementation of a gesture recognition algorithm to allow a more efficient underwater human-robot collaboration.

ACKNOWLEDGMENTS

This study is financed through Estonian Research Council Grant IUT-339. The authors would like to thank the "Observatoire Océanologique de Banyuls-sur-mer" for providing scientific divers and experimental setups. The authors would also like to thank Christian Meurer, Jaan Rebane, and Roza Gkliva for their valuable reviews and comments to improve this study.

ORCID

Walid Remmas  <https://orcid.org/0000-0001-8690-0496>

REFERENCES

Aggogeri, F., Mikolajczyk, T., & O'Kane, J. (2019). Robotics for rehabilitation of hand movement in stroke survivors. *Advances in Mechanical Engineering*, 11(4). <https://doi.org/10.1177/1687814019841921>

Bernard, T., Martusevich, K., Rolins, A. A., Spence, I., Troshchenko, A., & Chintalapati, S. (2018). A novel mars rover concept for astronaut operational support on surface eva missions. In *2018 AIAA SPACE and Astronautics Forum and Exposition* (p. 5154).

Bjelonic, M. (2016–2018). YOLO ROS: Real-time object detection for ROS. https://github.com/leggedrobotics/darknet_ros

Buelow, H., & Birk, A. (2011). Diver detection by motion-segmentation and shape-analysis from a moving vehicle. In *OCEANS'11 MTS/IEEE KONA* (pp. 1–7). IEEE.

Cao, Y., Xu, J., Lin, S., Wei, F., & Hu, H. (2019). GCNet: Non-local networks meet squeeze-excitation networks and beyond. In *2019 IEEE/CVF International Conference on Computer Vision Workshop (ICCVW), Seoul, Korea (South)* (pp. 1971–1980). <https://doi.org/10.1109/ICCVW.2019.00246>

Cardozo, P. O., dosSantos, M. M., Lilles, P., & Silva, S. (2017). Forward looking sonar scene matching using deep learning. In *2017 16th IEEE International Conference on Machine Learning and Applications (ICMLA)* (pp. 574–579).

Chavez, A. G., Mueller, C. A., Birk, A., Babic, A., & Miskovic, N. (2017). Stereo-vision based diver pose estimation using lstm recurrent neural networks for auv navigation guidance. In *OCEANS 2017-Aberdeen* (pp. 1–7). IEEE.

Chavez, A. G., Pflingstorn, M., Birk, A., Rendulić, I., & Misković, N. (2015). Visual diver detection using multi-descriptor nearest-class-mean random forests in the context of underwater human robot interaction (hri). In *OCEANS 2015-Genova* (pp. 1–7). IEEE.

Chemori, A., Kuusmik, K., Salumae, T., & Kruusmaa, M. (2016). Depth control of the biomimetic U-CAT turtle-like auv with experiments in real operating conditions. *2016 IEEE International Conference on Robotics and Automation (ICRA)* (pp. 4750–4755).

Cheng, C., & Jiang, B.-T. (2012). A robust visual servo scheme for underwater pipeline following. In *2012 19th International Conference on Systems, Signals and Image Processing (IWSSIP)* (pp. 456–459).

Choi, H., Woo, J., & Kim, N. (2017). Localization of an underwater acoustic source for acoustic pinger-based transit task in 2016 maritime robot challenge. In *2017 IEEE Underwater Technology (UT)* (pp. 1–7).

Colgate, E., Wannasupphoprasit, W., & Peshkin, M. (1996). Cobots: robots for collaboration with human operators. In Y. Kwon, D. Davis, & H. Chung (Eds.), *Proceedings of the ASME dynamic systems and control division* (Vol. 58, pp. 433–439). ASME.

Costanzi, R., Monnini, N., Ridolfi, A., Allotta, B., & Caiti, A. (2017). On field experience on underwater acoustic localization through USBL modems. In *OCEANS 2017-Aberdeen* (pp. 1–5).

de Langis, K., & Sattar, J. (2020). Realtime multi-diver tracking and re-identification for underwater human-robot collaboration. In *2020 IEEE International Conference on Robotics and Automation (ICRA), Paris, France* (pp. 11140–11146). <https://doi.org/10.1109/ICRA40945.2020.9197308>

DeMarco, K. J., West, M. E., & Howard, A. M. (2013). Sonar-based detection and tracking of a diver for underwater human-robot interaction scenarios. In *2013 IEEE International Conference on Systems, Man, and Cybernetics* (pp. 2378–2383). IEEE.

Duan, K., Bai, S., Xie, L., Qi, H., Huang, Q., & Tian, Q. (2019). Centernet: Keypoint triplets for object detection. In *Proceedings of the IEEE International Conference on Computer Vision* (pp. 6569–6578).

Dudek, G., Jenkin, M., Prahacs, C., Hogue, A., Sattar, J., Giguere, P., German, A., Liu, H., Saunderson, S., Ripsman, A., Simhon, S., Torres, L., Milios, E., Zhang, P., & Rekleitis, I. (2005). A visually guided swimming robot. In *2005 IEEE/RSJ International Conference on Intelligent Robots and Systems* (pp. 3604–3609).

Duntley, S. Q. (1963). Light in the sea*. *Journal of the Optical Society of America A*, 53(2), 214–233.

GomezChavez, A., Ranieri, A., Chiarella, D., Zereik, E., Babić, A., & Birk, A. (2019). Caddy underwater stereo-vision dataset for human-robot interaction (hri) in the context of diver activities. *Journal of Marine Science and Engineering*, 7(1), 16.

Han, K. M., & Choi, H. T. (2011). Shape context based object recognition and tracking in structured underwater environment. In *2011 IEEE International Geoscience and Remote Sensing Symposium* (pp. 617–620).

Hentout, A., Aouache, M., Maoudj, A., & Akli, I. (2019). Human-robot interaction in industrial collaborative robotics: A literature review of the decade 2008-2017. *Advanced Robotics*, 33(15–16), 764–799.

Howard, A. G., Zhu, M., Chen, B., Kalenichenko, D., Wang, W., Weyand, T., Andreetto, M., & Adam, H. (2017). MobileNets: Efficient convolutional neural networks for mobile vision applications. arXiv preprint arXiv:1704.04861.

Islam, M. J., Fulton, M., & Sattar, J. (2019). Toward a generic diver-following algorithm: Balancing robustness and efficiency in deep visual detection. *IEEE Robotics and Automation Letters*, 4(1), 113–120.

Islam, M. J., Ho, M., & Sattar, J. (2019). Understanding human motion and gestures for underwater human-robot collaboration. *Journal of Field Robotics*, 36(5), 851–873.

Jensen, F. B., Kuperman, W. A., Porter, M. B., & Schmidt, H. (2011). *Computational ocean acoustics*. Springer Science & Business Media.

- Kakinuma, K., Hashimoto, M., & Takahashi, K. (2012). Outdoor pedestrian tracking by multiple mobile robots based on slam and gps fusion. In 2012 IEEE/SICE International Symposium on System Integration (SII) (pp. 422–427).
- Kalman, R. E. (1960). A new approach to linear filtering and prediction problems. *Journal of Basic Engineering*, 82(1), 35.
- Kamal, S., Mohammed, S. K., Pillai, P. R. S., & Supriya, M. H. (2013). Deep learning architectures for underwater target recognition. In 2013 Ocean Electronics (SYMPOL) (pp. 48–54).
- Kasetkasem, T., Worasawate, D., Tipsuwan, Y., Thienviboon, P., & Hoonsuwan, P. (2017). A pinger localization algorithm using sparse representation for autonomous underwater vehicles. In 2017 14th International Conference on Electrical Engineering/Electronics, Computer, Telecommunications and Information Technology (ECTI-CON) (pp. 533–536).
- Kim, B., & Yu, S. (2017). Imaging sonar based real-time underwater object detection utilizing adaboost method. In 2017 IEEE Underwater Technology (UT) (pp. 1–5).
- Kim, D., Lee, D., Myung, H., & Choi, H. (2012). Object detection and tracking for autonomous underwater robots using weighted template matching. In 2012 Oceans-Yeosu (pp. 1–5).
- LeCun, Y., Bengio, Y., & Hinton, G. (2015). Deep learning. *Nature*, 521(7553), 436–444.
- Lee, P.-M., Jeon, B.-H., & Kim, S.-M. (2003). Visual servoing for underwater docking of an autonomous underwater vehicle with one camera. In *Oceans 2003. Celebrating the Past ...Teaming Toward the Future* (Vol. 2, pp. 677–682) (IEEE Cat. No.03CH37492)
- Lee, S. (2017). Deep learning of submerged body images from 2d sonar sensor based on convolutional neural network. In 2017 IEEE Underwater Technology (UT) (pp. 1–3).
- Lekkala, K. K., & Mittal, V. K. (2016). Simultaneous aerial vehicle localization and human tracking. In 2016 IEEE Region 10 Conference (TENCON) (pp. 379–383).
- Li, Y., Chen, Y., Wang, N., & Zhang, Z. (2019). Scale-aware trident networks for object detection. In *Proceedings of the IEEE international conference on computer vision* (pp. 6054–6063).
- Mamdani, E. H., & Baaklini, N. (1975). Prescriptive method for deriving control policy in a fuzzy-logic controller. *Electronics Letters*, 11(25), 625–626.
- Mandić, F., Rendulić, I., Mišković, N., & Nad, Đ. (2016). Underwater object tracking using sonar and USBL measurements. *Journal of Sensors*, 1–10. <https://doi.org/10.1155/2016/8070286>
- Mišković, N., Bibuli, M., Birk, A., Caccia, M., Egi, M., Grammer, K., Marroni, A., Neasham, J., Pascoal, A., Vasilijević, A., & Vukić, Z. (2015). Overview of the fp7 project "caddy-cognitive autonomous diving buddy". In *OCEANS 2015-Genova* (pp. 1–5).
- Petillot, Y. R., Reed, S. R., & Bell, J. M. (2002). Real time auv pipeline detection and tracking using side scan sonar and multi-beam echosounder. In *OCEANS '02 MTS/IEEE* (Vol. 1, pp. 217–222).
- Prabowo, M. R., Hudayani, N., Purwiyanti, S., Sulistiyanti, S. R., & Setyawan, F. X. A. (2017). A moving objects detection in underwater video using subtraction of the background model. In 2017 4th International Conference on Electrical Engineering, Computer Science and Informatics (EECSI) (pp. 1–4).
- Preisig, J. (2007). Acoustic propagation considerations for underwater acoustic communications network development. *ACM SIGMOBILE Mobile Computing and Communications Review*, 11(4), 2–10.
- Preston, V., Salumäe, T., & Kruusmaa, M. (2018). Underwater confined space mapping by resource-constrained autonomous vehicle. *Journal of Field Robotics*, 35(7), 1122–1148.
- Redmon, J., & Farhadi, A. (2018). Yolov3: An incremental improvement. arXiv.
- Remmas, W. (2017). *Modélisation et commande du robot sous-marin bio-inspiré U-CAT* (Master's thesis). National Polytechnic School of Constantine, Algeria.
- Ren, P., Fang, W., & Djahel, S. (2017). A novel yolo-based real-time people counting approach. In 2017 International Smart Cities Conference (ISC2) (pp. 1–2).
- Robinson, H., MacDonald, B., & Broadbent, E. (2014). The role of healthcare robots for older people at home: A review. *International Journal of Social Robotics*, 6(4), 575–591.
- Salumäe, T., Chemori, A., & Kruusmaa, M. (2016). Motion control architecture of a 4-fin u-cat auv using dof prioritization. In 2016 IEEE/RSJ International Conference on Intelligent Robots and Systems (IROS) (pp. 1321–1327).
- Salumäe, T., Chemori, A., & Kruusmaa, M. (2019). Motion control of a hovering biomimetic four-fin underwater robot. *IEEE Journal of Oceanic Engineering*, 44(1), 54–71.
- Sattar, J., & Dudek, G. (2007). Where is your dive buddy: tracking humans underwater using spatio-temporal features. In 2007 IEEE/RSJ International Conference on Intelligent Robots and Systems (pp. 3654–3659).
- Sattar, J., & Dudek, G. (2009). Underwater human-robot interaction via biological motion identification. In *Robotics: Science and Systems*.
- Shkurti, F., Chang, W., Henderson, P., Islam, M. J., Higuera, J. C. G., Li, J., Manderson, T., Xu, A., Dudek, G., & Sattar, J. (2017). Underwater multi-robot convoying using visual tracking by detection. In 2017 IEEE/RSJ International Conference on Intelligent Robots and Systems (IROS) (pp. 4189–4196).
- Song, Y., Zhu, Y., Li, G., Feng, C., He, B., & Yan, T. (2017). Side scan sonar segmentation using deep convolutional neural network. In *OCEANS 2017-Anchorage* (pp. 1–4).
- Viola, P., & Jones, M. (2001). Rapid object detection using a boosted cascade of simple features. In *Proceedings of the 2001 IEEE Computer Society Conference on Computer Vision and Pattern Recognition, CVPR 2001* (Vol. 1, p. 1).
- Xia, Y., & Sattar, J. (2019). Visual diver recognition for underwater human-robot collaboration. In 2019 International Conference on Robotics and Automation (ICRA) (pp. 6839–6845). IEEE.
- Yagimli, M., & Varol, H. S. (2009). A GPS-based system design for the recognition and tracking of moving targets. In 2009 4th International Conference on Recent Advances in Space Technologies (pp. 6–12).
- Yu, S.-C., Ura, T., Fujii, T., & Kondo, H. (2001). Navigation of autonomous underwater vehicles based on artificial underwater landmarks. In *MTS/IEEE Oceans 2001. An Ocean Odyssey. Conference Proceedings* (Vol. 1, pp. 409–416). (IEEE Cat. No. 01CH37295).
- Zhao, S., Lu, T.-F., & Anvar, A. (2009). Automatic object detection for auv navigation using imaging sonar within confined environments. In 2009 4th IEEE Conference on Industrial Electronics and Applications (pp. 3648–3653).
- Zou, J., & Tseng, Y. (2012). Visual track system applied in quadrotor aerial robot. In 2012 Third International Conference on Digital Manufacturing Automation (pp. 1025–1028).

SUPPORTING INFORMATION

Additional supporting information may be found online in the Supporting Information section.

How to cite this article: Remmas W, Chemori A, Kruusmaa M. Diver tracking in open waters: A low-cost approach based on visual and acoustic sensor fusion. *J Field Robotics*. 2021;38: 494–508. <https://doi.org/10.1002/rob.21999>

Appendix 2: Publication II

Publication II:

Walid Remmas, Ahmed Chemori, and Maarja Kruusmaa. Inverse-model intelligent control of fin-actuated underwater robots based on drag force propulsion. *Ocean Engineering*, 239:109883, 2021



Contents lists available at ScienceDirect

Ocean Engineering

journal homepage: www.elsevier.com/locate/oceaneng

Inverse-model intelligent control of fin-actuated underwater robots based on drag force propulsion

Walid Remmas^{a,b,*}, Ahmed Chemori^b, Maarja Kruusmaa^a

^a Department of Computer Systems, Tallinn University of Technology, Tallinn, Estonia

^b LIRMM, University of Montpellier, CNRS, Montpellier, France

ARTICLE INFO

Keywords:

Fin-actuated robot
Modelling
Underwater robot
Biomimetic
AUV

ABSTRACT

Fin-actuated underwater robots usually control motion by changing the locomotion primitives of the fins, such as frequency, amplitude, phase shift, or in more complicated cases also the angle of attack. Modelling the generated thrust by an oscillating fin results in a highly non-linear model, thus making it difficult to derive a respective inverse model. In this work, we derived a dynamic model relating the generated thrust to the fins oscillating amplitude and frequency, and proposed the associated inverse-model. The proposed model's accuracy is evaluated by comparing both the theoretical and measured generated thrust for various frequencies. Furthermore, using the proposed fin model, we demonstrate hovering experimental results with the robot U-CAT. The results demonstrate the possibility to control fin-actuated vehicles using the proposed model to generate the fins oscillation amplitudes as control input.

1. Introduction

Underwater vehicles are capable of operating in different environments considered to be beyond the reach of human divers. Moreover, they can be used in hazardous environments and can operate as long as needed when tethered. Bio-inspired Autonomous Underwater Vehicles particularly, have received considerable consideration (Triantafyllou et al., 2004; Mannam et al., 2020), as they promise to harness optimization over millions of years of evolution.

Biorobotic technology has become one of the hot-spots in underwater robotics research in recent years (RB et al., 2018; Scaradozzi et al., 2017). Inspired by the speed and agility of marine animals, the robotics community has created new propulsion systems that are able to imitate nature. Airfoil propulsion is common for many species. Flying animals (birds, bats, insects) generate both thrust and lift with flapping motions, while certain marine species use fin flapping to generate thrust mainly. Much effort has recently been made in the design of fin-actuated robots (Morgansen et al., 2007; Wen et al., 2011; Georgiades et al., 2009; Licht et al., 2004).

Bio-inspired propulsion offers various advantages over conventional propellers: (i) Fin-actuated vehicles offer better locomotion efficiency (Yu and Wang, 2005). (ii) Biomimetic fins are environmentally benign, whereas screw propellers or turbines may harm the aquatic vegetation and animals (Kruusmaa et al., 2020). (iii) Fins can be used for propulsion, maneuvering, and motion stabilization (Weymouth, 2016). Fin-actuated underwater vehicles (Licht, 2008) usually

control motion by changing the locomotion primitives of the fins, such as frequency, amplitude, phase shift, or in more complicated cases also the angle of attack, stiffness or surface area. Previously, fin-actuated robots have been controlled using adaptive control (Plamondon and Nahon, 2013), PID control (Geder et al., 2013b), RISE control (Chemori et al., 2016), fuzzy logic control (Remmas et al., 2021), prioritization-based control (Salumae et al., 2016) and bio-inspired CPG control (Yao et al., 2013; Bal et al., 2019).

To effectively control fin-actuated robots, a dynamic model relating the fin's actuation parameters (fin oscillations' amplitude, angle of attack, and frequency) to the generated thrust is essential. Several studies have been carried out in the literature to model the generated thrust by a flapping foil. In Plamondon and Nahon (2009), the authors defined the average thrust as a function of the mass flow rate. The amplitude and frequency of the oscillating paddle are computed based on an optimization function. However, the proposed function is valid only for a certain range of mass flow rates. Authors in Giguere et al. (2006) proposed a model based on lift force generated by the fins. The proposed model was used to simulate the robot's dynamics. The studies in Ramasamy and Singh (2010), Singh et al. (2004) and Geder et al. (2013a) uses computational fluid dynamics to parameterize the forces generated by a mechanical flapping foil. The drawback is that the proposed model cannot run in real-time on robots with constrained computing capabilities. Authors in Harper et al. (1998) proposed a

* Corresponding author at: Department of Computer Systems, Tallinn University of Technology, Tallinn, Estonia.

E-mail addresses: walid.remmas@taltech.ee (W. Remmas), ahmed.chemori@lirmm.fr (A. Chemori), maarja.kruusmaa@taltech.ee (M. Kruusmaa).

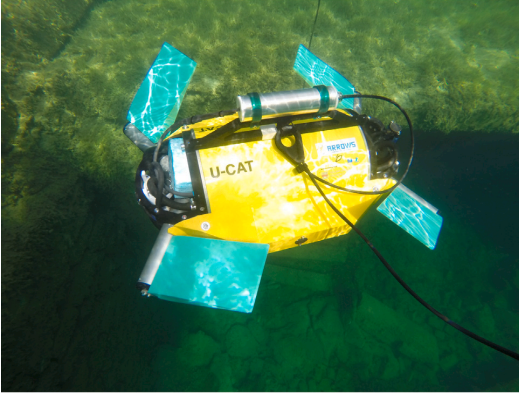


Fig. 1. View of U-CAT bio-mimetic AUV operating in real conditions in Rumm Lake in Estonia. The flippers (flexible green parts) are made of Silicon and actuated with Brushless DC (BLDC) motors. (For interpretation of the references to colour in this figure legend, the reader is referred to the web version of this article.)

model which is presented as a low-order set of ordinary differential equations. Nevertheless, the approach in the paper involved only open-loop control.

In the present paper we propose a solution that allows the control of fin-actuated vehicles. A nonlinear analytical model based on drag-force generation is proposed and identified using experimental data. Most importantly we derived its associated inverse model, to control the generated thrust through amplitude and frequency modulation. The model is validated experimentally to control two degrees of freedom of a fin-actuated underwater robot U-CAT (Salumäe et al., 2014). The main contributions of this paper are as follows:

(1): An analytical model relating the fins' generated thrust force to the fins oscillating amplitudes and frequency is investigated.

(2): An associated inverse model is also derived, discussed, and validated experimentally. The proposed inverse model is used to compute the required fins oscillating amplitude and frequency to control the robot.

(3): The proposed fin-model is implemented and validated experimentally for various operating conditions on the real fin-actuated robot to control its depth and yaw angle using amplitude modulation with various oscillating frequencies as control input.

The rest of the paper is organized as follows. Section 2 introduces the description and modelling of U-CAT biomimetic underwater vehicle. Then, Section 3 is devoted to the proposed nonlinear analytical model for U-CAT soft fins, as well as the thrust control allocations. The controller is discussed in Section 4 and the obtained experimental results are presented and discussed in Section 5. The paper ends with some concluding remarks and future work directions, in Section 6.

2. U-CAT biomimetic AUV: Description and modelling

This section is devoted to the description of U-CAT biomimetic AUV, as well as its dynamic modelling.

2.1. Description of U-CAT biomimetic AUV

U-CAT (cf. Fig. 1) is an autonomous biomimetic underwater robot developed within the European Union 7th Framework project ARROWS (Salumäe et al., 2014) (Archaeological Robot Systems for the World Seas). As opposed to other bio-inspired underwater vehicles, the four-finned design of this vehicle is motivated solely by the end-user requirements and environmental constraints of the tasks in shipwreck

Table 1

Main technical specifications of the U-CAT robot.

Technical specification	Specification/Description
Attitude sensor	MPU-6050 IMU
Depth sensor	GEMS 22CS Series Pressure Sensor
Batteries	4x HP Compaq NX8200 8cell batteries
Maximal speed (surge)	0.25 m/s
Maximal depth	100 m
Autonomy	~6 h
Mass	19 kg
Dimensions	560 mm × 329 mm × 258 mm
Fins' material	Zhermack Elite Double 22

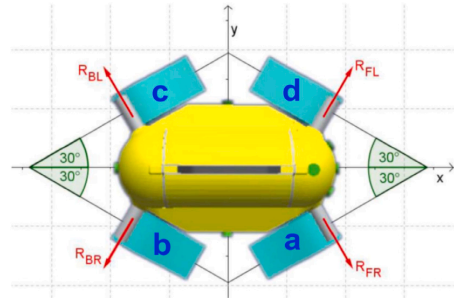


Fig. 2. Definition of the four fins and illustration of their initial configuration in hover mode.

inspection. Among others, it should closely video-inspect underwater objects. To fulfil the needs of shipwreck inspection for archaeological applications, U-CAT has been developed with the following main design requirements (Salumäe et al., 2014): (i) The main interest is the video footage from the interior of the shipwreck to identify objects of interest, (ii) The robot has to penetrate in confined spaces, accordingly, it should be small and highly maneuverable, (iii) The vehicle must also be capable of silent motion in order to not disturb the bottom sediments that would make visual observations impossible, (iv) The vehicle has to be untethered as the cable would significantly constrain the vehicle motions inside the wreck, (v) The cost of the vehicle has to be affordable for archaeologists with a limited budget. U-CAT has been specifically designed to meet all these end-user requirements of underwater archaeologists. Consequently, a 4-flipper design was emerged to control its six DOFs. The four motors actuating the fins are oriented as illustrated in Fig. 2. This configuration allows the robot to be holonomic. The fins were designed to point outwards to have more force generated in surge direction, as control in sway direction is only used for slow and precise movements within confined spaces. Moreover, the robot's centre of mass is positioned slightly below its centre of buoyancy, which makes U-CAT naturally stable in roll in pitch. The four independently driven flippers are used to achieve a high maneuverability in six DOFs, as illustrated in Fig. 3. Further technical specifications about U-CAT are detailed in Table 1.

2.2. Hydrodynamic model of the vehicle

Through considering inertial generalized forces, gravity and buoyancy, hydrodynamic effects and generalized forces, the dynamic model of an underwater vehicle (Fossen, 2002) may be expressed as follows:

$$M \dot{v} + C(v)v + D(v)v + g(\eta) = \tau \quad (1)$$

$$\dot{\eta} = J(\eta)v \quad (2)$$

where $\eta = [x, y, z, \varphi, \theta, \psi]^T$, $v = [u, v, w, p, q, r]^T$ represent the vectors of the vehicle positions in the earth-fixed frame R_e and the velocities

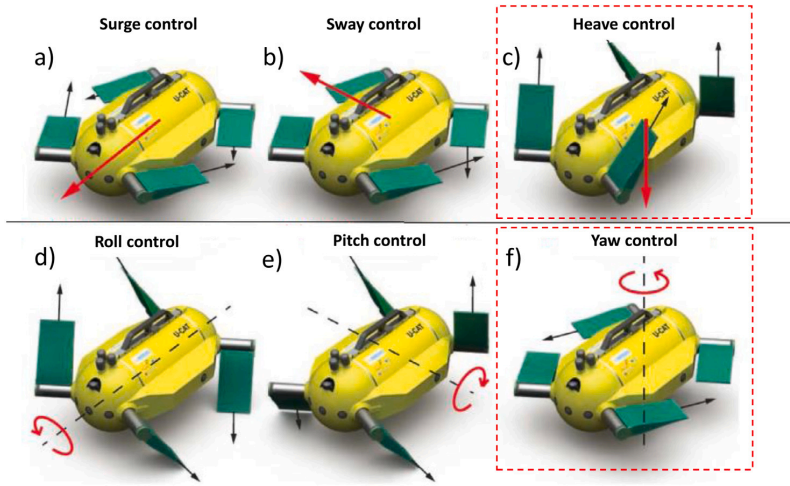


Fig. 3. Illustration of how the four independently driven flippers are used to separately actuate the six DOFs of the robot. The DOFs framed in red are the subject of the actual study regarding control (i.e. depth and yaw).

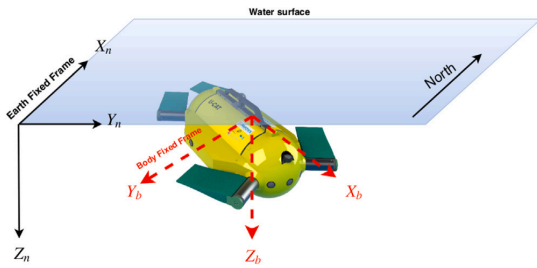


Fig. 4. Illustration of the Earth Fixed Frame R_n (North East Down convention) and the robot's Body Fixed Frame R_b .

in the body-fixed frame R_b respectively (cf. Fig. 4). $J(\eta) \in \mathbb{R}^{6 \times 6}$ represents a transformation matrix, mapping from the body-fixed frame to the earth-fixed frame. The matrices M , C , and D denote the inertia including the added mass, the Coriolis-centripetal including the added mass, and the damping respectively. The vector g represents the gravitational/buoyancy forces and moments. The term τ represents the vector of control inputs.

Eq. (1) describes the dynamics of the system in six DOFs, including the three translations and the three rotations. The input vector $\tau \in \mathbb{R}^6$ considers six actions on the system to fully control it. The hydrodynamic parameters of this model have been experimentally identified on U-CAT prototype.

3. Fin modelling and thruster control allocation

U-CAT has a special four-fin actuation system, different from other fins-based biomimetic actuated robots. In this section we are interested in explaining how the robot fins are modelled using mathematical equations as well as the thrust control allocation. These mathematical relationships should be able to relate the control action (i.e. the amplitude of oscillations of the fins or their frequency) to the thrust generated forces by the fins.

3.1. Fin modelling

The thrust generation by fins can be classified into *drag-based* and *lift-based* propulsion (Vogel, 2003). The amazing quick fish motions are mainly generated by an impacting force caused by a viscous drag known as drag-based thrust related to vortex generation (Ahlborn et al., 1997). However, lift-based thrust is not very suited for quick motions, since it is generated in a continuous flow with an appropriate angle of attack of the fins, as observed in large fish with high-speed swimming. In the case of U-CAT, its actuation fins can be considered as caudal fins (i.e. tail fins). The oscillatory locomotion of a tail fin may generate thrust by a propulsive flow that is directed backward (Sfakiotakis et al., 1999). When it comes to the problem of control of such robots (i.e. biorobotic flapping fin-actuated robots), the need of a model characterizing the relationship between the fin actuation parameters and the generated thrust force, can be noticed.

As illustrated in Fig. 5, three main parameters can fully characterize the generated thrust; namely (i) the amplitude of oscillations, (ii) the frequency of oscillations, and (iii) the angle of attack. In the sequel, an analysis is made to clearly explain how a needed thrust force is converted into fins oscillating magnitude (assuming a constant oscillating frequency), for the case of U-CAT. Two models will be introduced, a simple empirical model and nonlinear analytical model.

3.1.1. The first fin model: A simple empirical fin model

The first proposed fin model was used in Chemori et al. (2016) for the case of depth control of U-CAT. The idea behind the proposed fin model was to find a relationship between the generated thrust force and the oscillating amplitude, since this last one was chosen as the control input of the hydrodynamic model of the vehicle. This relationship was experimentally identified on the test-bed of U-CAT leading to a second order polynomial function between F and θ . The experimental procedure consists in generating oscillations of the fin for different values of the amplitude and the frequency and measure the generated thrust force. As reported in Salumäe et al. (2019), the obtained experimental results are summarized in the curves of Fig. 6. For instance, for the case of an oscillating frequency of 1.1 Hz, the following relationship between the required thrust force and the oscillating amplitude was obtained based on a polynomial interpolation (Chemori et al., 2016):

$$\theta = -0.01170 \left(\frac{F}{4} \right)^2 + 0.4363 \left(\frac{F}{4} \right) + 0.2480 \quad (3)$$

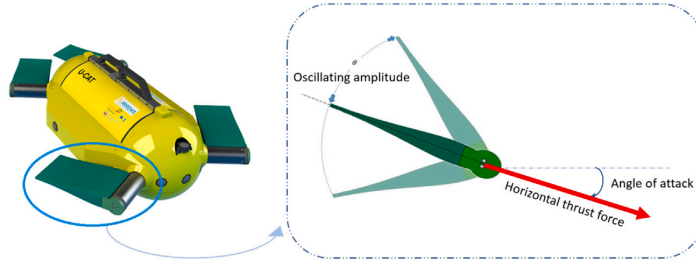


Fig. 5. Illustration of the oscillating motion on one fin and its main characteristics.

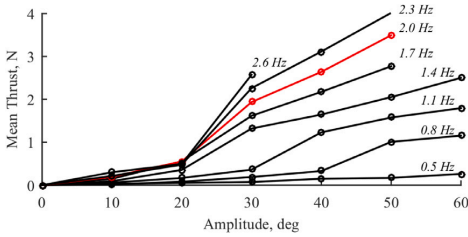


Fig. 6. Evolution of the generated mean fin thrust for different actuation parameters (oscillation amplitude ranging from 0 to 60° and oscillation frequency ranging from 0.5 Hz to 2.6 Hz) (Salumäe et al., 2019).

where θ denotes the oscillating amplitude, and F stands for the generated thrust force by the four fins of the robot.

3.1.2. The proposed fin model: A nonlinear analytical model

In the aim of improving the model of the fins and its fidelity, a more advanced model had to be computed. We investigate a drag-based force model to estimate the generated thrust by an oscillating fin. In the oscillating motion of a fin (as illustrated in Fig. 5), the rotational force must be sufficient to overcome the inertia and drag. In Azuma (2006) the author proposed a force balance expression for fin paddling as a simple linear motion. Accordingly, to estimate the fin rotation required force, a rotational force balance had to be considered. Then the force balance of a rotating fin was expressed as a torque balance between the angular momenta of the oscillating motion of a tail fin and the drag as follows (Kikuchi et al., 2014):

$$I \frac{d\omega}{dt} = r_c(F_f - D_f) \tag{4}$$

$$D_f = \frac{1}{2} C_{d_{rot}} \rho (r_c \omega)^2 A_f = \frac{C_{d_{rot}}}{2} \rho V r_c \omega \tag{5}$$

where I denotes the inertia moment of the rotating fin, ω represents the angular velocity of the fin, F_f is the force for rotating the fin, r_c is the distance between the rotation axis and the centre of gravity of the fin, and D_f is the drag acting on the fin. $C_{d_{rot}}$ stands for the rotational drag coefficient, and A_f is the projection area of the fin. Eq. (5) can be reformulated differently to include momentum of the transported fluid whose volume is V . In other words, this implies that the fin converts the momentum of fluids to drag. The angular component in parallel to the swimming direction of the rotational force is used as thrust F . It can be expressed by the following relationship:

$$F = F_f \sin|\theta| = \left(\frac{C_{d_{rot}} \rho V r_c \omega}{2} + \frac{I}{r_c} \frac{d\omega}{dt} \right) \sin|\theta| \tag{6}$$

where θ is the angle of the fin, being the angle between the fin cord line and the thrust direction. Eq. (6) characterizes the instantaneous thrust generated by a rotating fin. The lift component is neglected

in our modelling approach since the main generated thrust for bio-inspired robots with low swimming velocities is drag-based. Moreover, neglecting the lift component makes the derivation of the inverse model analytically possible, and its implementation in real-time feasible.

Now the idea is to find the relationship between the oscillation amplitude and the generated thrust. A fin obtains the thrust force through a reaction of motion of the surrounding fluid induced by its rotation. The rotating fin translates the force of fin rotation into a thrust. In drag-based thrust generation, the thrust is related to drag, which is based on a momentum transfer theory (Schlichting, 1979). In fact, the fluid surrounding a rotating fin is pushed out at a velocity corresponding to the fin velocity, which accordingly enables the fin to obtain a drag as thrust. The theoretical thrust generated by a rotating fin was estimated by momentum theory, and can be expressed as follows (Kikuchi et al., 2014):

$$\bar{F} = \int \left(\frac{C_{d_{rot}} \rho V r_c \omega}{2} + \frac{I}{r_c} \frac{d\omega}{dt} \right) \sin|\theta| d\theta \tag{7}$$

where \bar{F} stands for time-averaged theoretical thrust during one cycle. Eq. (7) can be rewritten as follows:

$$\bar{F} = 2 \int_{-\theta_{max}}^{\theta_{max}} \left(\frac{C_{d_{rot}} \rho V r_c \omega}{2} + \frac{I}{r_c} \frac{d\omega}{dt} \right) \sin|\theta| d\theta \tag{8}$$

and due to symmetry, Eq. (8) can be rewritten as follows:

$$\bar{F} = 4 \int_0^{\theta_{max}} \left(\frac{C_{d_{rot}} \rho V r_c \omega}{2} + \frac{I}{r_c} \frac{d\omega}{dt} \right) \sin(\theta) d\theta \tag{9}$$

In the case of U-CAT control, we consider that the oscillating frequency is constant and we use the oscillation amplitude as a control input. Consequently, the angular acceleration $\frac{d\omega}{dt}$ will be equal to zero. Then, Eq. (9) may be reduced to:

$$\bar{F} = 2 \int_0^{\theta_{max}} (C_{d_{rot}} \rho V r_c \omega) \sin(\theta) d\theta \tag{10}$$

From Eq. (10), one can deduce the thrust:

$$\bar{F} = -2(C_{d_{rot}} \rho V r_c \omega) (\cos(\theta_{max}) - 1) \tag{11}$$

Now, the inversion of Eq. (11) leads to the expression of the control input (i.e the oscillating amplitude) in terms of the required thrust force, as follows :

$$\theta_{max} = \arccos \left(\frac{-\bar{F}}{2C_{d_{rot}} \rho V r_c \omega} + 1 \right) \tag{12}$$

knowing that $V = A_f \omega r_c$ we can express equation (12) in function of the needed thrust \bar{F} and the oscillating frequency f as follows:

$$\theta_{max} = \arccos \left(\frac{-\bar{F}}{8C_d \rho A_f (r_c \pi f)^2} + 1 \right) \tag{13}$$

In Eq. (13), all constants are known (as summarized in Table 2), and the coefficient C_d was identified based on the experimental fins' thrust data (Gkliva et al., 2018). A minimal RMS¹ error between the

¹ RMS: Root Mean Square.

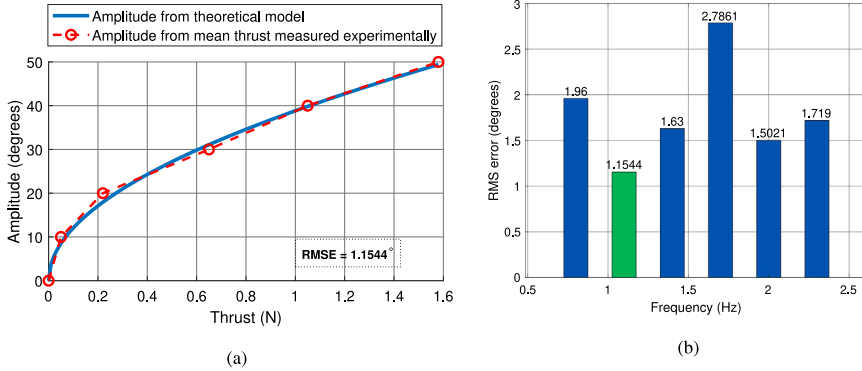


Fig. 7. (a): Validation of the proposed theoretical model for fin amplitude allocation, with experimental data for a constant frequency $f = 1.1$ Hz. (b): Evolution of the RMS error between the proposed theoretical model and the experimental data for different frequencies (in green $f = 1.1$ Hz, is the robot's fins' constant oscillating frequency used within our control scheme.)

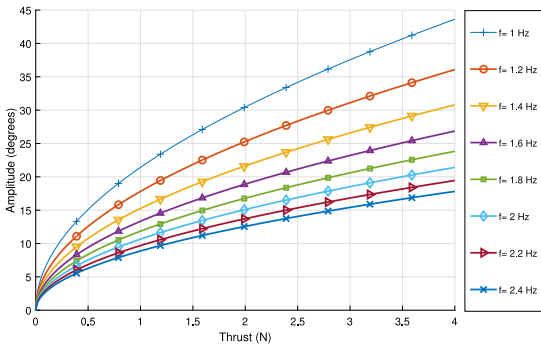


Fig. 8. Estimated single fin needed oscillating amplitude versus the required thrust for different oscillating frequencies.

Table 2
Summary of the fin's parametric values of the theoretical model.

ρ (kg/m ³)	A_f (m ²)	R_c (m)
997	0.02	0.1

experimental assessment of the fins and the proposed analytical model is obtained for $C_d = 0.23$. Fig. 7a depicts the evolution of the oscillating amplitude versus the horizontal thrust. It can be noticed that the proposed inverse solution matches the experimental data, with an RMS error of 1.154°. Moreover, the proposed analytical inverse model is valid for various frequencies, as illustrated in Fig. 7b, where the RMS error between the proposed model and the gathered experimental data is less than 3° for all the studied frequencies. This clearly shows that the proposed model is able to capture the main dynamics of the generated thrust.

Based on Eq. (11), one can plot the evolution of the required oscillating amplitude versus the thrust force and for different values of the oscillating frequency. The obtained result is displayed in Fig. 8, where we can observe different curves, each one corresponds to a chosen frequency. From this result, it can be noticed that for a given needed thrust force, the higher is the frequency the lower is the needed amplitude of oscillations. Using Eq. (13), a 3D plot of the needed control input (i.e. the fin oscillating amplitude) in function of the required thrust force and the fins oscillating frequency can be depicted. The obtained result is displayed in Fig. 9a. Besides, using Eq. (11), one can also plot in 3D the evolution of the thrust force versus both fins

oscillating amplitude and frequency. This result is illustrated in the 3D plot of Fig. 9b. According to the results of Fig. 9b, one can observe that low oscillation frequencies are not able to produce enough thrust force whatever the oscillating amplitude. However, with higher frequencies, one can have a fast thrust increasing with the oscillating amplitude.

In the sequel we will be interested in the thrust control allocation used in the proposed control scheme and implemented in U-CAT.

3.2. Thrust control allocation

In the previous section, the model of fins was presented, it enables to compute the needed oscillation amplitude for a given frequency to generate a required thrust force. Now let us tackle the problem of computation of the angle of attack in the case of multi-degrees-of-freedom control while dealing with the saturation of the control action. All these issues are addressed in the following.

3.2.1. Saturation

According to the fins model introduced above and particularly the curves of Figs. 9a and 9b, the thrust force depends mainly on two parameters, namely the oscillation frequency and the amplitude. For instance, for a frequency of 1.1 Hz, the maximum thrust force is 7.2 N, achievable by the four flippers of the robot (i.e. a thrust of 1.8 N generated by each flipper). The control vector that gathers the forces for the case of 3-DOF control (surge, depth and yaw) is denoted by $\tau = [F_x, F_z, F_\psi]$ and the normalized vector is expressed as:

$$\tau_{norm} = [F_{x_{norm}}, F_{z_{norm}}, F_{\psi_{norm}}].$$

3.2.2. Fins direction control

Since we are interested in the control of U-CAT AUV in hover mode (Salumäe et al., 2019), the fins orientation is initialized as follows:

$$\Phi_{initial} = [\Phi_a, \Phi_b, \Phi_c, \Phi_d]^T = [0, -\pi, -\pi, 0]^T \quad (14)$$

Where a and d stand for the right and left front fins respectively, b and c stand for the right and left back fins respectively (as illustrated in Fig. 2).

Using the prioritizing functions described in the previous section, the fins directions will be either in the same initial configuration (for surge action), or will be reoriented vertically (upward or downward

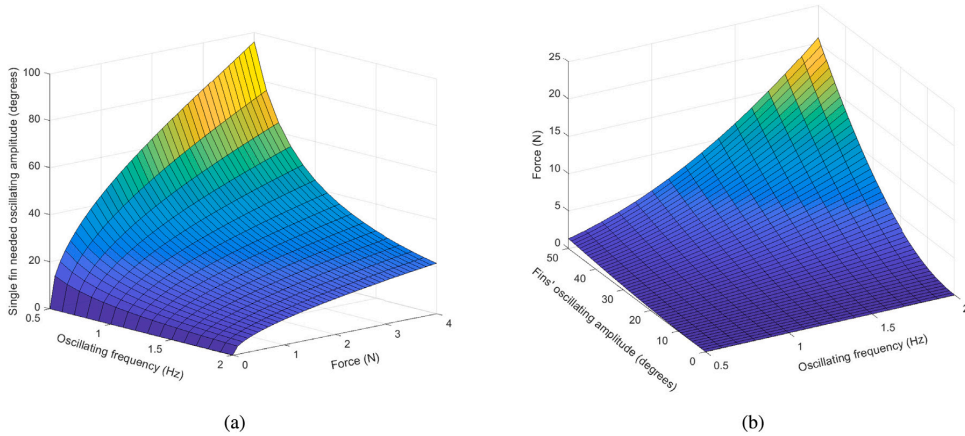


Fig. 9. (a): Evolution of a Single fin oscillating amplitude in function of the required thrust and the oscillating frequency. (b): Evolution of the estimated thrust generated by the four fins in function of the oscillating amplitude and oscillating frequency.

depending on the heave action direction) using the following equation:

$$\begin{bmatrix} \Phi_a \\ \Phi_b \\ \Phi_c \\ \Phi_d \end{bmatrix} = \begin{bmatrix} 0 \\ -\pi \\ -\pi \\ 0 \end{bmatrix} + \begin{bmatrix} 1 \\ 1 \\ 1 \\ 1 \end{bmatrix} F_{z_{norm}} \frac{\pi}{2} \quad (15)$$

This allows the robot to be in the configuration (a) illustrated in Fig. 3 when surge action is high, and to smoothly switch to configuration (c), the orientation angle varies from $\frac{\pi}{2}$ to $-\frac{\pi}{2}$ depending on the heave action. The yaw control is achieved by oscillating at the same time either fins *a* and *c* or fins *b* and *d*. Even if the yaw propulsion is more efficient when the fins are oriented as in the initial configuration (illustrated in Fig. 2), this equation allows to control three DOFs at the same time (namely surge, heave, and yaw).

3.2.3. Fins oscillating amplitude control

As stated above, three main parameters can be used in motion control of U-CAT; namely (i) the fins oscillation frequency, (ii) the fins oscillation amplitude, and (iii) angle of attack. In this work we consider that the oscillation frequency is constant (equal to 1.1 Hz), the two other parameters should be enough to control the motion of the vehicle. The oscillation amplitude is used as a control input to define the needed thrust force to achieve the desired motion. The angle of attack should be computed in real-time to define the best orientation of this thrust force as stated in the previous section. The required fins oscillating amplitude is given by the following relationship:

$$\theta(F) = \arccos\left(\frac{-F}{2C_{d,r} \rho V r_c \omega} + 1\right) \quad (16)$$

For instance, in the case of 3-DOF control (surge, depth, and yaw), the vector of amplitudes of oscillation of the fins is expressed by:

$$\begin{bmatrix} A_a \\ A_b \\ A_c \\ A_d \end{bmatrix} = \begin{bmatrix} H(F_x) & 1 & H(-F_y) \\ H(-F_x) & 1 & H(F_y) \\ H(-F_x) & 1 & H(-F_y) \\ H(F_x) & 1 & H(F_y) \end{bmatrix} \begin{bmatrix} \theta(F_x) \\ \theta(F_z) \\ \theta(F_y) \end{bmatrix} \quad (17)$$

where *a*, *b*, *c* and *d* stand for the different fins of U-CAT as illustrated in Fig. 2, *H*(.) is the Heaviside function and θ (.) is the function (16) converting the propulsion force into fins oscillating amplitude.

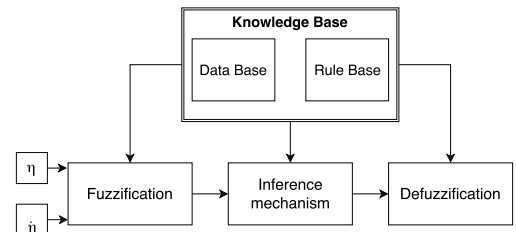


Fig. 10. Block diagram of the proposed Fuzzy logic controller.

4. Fuzzy logic control using the inverse fin model

In this study, a Mamdani fuzzy controller is implemented for trajectory tracking. The choice of this controller has been made based on a comparative study of various control schemes in different operating conditions (nominal case, buoyancy change, external disturbance rejection) (Remmas et al., 2017). The fuzzy controller gave the best results for heading and depth control in terms of tracking performance accuracy, and in terms of sudden changes (chattering) in the control force output. U-CAT is a highly maneuverable AUV, and is sensitively affected by sudden changes outputs. Therefore, the fuzzy logic controller was chosen as it gave the best performance.

To synthesize a Mamdani-based fuzzy controller, it is necessary to go through the following four steps:

- Step 1: Fuzzy knowledge base construction
- Step 2: Fuzzification of the system inputs
- Step 3: Execute all applicable rules in the rulebase
- Step 4: Defuzzification of the fuzzy outputs to get crisp values

The control architecture of the resulting fuzzy Inference System is illustrated in Fig. 10.

4.1. Fuzzy knowledge base

The Mamdani controller is mainly based on expertise and intuition, that can be exploited in two bases: a data base, and a rule base.

The data base includes all the fuzzy variables (the controller inputs and outputs: in our case the inputs are the robot depth and yaw angle $\eta \in \mathbb{R}^{2 \times 1}$ expressed in earth frame and their first-time derivative $\dot{\eta} \in$

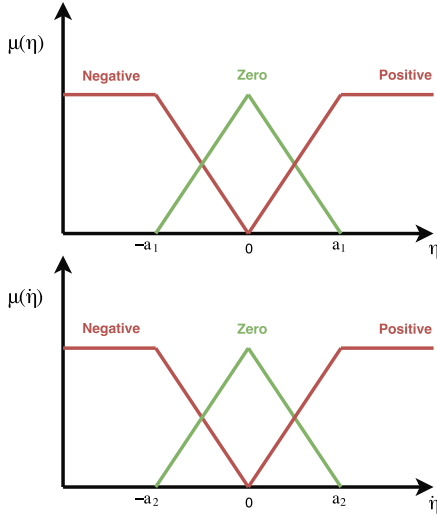


Fig. 11. View of the membership functions for both inputs η and $\dot{\eta}$ of the proposed fuzzy controller.

Table 3
Inference table of the proposed Mamdani fuzzy controller.

η	$\dot{\eta}$	Negative	Zero	Positive
Negative	Negative	Negative	Negative	Zero
Zero	Negative	Negative	Zero	Positive
Positive	Zero	Zero	Positive	Positive

$\mathbb{R}^{2 \times 1}$, the output of the controller will be the needed thrust force vector $\tau \in \mathbb{R}^{2 \times 1}$). The membership functions are illustrated in Fig. 11 and the rule table is summarized in 3.

The membership functions are of trapezoidal type, and are defined as follows:

$$\eta = \{[Negative, Zero, Positive], Trapezoidal, [-a_1, a_1]\}$$

$$\dot{\eta} = \{[Negative, Zero, Positive], Trapezoidal, [-a_2, a_2]\}$$

According to this inference table, our controller is characterized by a fuzzy knowledge base including the following nine rules:

- R1: If η is Negative **And** $\dot{\eta}$ is Negative **Then** the Force is Negative.
- R2: If η is Negative **And** $\dot{\eta}$ is Zero **Then** the Force is Negative.
- R3: If η is Negative **And** $\dot{\eta}$ is Positive **Then** the Force is Zero.
- R4: If η is Zero **And** $\dot{\eta}$ is Negative **Then** the Force is Negative.
- R5: If η is Zero **And** $\dot{\eta}$ is Zero **Then** the Force is Zero.
- R6: If η is Zero **And** $\dot{\eta}$ is Positive **Then** the Force is Positive.
- R7: If η is Positive **And** $\dot{\eta}$ is Negative **Then** the Force is Zero.
- R8: If η is Positive **And** $\dot{\eta}$ is Zero **Then** the Force is Positive.
- R9: If η is Positive **And** $\dot{\eta}$ is Positive **Then** the Force is Positive.

4.2. Fuzzification process

To use the Mamdani controller, the measured data collected with U-CAT sensors is converted into fuzzy values. To this end, the previously defined membership functions are used. Each value of the input vectors $\eta \in \mathbb{R}^{2 \times 1}$ and $\dot{\eta} \in \mathbb{R}^{2 \times 1}$ will have three membership degree values: $\mu_{Negative}$, μ_{Zero} and $\mu_{Positive}$ where μ_i take real values in the interval [0, 1].

4.3. Inference engine

In our case study for the control of the robot U-CAT, the chosen t -norm operation is the minimum t -norm, and the used t -conorm operation is the maximum t -conorm. The membership degrees of the nine rules are computed using t -norm operation as follows:

$$\begin{cases} \mu_{R1} = \min(\mu_{neg}(\tilde{\eta}), \mu_{neg}(\dot{\tilde{\eta}})) \\ \mu_{R2} = \min(\mu_{neg}(\tilde{\eta}), \mu_{zer}(\dot{\tilde{\eta}})) \\ \mu_{R3} = \min(\mu_{neg}(\tilde{\eta}), \mu_{pos}(\dot{\tilde{\eta}})) \\ \vdots \\ \mu_{R9} = \min(\mu_{pos}(\tilde{\eta}), \mu_{pos}(\dot{\tilde{\eta}})) \end{cases} \quad (18)$$

The variable $\tilde{\eta}$ denotes the error between the current and the desired state $\tilde{\eta} = \eta - \eta_d$, and $\dot{\tilde{\eta}}$ stands for its first-time derivative.

We conclude the membership degree of the output (thrust force to be generated by the robot's fins) using the chosen t -conorm as follows :

$$\begin{cases} \mu_{neg}(\tau) = \max(\mu_{R1}, \mu_{R2}, \mu_{R4}) \\ \mu_{zer}(\tau) = \max(\mu_{R3}, \mu_{R5}, \mu_{R7}) \\ \mu_{pos}(\tau) = \max(\mu_{R6}, \mu_{R8}, \mu_{R9}) \end{cases} \quad (19)$$

4.4. Defuzzification process

In the literature, the following five defuzzifying methods are the most used:

- Centroid of area (COA) method,
- Bisector of area (BOA) method,
- Mean of maximum (MOM) method,
- Smallest of maximum (SOM) method, and
- Largest of maximum (LOM) method.

In our case we have chosen to use the Centre Of Gravity (COG) method. Consequently, the output of the inference engine (representing the control input of the robot) will then be computed as follows:

$$\tau = \frac{c_1 \mu_{neg}(\tau) + c_2 \mu_{zer}(\tau) + c_3 \mu_{pos}(\tau)}{\mu_{neg}(\tau) + \mu_{zer}(\tau) + \mu_{pos}(\tau)} \quad (20)$$

where c_1 , c_2 and c_3 are constants. In our case $c_1 = -c_3$, $c_3 > 0$ and $c_2 = 0$, c_3 is the maximum achievable propulsion force by the four fins of the robot.

5. Experimental results

In this section, the obtained experimental results are presented and discussed. The experiments were carried out in a laboratory water-tank. The water-tank has a limited depth of approximately 1 metre, therefore, the desired depth trajectory was generated to satisfy this constraint. For all the presented scenarios, the desired depth trajectory varies from 0 to 0.8 m, and the desired yaw angle varies from 0 to 1.5 rads.

To demonstrate the performance and robustness of the proposed control scheme, different experimental scenarios have been studied for the case of 2-DOF (depth and yaw) motion control. Accordingly, the following experimental scenarios have been conducted:

- **Scenario 1 (Nominal case):** In this scenario, The robot is not subject to any external disturbance or uncertainty. To demonstrate the validity of the proposed fin model, this scenario was conducted five times using five different oscillating frequencies (0.8 Hz, 1.1 Hz, 1.4 Hz, 1.7 Hz, 2.0 Hz).
- **Scenario 2 (Robustness test):** A buoyancy foam was attached on the robot to increase its buoyancy in order to test the robustness of the control law towards this unexpected change. This experiment was conducted using a constant oscillating frequency (1.1 Hz).

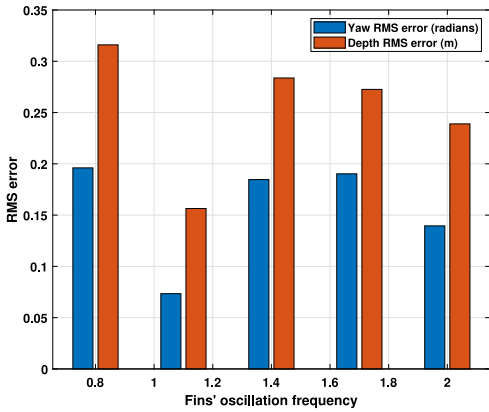


Fig. 12. RMS tracking errors for the nominal case using different fins oscillating frequencies.

- **Scenario 3 (External disturbances rejection):** the robot is subject to an external disturbing force. This experiment was conducted using a constant oscillating frequency (1.1 Hz).

It is worth to note that the parameters of the proposed controller are tuned for the nominal case and kept the same for all the other scenarios. The parameter to be varied for Scenario 2 is the robot's buoyancy B . For Scenario 3, the external disturbance is applied in such a way to affect mainly the yaw angle of the vehicle. The sampling period (sensors feedback sample time) was set to 100 ms. The controller's loop runs at a frequency of 5 Hz. The parameters of the proposed Mamdani fuzzy controller are summarized in Table 4.



Fig. 14. U-CAT pictured with an added buoyancy foam fixed on its top.

Table 4
Summary of the universe of discourse parameters used in the membership functions.

	a_1	a_2	C_1	C_2	C_3
Depth z	0.18	0.1	-8.5	0	8.5
Yaw ψ	0.24	0.08	-4.8	0	4.8

5.1. Experimental scenario 1: Control in nominal case

The RMS errors for depth and yaw tracking are depicted in Fig. 12. Fig. 12 shows that the proposed fin model gives satisfactory results for all the tested oscillating frequencies ranging from 0.8 Hz to 2 Hz. The best performance was obtained when the fin's oscillating frequency is set to 1.1 Hz, with RMS errors of 0.15 m and 4.01° for depth and yaw tracking respectively. The obtained tracking results with an oscillating frequency of 1.1 Hz are shown in Fig. 13. We notice on Fig. 13 that the proposed control scheme ensures satisfying results in the nominal

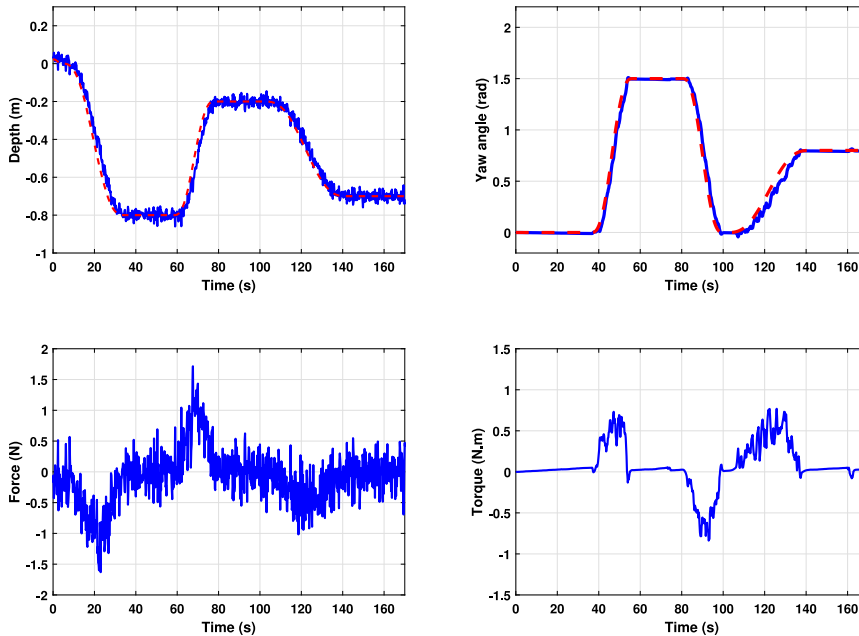


Fig. 13. Obtained experimental results using the proposed fin model and a fuzzy-logic controller in the nominal case (at an oscillating fins frequency of 1.1 Hz).

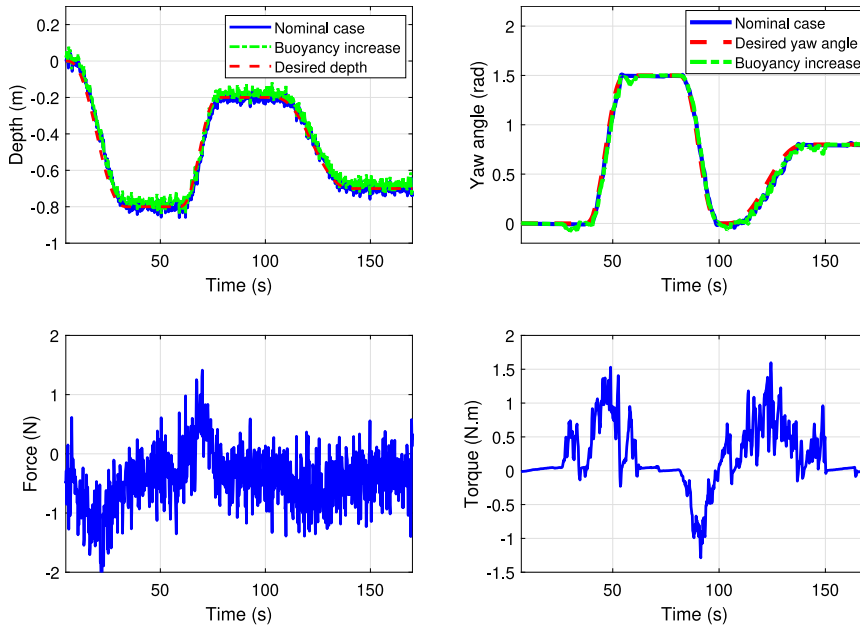


Fig. 15. Obtained experimental results using the proposed fuzzy-logic controller in the case of an increased buoyancy.

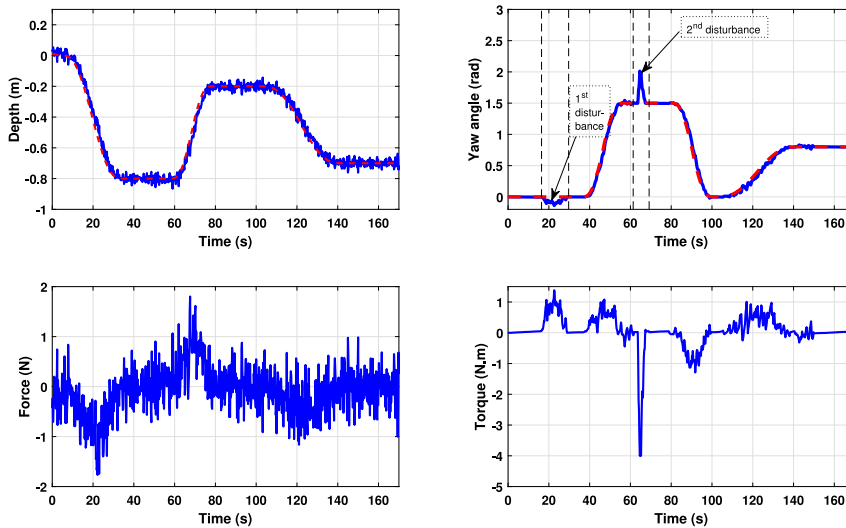


Fig. 16. Obtained experimental results using the proposed fuzzy logic control for external disturbances rejection scenario.

case. The robot is able to track the desired trajectories, even when both degrees of freedom are varying at the same time. The associated control signal for depth varies with a high frequency, but this results in small fins direction changes, and the control performance is not affected. In this case, both control signals are within the admissible region of the robot actuators.

5.2. Experimental scenario 2: Robustness test towards buoyancy change

In this scenario, a buoyancy foam of 300 cm³ was fixed on the top centre of the robot to increase its buoyancy, as shown in Fig. 14.

The robot floats to the surface when the fins are not actuated since the robot's neutral buoyancy is lost in this configuration. The obtained experimental results for this second scenario are depicted in Fig. 15. We can notice that, despite the increased buoyancy, the robot is able to track both desired trajectories for depth and yaw simultaneously. Slight oscillations can be noticed for yaw tracking, which is due to the robot's fins constant movement to compensate for the increased buoyancy. The depicted RMS errors for this scenario are 0.29 m and 10.42° for depth and yaw tracking respectively. Despite the increased buoyancy, the robot's tracking performance remains accurate.

5.3. Experimental scenario 3: External disturbances rejection

In this scenario, the robot was subject to an external disturbance. A stick was used to disturb the robot twice and orient it at a random angle. A first slight disturbance was applied while the robot was diving, then a stronger one was applied when robot reached a stable depth. The results are shown in Fig. 16. The time of the disturbances is shown in the top right plot of Fig. 16. For the first external disturbance, we notice that the robot recovered to the desired yaw angle, even-though it was in a diving phase (fins oriented vertically). For the second stronger disturbance, the robot managed to recover quicker since the fins were oriented horizontally when the robot was not in a diving phase, which produces a greater torque force by the four fins. The depicted RMS errors for this scenario are 0.17 m and 14.64° for depth and yaw tracking respectively.

6. Conclusion and future work

In this paper, the problem of dynamic modelling and control of fin-actuated underwater vehicles was tackled. In terms of modelling, beyond the dynamic model of the vehicle, the idea was to find an appropriate dynamic model representing the fins of the robot. The proposed model is based on a nonlinear analytical relationship between the amplitude and frequency of oscillations, and the needed thrust force to control fin-actuated vehicles. The model was validated experimentally evaluated by comparing the generated thrust for various operating frequencies. The results confirm the validity of the proposed model for various oscillating frequencies. The proposed model and its respective inverse model were both implemented on a fin-actuated AUV and several experiments were carried out and discussed. Using the proposed model, we show the possibility to use amplitude modulation with a predefined constant frequency to control a fin-actuated AUV. The obtained results show the effectiveness and robustness of the proposed model for numerous oscillating frequencies. In future work, we will investigate the accuracy of the proposed model in different Reynold regimes and different flow velocities. Moreover, we plan to develop solutions that allow to use both amplitude and frequency modulation as control inputs.

CRedit authorship contribution statement

Walid Remmas: Conception and design of study, Acquisition of data, Analysis and/or interpretation of data, Drafting the manuscript, Revising the manuscript critically for important intellectual content, Approval of the version of the manuscript to be published. **Ahmed Chemori:** Conception and design of study, Drafting the manuscript, Revising the manuscript critically for important intellectual content, Approval of the version of the manuscript to be published. **Maarja Kruusmaa:** Conception and design of study, Drafting the manuscript, Revising the manuscript critically for important intellectual content, Approval of the version of the manuscript to be published.

Declaration of competing interest

The authors declare that they have no known competing financial interests or personal relationships that could have appeared to influence the work reported in this paper.

Acknowledgements

This work is financed through Estonian Research Council Grant IUT-339.

References

- Ahlborn, B., Chapman, S., Stafford, R., Harper, R., 1997. Experimental simulation of the thrust phases of fast-start swimming of fish. *J. Exp. Biol.* (200), 2301–2312.
- Azuma, A., 2006. Swimming by Fanning. *American Institute of Aeronautics and Astronautics*, pp. 313–386.
- Bal, C., Koca, G.O., Korkmaz, D., Akpolat, Z.H., Ay, M., 2019. CPG-based autonomous swimming control for multi-tasks of a biomimetic robotic fish. *Ocean Eng.* 189, 106334.
- Chemori, A., Kuusmik, K., Salumae, T., Kruusmaa, M., 2016. Depth control of the biomimetic U-CAT Turtle-like AUV with experiments in real operating conditions. In: *Proceedings of the IEEE International Conference on Robotics and Automation (ICRA'16)*. Stockholm, Sweden. pp. 4750–4755.
- Fossen, T., 2002. *Marine Control Systems: Guidance, Navigation and Control of Ships, Rigs and Underwater Vehicles*. Marine Cybernetics, As, Trondheim.
- Geder, J.D., Ramamurti, R., Pruessner, M., Palmisano, J., 2013a. Maneuvering performance of a four-fin bio-inspired UUV. In: *2013 OCEANS-San Diego*. IEEE, pp. 1–7.
- Geder, J., et al., 2013b. Maneuvering performance of a four-fin bio-inspired UUV. In: *Oceans-San Diego*. pp. 1–7.
- Georgiades, C., Nahon, M., Buehler, M., 2009. Simulation of an underwater hexapod robot. *Ocean Eng.* 36 (1), 39–47.
- Giguere, P., Prahacs, C., Dudek, G., 2006. Characterization and modeling of rotational responses for an oscillating foil underwater robot. In: *2006 IEEE/RSJ International Conference on Intelligent Robots and Systems*. IEEE, pp. 3000–3005.
- Gkliva, R., Sfakiotakis, M., Kruusmaa, M., 2018. Development and experimental assessment of a flexible robot fin. In: *2018 IEEE International Conference on Soft Robotics (RoboSoft)*. IEEE, pp. 208–213.
- Harper, K.A., Berkemeier, M.D., Grace, S., 1998. Modeling the dynamics of spring-driven oscillating-foil propulsion. *IEEE J. Ocean. Eng.* 23 (3), 285–296.
- Kikuchi, K., Uehara, Y., Kubota, Y., Mochizuki, O., 2014. Morphological considerations of fish fin shape on thrust generation. *J. Appl. Fluid Mech.* 7 (4), 625–632.
- Kruusmaa, M., Gkliva, R., Tuhtan, J., Tuvikene, A., Alfrdsen, J., 2020. Salmon behavioural response to robots in an aquaculture sea cage. *R. Soc. Open Sci.* 7 (3), 191220.
- Licht, S.C., 2008. *Biomimetic Oscillating Foil Propulsion to Enhance Underwater Vehicle Agility and Maneuverability*. DTIC Document.
- Licht, S., Hover, F., Triantafyllou, M.S., 2004. Design of a flapping foil underwater vehicle. In: *Proceedings of the 2004 International Symposium on Underwater Technology (IEEE Cat. No. 04EX869)*. IEEE, pp. 311–316.
- Mannan, N.P.B., MahubAlam, M., Krishnankutty, P., 2020. Review of biomimetic flexible flapping foil propulsion systems on different planetary bodies. *Results Eng.* 100183.
- Morgansen, K.A., Triplett, B.I., Klein, D.J., 2007. Geometric methods for modeling and control of free-swimming fin-actuated underwater vehicles. *IEEE Trans. Robot.* 23 (6), 1184–1199.
- Plamondon, N., Nahon, M., 2009. A trajectory tracking controller for an underwater hexapod vehicle. *Bioinspiration Biomim.* 4 (3), 036005.
- Plamondon, N., Nahon, M., 2013. Adaptive controller for a biomimetic underwater vehicle. *J. Unmanned Veh. Syst.* 1, 1–13.
- Ramasamy, S., Singh, S.N., 2010. Biology-inspired robust dive plane control of non-linear AUV using pectoral-like fins. *Appl. Bionics Biomech.* 7 (2), 153–168.
- RB, A.A., Hemakumar, B., Prasad, M., 2018. Robotic fish locomotion & propulsion in marine environment: A survey. In: *2018 2nd International Conference on Power, Energy and Environment: Towards Smart Technology (ICEPE)*. IEEE, pp. 1–6.
- Remmas, W., Chemori, A., Belarbi, P.K., de Constantine, E.N.P., 2017. Modelling and Control of a Bio-Inspired Underwater Vehicle U-CAT (Master's thesis). National Polytechnic School of Constantine, Algeria.
- Remmas, W., Chemori, A., Kruusmaa, M., 2016. Diver tracking in open waters: A low-cost approach based on visual and acoustic sensor fusion. *J. Field Robot.* n/a. <http://dx.doi.org/10.1002/rob.21999>.
- Salumae, T., Chemori, A., Kruusmaa, M., 2016. Motion control architecture of a 4-fin U-CAT AUV using DOF prioritization. In: *Proceedings of the IEEE International Conference on Intelligent Robots and Systems (IROS'16)*. Daejeon, Korea. pp. 447–452.
- Salumae, T., Chemori, A., Kruusmaa, M., 2019. Motion control of a hovering biomimetic four-fin underwater robot. *IEEE J. Ocean. Eng.* 44 (1), 54–71. <http://dx.doi.org/10.1109/JOE.2017.2774318>.
- Salumae, T., Raag, R., Rebane, J., Ernits, A., Toming, G., Ratas, M., Kruusmaa, M., 2014. The ARROWS project: adapting and developing robotics technologies for underwater archaeology. In: *IEEE Oceans-St. John's*. pp. 1–5.
- Salumae, T., Raag, R., Rebane, J., Ernits, A., Toming, G., Ratas, M., Kruusmaa, M., 2014. Design principle of a biomimetic underwater robot u-cat. In: *Oceans-St. John's*, 2014. IEEE, pp. 1–5.
- Scaradozzi, D., Palmieri, G., Costa, D., Pinelli, A., 2017. BCF swimming locomotion for autonomous underwater robots: a review and a novel solution to improve control and efficiency. *Ocean Eng.* 130, 437–453.
- Schlichting, H., 1979. *Boundary-Layer Theory*, Vol. xxii. McGraw-Hill, New York.
- Sfakiotakis, M., Lane, D., Davies, J., 1999. Review of fish swimming modes for aquatic locomotion. *IEEE J. Ocean. Eng.* 24 (2), 237–252.

- Singh, S.N., Simha, A., Mittal, R., 2004. Biorobotic AUV maneuvering by pectoral fins: inverse control design based on CFD parameterization. *IEEE J. Ocean. Eng.* 29 (3), 777–785.
- Triantafyllou, M.S., Techet, A.H., Hover, F.S., 2004. Review of experimental work in biomimetic foils. *IEEE J. Ocean. Eng.* 29 (3), 585–594.
- Vogel, S., 2003. *Comparative Biomechanics : Life's Physical World*, Vol. xii. Princeton University Press.
- Wen, L., Wang, T., Wu, G., Liang, J., Wang, C., 2011. Novel method for the modeling and control investigation of efficient swimming for robotic fish. *IEEE Trans. Ind. Electron.* 59 (8), 3176–3188.
- Weymouth, G.D., 2016. Biologically inspired force enhancement for maritime propulsion and maneuvering. arXiv preprint [arXiv:1609.06559](https://arxiv.org/abs/1609.06559).
- Yao, G., et al., 2013. Development of a turtle-like underwater vehicle using central pattern generator. In: *IEEE International Conference on Robotics and Biomimetics (ROBIO)*. Shenzhen, China. pp. 44–49.
- Yu, J., Wang, L., 2005. Parameter optimization of simplified propulsive model for biomimetic robot fish. In: *Proceedings of the 2005 IEEE International Conference on Robotics and Automation*. IEEE, pp. 3306–3311.



Walid Remmas received his M.Sc. degree in control system engineering from the Polytechnic School of Constantine, Algeria, in 2017. He received his second M.Sc. degree in robotics from the University of Montpellier, France, in 2018. He is currently working toward the Ph.D. degree with the Centre for Biorobotics at Tallinn University of Technology, Estonia. His research interests include intelligent control, underwater robotics, and biorobotics.



Ahmed Chemori received the M.Sc. and Ph.D. degrees both in automatic control from the Grenoble Institute of Technology, Grenoble, France, in 2001 and 2005, respectively. He has been a Postdoctoral Fellow with the Automatic Control Laboratory, Grenoble, France, in 2006. He is currently a tenured Research Scientist in automatic control and robotics with the Montpellier Laboratory of Informatics, Robotics, and Microelectronics (LIRMM). His research interests include nonlinear adaptive, robust and predictive control and their real-time applications in robotics.



Maarja Kruusmaa received her Ph.D. in Computer Engineering from Chalmers University of Technology, in 2002. Currently, she heads the Center for Biorobotics at Tallinn University of Technology, Estonia. Her research interests include underwater robotics, biorobotics, flow sensing, and experimental fluid dynamics.

Appendix 3: Publication III

Publication III:

Walid Remmas, Ahmed Chemori, and Maarja Kruusmaa. Fault-tolerant control allocation for a bio-inspired underactuated auv in the presence of actuator failures: Design and experiments. *Ocean Engineering*, 15(20):54–66, 2023



Contents lists available at ScienceDirect

Ocean Engineering

journal homepage: www.elsevier.com/locate/oceaneng

Fault-tolerant control allocation for a bio-inspired underactuated AUV in the presence of actuator failures: Design and experiments[☆]

Walid Remmas^{a,b,*}, Ahmed Chemori^b, Maarja Kruusmaa^a^a Department of Computer Systems, Tallinn University of Technology, Tallinn, Estonia^b LIRMM, University of Montpellier, CNRS, Montpellier, France

ARTICLE INFO

Keywords:

Fault-tolerance
 Fin-actuated robot
 Control allocation
 Underwater robot
 Bio-inspired
 Sliding mode control

ABSTRACT

In this paper, we present the mathematical design and implementation of a fault-tolerant control scheme for a bio-inspired underwater robot with four flexible fins. The proposed active fault-tolerant control scheme re-configures the force allocation matrix using the elimination of column method, depending on which fin actuator is faulty. The proposed method allows to decouple the 6-DOF controllable underwater vehicle using the remaining three fins. The efficacy of the proposed method is assessed experimentally for trajectory tracking of an ellipsoidal-shaped trajectory using two different controllers, namely PID control and Sliding Mode control. The obtained results show that the combination of a sliding mode controller with the proposed fault-tolerant control allocation approach ensures an efficient trajectory tracking control performance when faults occur.

1. Introduction

Autonomous Underwater Vehicles (AUVs) are often deployed in challenging environments, where they should function reliably even in the presence of components' failures. Fault-tolerant Control (FTC) for underwater robots is of high importance, as it ensures a more robust and reliable autonomy, and reduces the risk of losing the vehicle during its mission.

The development of effective fault-tolerant control strategies for thruster-based underwater robots has been an active area of research in recent years (Antonelli, 2003; Liu et al., 2022a). Researchers have explored a range of techniques, dealing with the three main components of FTC: (i) fault detection, (ii) fault isolation, and (iii) fault accommodation. Fault detection involves recognizing when a failure has occurred that prevents the vehicle from operating correctly. Fault isolation involves identifying the cause of the failure and its location. Fault detection and isolation have been studied extensively, and the reader can refer to Antonelli (2003), Samy et al. (2011) and Liu et al. (2022a) and the references therein. Finally, fault accommodation, which is investigated in this work, involves controlling the vehicle to execute a desired task in the presence of a failure (see Fig. 1).

Fault accommodation has been addressed in the literature using two main approaches, namely active and passive FTC. Active fault-tolerant control, such as control reconfiguration (Ni, 2001; Sarkar et al., 2002) and control allocation (Omerdic and Roberts, 2004; Alwi and Edwards, 2008; bal, 2017), involves continuously monitoring the system for

potential failures and implementing corrective measures to prevent or mitigate the effects of any hardware failures. Passive fault-tolerant control (Liu et al., 2022; Wang et al., 2015), on the other hand, relies on the inherent redundancy and robustness of the system design to tolerate failures and continue operating without the need for active monitoring or intervention.

Most of the above-mentioned studies have focused on thruster-actuated designs of AUVs. However, fin-actuated AUVs have garnered significant attention (RB et al., 2018; Scaradozzi et al., 2017), due to their improved locomotion efficiency (Yu and Wang, 2005) and maneuverability (Weymouth, 2016). Despite this, the topic of fault-tolerant control for fin-actuated AUVs has received little attention in the literature. As far as the authors are aware, the only work on fault-tolerant control for a bio-inspired robot was published in Yang et al. (2018). The authors in Yang et al. (2018) proposed a passive FTC scheme using a central pattern generator based controller to correct the heading of fish-like robot with a multi-joint tail design.

This paper focuses on active fault-tolerant control of a four fin-actuated AUV in the presence of actuator failures. A control allocation switching mechanism is proposed to accurately re-distribute the fins' forces when a failure occurs. The proposed FTC method is based on the column elimination method (Yang et al., 1998; Podder and Sarkar, 1999; Fasano et al., 2015; Kadiyam et al., 2020), which is adapted and applied to the specific challenges posed by the highly coupled and highly nonlinear fin-based actuation system. The proposed FTC

[☆] This work was supported by ROBOTURTLE KIM Sea & Coast Research project.

* Corresponding author at: Department of Computer Systems, Tallinn University of Technology, Tallinn, Estonia.

E-mail addresses: walid.remmas@taltech.ee (W. Remmas), ahmed.chemori@lirmm.fr (A. Chemori), maarja.kruusmaa@taltech.ee (M. Kruusmaa).



Fig. 1. View of U-CAT robot during an inspection mission in a submerged structure.

scheme has been experimentally evaluated for controlling three degrees of freedom, using two different controllers: PID control and Sliding mode control. The main contributions of this paper are as follows:

- The development and application of FTC scheme for fin-actuated AUVs, which considers the unique challenges of highly coupled and highly nonlinear fin-based actuation systems.
- The experimental assessment of the proposed FTC scheme in controlling three degrees of freedom, using both PID and Sliding mode controllers.
- A comprehensive experimental analysis is provided, including multiple scenarios to assess the robustness and adaptability of the proposed FTC scheme.
- The work highlights the challenges and complexities of implementing fault-tolerant control on a highly coupled, under-actuated AUV, and discusses potential directions for future research in this area.
- The paper contributes to the understanding of how control allocation switching mechanisms can be employed effectively for fin-actuated AUVs, and can potentially serve as a foundation for future studies on fault-tolerant control for similar systems.
- To the best of the authors' knowledge, the presented work is the first one dealing with active fault-tolerant control of fin-actuated underwater robots.

The remainder of the paper is organized in the following manner: Section 2 provides a detailed description of the fin-actuated AUV and its dynamic model, and outlines the problem of control allocation for such systems. In Section 3, we present our proposed fault-tolerant control solution and the corresponding control laws that have been implemented. Section 4 presents the experimental setup, including the various scenarios that were studied, and presents the obtained results. Finally, we offer some concluding remarks and suggest potential directions for future work in Section 5.

2. Background and problem formulation

This section begins by presenting the fin-actuated AUV U-CAT (c.f. Fig. 1), as well as its hydro-dynamic model. We also presents the problem formulation, which outlines the specific problem that the proposed FTC scheme aims to solve.

2.1. U-CAT biomimetic AUV

U-CAT is a biomimetic underwater vehicle able to easily move and maneuver along six degrees of freedom using its four flexible

fins (Salumäe et al., 2014). It was designed for the inspection of confined environments such as shipwrecks and underwater structures autonomously or semi-autonomously. It was used in previous works for various applications, such as vision-based navigation (Preston et al., 2018), validation of control schemes for fin-actuated vehicles (Chemori et al., 2016; Meurer et al., 2019; Remmas et al., 2021a; Salumäe et al., 2016, 2019), and study of fish/robot interaction (Kruusmaa et al., 2020). Further technical details about U-CAT can be found in Remmas et al. (2021b).

2.2. AUV dynamic model

This subsection describes the kinematic and dynamic models of the AUV, moving in six degrees of freedom. It can be expressed, following Fossen's notation, as Fossen (2011):

$$\begin{aligned} \dot{\eta} &= J(q)v \\ M\dot{v} + n(\eta, v) &= \tau \\ n(\eta, v) &= C(v)v + D(v)v + g(\eta) \end{aligned} \quad (1)$$

where $\eta = [x, y, z, \Phi, \theta, \psi]^T \in \mathbb{R}^6$ represents the vector of the vehicle's position and orientation in the earth-fixed frame R_n , and $v = [u, v, w, p, q, r]^T \in \mathbb{R}^6$ represents the vector of linear and angular velocities in the body-fixed frame R_b . The matrix $M \in \mathbb{R}^{6 \times 6}$ is the mass matrix of the robot, $C(v) \in \mathbb{R}^{6 \times 6}$ denotes the Coriolis and centripetal matrix, $D(v) \in \mathbb{R}^{6 \times 6}$ is the hydrodynamic damping matrix, and $g(\eta) \in \mathbb{R}^6$ denotes the restoring forces and moments due to buoyancy and gravity. The generalized forces and moments on the vehicle, expressed in the body-fixed frame, are represented by $\tau = [\tau_x, \tau_y, \tau_z, \tau_\Phi, \tau_\theta, \tau_\psi]^T$.

The Jacobian $J(\eta)$ is expressed, using the Euler angles notation, to map the velocities expressed in R_b to the earth-fixed frame R_n such that:

$$J(\eta) = \begin{bmatrix} R(\eta) & 0_{3 \times 3} \\ 0_{3 \times 3} & T(\eta) \end{bmatrix} \quad (2)$$

with its inverse as follows:

$$J(\eta)^{-1} = \begin{bmatrix} R(\eta)^T & 0_{3 \times 3} \\ 0_{3 \times 3} & T(\eta)^T \end{bmatrix} \quad (3)$$

where the matrices $R(\eta)$ and $T(\eta)$ are defined as:

$$R(\eta) = \begin{bmatrix} c\psi c\theta & -s\psi c\theta & c\psi s\theta s\Phi & s\psi s\theta s\Phi + c\psi s\theta c\Phi \\ s\psi c\theta & c\psi c\theta & s\psi s\theta s\Phi & -c\psi s\theta s\Phi + s\psi s\theta c\Phi \\ -c\theta & & c\theta s\Phi & c\theta c\Phi \end{bmatrix}$$

$$T(\eta) = \begin{bmatrix} 1 & s\Phi t\theta & c\Phi t\theta \\ 0 & c\Phi & -s\Phi \\ 0 & \frac{s\Phi}{c\theta} & \frac{c\Phi}{c\theta} \end{bmatrix}$$

with $c = \cos(\cdot)$, $s = \sin(\cdot)$, and $t = \tan(\cdot)$.

2.3. Problem formulation of control allocation

Fin-actuated AUV's can achieve locomotion by moving their fins with an oscillatory profile (Low, 2011). For the motion control of U-CAT AUV, we propose to use the following oscillatory profile:

$$\varphi_i(t) = A_i \sin(\omega t) + \phi_i \quad i = 1 \dots 4 \quad (4)$$

where $\varphi_i(t)$ is the instantaneous angle of each fin i , A_i denotes the oscillating amplitude, ω the oscillating frequency, and ϕ_i the zero-direction angle. The indices $i = \{1, 2, 3, 4\}$ are allocated for the Front Right (FR), Rear Right (RR), Rear Left (RL), and Front Left (FL) fins, respectively.

When a fin is oscillating, we assume that it generates a constant thrust force f_i along the zero-direction angle ϕ_i , which is the mean thrust force generated from one flapping cycle (Ren et al., 2015;

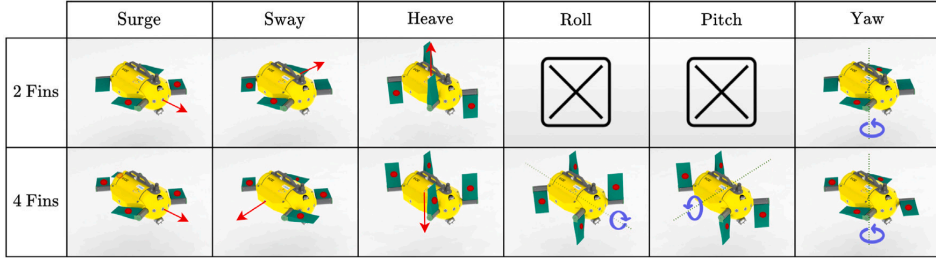


Fig. 2. Illustration of the various fin configurations allowing to control the robot in each DOF using either 2 or 4 fins. The actuated fins for each configuration are highlighted with a red dot.

Xie et al., 2018). The generated fin forces can then be mapped to body-frame wrench τ using the following nonlinear model:

$$\begin{aligned}
 \tau_x &= c\psi_f (c\phi_1 f_1 - c\phi_2 f_2 - c\phi_3 f_3 + c\phi_4 f_4) \\
 \tau_y &= s\psi_f (-c\phi_1 f_1 - c\phi_2 f_2 + c\phi_3 f_3 + c\phi_4 f_4) \\
 \tau_z &= s\phi_1 f_1 + s\phi_2 f_2 + s\phi_3 f_3 + s\phi_4 f_4 \\
 \tau_\phi &= M_\phi (s\phi_1 f_1 + s\phi_2 f_2 - s\phi_3 f_3 - s\phi_4 f_4) \\
 \tau_\theta &= M_\theta (-s\phi_1 f_1 + s\phi_2 f_2 + s\phi_3 f_3 - s\phi_4 f_4) \\
 \tau_\psi &= M_\psi (-c\phi_1 f_1 + c\phi_2 f_2 - c\phi_3 f_3 + c\phi_4 f_4)
 \end{aligned} \tag{5}$$

The constant $\psi_f = 30^\circ = 0.52$ rad, denotes the fin orientation angle in the body frame as illustrated in Fig. 3, and the constants $M_\phi = 0.15$, $M_\theta = 0.26$, and $M_\psi = 0.29$, denote the moment arm values along roll, pitch, and yaw axes, respectively.

The equation system described in (5) can be rewritten in a compact matrix form as $B[H_c, V_c]^T = \tau_n$, equivalent to:

$$\begin{bmatrix}
 C_h^1 & C_h^2 & C_h^3 & C_h^4 & C_v^1 & C_v^2 & C_v^3 & C_v^4 \\
 1 & -1 & -1 & 1 & 0 & 0 & 0 & 0 \\
 -1 & -1 & 1 & 1 & 0 & 0 & 0 & 0 \\
 0 & 0 & 0 & 0 & 1 & 1 & 1 & 1 \\
 0 & 0 & 0 & 0 & 1 & 1 & -1 & -1 \\
 0 & 0 & 0 & 0 & -1 & 1 & 1 & -1 \\
 -1 & 1 & -1 & 1 & 0 & 0 & 0 & 0
 \end{bmatrix}
 \begin{bmatrix}
 H_c \\
 V_c
 \end{bmatrix}
 = \tau_n \tag{6}$$

with $\tau_n = [\frac{\tau_x}{c\psi_f}, \frac{\tau_y}{s\psi_f}, \tau_z, \frac{\tau_\phi}{M_\phi}, \frac{\tau_\theta}{M_\theta}, \frac{\tau_\psi}{M_\psi}]^T$. The generated thrust forces, projected on the horizontal and vertical planes of the body-fixed frame, are denoted as follows:

$$H_c = [c\phi_1 f_1, c\phi_2 f_2, c\phi_3 f_3, c\phi_4 f_4]^T \tag{7}$$

$$V_c = [s\phi_1 f_1, s\phi_2 f_2, s\phi_3 f_3, s\phi_4 f_4]^T \tag{8}$$

The symbols C_h^i and C_v^i (for $i = 1 \dots 4$) are used as labels for the columns of the allocation matrix.

3. Proposed fault tolerant control unit

Before describing the proposed fault-tolerant control scheme (cf. Fig. 4), let us introduce the detailed steps to solve the control-allocation problem in the nominal case, i.e. where all fins are fully functional. The control allocation problem was solved in previous works following an empirical approach (Salumäe et al., 2016). In this study we present an analytical solution that solves the linear algebraic set of equations, presented in (6). The system is considered to be virtually over-actuated, since the fins have an infinite number of possible configurations. The simplest and straightforward solution would be to take directly the Moore–Penrose inverse (Penrose, 1955), such that $[H_c, V_c]^T = B^\dagger \tau_n$,

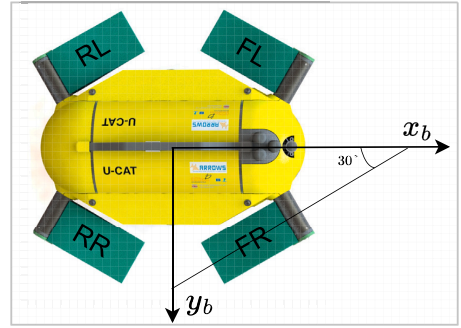


Fig. 3. Illustration of U-CAT's fins configuration. The robot front right, rear right, rear left, and front left are denoted by FR, RR, RL, and FL, respectively.

where $B^\dagger = B^T(BB^T)^{-1}$ results in the following:

$$B^\dagger = \frac{1}{4}
 \begin{bmatrix}
 1 & -1 & 0 & 0 & 0 & -1 \\
 -1 & -1 & 0 & 0 & 0 & 1 \\
 -1 & 1 & 0 & 0 & 0 & -1 \\
 1 & 1 & 0 & 0 & 0 & 1 \\
 0 & 0 & 1 & 1 & -1 & 0 \\
 0 & 0 & 1 & 1 & 1 & 0 \\
 0 & 0 & 1 & -1 & 1 & 0 \\
 0 & 0 & 1 & -1 & -1 & 0
 \end{bmatrix} \tag{9}$$

This leads to the following solution where the fins' forces and orientations are still coupled:

$$c\phi_1 f_1 = \frac{1}{4} \left(\frac{\tau_x}{c\psi_f} - \frac{\tau_y}{s\psi_f} - \frac{\tau_\psi}{M_\psi} \right) \tag{10}$$

$$c\phi_2 f_2 = \frac{1}{4} \left(-\frac{\tau_x}{c\psi_f} - \frac{\tau_y}{s\psi_f} + \frac{\tau_\psi}{M_\psi} \right) \tag{11}$$

$$c\phi_3 f_3 = \frac{1}{4} \left(-\frac{\tau_x}{c\psi_f} + \frac{\tau_y}{s\psi_f} - \frac{\tau_\psi}{M_\psi} \right) \tag{12}$$

$$c\phi_4 f_4 = \frac{1}{4} \left(\frac{\tau_x}{c\psi_f} + \frac{\tau_y}{s\psi_f} + \frac{\tau_\psi}{M_\psi} \right) \tag{13}$$

$$s\phi_1 f_1 = \frac{1}{4} \left(\tau_z + \frac{\tau_\phi}{M_\phi} - \frac{\tau_\theta}{M_\theta} \right) \tag{14}$$

$$s\phi_2 f_2 = \frac{1}{4} \left(\tau_z + \frac{\tau_\phi}{M_\phi} + \frac{\tau_\theta}{M_\theta} \right) \tag{15}$$

$$s\phi_3 f_3 = \frac{1}{4} \left(\tau_z - \frac{\tau_\phi}{M_\phi} + \frac{\tau_\theta}{M_\theta} \right) \tag{16}$$

$$s\phi_4 f_4 = \frac{1}{4} \left(\tau_z - \frac{\tau_\phi}{M_\phi} - \frac{\tau_\theta}{M_\theta} \right) \tag{17}$$

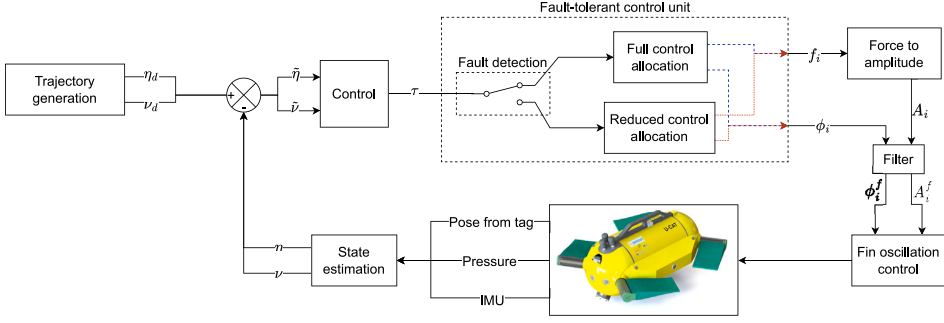


Fig. 4. Block Diagram illustration of the proposed fault-tolerant control strategy.

By dividing Eqs. (14) (15) (16) (17) by Eqs. (10) (11) (12) (13), respectively, we can deduce the zero-direction angles ϕ_1 , ϕ_2 , ϕ_3 and ϕ_4 as follows:

$$\phi_1 = \text{atan}\left(\frac{\tau_z + \frac{\tau_\phi}{M_\phi} - \frac{\tau_\theta}{M_\theta}}{\frac{\tau_x}{c\psi_f} - \frac{\tau_y}{s\psi_f} - \frac{\tau_\psi}{M_\psi}}\right) \quad (18)$$

$$\phi_2 = \text{atan}\left(\frac{\tau_z + \frac{\tau_\phi}{M_\phi} + \frac{\tau_\theta}{M_\theta}}{\frac{-\tau_x}{c\psi_f} - \frac{\tau_y}{s\psi_f} + \frac{\tau_\psi}{M_\psi}}\right) \quad (19)$$

$$\phi_3 = \text{atan}\left(\frac{\tau_z - \frac{\tau_\phi}{M_\phi} + \frac{\tau_\theta}{M_\theta}}{\frac{-\tau_x}{c\psi_f} + \frac{\tau_y}{s\psi_f} - \frac{\tau_\psi}{M_\psi}}\right) \quad (20)$$

$$\phi_4 = \text{atan}\left(\frac{\tau_z - \frac{\tau_\phi}{M_\phi} - \frac{\tau_\theta}{M_\theta}}{\frac{\tau_x}{c\psi_f} + \frac{\tau_y}{s\psi_f} + \frac{\tau_\psi}{M_\psi}}\right) \quad (21)$$

The fins' forces f_1 , f_2 , f_3 and f_4 are derived by respectively summing and squaring the Eqs. (10) and (14), (11) and (15), (12) and (16), and finally (13) and (17), which leads to the following expressions:

$$f_1 = \frac{1}{4} \sqrt{\left(\frac{\tau_x}{c\psi_f} - \frac{\tau_y}{s\psi_f} - \frac{\tau_\psi}{M_\psi}\right)^2 + \left(\tau_z + \frac{\tau_\phi}{M_\phi} - \frac{\tau_\theta}{M_\theta}\right)^2} \quad (22)$$

$$f_2 = \frac{1}{4} \sqrt{\left(\frac{-\tau_x}{c\psi_f} - \frac{\tau_y}{s\psi_f} + \frac{\tau_\psi}{M_\psi}\right)^2 + \left(\tau_z + \frac{\tau_\phi}{M_\phi} + \frac{\tau_\theta}{M_\theta}\right)^2} \quad (23)$$

$$f_3 = \frac{1}{4} \sqrt{\left(\frac{-\tau_x}{c\psi_f} + \frac{\tau_y}{s\psi_f} - \frac{\tau_\psi}{M_\psi}\right)^2 + \left(\tau_z - \frac{\tau_\phi}{M_\phi} + \frac{\tau_\theta}{M_\theta}\right)^2} \quad (24)$$

$$f_4 = \frac{1}{4} \sqrt{\left(\frac{\tau_x}{c\psi_f} + \frac{\tau_y}{s\psi_f} + \frac{\tau_\psi}{M_\psi}\right)^2 + \left(\tau_z - \frac{\tau_\phi}{M_\phi} - \frac{\tau_\theta}{M_\theta}\right)^2} \quad (25)$$

The derived solution presented above for controlling the fins' orientations and thrust forces is not optimal for accurately tracking time-varying trajectories, since all the four fins need to be actuated regardless of the control input τ . This may cause for instance the four fins to rotate 180 degrees when the surge component changes its sign. To tackle this issue, we propose to take advantage of the symmetrical configuration of U-CAT fins. Indeed, for forces and torques produced in the horizontal plane of the body-fixed frame such as surge, sway and yaw, only two fins can be used to move in one direction, as illustrated in Fig. 2. We can consequently reformulate the control allocation as follows:

$$\phi_1 = \text{atan}\left(\frac{\tau_z + \frac{\tau_\phi}{M_\phi} - \frac{\tau_\theta}{M_\theta}}{2\left(\frac{H(\tau_x)\tau_x}{c\psi_f} - \frac{H(-\tau_y)\tau_y}{s\psi_f} - \frac{H(-\tau_\psi)\tau_\psi}{M_\psi}\right)}\right) \quad (26)$$

$$\phi_2 = \text{atan}\left(\frac{\tau_z + \frac{\tau_\phi}{M_\phi} + \frac{\tau_\theta}{M_\theta}}{2\left(-\frac{H(-\tau_x)\tau_x}{c\psi_f} - \frac{H(-\tau_y)\tau_y}{s\psi_f} + \frac{H(\tau_\psi)\tau_\psi}{M_\psi}\right)}\right) \quad (27)$$

$$\phi_3 = \text{atan}\left(\frac{\tau_z - \frac{\tau_\phi}{M_\phi} + \frac{\tau_\theta}{M_\theta}}{2\left(-\frac{H(\tau_x)\tau_x}{c\psi_f} + \frac{H(\tau_y)\tau_y}{s\psi_f} - \frac{H(-\tau_\psi)\tau_\psi}{M_\psi}\right)}\right) \quad (28)$$

$$\phi_4 = \text{atan}\left(\frac{\tau_z - \frac{\tau_\phi}{M_\phi} - \frac{\tau_\theta}{M_\theta}}{2\left(\frac{H(\tau_x)\tau_x}{c\psi_f} + \frac{H(\tau_y)\tau_y}{s\psi_f} + \frac{H(\tau_\psi)\tau_\psi}{M_\psi}\right)}\right) \quad (29)$$

$$f_1 = \frac{1}{4} \left[2\left(\frac{H(\tau_x)\tau_x}{c\psi_f} + \frac{-H(-\tau_y)\tau_y}{s\psi_f} + \frac{-H(-\tau_\psi)\tau_\psi}{M_\psi}\right)^2 + \left(\tau_z + \frac{\tau_\phi}{M_\phi} - \frac{\tau_\theta}{M_\theta}\right)^2 \right]^{\frac{1}{2}} \quad (30)$$

$$f_2 = \frac{1}{4} \left[2\left(\frac{-H(-\tau_x)\tau_x}{c\psi_f} + \frac{-H(-\tau_y)\tau_y}{s\psi_f} + \frac{H(\tau_\psi)\tau_\psi}{M_\psi}\right)^2 + \left(\tau_z + \frac{\tau_\phi}{M_\phi} + \frac{\tau_\theta}{M_\theta}\right)^2 \right]^{\frac{1}{2}} \quad (31)$$

$$f_3 = \frac{1}{4} \left[2\left(\frac{-H(-\tau_x)\tau_x}{c\psi_f} + \frac{H(\tau_y)\tau_y}{s\psi_f} + \frac{-H(-\tau_\psi)\tau_\psi}{M_\psi}\right)^2 + \left(\tau_z - \frac{\tau_\phi}{M_\phi} + \frac{\tau_\theta}{M_\theta}\right)^2 \right]^{\frac{1}{2}} \quad (32)$$

$$f_4 = \frac{1}{4} \left[2\left(\frac{H(\tau_x)\tau_x}{c\psi_f} + \frac{H(\tau_y)\tau_y}{s\psi_f} + \frac{H(\tau_\psi)\tau_\psi}{M_\psi}\right)^2 + \left(\tau_z - \frac{\tau_\phi}{M_\phi} - \frac{\tau_\theta}{M_\theta}\right)^2 \right]^{\frac{1}{2}} \quad (33)$$

Once the required force for each fin is computed, it should be converted to a fin-oscillating amplitude using the inverse model described in Remmas et al. (2021b) as follows:

$$A_i = \arccos\left(\frac{-f_i}{2C_d \rho S_f (r_c \omega)^2} + 1\right) \quad (34)$$

where ω denotes the angular velocity of the fin, ρ is the water density, r_c is the distance between the rotation axis and the center of gravity of the fin, S_f is the projection area of the fin, and C_d stands for the drag coefficient. The drag coefficient C_d was identified experimentally in our previous work (Remmas et al., 2021b). The above mentioned parameters are summarized in Table 1.

The resulting amplitudes A_i and zero-directions ϕ_i are then filtered using a second order filter. This is to ensure smooth and continuous transitions, which may significantly reduce the effect of the non-modeled fin lateral forces. The expressions of the used filters are as follows:

$$\ddot{A}_i^f + 2\gamma_A \dot{A}_i^f + \gamma_A^2 (A_i^f - A_i) = 0 \quad (35)$$

$$\ddot{\phi}_i^f + 2\gamma_\phi \dot{\phi}_i^f + \gamma_\phi^2 (\phi_i^f - \phi_i) = 0 \quad (36)$$

Table 1
Parametric values of the force to amplitude model (34).

ρ (kg/m ³)	S_f (m ²)	ω (rad/s)	r_c (m)	C_d
997	0.02	4π	0.1	0.23

Table 2
Numerical values of B_r^{-1} for all possible faulty fin cases.

FR						RR							
$\frac{1}{2}$	-1	0	0	0	1	$\frac{1}{2}$	1	0	0	0	0	-1	
	-1	1	0	0	0		0	0	1	0	0	-1	
	0	1	0	0	0		1	1	1	0	0	0	
	0	0	1	1	0		0	0	0	1	1	0	
	0	0	0	-1	1		0	0	0	1	0	1	
0	0	1	0	-1	0	0	0	0	-1	-1	0		
FL						RL							
$\frac{1}{2}$	0	-1	0	0	0	-1	$\frac{1}{2}$	1	-1	0	0	0	0
	-1	-1	0	0	0	0		0	-1	0	0	1	
	-1	0	0	0	0	-1		1	0	0	0	0	
	0	0	1	0	-1	0		0	0	0	1	-1	
	0	0	0	1	1	0		0	0	1	0	1	
0	0	1	-1	0	0	0	0	1	-1	0	0		

where $\gamma_A = 10$ and $\gamma_\phi = 3$ are positive constants. The values of ϕ_i^f and A_i^f are computed using Euler's integration method, with a step-size of 0.01 s, and are then sent to the low-level control of the fins' motors to achieve the desired oscillation profile.

3.1. Control-allocation based FTC

An actuation fault may occur due to various reasons, it can be of mechanical or electrical cause. In both cases, one or several fins may become either malfunctioning, or totally fail to function. In this study, we consider the case of fin failure, and assume that the fault can be identified and isolated. We also assume that only one actuator failure occurs at a time. Throughout the remainder of this paper, when referring to a fin as "faulty", it implies that the fin is completely nonfunctional.

When an actuation failure occurs, we use the elimination of column method to adapt the control allocation system. The matrix B reported in Eq. (6) is then reduced by two columns depending on which fin is faulty (cf. illustration of Fig. 3). The two following columns are eliminated depending on which fin is faulty:

- C_h^1 and C_v^1 , when the fin FR is faulty
- C_h^2 and C_v^2 , when the fin RR is faulty
- C_h^3 and C_v^3 , when the fin RL is faulty
- C_h^4 and C_v^4 , when the fin FL is faulty

Once the two columns are identified and eliminated, the reduced matrix denoted by $A_r \in \mathbb{R}^{6 \times 6}$ becomes a full rank square matrix. This means that, in the case of a faulty fin scenario, A_r is invertible, and there exists only one fin configuration that solves the control allocation problem. Moreover, its inverse A_r^{-1} can be generalized to all the faulty cases listed above, as follows:

$$B_r^{-1} = \begin{bmatrix} H_1^1 & H_2^2 & 0 & 0 & 0 & V_1^1 \\ H_1^1 & H_2^2 & 0 & 0 & 0 & V_2^1 \\ H_2^1 & H_3^2 & 0 & 0 & 0 & V_3^1 \\ 0 & 0 & H_4^1 & V_4^1 & V_4^2 & 0 \\ 0 & 0 & H_5^1 & V_5^1 & V_5^2 & 0 \\ 0 & 0 & H_6^1 & V_6^1 & V_6^2 & 0 \end{bmatrix} \quad (37)$$

The resulting values of the B_r^{-1} for all faulty fin cases are summarized in Table 2.

Following the same solving procedure detailed in Eqs. (10) to (25), we can deduce both the required forces and zero-direction angles

required for the three healthy fins, as follows:

$$f_i \cos(\phi_i) = H_i^1 \frac{\tau_x}{c\psi_f} + H_i^2 \frac{\tau_y}{s\psi_f} + V_i^1 \frac{\tau_\psi}{M_\psi} = \Gamma_i^h \quad (i = 1 \dots 3) \quad (38)$$

$$f_i \sin(\phi_i) = H_{i+3}^1 \tau_z + V_{i+3}^1 \frac{\tau_\phi}{M_\phi} + V_{i+3}^2 \frac{\tau_\theta}{M_\theta} = \Gamma_i^v \quad (i = 1 \dots 3) \quad (39)$$

The required zero-direction angles and forces are then derived and expressed as:

$$f_i = \sqrt{\Gamma_i^h{}^2 + \Gamma_i^v{}^2} \quad (i = 1 \dots 3) \quad (40)$$

$$\phi_i = \text{atan}\left(\frac{\Gamma_i^v}{\Gamma_i^h}\right) \quad (i = 1 \dots 3) \quad (41)$$

The computed forces f_i are then transformed into fin oscillation amplitudes A_i using (34). Finally A_i and ϕ_i are filtered using (35) and (36).

The resulting fin oscillating amplitudes A_i^f and zero-direction angles ϕ_i^f are allocated to the respective fins in an ascending order of i as follows:

- RR, RL and FL, when the FR fin is faulty.
- FR, RL, and FL, when the RR fin is faulty.
- FR, RR, and FL, when the RL fin is faulty.
- FR, RR and RL, when the FL fin is faulty.

It is important to note that during the transition from one control allocation matrix to another one leads to varying fin oscillation parameters. This primarily results in different commanded zero-directions and amplitudes for the fins, generating a finite amount of non-modeled external disturbance during rotation, which can be managed by selecting suitable control parameters. Moreover, the coefficients γ_A and γ_{ϕ_i} of the second-order filters, as indicated in Eqs. (35) and (36), have been manually adjusted to ensure smooth transitions with minimal external disturbance during changes in fin zero-direction angles.

3.2. Implemented controllers

To study the performance of the proposed FTC scheme for trajectory tracking, we implemented two controllers, namely a PID and a Sliding Mode controller. Let us define the tracking error and its derivative as follows:

$$\tilde{\eta} = \eta_d - \eta \quad (42)$$

$$\tilde{v} = J^{-1} \dot{\eta}_d - \dot{v} \quad (43)$$

3.2.1. PID control

A conventional PID controller was implemented as a base-line control law to assess the performance in terms of trajectory tracking using the proposed FTC scheme. There are several variants of PID controllers for AUVs control (Fossen, 2011). In this study we adopt the model-free one, as we do not have a high confidence in values of the hydrodynamic parameters of the model defined in (1). The control input is expressed as:

$$\tau_{PID} = K_p \tilde{\eta} + K_d \tilde{v} + K_i \int_0^{t_1} \tilde{\eta}(t) dt \quad (44)$$

where the $K_p \in \mathbb{R}^{6 \times 6}$, $K_d \in \mathbb{R}^{6 \times 6}$ and $K_i \in \mathbb{R}^{6 \times 6}$ are diagonal positive-definite matrices.

3.2.2. Sliding mode control

In addressing the necessity for robustness against uncertain parameters in the model, we propose the implementation of a Sliding Mode (SM) controller. SM control is widely recognized for its superior performance in managing system uncertainties, disturbances, and nonlinearities, as compared to traditional PID control methods. The design methodology of the SM controller yields a closed-loop system exhibiting insensitivity to both disturbances and uncertainties (Utkin,

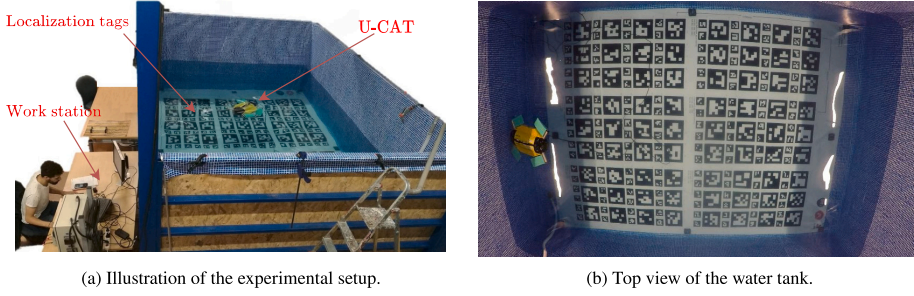


Fig. 5. The experimental setup used for real-time experiments at LIRMM laboratory (Montpellier, France).

2013; Slotine et al., 1991). A comprehensive body of research exists on Sliding Mode control in the literature (Gambhire et al., 2021). In this study, we focus on the design and implementation of a first-order SM controller. To do so, we define first the sliding surface $s = \tilde{v} + \alpha\tilde{\eta}$, where α is a 6×6 diagonal matrix with positive coefficients. We consider then the positive-definite Lyapunov function $V = \frac{1}{2}s^2$. To ensure asymptotic stability, the control law should ensure $\dot{V} < 0$ (Edwards and Spurgeon, 1998). Which leads to the following control law:

$$\tau = n(\eta, v) + M(J^{-1}\dot{\eta}_d + \dot{J}^{-1}\dot{\eta}_d + \alpha(\eta_d - \eta) + K \operatorname{sign}(s)) \quad (45)$$

To avoid the chattering phenomena, inherent to first-order SM, and caused by the $\operatorname{sign}()$ function, we propose to use a hyperbolic tangent function instead. The resulting control law becomes:

$$\tau_{SM} = n(\eta, v) + M(J^{-1}\dot{\eta}_d + \dot{J}^{-1}\dot{\eta}_d + \alpha(\eta_d - \eta) + K \tanh(As)) \quad (46)$$

where K and A are 6×6 diagonal matrices with positive coefficients.

4. Real-time experiments and results

The experimental setup and tested scenarios for evaluating the proposed FTC solution are presented in this section. The results obtained from the experiments are discussed in the following subsection. All of the conducted experiments were video-recorded, and can be visualized in the attached complementary video.

4.1. Experimental setup

A series of validation experiments were performed in a laboratory pool of 1.30 m depth (c.f. Fig. 5(a)) to evaluate the proposed fault-tolerant control allocation method. These experiments include a large grid of size 3 m \times 4 m (cf. Fig. 5(b)). The grid contains 328 ArUco markers (Garrido-Jurado et al., 2014), 72 of size 0.25 m and 216 of size 0.1 m. The onboard camera captures images at a frequency of 10 Hz, and the detected markers are used to provide the robot with its actual position measurements in the Earth fixed frame R_n .

The shallow depth of the pool restricts the range of motion of some degrees of freedom that can be explored, it also affects the vision-based odometry, as the tags can no longer be detected when going deeper, therefore, the chosen reference trajectory to be tracked was a planar elliptic trajectory. The trajectory was generated using the second degree Ordinary Differential Equation denoted in (47). Using a set of pre-filtered desired set-points $\eta_p = [x_p, y_p, z_p, \psi_p]$, the filter generates continuous desired positions $\eta_d = [x_d, y_d, z_d, \psi_d]$, velocities $\dot{\eta}_d = [\dot{x}_d, \dot{y}_d, \dot{z}_d, \dot{\psi}_d]$ and accelerations $\ddot{\eta}_d = [\ddot{x}_d, \ddot{y}_d, \ddot{z}_d, \ddot{\psi}_d]$.

$$\ddot{\eta}_d + 2\gamma\dot{\eta}_d = \gamma^2(\eta_d - \eta_p) \quad (47)$$

The filter is implemented to guarantee the generation of smooth, continuous, and feasible velocities and accelerations, even in the presence of non-linearity in the desired set-points. A double Euler integration is then performed to get the desired states η_d , $\dot{\eta}_d$ and $\ddot{\eta}_d$.

Table 3

Trajectory generation parameters.					
L_x	ω_x	L_y	ω_y	ζ	γ
1.2	0.06	0.75	0.06	0.2	5.0

The pre-filtered set-points were then designed to achieve a 2D ellipsoidal-shaped trajectory, whose time-trajectories are expressed as follows:

$$x_p(t) = x_i + L_x(-\cos(\omega_x t) + 1) \quad (48)$$

$$y_p(t) = y_i + L_y \sin(\omega_y t) \quad (49)$$

$$z_p(t) = 0.3 \quad (50)$$

$$\psi_p(t) = \operatorname{atan2}(y_d(t + \zeta) - y_p(t), x_d(t + \zeta) - x_p(t)) \quad (51)$$

Although both of the PID and SM controllers were designed to control the robot in 6 DOFs, the robot at this stage can only be controlled in surge, heave, and yaw DOFs. Sway movement is not efficient with the fins positioned at 30 degrees, and this limitation can be addressed in the future with a better mechanical design that allows a more balanced control between all DOFs. To precisely follow a given 3D trajectory, which is essential for underwater exploration or surveying missions, we control the y position indirectly by adjusting the Line of Sight in the desired yaw ψ_p with a look-ahead parameter ζ (Fossen et al., 2003). The robot is mechanically stable in roll and pitch by design and thus it is not necessary to control these DOFs.

The parameter γ was tuned manually to guarantee feasible accelerations by the robot in the case where ψ_p changes abruptly because of the non-continuous $\operatorname{atan2}$ function (51). The parameters values for trajectory generation are summarized in Table 3. The offset parameters x_i and y_i are selected based on the measured initial location of the robot, such that the trajectory would start from that point in space.

The following experimental scenarios were evaluated for both the PID and SM controller for the tracking of the above-defined trajectory:

- Scenario 1 (Nominal): All fins are healthy.
- Scenario 2 (RR): The rear right fin is faulty.
- Scenario 3 (RL): The rear left fin is faulty.
- Scenario 4 (FL): The front left fin is faulty.
- Scenario 5 (FR): The front right fin is faulty.

The gains for the PID and SM controllers were determined through a process of iterative testing and adjustment to achieve optimal performance in the nominal case, where all fins are functioning properly. In order to evaluate the robustness of the two controllers, the same set of parameters were used for all other scenarios without further modification. The numerical values of the gains for the PID and SM controllers are reported in Tables 4 and 5, respectively. The obtained results are presented in the next subsection.

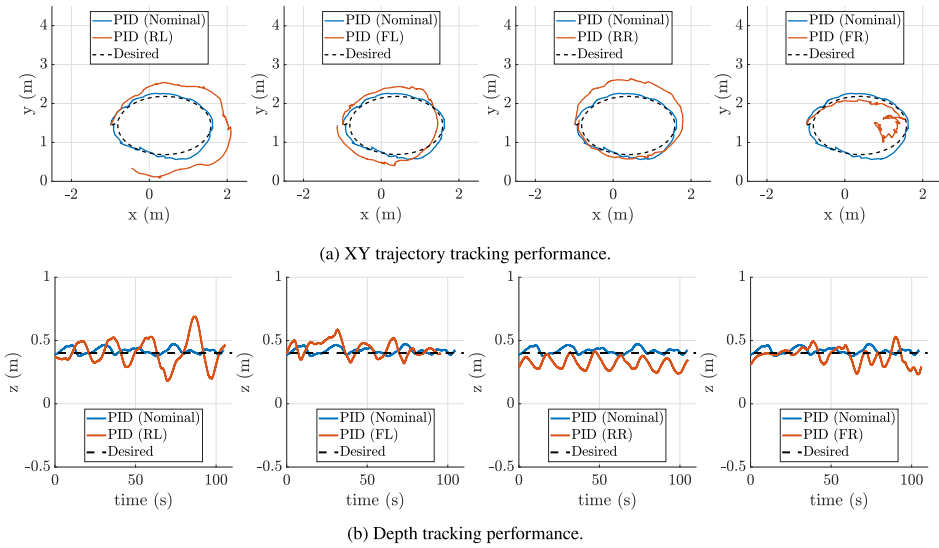


Fig. 6. Trajectory tracking results across the different experimental scenarios using the PID controller.

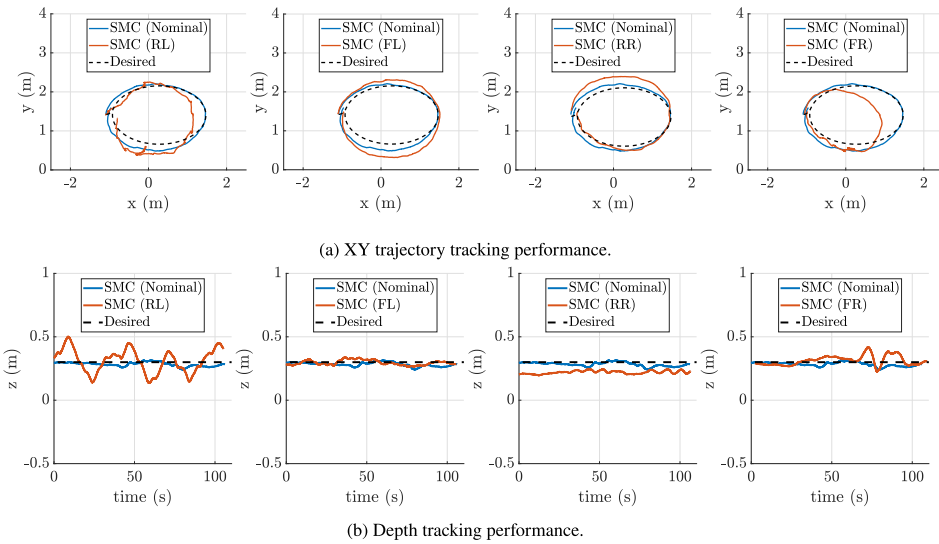


Fig. 7. Trajectory tracking results across the different experimental scenarios using the SMC controller.

Table 4

The numerical values of the gains for the PID controller.

	K_p	K_d	K_i
Surge	1.15	1.2	0.18
Heave	6.2	1.4	0.7
Yaw	0.35	1.5	0.8

Table 5

The numerical values of the gains for the SMC controller.

	K	α	A
Surge	1.4	0.8	1
Heave	1.3	2.95	1
Yaw	0.9	1.7	1

4.2. Obtained results and discussion

In this section, we present the experimental results obtained from implementing the proposed FTC scheme with PID and SM controllers

for the previously described scenarios. The performance of each controller is assessed based on a single complete lap of the elliptical trajectory.

For Scenario 1 (nominal), both the PID and SM controllers enable the robot to accurately track the desired trajectory, as shown in Figs. 6

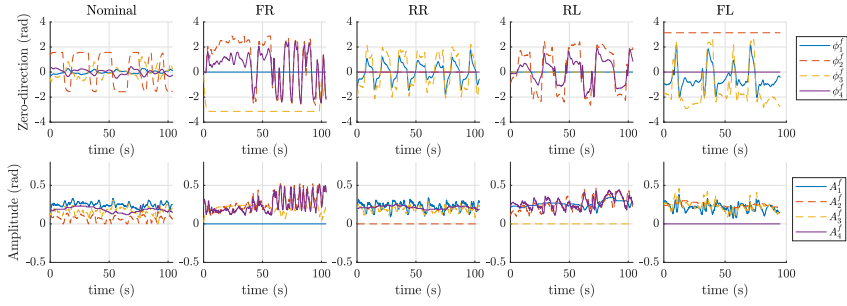


Fig. 8. Time-series of the generated zero-direction angles and amplitudes for the different experimental scenarios using the PID controller.

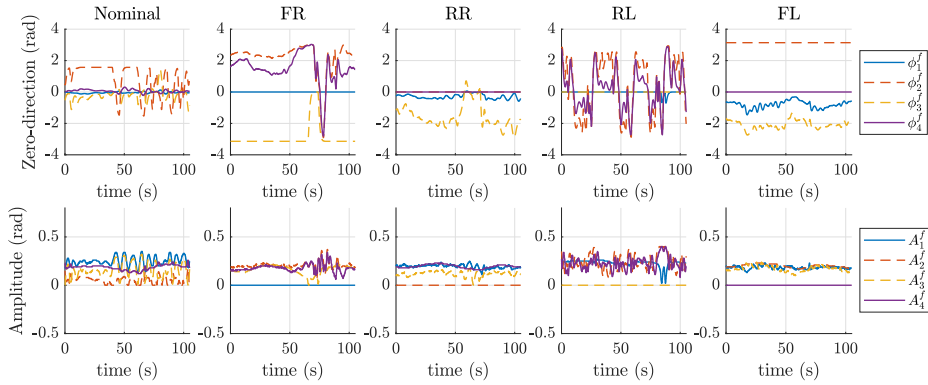


Fig. 9. Time-series of the generated zero-direction angles and amplitudes for the different experimental scenarios using the SMC controller.

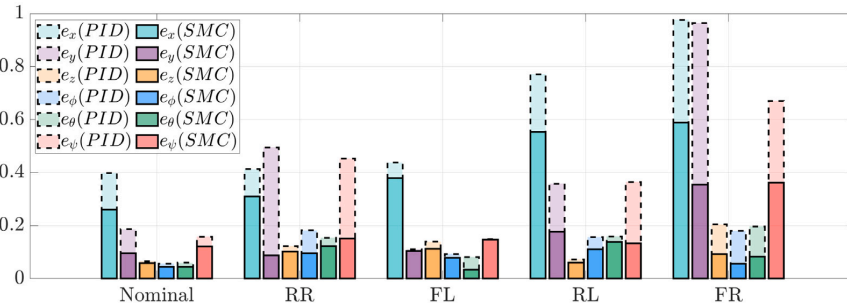


Fig. 10. Bar plot of the RMS errors for trajectory tracking of all the studied scenarios. The errors for the position and orientation, expressed in meters and radians, respectively, are reported for a single trial for each case.

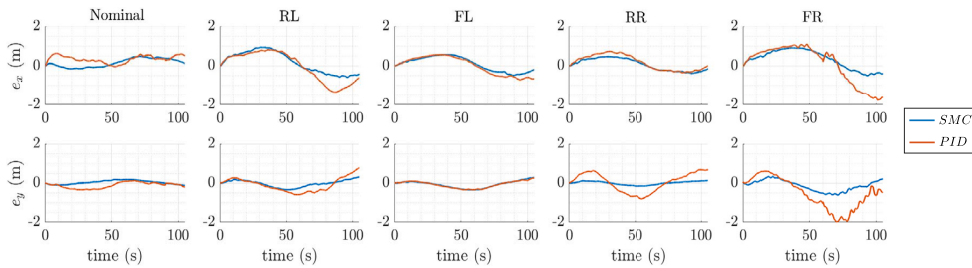


Fig. 11. Tracking errors of x and y positions for all the studied scenarios. The errors are depicted for each scenario, illustrating the performance of the control strategies in various fault conditions.

and 7, respectively. The PID controller displays increased oscillations in the zero-direction angle of the rear right fin, which primarily contributes to depth adjustments, as illustrated in Fig. 8. In contrast, the SM controller demonstrates reduced oscillation in the zero-direction angle of the rear right fin as shown in 9, resulting in improved tracking performance in terms of root mean square errors (RMS), as displayed in Fig. 10. The tracking errors for x and y , reported in Fig. 11, reveal that the robot lags slightly behind the reference trajectory when tracking the long side of the ellipse but catches up when tracking the short side.

In Scenario 2 (faulty rear right fin), the tracking performance slightly deteriorates when using the PID controller, as demonstrated in Fig. 6. An offset in depth tracking, accompanied by oscillations, results from the robot's positive buoyancy and the fins' inability to generate adequate heave force without switching configuration, as depicted in Fig. 8. Conversely, the SM controller facilitates better tracking performance when the rear right fin is faulty, as exhibited in Fig. 7. Although depth tracking performance is slightly compromised, overall trajectory tracking remains satisfactory. The fin zero-directions are significantly smoother, as shown in Fig. 9.

In Scenario 3 (faulty rear left fin), the tracking performance for all degrees of freedom declines significantly when using the PID controller, as displayed in Fig. 6. The rear left fin plays a vital role in adjusting the heading for a clockwise trajectory, and to compensate, the PID generates control inputs that lead to oscillatory behavior in the fins' zero-directions. In contrast, the SM controller offers superior tracking performance, as depicted in Fig. 7 and demonstrated in Fig. 10. A comparison of the tracking errors for x and y between the two controllers is shown in Fig. 11, which clearly highlights the superior performance of the SMC controller.

In Scenario 4 (faulty front left fin), tracking performance is slightly worse compared to the nominal case when using the PID controller, as evidenced in Fig. 6. Since the front left fin is primarily responsible for generating surge force, the only DOF affected by its loss is the tracking of x , as shown in Fig. 10. Additionally, Fig. 8 shows that the rear right fin switches orientation to π to compensate for the required surge force and heading yaw adjustments. The SM controller, however, ensures excellent depth control tracking and accurate overall trajectory tracking, as displayed in Fig. 7. The generated zero-directions are considerably smoother, as illustrated in Fig. 9, leading to better performance.

In Scenario 5 (faulty front right fin), the PID controller fails to correctly track the reference trajectory, as shown in Fig. 6. Since the front right fin plays a significant role in both generating surge force and adjusting the heading for tracking a clockwise trajectory, the remaining fins struggle to properly compensate for this loss with the PID inputs. As illustrated in Fig. 8, the fin zero-direction of the front left fin constantly switches signs after the first 50 s, which coincides with making a hard turn. On the other hand, the SM controller enables improved tracking performance for all degrees of freedom, as depicted in Fig. 7. The importance of the front-right fin for tracking this specific trajectory is also noticeable, although the SM controller handles it better than the PID.

Overall, the proposed FTC scheme with the SM controller provides satisfactory tracking performance in the presence of fin failures. The results demonstrate that the robot can follow the reference trajectory using only the three highly-coupled healthy fins, without the need for adjusting the controller gains.

These results also indicate the effectiveness of the proposed FTC scheme in handling actuation failures, even in the worst-case scenario for tracking the studied reference trajectory. This is particularly important for a symmetrical robot with a symmetrical design, as the worst-case scenario can be deduced based on the type of reference trajectory. This information can be utilized to design high-level controllers that adapt the reference trajectory and bypass worst-case scenarios.

5. Conclusion and future works

In conclusion, this paper has addressed the problem of fault-tolerant control for a highly coupled fin-actuated AUV. We have proposed an active fault-tolerant control scheme that utilizes a control allocation switching mechanism to properly allocate controller forces to healthy fins in the event of a fault. The effectiveness of the proposed method was evaluated through experimental studies involving trajectory tracking tasks using two different control laws: PID and sliding mode control. The results indicate that the use of a robust controller, such as sliding mode control, in conjunction with the proposed fault-tolerant control scheme, allows for superior handling of faulty cases compared to conventional PID control.

While the main focus of our work is on the fault-tolerant control allocation strategy, which is independent of specific disturbances such as sea currents, we acknowledge that the influence of sea currents can be an important factor in real-world applications. Although our experiments do not specifically address the impact of external disturbances such as sea currents, our analysis provides insights into the performance and effectiveness of the proposed control strategy under actuator failure scenarios. As part of future work, we plan to evaluate the performance of the proposed control strategy in environments with sea currents, which will help to further validate the robustness and applicability of our approach.

We also plan to extend the proposed method to more complex cases, allowing for additional degrees of freedom control. This would enable more comprehensive and precise trajectory tracking under demanding conditions. Moreover, we plan to address the challenges associated with handling multiple actuation faults simultaneously, developing adaptive fault-tolerant strategies that can cope with various fault scenarios. This would further enhance the reliability and performance of fin-actuated AUVs, ensuring their safe and efficient operation in the presence of faults.

CRedit authorship contribution statement

Walid Remmas: Conception and design of study, Acquisition of data, Analysis and/or interpretation of data, Writing – original draft , Writing – review & editing. **Ahmed Chemori:** Conception and design of study, Writing – original draft , Writing – review & editing. **Maarja Kruusmaa:** Conception and design of study, Writing – original draft , Writing – review & editing.

Declaration of competing interest

The authors declare that they have no known competing financial interests or personal relationships that could have appeared to influence the work reported in this paper.

Data availability

Data will be made available on request.

Acknowledgment

All authors approved the version of the manuscript to be published.

Appendix A. Supplementary data

Supplementary material related to this article can be found online at <https://doi.org/10.1016/j.oceaneng.2023.115327>.

References

- Baldini, A., Ciabattoni, L., Felicetti, R., Ferracuti, F., Monteriù, A., Fasano, A., Freddi, A., 2017. Active Fault Tolerant Control of Remotely Operated Vehicles via Control Effort Redistribution. In: International Design Engineering Technical Conferences and Computers and Information in Engineering Conference, Volume 9: 13th ASME/IEEE International Conference on Mechatronic and Embedded Systems and Applications, p. V009T07A002.
- Alwi, H., Edwards, C., 2008. Fault tolerant control using sliding modes with on-line control allocation. *Automatica* 44, 1859–1866.
- Antonelli, G., 2003. A survey of fault detection/tolerance strategies for AUVs and ROVs. In: *Fault Diagnosis and Fault Tolerance for Mechatronic Systems: Recent Advances*. Springer, pp. 109–127.
- Chemori, A., Kuusmik, K., Salumäe, T., Kruusmaa, M., 2016. Depth control of the biomimetic U-CAT turtle-like AUV with experiments in real operating conditions. In: 2016 IEEE International Conference on Robotics and Automation. ICRA, IEEE, pp. 4750–4755.
- Edwards, C., Spurgeon, S., 1998. *Sliding Mode Control: Theory and Applications*. Crc Press.
- Fasano, A., Ferracuti, F., Freddi, A., Longhi, S., Monteriù, A., 2015. A virtual thruster-based failure tolerant control scheme for underwater vehicles. *IFAC-PapersOnLine* 48, 146–151.
- Fossen, T.I., 2011. *Handbook of Marine Craft Hydrodynamics and Motion Control*. John Wiley & Sons.
- Fossen, T.I., Breivik, M., Skjetne, R., 2003. Line-of-sight path following of underactuated marine craft. *IFAC Proc. Vol.* 36, 211–216.
- Gambhire, S.J., Kishore, D.R., Londhe, P.S., Pawar, S.N., 2021. Review of sliding mode based control techniques for control system applications. *Int. J. Dyn. Control* 9, 363–378.
- Garrido-Jurado, S., Muñoz-Salinas, R., Madrid-Cuevas, F.J., Marín-Jiménez, M.J., 2014. Automatic generation and detection of highly reliable fiducial markers under occlusion. *Pattern Recognit.* 47, 2280–2292.
- Kadiyam, J., Parashar, A., Mohan, S., Deshmukh, D., 2020. Actuator fault-tolerant control study of an underwater robot with four rotatable thrusters. *Ocean Eng.* 197, 106929.
- Kruusmaa, M., Gkliva, R., Tuhtan, J., Tuvikene, A., Alfredsen, J., 2020. Salmon behavioural response to robots in an aquaculture sea cage. *R. Soc. Open Sci.* 7, 191220.
- Liu, F., Tang, H., Qin, Y., Duan, C., Luo, J., Pu, H., 2022a. Review on fault diagnosis of unmanned underwater vehicles. *Ocean Eng.* 243, 110290.
- Liu, X., Zhang, M., Liu, X., Zhao, W., 2022. Finite-time extended state observe based fault tolerant control for autonomous underwater vehicle with unknown thruster fault. *Journal of Marine Science and Engineering* 10.
- Low, K.H., 2011. Current and future trends of biologically inspired underwater vehicles. In: 2011 Defense Science Research Conference and Expo. DSR, IEEE, pp. 1–8.
- Meurer, C., Simha, A., Kotta, Ü., Kruusmaa, M., 2019. Nonlinear orientation controller for a compliant robotic fish based on asymmetric actuation. In: 2019 International Conference on Robotics and Automation. ICRA, IEEE, pp. 4688–4694.
- Ni, L., 2001. *Fault-Tolerant Control of Unmanned Underwater Vehicles* (Ph.D. thesis). Virginia Polytechnic Institute and State University.
- Omerdic, E., Roberts, G., 2004. Thruster fault diagnosis and accommodation for open-frame underwater vehicles. *Control Eng. Pract.* 12, 1575–1598.
- Penrose, R., 1955. A generalized inverse for matrices. In: *Mathematical Proceedings of the Cambridge Philosophical Society*, vol. 51, Cambridge University Press, pp. 406–413.
- Podder, T.K., Sarkar, N., 1999. Fault tolerant decomposition of thruster forces of an autonomous underwater vehicle. In: *Proceedings 1999 IEEE International Conference on Robotics and Automation* (Cat. No. 99CH36288C). 1, IEEE, pp. 84–89.
- Preston, V., Salumäe, T., Kruusmaa, M., 2018. Underwater confined space mapping by resource-constrained autonomous vehicle. *J. Field Robotics* 35, 1122–1148.
- RB, A.M.A., Hemakumar, B., Prasad, M., 2018. Robotic fish locomotion & propulsion in marine environment: A survey. In: 2018 2nd International Conference on Power, Energy and Environment: Towards Smart Technology. ICEPE, IEEE, pp. 1–6.
- Remmas, W., Chemori, A., Kruusmaa, M., 2021a. Diver tracking in open waters: A low-cost approach based on visual and acoustic sensor fusion. *J. Field Robotics* 38, 494–508.
- Remmas, W., Chemori, A., Kruusmaa, M., 2021b. Inverse-model intelligent control of fin-actuated underwater robots based on drag force propulsion. *Ocean Eng.* 239, 109883.
- Ren, Z., Wang, T., Wen, L., 2015. Hydrodynamic function of a robotic fish caudal fin: Effect of kinematics and flow speed. In: 2015 IEEE/RSJ International Conference on Intelligent Robots and Systems. IROS, IEEE, pp. 3882–3887.
- Salumäe, T., Chemori, A., Kruusmaa, M., 2016. Motion control architecture of a 4-fin U-CAT AUV using DOF prioritization. In: 2016 IEEE/RSJ International Conference on Intelligent Robots and Systems. IROS, IEEE, pp. 1321–1327.
- Salumäe, T., Chemori, A., Kruusmaa, M., 2019. Motion control of a hovering biomimetic four-fin underwater robot. *IEEE J. Ocean. Eng.* 44, 54–71.
- Salumäe, T., Raag, R., Rebane, J., Ernits, A., Toming, G., Ratas, M., Kruusmaa, M., 2014. Design principle of a biomimetic underwater robot u-cat. In: 2014 Oceans-St. John's. IEEE, pp. 1–5.
- Samy, I., Postlethwaite, I., Gu, D.-W., 2011. Survey and application of sensor fault detection and isolation schemes. *Control Eng. Pract.* 19, 658–674.
- Sarkar, N., Podder, T.K., Antonelli, G., 2002. Fault-accommodating thruster force allocation of an AUV considering thruster redundancy and saturation. *IEEE Trans. Robot. Autom.* 18, 223–233.
- Scaradozzi, D., Palmieri, G., Costa, D., Pinelli, A., 2017. BCF swimming locomotion for autonomous underwater robots: A review and a novel solution to improve control and efficiency. *Ocean Eng.* 130, 437–453.
- Slotine, J.-J.E., Li, W., et al., 1991. *Applied Nonlinear Control*, volume 199. Prentice hall Englewood Cliffs, NJ.
- Utkin, V.I., 2013. *Sliding Modes in Control and Optimization*. Springer Science & Business Media.
- Wang, Y., Wilson, P.A., Liu, X., et al., 2015. Adaptive neural network-based backstepping fault tolerant control for underwater vehicles with thruster fault. *Ocean Eng.* 110, 15–24.
- Weymouth, G.D., 2016. **Biologically inspired force enhancement for maritime propulsion and maneuvering.** arXiv preprint arXiv:1609.06559.
- Xie, O., Zhu, Q., Shen, L., Ren, K., 2018. Kinematic study on a self-propelled bionic underwater robot with undulation and jet propulsion modes. *Robotica* 36, 1613–1626.
- Yang, Y., Wang, J., Wu, Z., Yu, J., 2018. Fault-tolerant control of a CPG-governed robotic fish. *Engineering* 4, 861–868.
- Yang, K.C., Yuh, J., Choi, S.K., 1998. Experimental study of fault-tolerant system design for underwater robots. In: *Proceedings. 1998 IEEE International Conference on Robotics and Automation* (Cat. No. 98CH36146), vol. 2, IEEE, pp. 1051–1056.
- Yu, J., Wang, L., 2005. Parameter optimization of simplified propulsive model for biomimetic robot fish. In: *Proceedings of the 2005 IEEE International Conference on Robotics and Automation*. IEEE, pp. 3306–3311.

Appendix 4: Publication IV

Publication IV:

Walid Remmas, Christian Meurer, Ahmed Chemori, and Maarja Kruusmaa. Control Allocation for 6-DOF Control of a Highly Manoeuvrable Under-actuated Bio-inspired AUV. *Submitted to IEEE Transactions on Robotics, 2023*

Control Allocation for 6-DOF Control of a Highly Manoeuvrable Under-actuated Bio-inspired AUV

Walid Remmas*, Christian Meurer*, Ahmed Chemori, *Senior Member, IEEE*, Maarja Kruusmaa

Abstract—Fin-driven autonomous underwater vehicles (AUVs) are distinguished by their ability to use fins for both thrust generation and vectoring, promising enhanced maneuverability while reducing the required actuators for six degrees of freedom (6-DOF) control. However, these dual-purpose fins pose complex challenges, demanding novel solutions. This study proposes a novel analytic control allocation method for under-actuated fin-actuated AUVs to achieve precise 6-DOF control. By integrating a state-of-the-art adaptive hybrid feedback controller with the proposed control allocation method, we enable an AUV with only four actuators to perform accurate and efficient 6-DOF trajectory tracking. This research includes extensive simulations and real-world experiments, allowing for thorough validation of the proposed method. In 6-DOF tracking simulations, the proposed control allocation method significantly outperformed state-of-the-art control allocation techniques, exhibiting superior performance, energy efficiency, and computational efficiency. The robustness and efficacy of the proposed methods were further confirmed in real-world pool experiments following complex 3D trajectories. Overall, the results from this study reveal potential for the proposed autonomy framework in enhancing the capabilities of under-actuated fin-actuated AUVs. By offering a compelling balance between high performance, energy efficiency, and computational efficiency, our method paves the way for more effective and versatile 6DOF tracking for under-actuated underwater robots.

Index Terms—Fin-actuated robot, 6-DOF control, AUV, Control allocation, Underactuated.

I. INTRODUCTION

There is a growing demand for scalable and versatile long-term monitoring systems as the importance of monitoring human induced changes in underwater ecosystems becomes increasingly relevant. Existing underwater monitoring systems often have static locations, providing dense temporal coverage but limited spatial coverage. To address this limitation, mobile monitoring platforms are being sought after as a solution. These platforms offer the potential for spatiotemporal density in observations, which is particularly valuable for monitoring complex and dynamic coastal underwater environments.

To be scalable and cost efficient, mobile monitoring systems should ideally operate autonomously, leading to an

increased interest in and use of autonomous underwater vehicles (AUVs). To autonomously fulfill higher level monitoring goals in complex environments, AUVs need to be capable of tracking trajectories in 3D space, requiring motion in several degrees of freedom (DOF) to be controlled simultaneously. Environmental conditions underwater are inherently dynamic and require therefore robust control strategies for trajectory tracking. Additionally, enabling such systems for large scale monitoring requires energy efficient solutions in terms of hardware and software. Classically, energy efficiency and the control of a maximum amount of DOF for agile motion require a trade-off between the number of employed actuators and the energy demand for such actuation. Another important aspect for long-term monitoring is its impact on the environment to be monitored, especially in regions which are dense with flora and fauna. Classic actuation relies on propellers, which can have a significant impact on the environment due to their mechanics and acoustics.

Designs drawing from bio-inspiration have shown promising results aiming towards minimally invasive actuation. Especially soft fin based actuator designs have been investigated for monitoring tasks that require a reduced impact on the environment, such as marine archaeology [1], in-situ observations of marine fauna [2], [3], and in monitoring scenarios where the seafloor interface should not be disturbed [4].

A lot of focus has been aimed at the development and testing of fish-like bio-inspired robots [5], [6], [2], which usually employ a caudal fin driven by an oscillatory rigid or flexible tail, which is oriented along the main body axes. Despite many proofs of concept, the resulting designs have not yet shown their efficacy in field applications, as their control remains very challenging. Additionally, fish-like robot designs are quite limited in their payload capacity, as a significant portion of the robot is allocated for the propulsion system. In contrast to that, "turtle-like" actuation designs, which employ four or more fins as flippers laterally adjacent to a rigid main hull [7], [8], [9], have shown the potential to create a highly agile system with a sufficient amount of space for scientific and observational payload.

Additionally, bio-inspired actuator designs can also somewhat alleviate the trade-off between agility and the necessary number of actuators. Generally, at least one actuator is used for each DOF to be controlled. If this is the case, the robot is said to be fully actuated in a mechanical sense, while more than one actuator per DOF would create an over-actuated system. While sufficient work exists to enable under-actuated robots to track trajectories in more DOF than they are actuated in, this has not been shown so far for full 6-DOF trajectory tracking. Herein

*These authors contributed equally to this work.

This work was supported in part by the Estonian Centre of Excellence in ICT Research project EXCITE (TAR16013).

W. Remmas (e-mail: walid.remmas@taltech.ee) is affiliated both with the Department of Computer Systems, Tallinn University of Technology, Tallinn, Estonia, and with LIRMM, University of Montpellier, CNRS, Montpellier, France.

C. Meurer (e-mail: cmeurer@marum.de) is with Center for Marine Environmental Sciences (MARUM), University of Bremen, Bremen, Germany

A. Chemori (e-mail: ahmed.chemori@lirmm.fr) is with LIRMM, University of Montpellier, CNRS, Montpellier, France.

M. Kruusmaa (e-mail: maarja.kruusmaa@taltech.ee) is with the Department of Computer Systems, Tallinn University of Technology, Tallinn, Estonia

lies a great potential for bio-inspired actuator designs that can be explored. For instance, the AUV underwater curious archaeology turtle (U-CAT) [9] only employs four actuators while being able to actively track all 6-DOF (see Fig. 3). As opposed to thruster driven vehicles, which have constant thrust vectors for each actuator or require additional actuators to change the thrust vector, bio-inspired designs like U-CAT can change their thrust vector freely with the same actuator. This can significantly reduce the required energy for actuation, compared to a standard fully actuated underwater vehicle.

However, the decrease in actuators comes at the expense of increased control complexity, as change in thrust vector and thrust production in a specific direction are tightly coupled and every change of thrust vector will create disturbances. Thus the full potential of such vehicles has not been fully utilized yet. They have been either manually controlled [2], [3] or only few DOF were actively controlled simultaneously [10], [11]. To fully leverage the potential of fin based vehicles for agile 3D motion tracking, it is thus necessary to improve their control architecture. Specifically, state-of-the-art 6-DOF control needs to be combined with efficient and reliable control allocation, which takes the specific actuator dynamics into account.

To address these challenges, we have developed and tested a novel control framework specifically designed for fin-based AUVs, with a particular focus on turtle-like configurations. Leveraging state-of-the-art control algorithms [12] and a highly efficient analytic control allocation method, our control framework enables, to the best of our knowledge, for the first time the full potential of fin based AUVs to simultaneously control all 6-DOF for trajectory tracking in 3D space using only four actuators.

II. PROBLEM FORMULATION AND RELATED WORK

Turtle-like fin driven vehicles have mostly been controlled manually or without feedback. A special focus was aimed at open loop gait generation [13], [14], [15], [16], [17] specifically focusing on gait generation using central pattern generators (CPGs) [14], [15], [16]. In terms of feedback based control, Geder et al. present a model-free control framework for either heading or depth control [11], and in [10] attitude control for different turning maneuvers is developed. Another model-free controller for the angular rate is used by Siegenthaler et al. to stabilize forward swimming [8]. All those solutions concentrate on one single DOF at a time, using simple model free control frameworks which are neither robust nor provably stable. Chemori et al. [18] investigated depth control for the U-CAT AUV, comparing a model-free RISE controller [19] to a standard PID control and showed that the RISE controller had a better performance in the tested scenario. This approach is still concentrating on a single DOF, but employs a robust controller, shown to be effective under external disturbances.

The control frameworks described so far have been employed for set point regulation, which indicates that path following and trajectory tracking, inherently necessary for monitoring tasks, are still understudied for the considered AUV types. In [20] and [21] modeling and model based

control of the Aqua AUV are presented for trajectory tracking control, but again only in single DOF at a time. Multi DOF control for attitude and heave of the Aqua AUV is presented by Giguere et al. [22]. They employed PID and PI controllers, where problems with control range and DOF coupling are avoided using gain scheduling. The approach resulted in adequate trajectory tracking, but required 45 control parameters to be tuned. Salumäe et al. [23] proposed a framework for the U-CAT AUV, which enabled motion in several DOF (surge, yaw, heave) simultaneously. However, only heave and yaw were controlled via feedback, while surge remained an open loop control. The authors used a model based approach, termed inverse dynamics (ID), which utilized feedback linearization with acceleration feedforward [24]. The proposed ID controller was shown to outperform a standard PID controller especially during scenarios which included external disturbances. Complexities and internal disturbances due to motion coupling were resolved by a DOF prioritization, which effectively decoupled surge from heave motions. However, this meant that heave and surge trajectories were not followed simultaneously.

While the approaches presented so far achieved satisfying results in the tested scenarios, they do not fully exploit the agility and versatility inherent in the fin based actuation. Additionally, experimental work by Smallwood and Whitcomb [25] convincingly concludes that adaptive model based control approaches should be favored over fixed model based controllers. Adaptive model based control for simultaneous tracking of 6-DOF has been thoroughly investigated and successfully implemented for standard AUVs using propeller based actuation [26], [27], [28].

However, the most common orientation representation for such frameworks relies on Euler angles, which contain singularities. To derive a control framework which is provably globally stable an efficient singularity free orientation parametrization is needed. Unit quaternions can be used to represent 3D orientation in an efficient and singularity free manner. Quaternion based controllers have been shown to be effective for orientation control [29], [30]. Nevertheless, global asymptotic stabilization can not be achieved with classical continuous-time state feedback [31]. Fjellstad and Fossen [32] introduced various discontinuous feedbacks to address the problem. However, as shown in [33] this can introduce instability to the control system. To overcome this, a hybrid feedback with a well defined switching logic can be used [34]. A hybrid adaptive control approach has been theoretically and experimentally shown to be effective for surface and underwater vehicle control by Basso et al. [12]. In their work a BlueROV2 (BlueRobotics) in heavy configuration was used to test the control framework. The vehicle employed 8 thrusters to follow trajectories in surge, sway, heave and yaw, while regulating roll and pitch to zero.

We use the hybrid adaptive control framework developed by Basso et al. [12] and test it for two control tasks: 1) full 6-DOF trajectory tracking, and 2) trajectory tracking for surge, sway, heave and yaw, while roll and pitch are to be regulated to zero. In contrast to [12] we also assume that no sway forces are available for the second control task. To that end, we incorporated a line-of-sight-based computation of yaw

trajectories into the trajectory generation process. The line-of-sight based yaw trajectory was designed to enable sway trajectory tracking even if insufficient or no forces could be generated in the sway DOF, which is a common issue for under-actuated underwater vehicles or can be induced by actuator faults. This makes the control framework more robust and durable. Additionally, the available actuators to realize the control commands are in our work reduced from 8 propeller driven thrusters to 4 oscillating fins requiring a different approach to control allocation.

Unlike traditional AUVs, which are typically designed to be either fully actuated or over-actuated, fin-actuated vehicles offer a unique advantage; they can utilize the fins not only for thrust generation but also for thrust vectoring, allowing for motion control in multiple DOF with fewer actuators. However, this advantage comes with complex challenges due to the need for precise control of both thrust magnitude and direction using the limited number of fin actuators. Effectively managing these challenges requires the development of specialized control allocation methods tailored to the unique characteristics of fin-actuated vehicles.

While several studies have addressed the control allocation problem for motion control in AUVs [35], these investigations have predominantly focused on propeller-based actuation systems. These studies have proposed various methodologies, such as direct control allocation [36], [37], daisy chaining [38], [39], and real-time optimization using constrained linear or quadratic programming [40], [41], [42], [43]. Additionally, recent advancements in AUV designs with tiltable thrusters have explored control allocation techniques to manage actuation redundancy [44], [45]. For instance, research has demonstrated the efficacy of pseudo-inverse control allocation methods with predefined tilting angles for stable hovering performance in propeller-based AUVs [44]. Decomposing the nonlinear force input term of tilting thrusters into horizontal and vertical directions, along with the utilization of pseudo-inverse and null-space solutions, has proven effective in minimizing thrust force [45].

However, it is important to acknowledge that control allocation methods developed for propeller-based actuation systems may not be directly applicable to fin-actuated vehicles. Unlike fixed thrusters, fins require rotation to change the direction of thrust, leading to delays and disturbances in control response. While tiltable thrusters need a similar amount of rotation, they do not create the same amount of disturbances due to the difference in geometry compared to fins, which create a significant amount of drag when rotated. Additionally, tiltable thrusters can theoretically produce thrust throughout the rotation, while thrust generation is halted during rotation for fin based actuation. These characteristics of fin actuation necessitate the development of tailored control allocation approaches that account for the specific characteristics of fin-actuated vehicles. We thus hypothesize, that a minimization of necessary fin rotations and a smart choice of the number of actuators contributing to each DOF are crucial for successful trajectory tracking.

Based on this hypothesis, we introduce an innovative control allocation method, enabling an under-actuated fin-actuated

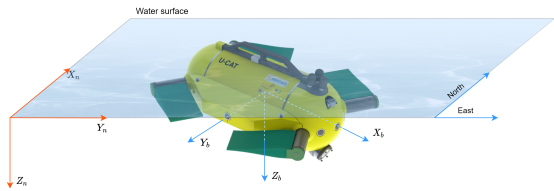


Fig. 1: Illustration of the earth fixed frame R_n (NED convention) and the body fixed frame R_b defined for the U-CAT AUV.

AUV with only four actuators to achieve 6-DOF trajectory tracking. We comprehensively evaluate the performance of our proposed framework through extensive Monte Carlo simulations, assessing its effectiveness in full 6-DOF trajectory tracking, including pitch and roll trajectories. Additionally, we experimentally validate our approach, demonstrating successful tracking in surge, heave, and yaw, as well as roll and pitch stabilization, using a bio-inspired turtle-like AUV equipped with only four actuators.

III. PRELIMINARIES

A. Unit quaternion arithmetic

Quaternions are an efficient orientation representation for movements in 6-DOFs [46]. More specifically, unit quaternions $q \in \mathbb{S}^3$, having the property $\|q\| = 1$ are used. They can be represented as a vector $q = (\mu, \varepsilon)$ constituting the quaternion's scalar $\mu \in \mathbb{R}$ and vector $\varepsilon \in \mathbb{R}^3$ parts. Note that we will follow the Hamiltonian notation for quaternions in this paper. We define the inverse of a unit quaternion as its complex conjugate:

$$q^{-1} = \bar{q} = \begin{bmatrix} \mu \\ -\varepsilon \end{bmatrix} \in \mathbb{S}^3 \quad (1)$$

and the unit quaternion's identity as:

$$1_q = \begin{bmatrix} 1 \\ 0_{3 \times 1} \end{bmatrix} \in \mathbb{S}^3 \quad (2)$$

Furthermore, we can define quaternion multiplication as:

$$q_1 \odot q_2 = \begin{bmatrix} \mu_1 \mu_2 - \varepsilon_1^T \varepsilon_2 \\ \mu_1 \varepsilon_2 + [\varepsilon_1]_{\times} \varepsilon_2 \end{bmatrix} \quad (3)$$

where $[\cdot]_{\times} \in \mathbb{R}^{3 \times 3}$, denotes the skew symmetric matrix representation

B. Kinematic and Dynamics modelling

The position of an underwater vehicle in the three dimensional space can be uniquely defined by a vector $p \in \mathbb{R}^3$ describing the origin of the body fixed frame with respect to a fixed inertial frame. The attitude of an underwater vehicle in three dimensional space can be represented by a rotation matrix $R \in SO(3)$ mapping the axes of the body fixed frame onto those of the inertial frame. The vehicles kinematics can

then be written by, using the linear $v \in \mathbb{R}^3$ and angular $w \in \mathbb{R}^3$ velocities expressed in body fixed frame, in the following form:

$$\begin{aligned}\dot{p} &= Rv \\ \dot{R} &= R[w]_{\times}\end{aligned}\quad (4)$$

For efficient and intuitive representation the rotation matrix can be represented by various three-parameter parametrizations such as Tate-Brian or Euler angles [26]. However, none of those parametrizations is globally non-singular, which makes them less conducive for use of 6-DOF vehicle control. An alternative solution is the use of the unit quaternion [32]. The map from a unit quaternion to a rotation matrix $R(q) : \mathbb{S}^3 \rightarrow SO(3)$ is described by:

$$R(q) := I_3 + 2\mu[\varepsilon]_{\times} + 2[\varepsilon]_{\times}^2 \quad (5)$$

Based on the definition in (3) R is a group homomorphism satisfying:

$$R(q_1)R(q_2) = R(q_1 \odot q_2) \quad (6)$$

and additionally $R^{-1}(q) = R^T(q) = R(q^{-1})$, as well as $R(1_q) = R(-1_q) = I_3$

Subsequently, the kinematic equations can be rewritten as:

$$\begin{aligned}\dot{p} &= R(q)v \\ \dot{q} &= \frac{1}{2}q \odot \chi(w) = T(q)w\end{aligned}\quad (7)$$

with $\chi : \mathbb{R}^3 \rightarrow \mathbb{R}^4$ defined as:

$$\chi(w) = \begin{bmatrix} 0 \\ w \end{bmatrix} \quad (8)$$

and $T(q)$ as:

$$T(q) = \frac{1}{2} \begin{bmatrix} -\varepsilon^T \\ \mu I_3 + [\varepsilon]_{\times} \end{bmatrix} \quad (9)$$

The 6-DOF kino-dynamic model, expressed in body frame, can then be formulated following Fossen's vectorial notation [24] as:

$$\begin{aligned}M\dot{v} + C(v)v + D(v)v + g(q) &= \tau \\ \dot{\eta} &= J(q)v\end{aligned}\quad (10)$$

Where $\eta = [p, q]^T \in \mathbb{R}^7$, $v = [v, w]^T \in \mathbb{R}^6$ represent the vectors of the vehicle poses in the earth-fixed frame R_n and the velocities in the body-fixed frame R_b respectively. The Jacobian $J(q)$ combines the linear and angular kinematic mappings in the following way:

$$J(q) = \begin{bmatrix} R(q) & 0_{3 \times 3} \\ 0_{4 \times 3} & T(q) \end{bmatrix} \quad (11)$$

with it's pseudoinverse:

$$J(q)^\dagger = \begin{bmatrix} R(q)^T & 0_{3 \times 4} \\ 0_{3 \times 3} & 4T(q)^T \end{bmatrix} \quad (12)$$

Note that the map defined by (5) is not injective, as it maps two opposite points on \mathbb{S}^3 to the same element in $SO(3)$, therefore the set of unit quaternions corresponding to $R(q) = I_3$ is $q = \pm 1_q$. This creates problems in the control design, as it needs to be decided to regulate the quaternion based orientation either to 1_q or -1_q . This leads, if not

considered properly to the so called unwinding phenomenon [31]. A commonly employed solution to this problem is the use of discontinuous feedback as shown in [32]. However, as shown in [33] this can introduce instability to the control system. Sanefelice et. al [47] have theoretically and practically shown, that a discrete memory-based switching mechanism can be used to decide to which identity unit quaternion the control framework should regulate. This however, transforms the continuous time system (10) into a hybrid system.

C. Hybrid Systems

To facilitate the benefits of the quaternion switching mechanism we need to employ a hybrid system framework, where continuous and discrete evolution of the system can occur. Let $x \in \mathbb{R}^n$ be the state of a hybrid system $\mathcal{H}(f, G, C, D)$, where the continuous evolution of the states is defined by the *flow map* $f : \mathbb{R}^n \rightarrow \mathbb{R}$ acting as $\dot{x} = f(x)$. In contrast, the discrete evolution of the states is defined by the *jump map* $G : \mathbb{R}^n \rightarrow \mathbb{R}^n$ acting as $x^+ = G(x)$. Furthermore, the two sets $C \subset \mathbb{R}^n$ and $D \subset \mathbb{R}^n$ indicate where continuous and discrete state evolution is possible respectively. Combining the given structures provides the hybrid system:

$$\mathcal{H} = \begin{cases} \dot{x} = f(x) & x \in C \\ x^+ = G(x) & x \in D \end{cases} \quad (13)$$

Robust stability theory is available for such systems, relying on the notion of a solution to a hybrid system and requiring some regularity conditions. The reader is referred to [48] for an extensive treatment of this matter. For this paper it suffices to introduce the notation given above, as we are implementing the control structure shown in [12] and can thus rely on the stability proofs given therein.

IV. AUTONOMY FRAMEWORK

The autonomy presented in this paper can be separated into three main tasks: planning, control and state estimation. Those tasks are in turn realized by various autonomy modules as shown in Fig. 2. In our use-case, the planning module will focus on creating analytic reference trajectories in all 6-DOF. Relevant parameters, such as footprint and desired velocity, are defined by user input. To enable the robot to follow the given trajectories, the control module employs a state-of-the-art hybrid adaptive 6-DOF tracking controller [12]. A novel control allocation framework is then employed to accurately and efficiently distribute the desired control action among the given actuators and transform desired forces into fin kinematics. Additionally, we use two state-of-the-art control allocation methods to compare to our proposed solution. On the actuator level, the desired fin kinematics are tracked by a standard PID controller for each actuator. The resulting vehicle motion is then estimated in the state estimation module, which is based on an Extended Kalman Filter (EKF). The EKF makes use of a simplified kinematic motion model, aided by orientation estimates and visual feedback from fiducial markers detected by a camera. Each of the autonomy modules will be described in detail in the following sections. This

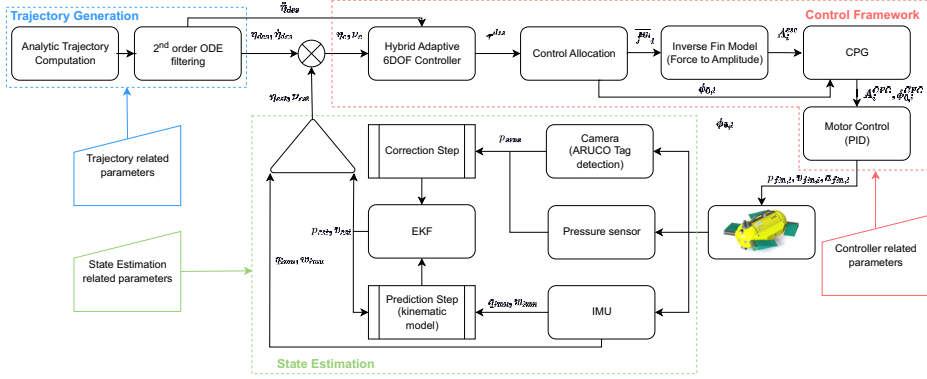


Fig. 2: Proposed autonomy architecture consisting of: 1) trajectory generation module in blue, 2) control module including hybrid adaptive 6-DOF controller and control allocation in red, 3) state estimation module with sensors and EKF in green.

description is prefaced with a short introduction to the U-CAT AUV as it serves as the experimental and simulated platform on which the autonomy framework with the hybrid adaptive controller and novel control allocation are tested.

A. Brief introduction of U-CAT

U-CAT (shown in Fig. 1) is an autonomous biomimetic underwater robot developed within the European Union 7th Framework project ARROWS [9] (Archaeological Robot Systems for the World Seas). As opposed to other bio-inspired underwater vehicles, the four-finned design of this vehicle allows it to actively control all 6-DOF. The four motors actuating the fins are oriented as illustrated in Fig. 1. This configuration allows the robot in theory to be holonomic. The fins were designed to point outwards to have more force generated in surge direction, as control in sway direction is only used for slow and precise movements within confined spaces. The four independently driven flippers are used to achieve a high maneuverability in 6-DOF. Further technical specifications about U-CAT are detailed in [49].

B. Trajectory generation

To test our proposed control framework we use two distinct trajectory tracking scenarios, full 6-DOF trajectory tracking (6T) and 3-DOF trajectory tracking (surge, heave, yaw) with roll and pitch stabilization (3T2S). In the 6T scenario we assumed that the robot can generate forces in all 6-DOF, while in the 3T2S scenario we assumed, that actuation in the sway direction is not efficient enough to be meaningful. The lack of available sway force makes the system non-holonomic and we implemented a look-ahead modification based on the respective state of the robot to generate a yaw trajectory, which ensured that the robot could still follow the desired trajectories without the need for sway forces. Within those two scenarios two types of looped analytic trajectories were tested. One trajectory is ellipsoidal, whereas the other one describes a Lissajous infinity figure.

In the 6T scenario for both trajectory types the roll trajectory prescribes a motion at a constant angular velocity, while the pitch trajectory points the surge axis of the robot along the generated positional trajectory in the vertical plane. In contrast, in the 3T2S scenario roll and pitch are to be stabilized at zero. The analytic description for both trajectory types in the two scenarios can be seen in Table I. In the given equations, $A_{x,y,z}$ describe the amplitudes of the looped trajectories in surge, sway and heave. The angular frequencies $\omega_{x,y,z}$ correlate with the desired velocities along the linear DOF, while $p_0 = [x_0, y_0, z_0]^T$ describes the starting position of the trajectory. For the roll DOF c_ϕ describes the roll coefficient, which specifies the desired roll velocity. Furthermore, the look-ahead time t^* and $\delta p_p(t, t^*) = p_p(t + t^*) - p_p(t)$ with $p_p = [y_p, y_p, z_p]^T$ are used to define yaw and pitch trajectories that point the robot's orientation along the positional trajectories in the horizontal and vertical plane respectively.

The analytic trajectories $\eta_p = [x_p, y_p, z_p, \phi_p, \theta_p, \psi_p]^T$ are then filtered through a pair of second order ordinary differential equations (ODEs) producing desired positions $\eta_d = [x_d, y_d, z_d, \psi_d]^T$, velocities $\dot{\eta}_d = [\dot{x}_d, \dot{y}_d, \dot{z}_d, \dot{\psi}_d]^T$ and accelerations $\ddot{\eta}_d = [\ddot{x}_d, \ddot{y}_d, \ddot{z}_d, \ddot{\psi}_d]^T$.

$$\ddot{\eta}_{d_1} + 2\gamma_1 \dot{\eta}_{d_1} = \gamma_1^2 (\eta_{d_1} - \eta_p) \quad (14)$$

$$\ddot{\eta}_d + 2\gamma_2 \dot{\eta}_d = \gamma_2^2 (\eta_d - \eta_{d_1}) \quad (15)$$

The ODE filters are implemented to guarantee the generation of smooth, continuous, and feasible velocities and accelerations, even in the presence of non-linearity, potentially induced by the lookahead components in yaw and pitch, in the desired set-points. The parameters γ_1 and γ_2 have been selected manually to guarantee feasible accelerations by the robot. A double Euler integration is then performed to get the desired states η_d , $\dot{\eta}_d$ and $\ddot{\eta}_d$. To conform with the 6-DOF tracking control framework the desired orientation represented by the Euler angles $[\phi_d, \theta_d, \psi_d]^T$ as well as their derivatives $[\dot{\phi}_d, \dot{\theta}_d, \dot{\psi}_d]^T$ and $[\ddot{\phi}_d, \ddot{\theta}_d, \ddot{\psi}_d]^T$ are transformed into unit quaternions [24].

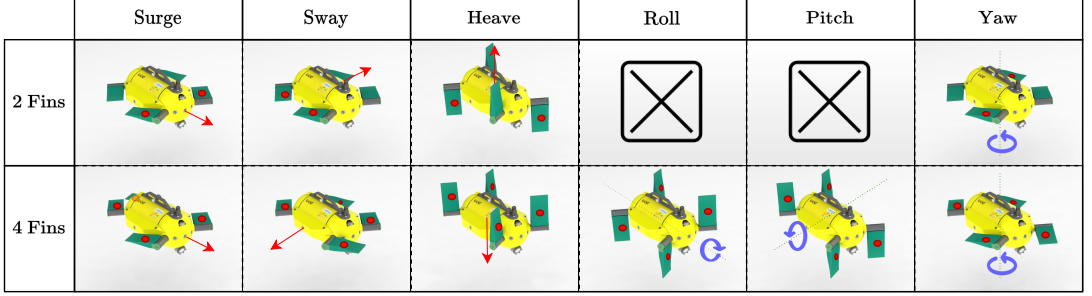


Fig. 3: Illustration of the different fin configurations for controlling the U-CAT robot in each degree of freedom, using either two or four fins. The fins responsible for actuation in each configuration are marked with a red dot.

TABLE I: Ellipsoid and Lissajous trajectory functions for 6T and 3T2S scenarios.

	DOF	Scenario 6T	Scenario 3T2S
Ellipsoid	$x_p(t)$	$A_x(-\cos(\omega_x t) + 1) + x_0$	$A_x(-\cos(\omega_x t) + 1) + x_0$
	$y_p(t)$	$A_y(\sin(\omega_y t)) + y_0$	$A_y(\sin(\omega_y t)) + y_0$
	$z_p(t)$	$A_z(-\cos(\omega_z t) + 1) + z_0$	$A_z(-\cos(\omega_z t) + 1) + z_0$
	$\phi_p(t)$	$c_{\phi} t$	0
	$\theta_p(t)$	$\frac{\pi}{2} - \arccos\left(\frac{-\delta z_p(t, \xi^*)}{\ \delta p_p(t, \xi^*)\ }\right)$	0
	$\psi_p(t)$	$\text{atan2}(\delta y_p(t, t^*), \delta x_p(t, t^*))$	$\text{atan2}(y_p(t + t^*) - y, x_p(t + t^*) - x)$
Lissajous	$x_p(t)$	$A_x(-\cos(l_x \omega_x t) + 1) + x_0$	$A_x(-\cos(\omega_x t) + 1) + x_0$
	$y_p(t)$	$A_y(\sin(l_y \omega_y t)) + y_0$	$A_y(\sin(\omega_y t)) + y_0$
	$z_p(t)$	$A_z(-\cos(\omega_z t) + 1) + z_0$	$A_z(-\cos(\omega_z t) + 1) + z_0$
	$\phi_p(t)$	$c_{\phi} t$	0
	$\theta_p(t)$	$\frac{\pi}{2} - \arccos\left(\frac{-\delta z_p(t, \xi^*)}{\ \delta p_p(t, \xi^*)\ }\right)$	0
	$\psi_p(t)$	$\text{atan2}(\delta y_p(t, t^*), \delta x_p(t, t^*))$	$\text{atan2}(\delta y_p(t + t^*), \delta x_p(t + t^*))$

C. Trajectory tracking controller

To show the efficacy of the proposed control allocation schemes and the autonomy framework we set up the control problem as trajectory tracking of 6-DOF.

1) *Error System and Control Problem:* Given a desired pose $\eta_d = (p_d, q_d)$, velocity $\dot{\eta}_d$ and acceleration $\ddot{\eta}_d$, as well as the instantaneous pose $\eta = (p, q)$ and velocity v we can then define the configuration error as:

$$\eta_e = \begin{pmatrix} p_e \\ q_e \end{pmatrix} = \begin{pmatrix} R(q_d)^{-1}(p_d - p) \\ \bar{q}_d^{-1} \odot q \end{pmatrix} \quad (16)$$

and the velocity error as:

$$v_e = v - J(q_d)^{\dagger} \dot{\eta}_d \quad (17)$$

where $v_r = J(q_d)^{\dagger} \dot{\eta}_d$ can be seen as the desired velocity in the inertial frame $\dot{\eta}_d$ expressed in the vehicle frame. Based on the assumption of slow movement we can define the time derivative of v_r as:

$$\dot{v}_r = J^{\dagger}(q_d) \ddot{\eta}_d \quad (18)$$

The error dynamics then become:

$$\mathcal{N} : \begin{cases} \dot{g}_e = g_e [v_e]_{\times} \\ \dot{v}_e = f_e(\eta_e, v_e, \dot{\eta}_d) \end{cases} \quad (19)$$

where

$$f_e(\eta_e, v_e, \dot{\eta}_d) := M^{-1}(\tau - C(v)v + D(v)v + g(q)) - J^{\dagger}(q_d) \ddot{\eta}_d \quad (20)$$

Now the control problem can be formulated in the following way [12]: For a given reference trajectory $(\eta_d, \dot{\eta}_d, \ddot{\eta}_d)$, design a hybrid feedback control law with output $\tau^{des} \in \mathbb{R}^6$ such that every solution to \mathcal{N} is bounded and converges to the compact set

$$\mathcal{B} = \{(\eta_e, v_e) : \eta_e \in \{p_e = 0, q_e = \pm 1_q\}, v_e = 0\} \quad (21)$$

2) *Hybrid Adaptive Controller:* We employ an adaptive hybrid feedback control law to solve the control problem. The control law is functionally equivalent with the one presented in Basso et al. [12] with slight differences in notation. Thus, we only briefly describe the used controller. For an in-depth analysis and stability proof the interested reader is referred to [12] and references therein. The control law will consist of an adaptive part based on Lyapunov design to estimate the system dynamics [50], of a potential function, also based on Lyapunov stability design, which includes a hysteretic switching mechanism [33], and of a proportional feedback part acting on a reference velocity error [12]. All parts are encoded by the flow and jump sets and the jump map of the resulting control system, which is essentially equivalent to a

PD+ control law [51] augmented by the hysteretic switching mechanism, which leads to a hybrid control structure. To construct the hybrid adaptive controller we first introduce a modified reference velocity $v_m \in \mathbb{R}^6$ and the corresponding reference velocity error $\zeta_v = v_m - v_r$, to ensure convergence to the set \mathcal{B} . The reference velocity error is characterized by the differential equation:

$$\Lambda \dot{\zeta}_v = -dV_q(\eta_e) - \text{diag}(K_d)\zeta_v \quad (22)$$

Where $K_d \in \mathbb{R}^6$ is a vector of strictly positive control gains, $\Lambda \in \mathbb{R}^{6 \times 6}$ is a diagonal matrix of strictly positive gains and $V_q(\eta_e)$ is potential function based on Lyapunov design [33]:

$$V_q(\eta_e) = 2k(1 - h\mu_e) + \frac{1}{2}p_e^T \text{diag}(K_p)p_e \quad (23)$$

with $k > 0$ and $K_p \in \mathbb{R}^3$ are strictly positive control gains. Furthermore, μ_e describes the real part of the quaternion error q_e and h is the hysteretic switching variable. Given the set $Q := \{-1, 1\}$ and by defining the hysteresis half-width $\varsigma \in (0, 1)$ we can define the flow and jump sets of the controller by:

$$C := \{(\eta_e, h) \in \mathbb{R}^3 \times \mathbb{S}^3 \times Q : h\mu_e \geq -\varsigma\} \quad (24)$$

$$D := \{(\eta_e, h) \in \mathbb{R}^3 \times \mathbb{S}^3 \times Q : h\mu_e \leq -\varsigma\} \quad (25)$$

and the jump map is subsequently defined by:

$$G(h) = -h \quad (26)$$

Using (22) the velocity error can now be redefined as:

$$\delta = v - v_m = v_e - \zeta_v \quad (27)$$

which reverts to $\delta = v_e$ for $\zeta_v = 0$. Therefore, the velocity tracking objective is achieved for $(\delta, \zeta_v) = 0$. This error definition is suggested to be advantageous in cases where the configuration error encoded by dV_q is large while the velocity error v_e is zero [12].

To make the controller adaptive, we assume that there exists a vector of l unknown model parameters $\theta \in \mathbb{R}^l$ and a known multidimensional function of data $\Phi : \mathbb{R}^3 \times \mathbb{S}^3 \times \mathbb{R}^6 \times \mathbb{R}^6 \rightarrow \mathbb{R}^{6 \times l}$ so that [26]:

$$M\dot{v}_m + C(v)v_m + D(v)v_m + g(q) = \Phi(\eta_e, \zeta, \dot{\zeta}, \delta, v_r, \dot{v}_r)\theta \quad (28)$$

The dynamics model (10) can be defined with $l = 23$ parameters to be estimated, so that the restoring forces can be described by:

$$g(q) = \begin{bmatrix} -R(q)^T e_3 \theta_1 \\ -[e_3] \times R(q)^T \theta_{2:4} \end{bmatrix} \quad (29)$$

with $e_3 = [0, 0, 1]^T$. Assuming symmetries in port/starboard and fore/aft directions and assuming the centre of gravity coincides with the origin of the body frame except in heave direction, the inertia matrix can be described by:

$$M = \begin{bmatrix} \theta_5 & 0 & 0 & 0 & \theta_{11} & 0 \\ 0 & \theta_6 & 0 & -\theta_{11} & 0 & 0 \\ 0 & 0 & \theta_7 & 0 & 0 & 0 \\ 0 & -\theta_{11} & 0 & \theta_8 & 0 & 0 \\ \theta_{11} & 0 & 0 & 0 & \theta_9 & 0 \\ 0 & 0 & 0 & 0 & 0 & \theta_{10} \end{bmatrix} \quad (30)$$

leading to the following formulation of the matrix for Coriolis and centripetal forces:

$$C(v) = \begin{bmatrix} 0_{3 \times 3} & [\theta_{5:7} \circ v] \times - [w] \times [\theta_{11} e_3] \times \\ [\theta_{5:7} \circ v] \times - [\theta_{11} e_3] \times [w] \times & [\theta_{8:10} \circ w] \end{bmatrix} \quad (31)$$

where \circ denotes the element wise product. The hydrodynamic damping matrix can be defined by:

$$D(v) = -\text{diag}(\theta_{11+j}) - \text{diag}(\theta_{17+j})|v| \quad (32)$$

with $j \in \{1, \dots, 6\}$.

Now we define $\hat{\theta} \in \mathbb{R}^{23}$ to be the estimate of θ and $\tilde{\theta} = \hat{\theta} - \theta$ to be the estimation error. By assuming that the parameter estimation vector θ is constant, i.e $\dot{\theta} = \hat{\theta}$ we can define a parameter update law based on Lyapunov design [50]:

$$\dot{\hat{\theta}} = -\Gamma^{-1} \Phi(\eta_e, \zeta_v, \dot{\zeta}_v, \delta, v_r, \dot{v}_r)^T \delta \quad (33)$$

where $\Gamma = \text{diag}(\gamma) \in \mathbb{R}^{23 \times 23}, \gamma > 0$ is the adaptation gain matrix.

To ensure that the parameter estimation stays bounded, we further assume that θ has known lower and upper bounds $\underline{\theta}$ and $\bar{\theta}$. Now we can define the convex set:

$$P_\varepsilon := \{\hat{\theta} \in \mathbb{R}^{23} : \underline{\theta} - \varepsilon \leq \hat{\theta} \leq \bar{\theta} + \varepsilon\}, \quad (34)$$

where $\varepsilon \in \mathbb{R}^{23}$ is a vector of strictly positive boundary layer lengths for each interval consisting of lower and upper bound. The introduction of the boundary layers is necessary to ensure smoothness of the parameter estimation. Now we can define the projection operator $Proj : \mathbb{R}^{23} \times P_\varepsilon \rightarrow \mathbb{R}^{23}$ as [52]:

$$Proj(f(), \hat{\theta}) := \begin{cases} f() & \text{if } f() \in T_{R, [\underline{\theta}, \bar{\theta}]}(\hat{\theta}) \\ (1 - g(\hat{\theta}))f() & \text{if } f() \notin T_{R, [\underline{\theta}, \bar{\theta}]}(\hat{\theta}) \end{cases} \quad (35)$$

where $g(\hat{\theta})$ is defined by:

$$g(\hat{\theta}) = \begin{cases} 0 & \text{if } \hat{\theta} \in (\underline{\theta}, \bar{\theta}) \\ \min\{1, \frac{\underline{\theta} - \hat{\theta}}{\varepsilon}\} & \text{if } \hat{\theta} \leq \underline{\theta} \\ \min\{1, \frac{\hat{\theta} - \bar{\theta}}{\varepsilon}\} & \text{if } \hat{\theta} \geq \bar{\theta} \end{cases} \quad (36)$$

and $T_{R, [\underline{\theta}, \bar{\theta}]}(\hat{\theta})$ represents the extended tangent cone to each interval:

$$T_{R, [\underline{\theta}, \bar{\theta}]}(\hat{\theta}) := \begin{cases} [0, \infty) & \text{if } \hat{\theta} \leq \underline{\theta} \\ (-\infty, \infty) & \text{if } \hat{\theta} \in (\underline{\theta}, \bar{\theta}) \\ (-\infty, 0] & \text{if } \hat{\theta} \geq \bar{\theta} \end{cases} \quad (37)$$

Finally the adaptive hybrid control law can be defined by combining (22), (23), (26), (33) and (35):

$$\begin{cases} \dot{\zeta}_v = \Lambda^{-1}(dV_q(\eta_e) + \text{diag}(K_d)\zeta_v) \\ \hat{\theta} = Proj(-\Gamma^{-1} \Phi(\eta_e, \zeta_v, \dot{\zeta}_v, \delta, v_r, \dot{v}_r)^T \delta, \hat{\theta}) \\ h^+ \in G(h) \\ \tau^{des} = \Phi(\eta_e, \zeta_v, \dot{\zeta}_v, \delta, v_r, \dot{v}_r)\theta_a - dV_q(\eta_e) - K_d \delta \end{cases} \quad \begin{matrix} (\eta_e, h) \in C \\ (\eta_e, h) \in D \end{matrix} \quad (38)$$

D. Control allocation

In this section, we present the control allocation process for our framework, which involves converting the desired control inputs into appropriate commands for the fin actuators. We begin by introducing the forward model of control allocation, which serves as the basis for our analysis.

Next, we discuss three different solutions to the control allocation problem (inverse models). The first solution is a naive pseudo-inverse approach, which provides a straightforward but less optimal allocation strategy. The second solution is an optimization-based approach, which aims to find an optimal distribution of control efforts using quadratic programming [40]. Finally, we introduce our proposed novel control allocation which minimises the change of fin rotations. We hypothesize that this minimization should lead to significantly less delays and minimal disturbances in control response.

We then present a model that enables the conversion of desired fin forces into oscillation amplitudes. This model takes into account the specific parameters of the fin actuators, allowing for precise control allocation.

Additionally, we incorporate a CPG algorithm, which plays a crucial role in smoothly driving the fin actuators. The CPG algorithm generates rhythmic patterns of oscillations, ensuring coordinated and synchronized movements of the fins.

Forward model:

To produce the wrenches required to control the 6-DOF body motions, U-CAT's actuation follows an oscillatory movement described by:

$$\varphi^{osc}(t) = A^{osc} \sin(\omega^{osc}t + \varphi_{off}^{osc}) + \phi_0 \quad (39)$$

with the oscillation amplitude A^{osc} , the oscillation rate ω^{osc} , the phase offset φ_{off}^{osc} and the zero direction of the oscillation ϕ_0 .

To simplify the modeling, the instantaneous thrust $f^{th}(\varphi^{osc})$ produced by each fin can be averaged over one oscillation period T_{osc} [53]:

$$\overline{f^{th}}(\varphi^{osc}) = \frac{1}{T_{osc}} \int_0^{T_{osc}} f^{th}(\varphi^{osc}, \tau^{int}) d\tau^{int} \quad (40)$$

with τ^{int} being the integration time variable. Given the averaged thrust of each fin, the control vector that describes the resulting wrenches in body frame $\tau = [\tau_x, \tau_y, \tau_z, \tau_\Phi, \tau_\Theta, \tau_\Psi]^T$ can be derived by a concatenated frame transformation of the thrust described as a vector along the i^{th} fin's zero direction $\overline{\mathbf{f}}^i = [\overline{f^{th}}, 0, 0, 0, 0, 0]^T$:

$$\tau = \sum_{m=0}^n [Ad_{T_{m,b}}] R(\phi_{0,m}) \overline{\mathbf{f}}^m \quad (41)$$

with n being the total number of fins. $R(\phi_{0,i})$ is the two dimensional rotation matrix for fin i which maps the thrust produced along $\phi_{0,i}$ to horizontal and vertical forces in the rest frame of the fin.

$$R(\phi_{0,i}) = \begin{bmatrix} c\phi_{0,i} & 0 & s\phi_{0,i} & \\ 0 & 1 & 0 & 0_{3 \times 3} \\ -s\phi_{0,i} & 0 & c\phi_{0,i} & \\ & 0_{3 \times 3} & & 0_{3 \times 3} \end{bmatrix} \quad (42)$$

with $s* \doteq \sin(*)$ and $c* \doteq \cos(*)$. Furthermore, $[Ad_{T_{i,b}}]$ is the adjoint representation of the homogeneous transformation matrix $T_{f,b}$ that is used to map wrenches produced in the static fin frame to the robot's body frame:

$$[Ad_{T_{i,b}}] = \begin{bmatrix} R(\Phi_i^{fin}) & 0_{3 \times 3} \\ [p_i^{fin}]_{\times} R(\Phi_i^{fin}) & R(\Phi_i^{fin}) \end{bmatrix} \quad (43)$$

with $p_i^{fin} = [x_i^{fin}, y_i^{fin}, z_i^{fin}]$ being the fin coordinates relative to the centre of the vehicle and with $R(\Phi_i)$ being the rotation matrix mapping from fin to body frame based on the orientation vector of the fin rest frame $\Phi_i^{fin} = [\phi_i^{fin}, \theta_i^{fin}, \psi_i^{fin}]^T$:

$$R(\Phi) = \begin{bmatrix} c\psi c\theta & -s\psi c\theta + c\psi s\theta s\phi & s\psi s\theta + c\psi c\theta s\phi \\ s\psi c\theta & c\psi c\theta + s\psi s\theta s\psi & -c\psi s\theta + s\psi c\theta s\phi \\ -s\theta & c\theta s\phi & c\theta c\phi \end{bmatrix} \quad (44)$$

The fin frames are arranged symmetrically (shown in Fig. 3) such that $\psi_1^{fin} = -\psi_2^{fin} - \pi = -\psi_3^{fin} = \psi_4^{fin} + \pi$, $x_1^{fin} = -x_2^{fin} = -x_3 = x_4^{fin}$, and $y_1^{fin} = y_2^{fin} = -y_3^{fin} = -y_4^{fin}$. Now by using (41) and defining $\psi^{fin} = |\psi_i^{fin}|$, $x^{fin} = x_1^{fin}$ and $y^{fin} = y_1^{fin}$ we can define the resulting wrenches as a system of six algebraic equations with the fins' zero directions $\phi_{0,1-4}$ and thrusts f^{th}_{1-4} as independent variables written in matrix form $AX = B$:

$$\begin{bmatrix} 1 & -1 & -1 & 1 & 0 & 0 & 0 & 0 \\ -1 & -1 & 1 & 1 & 0 & 0 & 0 & 0 \\ 0 & 0 & 0 & 0 & 1 & 1 & 1 & 1 \\ 0 & 0 & 0 & 0 & 1 & 1 & -1 & -1 \\ 0 & 0 & 0 & 0 & -1 & 1 & 1 & -1 \\ -1 & 1 & -1 & 1 & 0 & 0 & 0 & 0 \end{bmatrix} \begin{bmatrix} c\phi_{0,1} \overline{f^{th}_1} \\ c\phi_{0,2} \overline{f^{th}_2} \\ c\phi_{0,3} \overline{f^{th}_3} \\ c\phi_{0,4} \overline{f^{th}_4} \\ s\phi_{0,1} \overline{f^{th}_1} \\ s\phi_{0,2} \overline{f^{th}_2} \\ s\phi_{0,3} \overline{f^{th}_3} \\ s\phi_{0,4} \overline{f^{th}_4} \end{bmatrix} = \begin{bmatrix} \tau_x \\ \tau_y \\ \tau_z \\ \tau_\Phi \\ \tau_\Theta \\ \tau_\Psi \\ \tau_y \\ \tau_x \\ \tau_z \\ \tau_\Theta \\ \tau_\Psi \\ \tau_x \end{bmatrix}$$

with $M_a = x^{fin} c\psi^{fin} - y^{fin} s\psi^{fin}$.

Inverse model:

Here, we present the three studied control allocation solutions that allows to control the robot in 6-DOF simultaneously.

1) *Direct solution:* Since the matrix A is of full rank, a non-unique solution for the system using the Moore-Penrose inverse exists, hence $X = A^T(AA^T)^{-1}B$. Given the aforementioned symmetric configuration of the $i = 1, \dots, 4$ fins, the solution can be expressed in the following form, where fin forces and orientations are still coupled:

$$c\phi_{0,i} \overline{f^{th}_i} = \frac{1}{4} \left(\frac{\tau_x}{c\psi_i} + \frac{\tau_y}{s\psi_i} + \frac{\text{sign}(\psi_i) \tau_\Psi}{M_a} \right) \quad (45)$$

$$s\phi_{0,i} \overline{f^{th}_i} = \frac{1}{4} \left(\tau_z + \frac{\tau_\Phi}{y_i} - \frac{\tau_\Theta}{x_i} \right) \quad (46)$$

By defining the sums of wrenches in (45) and (46) in terms of horizontal f_i^{hor} and vertical f_i^{vert} contributions respectively as:

$$f_i^{hor} = \frac{\tau_x}{c\psi_i} + \frac{\tau_y}{s\psi_i} + \frac{\text{sign}(\psi_i) \tau_\Psi}{M_a} \quad (47)$$

$$f_i^{ver} = \tau_z + \frac{\tau_\Phi}{y_i} - \frac{\tau_\Theta}{x_i} \quad (48)$$

and then dividing equation (46) by equation (45), we can deduce the zero direction $\phi_{0,i}$ for each fin as follows:

$$\phi_{0,i} = \arctan 2 \left(f_i^{ver}, f_i^{hor} \right) \quad (49)$$

The thrust forces required by each fin are then derived by squaring and adding equations (45) and (46):

$$\overline{f_i^{th}} = \frac{1}{4} \sqrt{(f_i^{hor})^2 + (f_i^{ver})^2} \quad (50)$$

For this control allocation method, denoted as CA_{inv} , it is important to note that all four fins need to be actuated regardless of the controller's output τ^{des} . This characteristic can lead to undesired fin rotations, such as all four fins rotating 180° when the surge component changes its sign. These rotations result in significant disturbances caused by the fin movements when changing the fin's orientation.

2) *Optimization based solution*: An alternative approach to solve the control allocation problem involves employing near real-time optimization techniques. In this optimization-based solution, the constraints presented in in Equation (IV-D) are reconfigured to relax the trigonometric functions involved as follows:

$$\min_{f_i^{th}} J = \overline{f_i^{th}}^T \overline{f_i^{th}} \quad (51)$$

Subject to:

$$\begin{aligned} \tau_x &= c\psi_f \left(\Gamma_1^{opt} \overline{f_1^{th}} - \Gamma_2^{opt} \overline{f_2^{th}} - \Gamma_3^{opt} \overline{f_3^{th}} + \Gamma_4^{opt} \overline{f_4^{th}} \right) \\ \tau_y &= s\psi_f \left(-\Gamma_1^{opt} \overline{f_1^{th}} - \Gamma_2^{opt} \overline{f_2^{th}} + \Gamma_3^{opt} \overline{f_3^{th}} + \Gamma_4^{opt} \overline{f_4^{th}} \right) \\ \tau_z &= \Lambda_1^{opt} \overline{f_1^{th}} + \Lambda_2^{opt} \overline{f_2^{th}} + \Lambda_3^{opt} \overline{f_3^{th}} + \Lambda_4^{opt} \overline{f_4^{th}} \\ \tau_\Phi &= y_f \left(\Lambda_1^{opt} \overline{f_1^{th}} + \Lambda_2^{opt} \overline{f_2^{th}} - \Lambda_3^{opt} \overline{f_3^{th}} - \Lambda_4^{opt} \overline{f_4^{th}} \right) \\ \tau_\Theta &= x_f \left(-\Lambda_1^{opt} \overline{f_1^{th}} + \Lambda_2^{opt} \overline{f_2^{th}} + \Lambda_3^{opt} \overline{f_3^{th}} - \Lambda_4^{opt} \overline{f_4^{th}} \right) \\ \tau_\Psi &= M_a \left(-\Gamma_1^{opt} \overline{f_1^{th}} + \Gamma_2^{opt} \overline{f_2^{th}} - \Gamma_3^{opt} \overline{f_3^{th}} + \Gamma_4^{opt} \overline{f_4^{th}} \right) \\ 1 &= \Gamma_i^{opt} + \Lambda_i^{opt} \quad i = 1 \dots 4 \\ -1 &\leq \Gamma_i^{opt} \leq 1 \quad i = 1 \dots 4 \\ -1 &\leq \Lambda_i^{opt} \leq 1 \quad i = 1 \dots 4 \\ 0 &\leq \overline{f_i^{th}} \leq F_{max} \quad i = 1 \dots 4 \end{aligned} \quad (52)$$

The objective of the cost function is to minimize the force exerted. It is worth noting that the optimization process does not include an additional term to minimize the zero-direction change, as it was found to be counterproductive and led to non-convergence of the algorithm.

The optimization problem is solved during runtime to find the optimal parameters $[\overline{f_i^{th}}, \Gamma_i^{opt}, \Lambda_i^{opt}]$ using Sequential Quadratic Programming (SQP) [54]. The initial conditions for

all parameters are set to 0. The zero-directions ϕ_0 are then computed using the following formula:

$$\phi_{0,i} = \text{atan2}(\Lambda_i^{opt}, \Gamma_i^{opt}) \quad i = 1 \dots 4 \quad (53)$$

This optimization-based solution for control allocation presents certain limitations. Firstly, it does not explicitly include the minimization of zero-direction change in its objective cost function, which will not guarantee finding the optimal solution for minimum zero-direction change. Secondly, the use of an iterative optimization algorithm requires more computation resources and capabilities to ensure timely execution within the hardware constraints.

Throughout the rest of the paper, the optimization-based control allocation method will be referred to as CA_{opt} .

3) *Proposed analytic solution*: To address the limitations of the two control allocation methods discussed, namely CA_{inv} and CA_{opt} , we propose a novel approach that analytically solves the control allocation problem while considering the minimization of the zero-direction change.

Taking advantage of the symmetrical configuration of UCAT's fins, we observe that for certain degrees of freedom such as surge, sway, heave, and yaw, it is possible to only employ two fins to provide a thrust vector to move in certain directions, as illustrated in Fig. 3.

In the following we derive the control allocation equations (49) and (50) as functions of the desired numbers n_d of fins used for the surge, sway, heave and yaw degrees of freedom, by utilizing Heaviside unit step functions $H(\cdot)$ [55, p. 61]. We re-define the sums of wrenches from equations (47) and (48) as:

$$f_i^{hor}(\tau, n_d) = \frac{h_H(\tau_x, c\psi_i, n_d)}{c\psi_i} + \frac{h_H(\tau_y, s\psi_i, n_d)}{s\psi_i} + \frac{h_H(\tau_\Psi, \psi_i, n_d)}{M_a} \quad (54)$$

$$f_i^{ver}(\tau, n_d) = h_H(\tau_z, -\psi_i, n_d) + \frac{\tau_\Phi}{y_i} - \frac{\tau_\Theta}{x_i} \quad (55)$$

with $\text{heav}(\cdot)$ determining the fin usage with Heaviside functions as:

$$h_H(\tau, s, n_d) = \begin{cases} 2 H(\text{sign}(s)\tau) & \tau \quad n_d = 2 \\ \tau & n_d = 4 \end{cases} \quad (56)$$

By inserting (54), (55) in (49) and (50) the zero direction and thrust force for each fin can be described by:

$$\phi_{0,i} = \arctan \left(\frac{f_i^{ver}(\tau, n_d)}{f_i^{hor}(\tau, n_d)} \right) \quad (57)$$

$$\overline{f_i^{th}} = \frac{1}{4} \sqrt{f_i^{hor}(\tau, n_d)^2 + f_i^{ver}(\tau, n_d)^2} \quad (58)$$

The proposed control allocation scheme described above allows the robot to have more flexibility in terms of movement.

Moreover, we can again exploit the fins symmetrical configuration to minimize the change in zero direction control. Indeed, when controlling forces and torques around the vertical plane, then the fins are oriented with angle of $\pm \frac{\pi}{2}$ according to equation (57). To avoid the non-linearity in the arctan

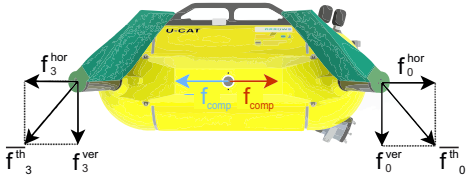


Fig. 4: Illustration of the horizontal force compensation principle to minimize the fins' zero-direction change when controlling vertical forces.

function, we can introduce two opposing horizontal forces that are naturally compensated, as illustrated in Fig. 4. We add a term f_{comp} such that:

$$\overline{f_i^{th}} = \frac{1}{4} \sqrt{(f_{comp} + f_i^{hor}(\tau, n_d))^2 + f_i^{hor}(\tau, n_d)^2} \quad (59)$$

with

$$f_{comp} = \alpha_{comp} \sum_j (1 - f_j^{norm}) |f_j^{norm}| \quad (60)$$

with $j = z, \Theta, \Psi$ and $f_j^{norm} = \frac{|\tau_j|}{f_j^{th_{max}}}$. This means that the compensation is not introduced in two cases: when $f_j^{norm} = 0$ and when $f_j^{norm} = 1$. The parameter α_{comp} is a scalar that weighs the effect of the introduced term f_c to minimize the zero-direction change, at the expense of higher oscillation amplitudes.

The proposed control allocation method will be referred to as CA_{prop} .

E. Force to amplitude

Once the required thrust $\overline{f_i^{th}}$ for each fin is computed, it is converted to a fin-oscillating amplitude using the inverse model described in [49] as follows:

$$A_i^{osc} = \arccos \left(\frac{-\overline{f_i^{th}}}{2C_d \rho S_f (r_c \omega^{osc})^2} + 1 \right) \quad (61)$$

where ω^{osc} denotes the angular rate of the fin, ρ is the water density, r_c is the distance between the rotation axis and the center of gravity of the fin, C_d stands for the drag coefficient, and S_f is the projection area of the fin. The resulting amplitudes A_i^{osc} and zero-directions $\phi_{0,i}$ are then filtered using a Central Pattern Generator (CPG) algorithm.

F. CPG algorithm

The CPG is used to ensure smooth and continuous transitions, which significantly reduces the effect of the non-modelled fin lateral forces. The equations of the CPG used in our study are adopted from [56]:

$$\dot{\zeta}_i^{CPG} = \omega_i^{osc} \quad (62)$$

$$\dot{A}_i^{CPG} = K_{amp} \left(\frac{K_{amp}}{4} (A_i^{osc} - A_i^{CPG}) - \dot{A}_i^{CPG} \right) \quad (63)$$

$$\dot{\phi}_{0,i}^{CPG} = K_{zd} \left(\frac{K_{zd}}{4} (\phi_{0,i} - \phi_{0,i}^{CPG}) - \dot{\phi}_{0,i}^{CPG} \right) \quad (64)$$

$$\phi_i^{CPG} = \phi_{0,i}^{CPG} + A_i^{CPG} \cos(\zeta_i^{CPG}) \quad (65)$$

where ϕ_i^{CPG} is the zero-direction angle (in radians) extracted from the oscillator and ζ_i^{CPG} , A_i^{CPG} and $\phi_{0,i}^{CPG}$ are state variables that encode the phase, amplitude and the zero-direction offset of the oscillations (in radians), respectively. The parameters ω_i^{osc} , A_i^{osc} and $\phi_{0,i}$ are control parameters for the desired angular rate, amplitude and offset of the oscillations generated by the control allocation.

G. State estimation

To provide the control framework with reliable information about the robot's state, we are using an EKF as presented in [57]. Position in the inertial frame $p \in \mathbb{R}^3$ and linear velocities $v \in \mathbb{R}^3$ are the states estimated by the filter $\xi = [p, v]^T \in \mathbb{R}^6$. A kinematic vehicle model assuming constant velocity is used in the filters prediction. The constant velocity assumption is justified for slow moving vehicles, and thus applicable in our scenario. Orientation information is assumed to be an input to the model. The filter prediction at time step k can be then described by:

$$\xi_k^- = \begin{bmatrix} p_{k-1} + R(q_k) \left(v_{k-1} + n_{k-1} \frac{t^2}{2} \right) \\ v + n_{k-1}^{acc} t \end{bmatrix} \quad (66)$$

with $n^{acc} \in \mathbb{R}^3$ representing zero-mean white Gaussian acceleration noise. The acceleration noise covariances are then represented by the system noise covariance matrix $Q = \text{diag}(\sigma_{acc}^2) \in \mathbb{R}^{3 \times 3}$

and the prediction covariance:

$$P_k^- = A_k^{EKF} P_{k-1} A_k^{EKF T} + W_k^{EKF} Q^{EKF} W_{k-1}^{EKF T} \quad (67)$$

with A^{EKF} and W^{EKF} being Jacobians of (66) with respect to the filter states and system noises respectively. The prediction is followed by the standard EKF correction step:

$$\begin{aligned} K_k &= P_k^- H^T (H P_k^- H^T + R^{EKF})^{-1} \\ \xi_k &= \xi_k^- + K_k (z_k - H_k \xi_k^-) \\ P_k &= (I - K_k H_k) P_k^- \end{aligned} \quad (68)$$

using asynchronous measurement updates $z_k = H_k \xi_k + s_k$, which make use of a variable size allocation for the observation matrix H_k as shown in Palomeras et al. [57] and where s_k is the measurement noise. Additionally, the standard notation applies with K_k being the Kalman gain and R^{EKF} describing the measurement covariance matrix.

V. NUMERICAL SIMULATIONS

We employed a simulation framework to provide a practical and efficient method for evaluating the presented autonomy framework, with specific focus on controller and control allocation, using U-CAT as test-platform. The simulation is purely written in Python for fast deployment, and is based on Fossen's vectorial dynamics model (10). Furthermore, a lift and drag based model is utilized to simulate the forces produced by the fins. Trajectory generation, control and state estimation are simulated according to the descriptions shown in the previous sections. To attain robust and reliable estimates of the performance of our proposed control allocation solution in comparison to the presented state of the art solutions C_{prop} and C_{inv} solutions we use Monte Carlo Simulations in combination with a set of assessment metrics. Those metrics are used to estimate tracking performance as well as, physical and computational efficiency. All simulations were run on a laptop with a 11th generation Intel Core i7-1165G7 processor and 16 GB RAM, running Ubuntu 20.04.6 LTS.

The following paragraphs detail the structure of simulation framework, including the models used to simulate the dynamics of the robot and fins, the Monte Carlo setup including modeled sensor noise, and the methodology for tuning the control system's hyper-parameters.

A. Dynamics simulation

The simulation of U-CAT's dynamics was performed using Fossen's hydrodynamic model presented in (10). The differential equations derived from this mode were solved using the 4th order Runge-Kutta algorithm with a step size of 0.01 s. This approach enabled the accurate representation of U-CAT's behaviour in controlled underwater environment, taking into account the various hydrodynamic parameters, and the effect of the fins' oscillations. The relevant parameters were identified with an approach described in [23].

The dynamic model used to simulate the fins of U-CAT was based on the rigid paddle model [59]. The validity of this model was demonstrated and validated in previous research [58] when simulating the underwater hexapod robot AQUA [60].

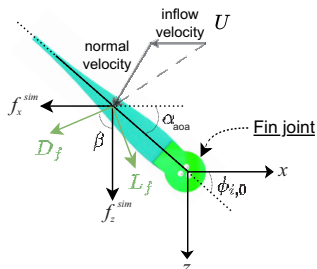


Fig. 5: Visualization of forces on i^{th} fin based on simple lift and drag model (model and figure adopted from [58]).

The fins of U-CAT are simulated to generate horizontal f_x^{sim} and vertical f_z^{sim} forces relative to the fin's rest frame, as depicted in Fig. 5 through the following expressions:

$$\begin{aligned} f_x^{sim} &= D_f \sin(\beta) + L_f \cos(\beta) \\ f_z^{sim} &= -L_f \sin(\beta) + D_f \cos(\beta) \end{aligned} \quad (69)$$

Where β represents the direction of flow impinging on the fin, and D_f and L_f denote the lift and drag forces, respectively. These forces are defined as:

$$\begin{aligned} L_f &= 0.5\rho U_f^2 S_f C_{Lmax} \sin(2\alpha_{aoa}) \\ D_f &= 0.5\rho U_f^2 S_f C_{Dmax} (1 - \cos(2\alpha_{aoa})) \end{aligned} \quad (70)$$

where α_{aoa} is the angle of attack, and U_f is the velocity of the flow impacting the fin. Additionally, C_{Lmax} and C_{Dmax} are the maximum lift and drag coefficients of the paddle, respectively, over the full 360° range of the angle of attack. The coefficients were tuned so that the resulting simulated thrust output was quantitatively similar to the output from laboratory experiments shown in [23].

Finally the resulting simulated wrenches in body frame can be computed by:

$$\boldsymbol{\tau}^{sim} = \sum_{m=0}^n [Ad_{T_{m,b}}] \mathbf{f}_m^{sim} \quad (71)$$

with $\mathbf{f}^{sim} = [f_x^{sim}, 0, f_z^{sim}, 0, 0, 0]^T$ being the vector of fin forces in the fin's rest frame, and $[Ad_{T_{m,b}}]$ defined as in (43). For a more in-depth discussion of the simulation of fin forces, the reader is encouraged to consult [58].

B. Monte Carlo Framework

We ran 500 iterations in a Monte Carlo simulation framework for the 3 studied control allocation methods, namely CA_{inv} , CA_{opt} and CA_{prop} , while keeping the other modules of the autonomy framework constant. In each run of the Monte Carlo simulations both a trajectory scenario (6T or 3T2S) and type (Ellipse or Lissajous) are picked at random. The relevant parameters for the specific trajectory are uniformly sampled from a bounded set as shown in Table II. Each trajectory tracking simulation is run for 400 s. Additionally, to ensure a more realistic trajectory tracking evaluation, we simulated the sensor suite shown in Fig. 2, including an IMU for orientation estimation, a pressure sensor for depth estimation and a camera based position estimator. For all sensors the true simulated state of the robot was used as basis and white Gaussian noise (WGN) with a zero mean was added. The variances for the WGN additions are chosen to reflect the sensor characteristics of the real vehicle used in subsequent experiments and are also shown in Table II. The controller gains provided by the GA were kept constant for each simulation run. The flowchart in Fig. 6 describes the full setup of the Monte Carlo simulation framework.

TABLE II: Permissible ranges of trajectory generation and sensor simulation parameters for Monte Carlo Simulations.

Ellipsoidal		Lissajous	
Trajectory generation			
$[x_0, A_x, \omega_x]$	[0.3, 0.5 - 2.5, 0.01 - 0.05]		
l_x	/	0.5 - 2.0	
$[A_y, \omega_y]$	[0.5 - 2.5, 0.01 - 0.05]		
l_y	/	0.5 - 2.0	
$[A_z, \omega_z, c_\phi]$	[0.1 - 0.5, 0.01 - 0.05, 0.05 - 0.15]		
r^*	0.1		
$[\gamma_1, \gamma_2]$	[7.0 ₆ ×1, 1.0 ₆ ×1]		
Sensor simulation			
σ_{pose}^{WGN}	[0.002, 0.002, 0.002, 0.0017, 0.0017, 0.0017] ^T		
State estimation			
σ_Q	[0.01, 0.01, 0.01, 0.02, 0.02, 0.01] ^T		
σ_R	[0.002, 0.002, 0.002] ^T		

C. Data Analysis

We defined several evaluation metrics, inspired by suggestions of Manhaes et al [61], to characterize the performance of our proposed control framework. Based on the tracking error with the orientation error represented by Euler angles $\Phi \eta_{e,j} = [p_{e,j}, \Phi_{e,j}]^T$ the following evaluation metrics were defined and used:

- **Root Mean Squared Error** between desired and estimated robot trajectory for linear and angular DOF [**RMSE_{lin}** and **RMSE_{ang}**]

$$RMSE = \sqrt{\frac{\sum_{j=1}^N \Phi \eta_{e,j}^T \Phi \eta_{e,j}}{N}} \quad (72)$$

- **Maximum Error Magnitude** between desired and estimated robot trajectory for linear and angular DOF [**MEM_{lin}** and **MEM_{ang}**]

$$MEM = \max \{ \|\Phi \eta_{e,1}\|, \|\Phi \eta_{e,2}\|, \dots, \|\Phi \eta_{e,N}\| \} \quad (73)$$

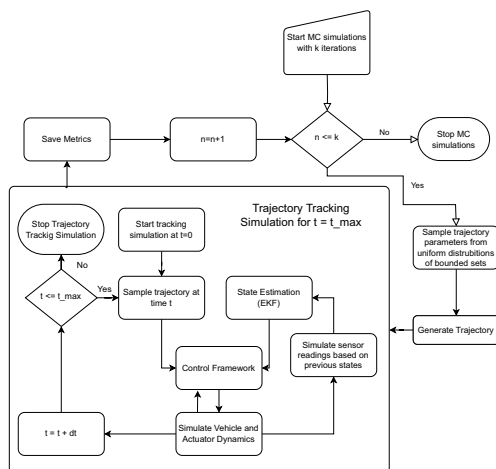


Fig. 6: Flowchart for Monte Carlo Simulations.

- **Mean Absolute Wrench [MAW]**

$$MAW = \frac{1}{N} \sum_{n=1}^N \left\| \frac{\tau_n^{sim}}{corr_{Ma}} \right\| \quad (74)$$

- **Maximum Wrench [MW]**

$$MW = \max \left\{ \left\| \frac{\tau_1^{sim}}{corr_{Ma}} \right\|, \left\| \frac{\tau_2^{sim}}{corr_{Ma}} \right\|, \dots, \left\| \frac{\tau_n^{sim}}{corr_{Ma}} \right\| \right\} \quad (75)$$

- **Median Computation Time** for control allocation [**MCT**]

$$MCT = med \{ dt_1^{ca}, dt_2^{ca}, \dots, dt_N^{ca} \} \quad (76)$$

- **Mean Allocation Error** for linear and angular degrees of freedom [**MAE_{lin}** and **MAE_{ang}**]

$$MAE = \frac{1}{N} \sum_{j=1}^N \left| \tau_j^{des} - \tau_j^{sim} \right| \quad (77)$$

Here N is defined as the number of data points for a specific simulation or experimental run. Furthermore, τ_j^{des} describes the commanded wrench, which is produced by the hybrid adaptive controller (38), whereas τ_j^{sim} describes the wrenches produced by the simulation of the oscillating fins (71). To correctly represent the wrench related metrics, the torques in the simulated wrenches τ^{sim} are converted into forces using the respective moment arms $corr_{Ma} = [0, 0, 0, x^{fin}, y^{fin}, M_d]^T$. The time it takes, given τ_j^{des} , for the respective control allocation algorithm to assign the fin kinematics is described by $dt_j^{ca} = t_{0,j}^{ca} - t_j^{ca}$.

RMSE and MEM describe average and maximum errors and thus an estimate of tracking performance, while MEM and MW provide a measure of energy consumption in terms of physical action demanded by the tested allocation frameworks. MCT in turn provides a measure of computational energy demanded by the allocation algorithms. Finally MAE can be used to evaluate the accuracy of the allocation algorithms which are tested. All evaluation metrics are computed for each single simulation run in the Monte Carlo framework and then the median with interquartile range (IQR) is computed over all runs, to provide a robust estimate of overall performance.

D. Hyper-parameters tuning

This section describes the hyper-parameters tuning process in numerical simulations for all the autonomy modules described in Section IV. The coefficients γ_1 and γ_2 of the trajectory generator were manually adjusted to ensure that the generated velocities and accelerations fall within the physically feasible range for the robot. The gain matrix $\Lambda = I_6$ was defined in accordance to [12]. The boundaries and boundary layers for the adaptive model estimation were defined to keep each variable within a range that is still physically plausible. To define the starting parameters of the adaptive part of the controller, model parameters identified in previous work [23] were taken as guiding values. However, to reflect the uncertainty in the identification process and to better estimate the quality of the adaptive part of the controller, parameters provided by model identification [23] were rounded and

decreased to base values like 10.0, 100.0 or 5.0. Finally, the adaptation gain matrix Γ was tuned manually based on simulation results. The numeric values for each parameter can be found in Table III.

To make the process of tuning the control gains K_p and K_d less arbitrary and to some extent repeatable, optimal gains were identified by using a genetic algorithm. For this automated tuning process we defined a combined reference trajectory consisting of both, an ellipse type and Lissajous type trajectory (see Fig 7). The parameters for both trajectory types were selected to be mean values of the parameter ranges used in the Monte Carlo simulations (see Table II). Based on this reference trajectory, we employed a *geneticalgorithm* package [62] to implement the Genetic Algorithm (GA) optimization technique for tuning the gains of the controller. We used the following GA algorithm parameters: a maximum number of iterations of 50, a population size of 20, a mutation probability of 0.45, an elitism ratio of 0.01, a crossover probability of 0.5, a parents portion of 0.25, and a uniform crossover type.

We defined a cost function Υ to be minimized such that:

$$\Upsilon = \sqrt{\frac{1}{N} \sum_{j=1}^N \Phi \eta_{e,j} Q^{GA} \Phi \eta_{e,j} + \tau_j^{sim} R^{GA} \tau_j^{sim}} \quad (78)$$

Where N is the total number of iterations, Q^{GA} and R^{GA} are positive-definite weighting matrices such that $Q^{GA} = \text{diag}([100, 100, 100, 50, 50, 50, 50])$ and $R^{GA} = \text{diag}(0.5, 0.5, 0.5, 0.5, 0.5, 0.5)$. Finally, the optimization was constrained by predefined boundaries for K_p and K_d of 0.1 to 50.0.

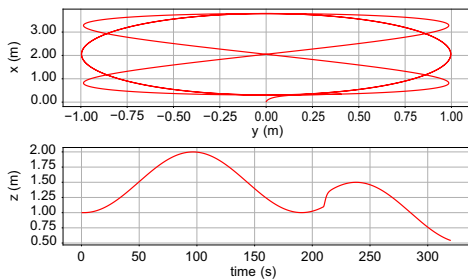


Fig. 7: Trajectory used for controller gain tuning with genetic algorithm. The trajectory is a combination of the ellipsoid and Lissajous trajectories presented in Table I.

To tune the parameters for the control allocation modules, we followed the following approach: The CPG parameters K_{amp} , K_{zd} and α_{comp} were tuned by running simulations with gains in range $[1 - 15]$, $[1 - 15]$, $[0 - 150]$ respectively, and assessing the allocation errors AE_{lin} and MAE_{ang} for the three studied control allocation methods. Studying the effect of α was relevant only for the case of the proposed control allocation method CA_{prop} . The numeric values for the parameters found are summarized in Table III. Moreover, the parametric values for the force to amplitude model denoted in (61) are summarized in Table IV.

Finally, the covariance matrices R^{EKF} and Q^{EKF} for the EKF were hand-tuned based on data from simulations and preliminary experiments.

VI. EXPERIMENTS

A. Experimental Setup

A series of validation experiments were conducted in a swimming pool to validate the control allocation methods (see Fig 8). The experimental setup included a fabric grid of size 3 m by 6 m containing 324 ArUco markers [63]. The grid consisted of 108 markers of size 0.25 m and 216 markers of size 0.1 m. These markers were used to provide the robot with position measurements in the Earth-fixed frame R_n using the onboard Chameleon PointGrey camera. The robot's EKF is updated with position measurements from the detected ArUco markers with a frequency of 10 Hz and with angular states from the onboard MPU-6050 IMU with a frequency of 100 Hz.

Two different control allocation methods were tested in these trials: the proposed analytic control allocation (CA_{prop}) and the state-of-the-art optimization-based control allocation (CA_{opt}). The SQP required for the optimization is provided by the library *ALGLIB* [64]. The naive control allocation method (CA_{inv}) was excluded from these experimental trials due to its demonstrated ineffectiveness for fin-actuated robots, as evidenced by the simulation results that will be presented in section VII-A.

The experiments were performed for the 3-degrees-of-freedom tracking scenario with roll and pitch stabilized (3T2S), employing two different trajectory types: ellipse and Lissajous. For each trajectory type and for each of the two tested control allocation methods, five trials were conducted, resulting in a total of 20 trials overall. The 6T was not considered in these experiments due to the potential loss of ArUco marker-based position feedback when controlling roll and pitch. Additionally, the distribution of centre of mass and centre of buoyancy created a passively stabilizing system which would have disturbed the controller and potentially exceeded the available control authority.

Many of the metrics used in simulation could not be directly transferred to the evaluation of the experimental results as essential parameters such as forces produced by the fins could not be measured. Therefore, the tracking errors for each DOF are presented as well as a root mean square metric for demanded forces/torques for every DOF. Finally, we provide mean and maximum computation times for the control allocation.

B. Hyper-parameter tuning in experiments

Starting from the identified values in the simulation, the controller parameters K_p and K_d were adjusted using a manual tuning process based on pool trials with CA_{prop} . The same parameters were then tested directly with the optimization-based control allocation method. Observations indicated that the values required no additional adjustments and provided a satisfactory performance. The controller parameters for both control allocation methods were therefore defined as $K_p = [1.9, 0.1, 3.7, 1.6]$ and $K_d = [8.5, 0.5, 8.8, 1.16, 2.58, 3.5]$.

TABLE III: Controller and control allocation parameters used in the simulation.

	CA_{prop}	CA_{opt}	CA_{inv}
K_p	[3.81, 3.39, 3.76, 3.93]	[4.25, 3.04, 2.794, 14]	[17.45, 4.31, 7.41, 14.65]
K_d	[3.46, 4.59, 4.41, 2.01, 3.39, 4.68]	[2.8, 4.0, 4.35, 1.89, 3.43, 3.7]	[16.02, 48.5, 8.83, 18.35, 6.07, 42.41]
K_{amp}	10		5
K_d	3		2
α_{comp}	30		-
f_{max}^h		5	
Λ		[1.0, 1.0, 1.0, 1.0, 1.0, 1.0]	
Γ		[1.0 _{23x1}]	
θ_{start}	[0.4 _{x1} , 50.0 _{3x1} , 1.0 _{3x1} , 0.1, -5.0, -50.0, -10.0, 0.2 _{x1} , -0.5, -10.0, -100.0, -200.0, -1.0 _{2x1} , -0.1]		
θ	[-2.0, -1.0 _{3x1} , 0.6 _{x1} , -5.0, -10.0, -50.0, -10.0, -5.0 _{2x1} , -0.5, -50.0, -500.0 _{2x1} , -2.0, -5.0, -1.0]		
$\dot{\theta}$		[2.0, 1.0 _{3x1} , 100.0 _{3x1} , 5.0 _{4x1} , 0.1 _{2x1}]	
$\ddot{\theta}$		[0.1 _{4x1} , 10.0 _{3x1} , 0.5 _{3x1} , 0.1, 1.0 _{3x1} , 0.1 _{3x1} , 5.0, 10.0 _{2x1} , 0.1 _{3x1}]	
ζ		0.1	

TABLE IV: Parameters for simulating fin dynamics and force to amplitude conversion.

ρ (kg/m ³)	S_f (m ²)	ω^{osc} (rad/s)	r_c (m)	C_d	C_{Lmax}	C_{Dmax}
997	0.02	4π	0.1	0.24	1.65	3.2

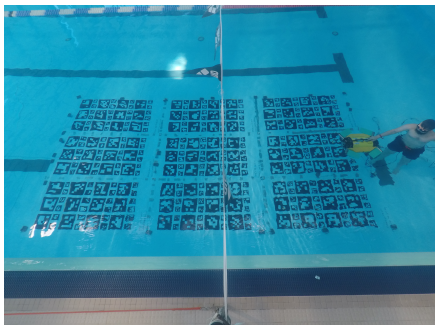


Fig. 8: Experimental setup at Keila swimming pool (Estonia).

The adaptive, control allocation, trajectory generation and EKF parameters obtained during the simulation tuning process (summarized in Table III) were kept the same in experiments.

VII. RESULTS AND DISCUSSION

In this section, we present and analyze the results obtained from the performed simulations and experiments. The first subsection is dedicated to a thorough comparison of the available control allocation strategies independently from of the overarching control framework. Subsequently, we present and discuss the results of our Monte Carlo simulations of the whole autonomy framework for two separate trajectory tracking scenarios; 6T and 3T2S. Finally, we present and discuss experimental results of the whole control framework for the 3T2S scenario with two different trajectory types (ellipse and Lissajous). All trajectory tracking results are discussed in light of the relevant performance metrics to quantify the various aspects of the tested solutions. Our goal is to thoroughly evaluate the performance of the proposed solution and provide a comprehensive analysis of its strengths and limitations.

A. Control allocation comparative results

The performance of the investigated control allocation methods was first evaluated in the simulation environment

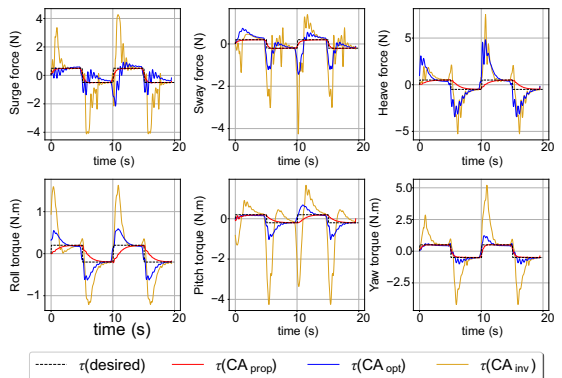


Fig. 9: Comparison of the studied control allocation approaches for tracking a desired control input.

in isolation by establishing a desired 6-DOF wrench vector, $\tau^{des} = [0.5, 0.5, 0.5, 0.2, 0.2, 0.2]^T$, programmed to switch sign every 5 seconds, as depicted in Fig. 9. The mean body forces produced by the fins under the influence of the various control allocation methods are displayed in Figure 9.

As displayed in Fig. 9, CA_{prop} generates body forces that align with the desired wrenches τ^{des} without any overshoot. This can be attributed to the minimization of the zero-direction change implemented in this method. A slight response delay can be noted for heave, roll, and pitch. In terms of MAE_{lin} and MAE_{ang} , as presented in Table VI, the proposed method CA_{prop} yields the most effective results.

In contrast, CA_{opt} exhibits a rapid response in the generated body forces and torques, but with a significant overshoot. This is mainly due to the lateral fin forces that emerge when the fins' zero-direction angles change abruptly, which results in greater linear MAE_{lin} and angular MAE_{ang} allocation errors, compared to the proposed control allocation method CA_{prop} .

Regarding CA_{inv} , the obtained results indicate that this method is not well-suited for fin-actuated vehicle control. This is because all fins contribute to wrenches in all DOF, without considering the change in the zero-direction angle. Fast or large changes in zero direction then cause a substantial overshoot in body forces, as evidenced in Figure 9.

These findings highlight the superior performance of the proposed method CA_{prop} over the other two control allocation

TABLE V: Numeric values of trajectory parameters used in experiments

	x_0	A_x	ω_x	A_y	ω_y	A_z	ω_z	t^*	γ_1	γ_2
Ellipsoidal	0.3	1.75	0.06	1.0	0.06	0.2	0.03	0.2	7.0	1.0
Lissajous	0.3	1.5	0.045	0.7	0.045	0.25	0.03	0.2	7.0	1.0

methods in terms of force allocation errors. This superior performance is due to the fact that CA_{prop} is analytically designed to minimize the change in zero-direction angle. For CA_{opt} , even though the change in zero-direction angle is not considered in the optimization cost function, the optimization algorithm tends to favor the solution closest to the initial conditions of the fins' zero-directions. This results in notably better performance compared to the pseudo-inverse method CA_{inv} .

TABLE VI: Comparison of control allocation methods (CA_{prop} , CA_{opt} , and CA_{inv}) in terms of mean allocation errors for linear (MAE_{lin}) and angular (MAE_{ang}) DOF.

	CA_{prop}	CA_{opt}	CA_{inv}
MAE_{lin} [N]	0.293	1.369	2.451
MAE_{ang} [Nm]	0.206	0.467	2.613

B. Trajectory tracking simulation - 6T Scenario

Table VII summarizes the results for the 6T scenario. For the majority of evaluation metrics, the proposed method (CA_{prop}) outperformed the two other methods. It achieved the lowest RMSE in both linear and angular measures, implying better tracking performance. The difference in tracking performance between CA_{prop} and CA_{inv} is very notable, going from small errors of 4.3 cm and 3.4 deg to significant deviations of 1.15 m and 103 deg. The simple pseudo-inverse based control allocation is clearly inadequate to provide satisfactory tracking. CA_{inv} creates too much disturbance during fin rotations, because all fins are considered for providing propulsion in each DOF. This is minimized by explicitly choosing the number of fins to contribute to each DOF and the introduced force compensation in CA_{prop} , leading to significantly better tracking. In CA_{opt} , the minimization of fin rotations is not explicitly defined, but seems to be implicitly taken into account.

Furthermore, CA_{prop} demonstrated the smallest median actuation efforts (MAW, MAE_{lin} , MAE_{ang}), which suggests more efficient energy usage compared to the other tested methods. Again, the differences to CA_{inv} are significant, whereas the differences to CA_{opt} are close or within the variability of the reported metrics.

Furthermore, CA_{prop} and CA_{opt} demanded significantly less forces with better tracking results compared to CA_{inv} . CA_{prop} had the smallest MAW while CA_{opt} had the smallest MW, although the differences are very small in both cases. CA_{inv} , however, had maximum wrench demands that were well outside of the maximum wrench magnitude of 12.5 N indicating that actuators were demanded to operate above their limits.

In terms of computation time for control allocation CA_{inv} is the fastest, which can be expected as it includes the least amount of computations. Even though not the fastest, CA_{prop} 's

MCT is significantly less than the CA_{opt} , highlighting the main advantage of our proposed approach over the optimization based solution. Especially for resource constraint systems, the roughly 40 fold decrease in computation time can be very relevant. Additionally, at high update rates, a median MCT of 3.33 ms can create a computational bottleneck for systems using CA_{opt} when other computationally resource heavy algorithms for navigation and planning are to be employed too. Moreover, the much higher MCT also leads to a significantly higher effort to compute the controller gains with the GA significantly increasing run-time and energy consumption.

Generally, the results for CA_{prop} and CA_{opt} show that it is possible to precisely and efficiently track trajectories in 6-DOF with only four available actuators, by combining a state-of-the-art hybrid adaptive controller with smart control allocation.

TABLE VII: Summary statistics for represented by median (IQR), of defined evaluation metrics for MonteCarlo simulation framework with 500 trials in the 6T scenario. Results are presented for 3 different control allocation scenarios: CA_{prop} , CA_{opt} , CA_{inv} .

Summary Statistic	CA_{prop}	CA_{opt}	CA_{inv}
$RMSE_{lin}$ [m]	0.04 (0.02)	0.05 (0.01)	1.15 (0.3)
$RMSE_{ang}$ [rad]	0.06 (0.003)	0.07 (0.008)	1.83 (0.18)
MEM_{lin} [m]	0.15 (0.01)	0.15 (0.01)	2.4 (0.72)
MEM_{ang} [rad]	0.53 (0.04)	0.55 (0.06)	4.42 (0.48)
MAW [N]	1.34 (0.28)	1.69 (0.17)	6.93 (1.02)
MW [N]	4.19 (0.22)	4.34 (0.28)	38.68 (6.52)
MCT [ms]	0.08 (0.002)	3.3 (0.19)	0.07 (0.002)
MAE_{lin} [N]	0.48 (0.04)	0.71 (0.03)	5.0 (0.34)
MAE_{ang} [Nm]	0.32 (0.03)	0.42 (0.03)	1.37 (0.11)

C. Trajectory tracking simulation - 3T2S Scenario

Table VIII presents the results for the 3T2S scenario. Similar to the 6T scenario, CA_{prop} and CA_{opt} performed equally well, while the naive control allocation method CA_{inv} showed no satisfactory performance with a significantly high RMSE and inefficient median actuation efforts. Additionally, the maximum demanded wrenches for CA_{inv} again exceeded the maximum wrench magnitude of 12.5 N. For CA_{prop} and CA_{opt} the metrics show no discernible difference between the two tracking scenarios, indicating that the trajectory based sway compensation was successful in compensating the lack of sway forces. The simulation results show, that the employed trajectory generation, control and control allocation framework has very promising potential for efficient and precise 3D trajectory tracking with roll and pitch stabilization for non-holonomic vehicles with only four actuators.

The results for both tracking scenarios suggest that the proposed CA_{prop} control allocation method offers a compelling balance between high performance and actuator efficiency,

with considerable advantages in computational efficiency compared to CA_{opt} . This makes CA_{prop} a promising solution for both 6T and 3T2S scenarios for fin-actuated underwater robots.

TABLE VIII: Summary statistics, represented by median (IQR), of defined evaluation metrics for Monte Carlo simulation framework with 500 trials in the 3T2S scenario. Results are presented for 3 different control allocation scenarios: CA_{prop} , CA_{opt} , CA_{inv} .

Summary Statistic	CA_{prop}	CA_{opt}	CA_{inv}
$RMSE_{lin}$ [m]	0.04 (0.02)	0.05 (0.02)	2.1 (1.21)
$RMSE_{ang}$ [rad]	0.06 (0.02)	0.09 (0.05)	1.74 (0.12)
MEM_{lin} [m]	0.13 (0.03)	0.15 (0.05)	4.17 (2.14)
MEM_{ang} [rad]	0.34 (0.49)	0.7 (0.67)	3.22 (0.07)
MAW [N]	1.27 (0.24)	1.6 (0.15)	4.87 (2.07)
MW [N]	4.09 (0.12)	3.86 (0.34)	34.35 (6.87)
MCT [ms]	0.08 (0.009)	3.8 (0.55)	0.07 (0.002)
MAE_{lin} [N]	0.42 (0.02)	0.63 (0.06)	4.66 (1.12)
MAE_{ang} [Nm]	0.34 (0.03)	0.47 (0.04)	1.37 (0.15)

D. Experimental Results

Fig. 10 shows the ellipse trajectory tracking result of one trial. The results demonstrate that both the proposed and optimal control allocation solutions provide good tracking performance for all controlled DOF. Moreover, the line of sight implementation allowed for the tracking of the non-directly commanded sway component of the trajectory. While the roll and pitch components were not actively tracked, the robot's passive stability in these DOF maintained their tracking error close to zero with slight oscillations due to the oscillatory actuation method.

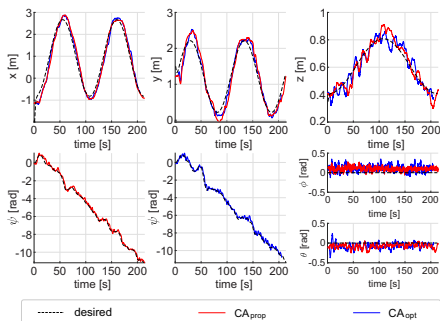


Fig. 10: Experimental tracking results for the 3D ellipsoidal trajectory: In dotted black line is the desired trajectory. In red line is performed trajectory using the proposed solution CA_{prop} . In blue line is performed trajectory using the optimal solution CA_{opt} .

Fig. 11 shows the whisker plot of all 5 runs for the ellipse trajectory tracking scenario. The results indicate that the optimal solution CA_{opt} slightly outperformed the proposed solution CA_{prop} in terms of tracking accuracy. The median error in tracking the surge component was higher for the proposed solution (33 cm) than for the optimal solution (22 cm).

This was due to the choice of controller gains, which were set to prevent the robot from overtaking the desired trajectory x_d , which would have resulted in the robot making a full turn.

Similarly, Fig. 12 shows the Lissajous trajectory tracking result of one trial, indicating good tracking performance for all controlled DOF with the non-directly commanded sway component of the trajectory also being tracked due to the line-of-sight implementation. The robot's passive stability in roll and pitch DOF maintained their tracking error close to 0 with slight oscillations due to the oscillatory actuation method.

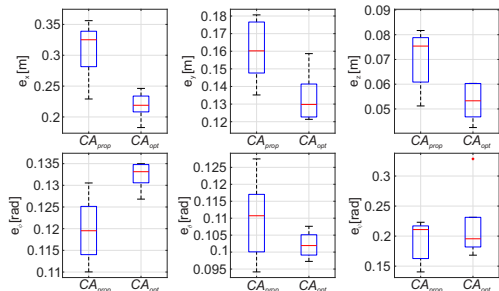


Fig. 11: Box-plot of tracking errors for the 3D ellipse trajectory.

Fig. 13 provides a box plot of all five runs for the Lissajous trajectory tracking scenario, showing that both solutions have good trajectory tracking performance. The largest median error was observed in tracking the surge component, with CA_{prop} having a median error of 41 cm and CA_{opt} having a median error of 25 cm. This can be again attributed to the specific controller gains employed to avoid the robot from surpassing the desired trajectory, resulting in the robot making a complete turn. We note that CA_{opt} gave a slightly better average tracking performance for all controlled DOF.

Generally, for both trajectories the tracking errors in

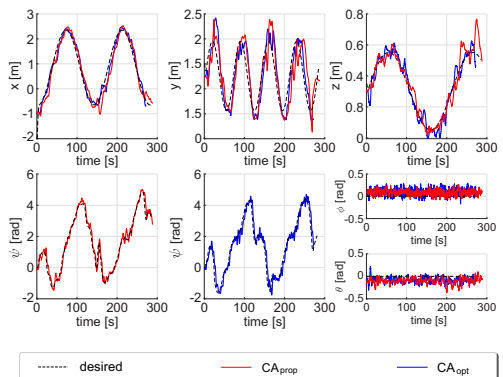


Fig. 12: Experimental tracking results for the 3D Lissajous trajectory: In dotted black line is the desired trajectory. In red line is performed trajectory using CA_{prop} solution. In blue line is performed trajectory using CA_{opt} solution.

the experiments were significantly higher compared to the simulation results. This can be explained by several simplifications and assumptions made for the simulations. During simulations we did not simulate the low-level motor control and assumed perfect and instantaneous tracking of the fin kinematics demanded by the CPG. However, for the physical vehicle, amplitude and frequency will not be perfectly tracked by the fin motors and each fin will exhibit certain time-lags. Additionally, the employed fin model (70) does not capture complex fluid-body interactions between the flexible fins and the surrounding water. During simulations we also did not assume any environmental disturbances. The experiments, however, were conducted in a public bath during regular opening hours. While one corner lane was reserved for the experiments, activity in the neighbouring lanes could affect the tracking experiments, specifically at low speeds. This is also a potential explanation for the superior performance of CA_{opt} compared to CA_{prop} , which is in contrast to the simulation results. During tests with CA_{opt} the amount of people in other lanes of the swimming pool and subsequent disturbances were less compared to tests with CA_{prop} . While such an effect should be fairly limited, the differences between the two control allocation algorithms was between 10cm to 15cm and below 1° making this a plausible explanation.

When comparing our RMSEs of maximal 8.5 cm in depth tracking and 11° in yaw tracking to the errors reported by previous control attempts for U-CAT or similar vehicles, 2.22 cm in depth set point stabilization and 2.91° in yaw tracking [65], 2.28 cm [18] in depth tracking and $1.2 \text{ cm} \pm 5.3 \text{ cm}$ again for depth tracking only, our depth and yaw tracking is slightly less accurate. However, in [18] and [22] only regulation to a constant depth without any tracking in other DOF was considered, while in [65] depth was again only regulated to a set-point and yaw was effectively decoupled from surge and heave. Taking this into account we show here a similar performance, while tracking more DOF than before. This comparison shows that the work presented here constitutes a significant step forward in terms of utilizing the agility and full potential of fin driven turtle like AUVs by expanding the tracked DOF while maintaining a similar level of accuracy compared to the state-of-the-art.

Given that we implemented the hybrid adaptive controller from Basso et al. [12], it makes sense to compare to their experimental results as well. Unfortunately, no numerical metrics for tracking performance are reported. However, based on the provided figures it seems that our tracking performance lies in a similar range, albeit slightly less accurate. When comparing the setup to Basso et al. [12] it should be noted that we can show a similar tracking performance with half the amount of actuators (8 vs 4) on a functionally non-holonomic system that lacks sway actuation. Additionally, we used a very rough approximation of the identified dynamics model [23] to populate the starting values for the adaptive parameters, whereas in [12] the starting values for the adaptive parameters were directly derived from an identified dynamics

model. We therefore conclude, that our results show a very satisfactory performance compared to the state-of-the-art in terms of control. Furthermore, we see a significant contribution of our work in the independent and successful replication of the work presented in [12] on a more complex system in terms of actuation. Additionally, we extended the applicability of the controller proposed by Basso et al. to non-holonomic systems.

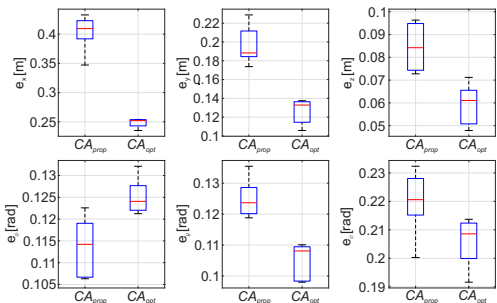


Fig. 13: Box-plot of tracking errors for the 3D Lissajous trajectory.

Fig. 14 shows the box-plot of the root mean square (RMS) of the generated controller outputs (τ^{des}) for both control allocation methods. The results indicate that the controller generated slightly higher forces in the linear directions surge and heave for CA_{prop} , and slightly lower torque for yaw. This can be explained by the introduction of the force compensation term f_{comp} (60) that minimizes change in zero-direction angle at the cost of an increase in necessary forces to compensate for the change in the thrust vector. This confirms a trade-off between disturbance minimization and energy efficiency regarding the actuators, which needs to be considered for each specific application.

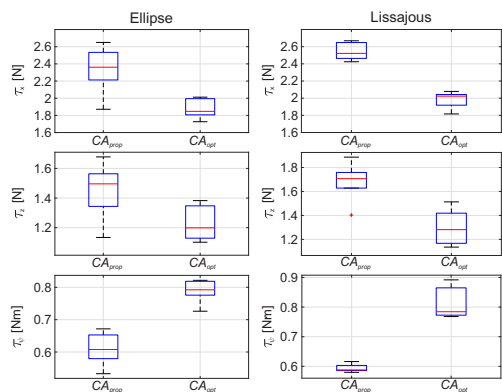


Fig. 14: Box-plot of root mean square forces and torques. Left: During ellipse trajectory. Right: During Lissajous trajectory.

The computation times for the two control allocation methods were calculated on the robot's Jetson TX2 embedded computer and are compared in Table IX. For the CA_{prop} method, the mean computation times for both ellipse

TABLE IX: Computation times for CA_{prop} and CA_{opt} methods

Trajectory type	CA_{prop}		CA_{opt}	
	Ellipse	Lissajous	Ellipse	Lissajous
Mean time (ms)	0.0068	0.0067	22.2779	21.0504
Max time (ms)	0.3199	0.1588	3931.6030	1812.4072

and Lissajous trajectories were very similar, approximately 0.0068 ms and 0.0067 ms respectively. The reported maximum computation time for both trajectories was less than a third of a millisecond. In contrast, the CA_{opt} method needed considerably longer computation times. The mean times were about 22 ms and 21 ms for the ellipse and Lissajous trajectories respectively. The maximum times increased drastically for the CA_{opt} method, with ≈ 3931 ms for the ellipse and ≈ 1812 ms for the Lissajous trajectory. The difference in computation times is higher than in the simulations, given that the the Jetson TX2 as embedded computer has less computational capacity compared to a laptop. This highlights the big advantage of our proposed control allocation method further. Finally, Fig. 15 a) and Fig. 15 b) show the mean accumulated rotations by the four fins for the ellipse and Lissajous trajectories, respectively. The results indicate that CA_{prop} demands less in terms of actuation efforts, which results in better energy efficiency.

A limitation of the presented experimental setup is that roll and pitch tracking or stabilization could not be tested. The standard configuration of centre of mass and centre of buoyancy of U-CAT created restoring moments to passively stabilize pitch and roll. However, in conjunction with unaccounted internal and periodic disturbances due to the fin oscillations this passive restoration seemed to have interfered with the ability for active stabilization, possibly exceeding the available control authority of the actuators. Nevertheless, active stabilization was possible in the simulations although the oscillation disturbances were taken into account by the fin dynamics simulation (71). We therefore conclude that the removal of passive restoring forces should enable active roll and pitch stabilization. However, the mechanical re-configuration of the vehicle to achieve the alignment of centre of mass and centre of buoyancy was beyond the scope of the current work. Another limitation of the work presented here lies within the tested velocities for tracking. Maximum tested velocities approached 0.2 m/s, which can be sufficient for many intended monitoring tasks. However, in the presence of strong water currents this limit can constitute a problem. One reason for the limited velocities tested was the available experimental setup, which did not allow the motion over bigger areas, implicitly limiting achievable velocities. Another limitation is the thrust output that can be generated by the current fin design. However, those limitations are mainly the results of engineering challenges and can be overcome. We don't see any fundamental limitations of the presented work in regards to attainable velocities within certain bounds.

Notwithstanding the present limitations we constitute that the obtained simulation and experimental results present a

comprehensive analysis of the proposed solution, highlighting its effectiveness and potential for further improvement. The experiments demonstrate that the proposed solution yields good tracking performance for all controlled DOF. Specifically, the methods are shown to effectively track complex 3D trajectories with minimal tracking error while maintaining efficient control, actuation efforts, and minimal computational time.

VIII. CONCLUSION AND FUTURE WORK

This study presented an in-depth investigation into 6-DOF tracking control using an under- and fin-actuated AUV. The core of our work was the development of an innovative analytic control allocation method for fin-driven AUVs. The allocation is supplemented by the adaptation and extension of a state-of-the-art hybrid adaptive controller, which facilitates globally stable 6-DOF trajectory tracking control. The novel control allocation method allows for simultaneous control of all six DOF using only four actuators. By addressing the specific challenges posed by fin-based actuation, our proposed method achieves both computational and energetic efficiency, enabling accurate trajectory tracking and improved efficiency.

The developed hybrid controller exhibits significant potential for enabling simultaneous 6-DOF control for an under-actuated fin-actuated AUV, thereby advancing the field towards more sophisticated and versatile underwater robots. This method was tested and validated through extensive Monte Carlo simulations and real-world experiments in a semi-controlled environment (public swimming pool), employing two types of 3D complex trajectories (ellipse and Lissajous) in three-degrees-of-freedom tracking and two-degrees-of-stability scenarios. The proposed analytic control allocation solution (CA_{prop}) was found to be robust and efficient in both the simulation and experimental settings, bringing us one step closer to realising fully autonomous 6-DOF navigation for fin-actuated AUVs.

In terms of future work, our goal is to extend this research to include fault-tolerant control for fin-actuated AUVs. Moreover, we intend to conduct real-world experiments in diverse underwater environments to further validate and refine our approach under varying conditions and challenges. To further optimise the efficiency and performance of control allocation for fin-actuated vehicles, the integration of advanced reinforcement learning techniques will be explored.

This research signifies a significant milestone in the field of under-actuated fin-actuated AUVs. By continuously striving to refine and expand upon this work, we aim to pioneer novel solutions that advance the capabilities of AUVs, making them more versatile and efficient for a broader range of underwater missions.

REFERENCES

- [1] B. Allotta, R. Costanzi, A. Ridolfi, O. Salvetti, M. Reggiannini, M. Krusmaa, T. Salumae, D. M. Lane, G. Frost, N. Tsiogkas *et al.*, "The arrows project: robotic technologies for underwater archaeology," in *IOP conference series: materials science and engineering*, vol. 364, no. 1. IOP Publishing, 2018, p. 012088.

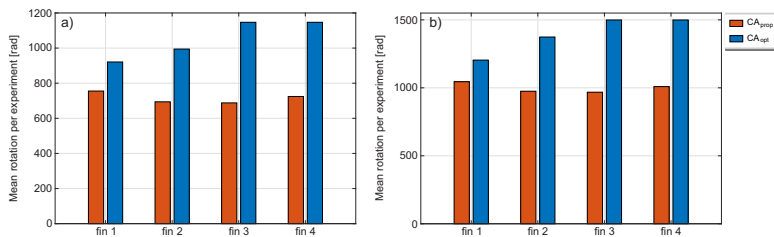


Fig. 15: Mean accumulated rotation of U-CAT's four fins per experiment for a) the ellipse trajectory and b) the Lissajous trajectory.

- [2] R. K. Katzschmann, J. DelPreto, R. MacCurdy, and D. Rus, "Exploration of underwater life with an acoustically controlled soft robotic fish," *Science Robotics*, vol. 3, no. 16, p. eaar3449, 2018.
- [3] M. Kruusmaa, R. Gkliva, J. Tuhtan, A. Tuvikene, and J. A. Alfreksen, "Salmon behavioural response to robots in an aquaculture sea cage," *Royal Society open science*, vol. 7, no. 3, p. 191220, 2020.
- [4] R. Bachmayer, A. Kausche, P. Riesen, and P. Gutierrez, "Concept development for a minimally invasive autonomous underwater vehicle," in *2020 IEEE/OES Autonomous Underwater Vehicles Symposium (AUV)*. IEEE, 2020, pp. 1–3.
- [5] B. P. Epps, P. Valdivia y Alvarado, K. Youcef-Toumi, and A. H. Tchet, "Swimming performance of a biomimetic compliant fish-like robot," *Experiments in fluids*, vol. 47, pp. 927–939, 2009.
- [6] T. Salumäe and M. Kruusmaa, "Flow-relative control of an underwater robot," *Proceedings of the Royal Society A: Mathematical, Physical and Engineering Sciences*, vol. 469, no. 2153, p. 20120671, 2013.
- [7] G. Dudek, P. Giguere, C. Prahacs, S. Saunderson, J. Sattar, L.-A. Torres-Mendez, M. Jenkin, A. German, A. Hogue, A. Ripsman *et al.*, "Aqua: An amphibious autonomous robot," *Computer*, vol. 40, no. 1, pp. 46–53, 2007.
- [8] C. Siegenthaler, C. Pradaliere, F. Günther, G. Hitz, and R. Siegwart, "System integration and fin trajectory design for a robotic sea-turtle," in *2013 IEEE/RSJ International Conference on Intelligent Robots and Systems*. IEEE, 2013, pp. 3790–3795.
- [9] T. Salumäe, R. Raag, J. Rebane, A. Ernits, G. Toming, M. Ratas, and M. Kruusmaa, "The arrows project: adapting and developing robotics technologies for underwater archaeology," in *IEEE Oceans-St. John's*, 2014, pp. 1–5.
- [10] S. C. Licht, "Biomimetic oscillating foil propulsion to enhance underwater vehicle agility and maneuverability," WOODS HOLE OCEANOGRAPHIC INSTITUTION MA, Tech. Rep., 2008.
- [11] J. D. Geder, R. Ramamurti, M. Pruessner, and J. Palmisano, "Maneuvering performance of a four-fin bio-inspired uuv," in *2013 OCEANS-San Diego*. IEEE, 2013, pp. 1–7.
- [12] E. A. Basso, H. M. Schmidt-Didlaukies, K. Y. Pettersen, and A. J. Sorensen, "Global asymptotic tracking for marine vehicles using adaptive hybrid feedback," *IEEE Transactions on Automatic Control*, 2022.
- [13] A. Konno, T. Furuya, A. Mizuno, K. Hishinuma, K. Hirata, and M. Kawada, "Development of turtle-like submergence vehicle," in *Proceedings of the 7th international symposium on marine engineering*, 2005.
- [14] K.-H. Low, C. Zhou, T. Ong, and J. Yu, "Modular design and initial gait study of an amphibian robotic turtle," in *2007 IEEE International Conference on Robotics and Biomimetics (ROBIO)*. IEEE, 2007, pp. 535–540.
- [15] W. Zhao, Y. Hu, L. Wang, and Y. Jia, "Development of a flipper propelled turtle-like underwater robot and its cpg-based control algorithm," in *2008 47th IEEE Conference on Decision and Control*. IEEE, 2008, pp. 5226–5231.
- [16] G. Yao, J. Liang, T. Wang, X. Yang, Q. Shen, Y. Zhang, H. Wu, and W. Tian, "Development of a turtle-like underwater vehicle using central pattern generator," in *2013 IEEE International Conference on Robotics and Biomimetics (ROBIO)*. IEEE, 2013, pp. 44–49.
- [17] C. Wang, G. Xie, X. Yin, L. Li, and L. Wang, "Cpg-based locomotion control of a quadruped amphibious robot," in *2012 IEEE/ASME International Conference on Advanced Intelligent Mechatronics (AIM)*. IEEE, 2012, pp. 1–6.
- [18] A. Chemori, K. Kuusmik, T. Salumäe, and M. Kruusmaa, "Depth control of the biomimetic u-cat turtle-like auv with experiments in real operating conditions," in *2016 IEEE International Conference on Robotics and Automation (ICRA)*. IEEE, 2016, pp. 4750–4755.
- [19] N. Fischer, D. Hughes, P. Walters, E. M. Schwartz, and W. E. Dixon, "Nonlinear rise-based control of an autonomous underwater vehicle," *IEEE Transactions on Robotics*, vol. 30, no. 4, pp. 845–852, 2014.
- [20] N. Plamondon and M. Nahon, "A trajectory tracking controller for an underwater hexapod vehicle," *Bioinspiration & biomimetics*, vol. 4, no. 3, p. 036005, 2009.
- [21] N. Plamondon, "Modeling and control of a biomimetic underwater vehicle," Ph.D. dissertation, McGill University, 2010.
- [22] P. Giguere, Y. Girdhar, and G. Dudek, "Wide-speed autopilot system for a swimming hexapod robot," in *2013 International Conference on Computer and Robot Vision*. IEEE, 2013, pp. 9–15.
- [23] T. Salumäe, A. Chemori, and M. Kruusmaa, "Motion control of a hovering biomimetic four-fin underwater robot," *IEEE Journal of Oceanic Engineering*, vol. 44, no. 1, pp. 54–71, 2017.
- [24] T. I. Fossen, *Handbook of marine craft hydrodynamics and motion control*. John Wiley & Sons, 2011.
- [25] D. A. Smallwood and L. L. Whitcomb, "The effect of model accuracy and thruster saturation on tracking performance of model based controllers for underwater robotic vehicles: experimental results," in *Proceedings 2002 IEEE International Conference on Robotics and Automation (Cat. No. 02CH37292)*, vol. 2. IEEE, 2002, pp. 1081–1087.
- [26] T. I. Fossen and S. I. Sagatun, "Adaptive control of nonlinear systems: A case study of underwater robotic systems," *Journal of Robotic Systems*, vol. 8, no. 3, pp. 393–412, 1991.
- [27] G. Antonelli, F. Caccavale, S. Chiaverini, and G. Fusco, "A novel adaptive control law for autonomous underwater vehicles," in *Proceedings 2001 ICRA. IEEE International Conference on Robotics and Automation (Cat. No. 01CH37164)*, vol. 1. IEEE, 2001, pp. 447–452.
- [28] K. D. von Ellenrieder, "Stable backstepping control of marine vehicles with actuator rate limits and saturation," *IFAC-PapersOnLine*, vol. 51, no. 29, pp. 262–267, 2018.
- [29] E. Fresk and G. Nikolakopoulos, "Full quaternion based attitude control for a quadrotor," in *2013 European control conference (ECC)*. IEEE, 2013, pp. 3864–3869.
- [30] S. Louis, L. Lapiere, Y. Onmek, K. G. Dejean, T. Claverie, and S. Villéger, "Quaternion based control for robotic observation of marine diversity," in *OCEANS 2017-Aberdeen*. IEEE, 2017, pp. 1–7.
- [31] S. P. Bhat and D. S. Bernstein, "A topological obstruction to continuous global stabilization of rotational motion and the unwinding phenomenon," *Systems & control letters*, vol. 39, no. 1, pp. 63–70, 2000.
- [32] O.-E. Fjellstad and T. I. Fossen, "Singularity-free tracking of unmanned underwater vehicles in 6 dof," in *Proceedings of 1994 33rd IEEE Conference on Decision and Control*, vol. 2. IEEE, 1994, pp. 1128–1133.
- [33] C. G. Mayhew, R. G. Sanfelice, and A. R. Teel, "Quaternion-based hybrid control for robust global attitude tracking," *IEEE Transactions on Automatic control*, vol. 56, no. 11, pp. 2555–2566, 2011.
- [34] A. R. Teel, "Robust hybrid control systems: An overview of some recent results," *Advances in control theory and applications*, pp. 279–302, 2007.
- [35] T. A. Johansen and T. I. Fossen, "Control allocation—a survey," *Automatica*, vol. 49, no. 5, pp. 1087–1103, 2013.
- [36] W. C. Durham, "Constrained control allocation," *Journal of Guidance, control, and Dynamics*, vol. 16, no. 4, pp. 717–725, 1993.

- [37] M. W. Oppenheimer, D. B. Doman, and M. A. Bolender, "Control allocation for over-actuated systems," in *2006 14th Mediterranean Conference on Control and Automation*. IEEE, 2006, pp. 1–6.
- [38] R. J. Adams, J. M. Buffington, A. G. Sparks, and S. S. Banda, *Robust multivariable flight control*. Springer Science & Business Media, 2012.
- [39] J. M. Buffington and D. F. Enns, "Lyapunov stability analysis of daisy chain control allocation," *Journal of Guidance, Control, and Dynamics*, vol. 19, no. 6, pp. 1226–1230, 1996.
- [40] M. Bodson, "Evaluation of optimization methods for control allocation," *Journal of Guidance, Control, and Dynamics*, vol. 25, no. 4, pp. 703–711, 2002.
- [41] J. A. Paradiso, "Adaptable method of managing jets and aerosurfaces for aerospace vehicle control," *Journal of Guidance, Control, and Dynamics*, vol. 14, no. 1, pp. 44–50, 1991.
- [42] O. Harkegard, "Efficient active set algorithms for solving constrained least squares problems in aircraft control allocation," in *Proceedings of the 41st IEEE Conference on Decision and Control, 2002.*, vol. 2. IEEE, 2002, pp. 1295–1300.
- [43] J. A. Petersen and M. Bodson, "Constrained quadratic programming techniques for control allocation," *IEEE Transactions on Control Systems Technology*, vol. 14, no. 1, pp. 91–98, 2005.
- [44] S. Jin, J. Kim, J. Kim, and T. Seo, "Six-degree-of-freedom hovering control of an underwater robotic platform with four tilting thrusters via selective switching control," *IEEE/ASME Transactions on mechatronics*, vol. 20, no. 5, pp. 2370–2378, 2015.
- [45] J. Bak, Y. Moon, J. Kim, S. Mohan, T. Seo, and S. Jin, "Hovering control of an underwater robot with tilting thrusters using the decomposition and compensation method based on a redundant actuation model," *Robotics and Autonomous Systems*, vol. 150, p. 103995, 2022.
- [46] Fjellstad and Fossen, "Quaternion feedback regulation of underwater vehicles," in *1994 Proceedings of IEEE International Conference on Control and Applications*. IEEE, 1994, pp. 857–862.
- [47] R. G. Sanfelice, M. J. Messina, S. E. Tuna, and A. R. Teel, "Robust hybrid controllers for continuous-time systems with applications to obstacle avoidance and regulation to disconnected set of points," in *2006 American Control Conference*. IEEE, 2006, pp. 6–pp.
- [48] R. Goebel, R. G. Sanfelice, and A. R. Teel, "Hybrid dynamical systems," *IEEE control systems magazine*, vol. 29, no. 2, pp. 28–93, 2009.
- [49] W. Remmas, A. Chemori, and M. Kruusmaa, "Inverse-model intelligent control of fin-actuated underwater robots based on drag force propulsion," *Ocean Engineering*, vol. 239, p. 109883, 2021.
- [50] J. Slotine and M. Di Benedetto, "Hamiltonian adaptive control of spacecraft," *IEEE Transactions on Automatic Control*, vol. 35, no. 7, pp. 848–852, 1990.
- [51] B. Paden and R. Panja, "Globally asymptotically stable 'pd+' controller for robot manipulators," *International Journal of Control*, vol. 47, no. 6, pp. 1697–1712, 1988.
- [52] M. Krstic, P. V. Kokotovic, and I. Kanellakopoulos, *Nonlinear and adaptive control design*. John Wiley & Sons, Inc., 1995.
- [53] Z. Ren, T. Wang, and L. Wen, "Hydrodynamic function of a robotic fish caudal fin: effect of kinematics and flow speed," in *2015 IEEE/RSJ International Conference on Intelligent Robots and Systems (IROS)*. IEEE, 2015, pp. 3882–3887.
- [54] P. T. Boggs and J. W. Tolle, "Sequential quadratic programming," *Acta numerica*, vol. 4, pp. 1–51, 1995.
- [55] R. Bracewell, *The Fourier Transform and its Applications, 3rd ed.* New York: McGraw-Hill, 2000.
- [56] A. Sproewitz, R. Moeckel, J. Maye, and A. J. Ijspeert, "Learning to move in modular robots using central pattern generators and online optimization," *The International Journal of Robotics Research*, vol. 27, no. 3–4, pp. 423–443, 2008.
- [57] N. Palomeras, S. Nagappa, D. Ribas, N. Gracias, and M. Carreras, "Vision-based localization and mapping system for auv intervention," in *2013 MTS/IEEE OCEANS-Bergen*. IEEE, 2013, pp. 1–7.
- [58] C. Georgiades, M. Nahon, and M. Buehler, "Simulation of an underwater hexapod robot," *Ocean Engineering*, vol. 36, no. 1, pp. 39–47, 2009.
- [59] A. J. Healey, S. Rock, S. Cody, D. Miles, and J. Brown, "Toward an improved understanding of thruster dynamics for underwater vehicles," *IEEE Journal of oceanic Engineering*, vol. 20, no. 4, pp. 354–361, 1995.
- [60] C. Georgiades, A. German, A. Hogue, H. Liu, C. Prahacs, A. Ripsman, R. Sim, L.-A. Torres, P. Zhang, M. Buehler et al., "Aqua: an aquatic walking robot," in *2004 IEEE/RSJ International Conference on Intelligent Robots and Systems (IROS)(IEEE Cat. No. 04CH37566)*, vol. 4. IEEE, 2004, pp. 3525–3531.
- [61] M. M. M. Manhaes, S. A. Scherer, L. R. Douat, M. Voss, and T. Rauschenbach, "Use of simulation-based performance metrics on the evaluation of dynamic positioning controllers," in *OCEANS 2017-Aberdeen*. IEEE, 2017, pp. 1–8.
- [62] R. M. Solgi, "geneticalgorithm," <https://pypi.org/project/geneticalgorithm/>, 2020, accessed: March 27, 2023.
- [63] S. Garrido-Jurado, R. Muñoz-Salinas, F. J. Madrid-Cuevas, and M. J. Marín-Jiménez, "Automatic generation and detection of highly reliable fiducial markers under occlusion," *Pattern Recognition*, vol. 47, no. 6, pp. 2280–2292, 2014.
- [64] A. Project, "Alglib," <https://www.alglib.net/>, 2023, accessed: March 27, 2023.
- [65] T. Salumäe, A. Chemori, and M. Kruusmaa, "Motion control architecture of a 4-fin u-cat auv using dof prioritization," in *2016 IEEE/RSJ International Conference on Intelligent Robots and Systems (IROS)*. IEEE, 2016, pp. 1321–1327.



Walid Remmas received his M.Sc. degree in control system engineering from the Polytechnic School of Constantine, Algeria, in 2017. He received his second M.Sc. degree in robotics from the University of Montpellier, France, in 2018. He is currently working toward the Ph.D. degree with the Centre for Biorobotics at Tallinn University of Technology, Estonia. His research interests include intelligent control, underwater robotics, and biorobotics.



Christian Meurer received his Ph.D. in Computer and Systems Engineering from Tallinn University of Technology (TalTech), Tallinn, Estonia in 2021. He is currently working as postdoctoral researcher at the Center for Marine Environmental Sciences (MARUM), University of Bremen, Bremen, Germany. His research interests include bio-inspired sensing and actuation for underwater vehicles, nonlinear modeling and control, as well as the design and development of small, low-cost, and robust AUVs for minimally invasive long-term monitoring

of the environment.



Ahmed Chemori received the M.Sc. and Ph.D. degrees both in automatic control from the Grenoble Institute of Technology, Grenoble, France, in 2001 and 2005, respectively. He has been a Postdoctoral Fellow with the Automatic Control Laboratory, Grenoble, France, in 2006. He is currently a tenured Research Scientist in automatic control and robotics with the Montpellier Laboratory of Informatics, Robotics, and Microelectronics. His research interests include nonlinear robust adaptive, and predictive control and their real-time applications in robotics.



environments and on flowable media and novel methods for underwater flow sensing.

Maarja Kruusmaa received her Ph.D. from Chalmers University of Technology in 2002 and since 2008 is a professor in Tallinn University of Technology (TalTech) as a PI of Centre for Biorobotics, a research group focusing on bio-inspired robotics, underwater robotics and novel underwater sensing technologies. 2017 - 2022 she was a visiting professor in NTNU AMOS (Centre for Excellence of Autonomous Marine Operations and Systems). Her research interests include novel locomotion mechanisms for underwater

Curriculum vitae

Mohamed Walid Remmas

Date of birth 15.01.1994
ORCID 0000-0001-8690-0496
E-mail walid.remmas@taltech.ee

Fields of research

ETIS RESEARCH FIELD: 4. Natural Sciences and Engineering; 4.13. Mechanical Engineering, Automation Technology and Manufacturing Technology; CERCS RESEARCH FIELD: T125 Automation, robotics, control engineering ; SPECIFICATION: Soft Robotics

Institutions and positions

01.12.2018– Tallinn University of Technology, School of Information
31.12.2023 Technologies, Department of Computer Systems, Junior
Researcher (0,80)

01.12.2018– Tallinn University of Technology, School of Information
31.08.2022 Technologies, Department of Computer Systems, Other staff
(0,50)

Additional information

Academic degrees

Mohamed Walid Remmas, Master's Degree, 2018, (sup) Ahmed Chemori; Maarja Kruusmaa, High-Level Control of a Biomimetic Turtle-Like AUV based on Data-Fusion, University of Montpellier.

Mohamed Walid Remmas, Master's Degree, 2017, (sup) Ahmed Chemori; Khaled Belarbi, Commande Avancée d'un Robot Sous-marin Bio-inspiré (Advanced control of a bio-inspired underwater robot), National Polytechnic School of Constantine.

Mohamed Walid Remmas, Phd student, (sup) Maarja Kruusmaa; Ahmed Chemori, Motion Control of Variable Stiffness Actuators, Tallinn University of Technology School of Information Technologies, Department of Computer Systems.

Honours & awards

2017 Best MSc student within the National Polytechnic School of Constantine

Education

01.09.2017– 31.08.2018	MSc Robotics, University of Montpellier, France
01.09.2014– 01.07.2017	Control systems Engineer degree, National Polytechnic School of Constantine, Algeria
01.09.2012– 30.06.2014	Preparatory school in Sciences and Technologies, EPST Oran, Algeria

Completed projects

- VFP19025 "Resilient Bio-inspired Modular Robotic Miners" (1.06.2019–31.05.2023); Principal Investigator: Maarja Kruusmaa; Tallinn University of Technology, School of Information Technologies, Department of Computer Systems (partner); Financier: European Commission; Financing: 633 750 EUR.
- PRG1243 "Multiscale Natural Flow Sensing for Coasts and Rivers" (1.01.2021–31.12.2021); Principal Investigator: Jeffrey Andrew Tuhtan; Tallinn University of Technology, School of Information Technologies, Department of Computer Systems; Financier: Estonian Research Council; Financing: 257 125 EUR.
- COVSG40 "Hospital robot carrier" (1.09.2020–31.12.2021); Principal Investigator: Innar Liiv; Tallinn University of Technology, School of Information Technologies, Department of Software Science; Financier: Estonian Research Council; Financing: 120 000 EUR.
- IUT33-9 "Bio-inspired underwater robots" (1.01.2015–31.12.2020); Principal Investigator: Maarja Kruusmaa; Tallinn University of Technology, School of Information Technologies, Centre for Biorobotics, Tallinn University of Technology, School of Information Technologies, Department of Computer Systems; Financier: Estonian Research Council; Financing: 843 084 EUR.

Supervised dissertations

- Tanel Kossas, Master's Degree, 2023, (sup) Mohamed Walid Remmas; Roza Gkliva, Tactile Navigation Algorithm for Autonomous Underground Mining Robots, Tallinn University of Technology, School of Information Technologies, Department of Computer Systems
- Kaarel Värk, Master's Degree, 2021, (sup) Christian Meurer; Mohamed Walid Remmas, Gaussian Process Based Dynamics Model Augmentation for an Autonomous Underwater Vehicle with Bio-Inspired Actuators, Tallinn University of Technology School of Information Technologies, Department of Computer Systems
- Moutaz Mohamed Fathy Ahmed Aboseada, Master's Degree, 2020, (sup) Jeffrey Andrew Tuhtan; Mohamed Walid Remmas, Underwater Object Detection Using Deep Learning, Tallinn University of Technology School of Information

Publications

2023

Remmas, Walid; Chemori, Ahmed; Kruusmaa, Maarja (2023). Fault-tolerant control allocation for a bio-inspired underactuated AUV in the presence of actuator failures: Design and experiments;. *Ocean Engineering*, 285, ARTN 115327.

2022

Remmas, Walid; Gkliva, Roza; Ristolainen, Asko (2022). Dynamic modelling of a screw actuator for improved locomotion control on various terrains. *EGU General Assembly 2022: EGU General Assembly 2022, Vienna, Austria, 23–27 May 2022*. Copernicus GmbH, EGU22-5726.

2021

Remmas, W., Chemori, A., & Kruusmaa, M. (2021). Inverse-model intelligent control of fin-actuated underwater robots based on drag force propulsion. *Ocean Engineering*, 239, 109883.

2021

Remmas, W., Chemori, A., & Kruusmaa, M. (2021). Diver tracking in open waters: A low-cost approach based on visual and acoustic sensor fusion. *Journal of Field Robotics*, 38(3), 494-508.

Curriculum vitae

Mohamed Walid Remmas

Sünniaeg 15.01.1994
ORCID 0000-0001-8690-0496
E-post walid.remmas@taltech.ee

Teadustöö põhisuunad

ETIS VALDKOND: 4. Loodusteadused ja tehnika; 4.13. Mehhanotehnika, automaatika, tööstustehnoloogia; CERCS VALDKOND: T125 Automatiseerimine, robotika, juhtimistehnika; TÄPSUSTUS: Soft Robotics

Töökohad ja ametid

01.12.2018–31.12.2023 Tallinna Tehnikaülikool, Infotehnoloogia teaduskond, Arvutisüsteemide instituut, nooremteadur (0,80)
01.12.2018–31.08.2022 Tallinna Tehnikaülikool, Infotehnoloogia teaduskond, Arvutisüsteemide instituut, doktorant-nooremteadur (0,50)

Lisainfo

- Co-teaching the Master's robotics class (IAS0060).

Teaduskraadid

Mohamed Walid Remmas, magistrikraad, 2018, (juh) Ahmed Chemori; Maarja Kruusmaa, High-Level Control of a Biomimetic Turtle-Like AUV based on Data-Fusion, Université de Montpellier.

Mohamed Walid Remmas, magistrikraad, 2017, (juh) Ahmed Chemori; Khaled Belarbi, Commande Avancée d'un Robot Sous-marin Bio-inspiré, Ecole Nationale Polytechnique de Constantine.

Mohamed Walid Remmas, doktorant, (juh) Maarja Kruusmaa; Ahmed Chemori, Motion Control of Variable Stiffness Actuators, Tallinna Tehnikaülikool, Infotehnoloogia teaduskond, Arvutisüsteemide instituut.

Teaduspreemiad ja tunnustused

2017 Best MSc student within the National Polytechnic School of Constantine

Haridustee

01.09.2017– 31.08.2018	MSc Robotics, University of Montpellier, France
01.09.2014– 01.07.2017	Control systems Engineer degree, National Polytechnic School of Constantine, Algeria
01.09.2012– 30.06.2014	Preparatory school in Sciences and Technologies, EPST Oran, Algeria

Lõppenud projektid

- VFP19025 "Kohanemisvõimelised kaevandusrobotid" (1.06.2019–31.05.2023); Vastutav täitja: Maarja Kruusmaa; Tallinna Tehnikaülikool, Infotehnoloogia teaduskond, Arvutisüsteemide instituut (partner); Finantseerija: Euroopa Komisjon; Eraldatud summa: 633 750 EUR.
- PRG1243 "Mitmemastaabiline looduslike veevoolude mõõtmine rannikualadele ja jõgedele" (1.01.2021–31.12.2021); Vastutav täitja: Jeffrey Andrew Tuhtan; Tallinna Tehnikaülikool, Infotehnoloogia teaduskond, Arvutisüsteemide instituut; Finantseerija: Sihtasutus Eesti Teadusagentuur; Eraldatud summa: 257 125 EUR.
- COVSG40 "Haigla transpordiroboti väljatöötamine" (1.09.2020–31.12.2021); Vastutav täitja: Innar Liiv; Tallinna Tehnikaülikool, Infotehnoloogia teaduskond, Tarkvarateaduse instituut; Finantseerija: Sihtasutus Eesti Teadusagentuur; Eraldatud summa: 120 000 EUR.
- IUT33-9 "Bioloogiast inspireeritud allveerobotid " (1.01.2015–31.12.2020); Vastutav täitja: Maarja Kruusmaa; Tallinna Tehnikaülikool, Infotehnoloogia teaduskond, Biorobotika keskus, Tallinna Tehnikaülikool, Infotehnoloogia teaduskond, Arvutisüsteemide instituut; Finantseerija: Sihtasutus Eesti Teadusagentuur; Eraldatud summa: 843 084 EUR.

Juhendatud väitekirjad

- Tanel Kossas, magistriskraad, 2023, (juh) Mohamed Walid Remmas; Roza Gkliva, Tactile Navigation Algorithm for Autonomous Underground Mining Robots (Tehislikel tundlatel põhinev navigatsioonialgoritm autonoomsetele maa-alustele kaevandusrobotitele), Tallinna Tehnikaülikool, Infotehnoloogia teaduskond, Arvutisüsteemide instituut
- Kaarel Värk, magistriskraad, 2021, (juh) Christian Meurer; Mohamed Walid Remmas, Gaussian Process Based Dynamics Model Augmentation for an Autonomous Underwater Vehicle with Bio-Inspired Actuators (Bio-inspireeritud aktuaatoritega autonoomse veealuse sõiduki dünaamilise mudeli täiustamine Gaussi protsessi abil), Tallinna Tehnikaülikool, Infotehnoloogia teaduskond, Arvutisüsteemide instituut
- Moutaz Mohamed Fathy Ahmed Aboseada, magistriskraad, 2020, (juh) Jeffrey Andrew Tuhtan; Mohamed Walid Remmas, Underwater Object Detection Using Deep Learning (Veealune objektituvastus kasutades süvaõpet), Tallinna Tehnikaülikool, Infotehnoloogia teaduskond, Arvutisüsteemide instituut.

Publikatsioonid

2023

Remmas, Walid; Chemori, Ahmed; Kruusmaa, Maarja (2023). Fault-tolerant control allocation for a bio-inspired underactuated AUV in the presence of actuator failures: Design and experiments;. *Ocean Engineering*, 285, ARTN 115327.

2022

Remmas, Walid; Gkliva, Roza; Ristolainen, Asko (2022). Dynamic modelling of a screw actuator for improved locomotion control on various terrains. *EGU General Assembly 2022: EGU General Assembly 2022, Vienna, Austria, 23–27 May 2022*. Copernicus GmbH, EGU22-5726.

2021

Remmas, W.; Chemori, A.; Kruusmaa, M. (2021). Inverse-model intelligent control of fin-actuated underwater robots based on drag force propulsion. *Ocean Engineering*, 239, ARTN109883.

2021

Remmas, W., Chemori, A., & Kruusmaa, M. (2021). Diver tracking in open waters: A low-cost approach based on visual and acoustic sensor fusion. *Journal of Field Robotics*, 38(3), 494-508.

ISSN 2585-6901 (PDF)
ISBN 978-9916-80-095-9 (PDF)